The University Of Sheffield.

Radiolysis and radiation damage effects in cements used in nuclear waste storage and disposal in the UK

Sarah Kearney

A thesis submitted in partial fulfilment of the requirements for the degree of Doctor of Philosophy

The University of Sheffield

Faculty of Engineering

Department of Materials Science and Engineering

June 2020

Abstract

UK policy for the management of intermediate level waste (ILW) employs processing via encapsulation in cementitious grouts to produce wasteforms suitable for safe long-term storage and disposal. These wasteforms are intended to provide a physical and chemical barrier to prevent the release of harmful radionuclides present within the ILW to the biosphere until decay to acceptable levels has occurred. This requires the cementitious grouts to be operational for potentially thousands of years in an extreme service environment involving exposure to radiation. The impact of high levels of radiation on these grouts, which are typically blends of Portland cement (PC) with high volume replacement by supplementary cementitious materials (SCMs), is not currently well understood. In order to allow appropriate design of a geological disposal facility (GDF), it is important to understand how the effects of radiation manifest in the encapsulation cements and what impact this may have on their performance.

This thesis investigates the impact of gamma and alpha radiation on grout formulations commonly used by the UK nuclear industry; these consisted of PC with high volume replacement by blast furnace slag (BFS) or pulverised fuel ash (PFA). Four blends representative of the Sellafield formulation envelope for BFS:PC (3:1, 3.44:1, 5.67:1 and 9:1) were investigated, together with a single 3:1 blend of PFA:PC. The BFS:PC grouts were subjected to gamma irradiation, with increasing levels of total absorbed dose up to 20 MGy achieved. Analysis found elevated carbonation considered to be caused by irradiation in samples with increasing total absorbed dose, which was linked with variations to the structural characteristics of the C-A-S-H. Minor variations to the microstructure (such as increased micro-cracking) were observed with increasing total dose, as was decreased strength. The impact of incorporation of simulant waste species (CeO_2) on gamma response and the subsequent leaching response of BFS:PC cement was investigated. Irradiated and control samples were subjected to leaching in simulant granitic groundwater using two different testing methodologies. The results for both samples showed the same response; development of a leached zone where decalcification of $Ca(OH)_2$ and C-S-H occurred, and formation of a carbonate rim.

Incorporation of powdered PuO_2 in BFS:PC and PFA:PC grouts allowed the impact of α-radiation to be investigated. The presence of cellulose (common in many Pu-containing waste streams) within these cements was also assessed, and was observed to cause a limited amount of variation to the proportions of phases present in the hydrate assemblage. Limited reaction of the PuO_2 was observed, however, variations to the phase assemblage were noted in the BFS cements containing PuO_2. Further investigation of the impact of α-radiation on cement microstructure and phase assemblage was

completed using He^{2+} ion accelerator experiments, and although a colour change was induced due to He^{2+} exposure no significant chemical or textural damage zones were observed in the samples.

Acknowledgements

Firstly, I have to express my gratitude to Professor John Provis for his constant positivity and enthusiasm for this project and all things cement related. Many thanks for giving me the opportunity to find out just how interesting cement can be! I would also like to thank Dr. Claire Corkhill, Dr. Mike Angus, and Dr. Martin Hayes for all the advice, support and input from academic and industrial perspectives into this project, which has been invaluable.

I am extremely grateful to Dr. Carolyn Pearce and Dr. Ruth Edge at the University of Manchester and Dalton Cumbrian Facility for facilitating and completing the gamma irradiations using the ^{60}Co irradiator, and to Dr. Shavkat Akhmadaliev for completing the He^{2+} ion irradiations at HZDR. I am also incredibly thankful to Dr. Elena Tajuelo Rodriguez and Dr. José David Arregui-Mena for collaborating with me on the characterisation of He^{2+} irradiated cement using TEM, and for making my time at Oak Ridge National Laboratory so enjoyable – you made me feel so welcome, and planned so much entertaining stuff to do, so thank you!

I owe an enormous amount to those who helped me in the Immobilisation Science Laboratory, whether it be for training me in the lab, helping me devise experimental setups that would actually work, teaching me how best to analyse data, or helping me when everything seemed broken, so a huge thank you to Dr. Oday Hussein, Dr. Brant Walkley, Dr. Rita Vasconcelos, Dr. Laura Gardner, Dr. Sam Walling and Dr. Seb Lawson.

I was especially lucky to be funded by EPSRC as part of the Next Generation Nuclear CDT, and am thrilled to have had such a great cohort to be part of over the past few years. Folks, especially my Sheffield lot - Sarah, Amber and Joe, thanks for all your help, support and winter school camaraderie. I would also like to thank everyone in the ISL for making it such a pleasure to be part of such a fun and dedicated group. Special thanks to my cement pals, Antonia, Rita and Dan, for all the chats and encouragement, I'm extremely grateful.

Finally, I have to thank my friends and family, without their support I would not have been able to come this far. Thank you for your belief in me, especially in those times when I had none in myself. You lot are the best.

Publications

Journal publications:

1. Kearney, S.A., McLuckie, B., Webb, K., Orr, R.M., Vatter, I.A., Yorkshire, A.S., Corkhill C.L., Hayes, M., Angus, M.J., Provis, J.L., *Effects of plutonium dioxide encapsulation on the physico-chemical development of Portland cement blended grouts., Journal of Nuclear Materials, 530, Article 151960, (2020)*.

Conference publications and presentations:

1. S. A. Kearney, C. L. Corkhill and J. L. Provis, Radiolysis and radiation damage effects in cements used in nuclear waste storage and disposal, 36th Cement and Concrete Science Conference, Cardiff, 2016. (Extended abstract and poster presentation)
2. S. A. Kearney, C. L. Corkhill and J. L. Provis, Radiolysis and radiation damage effects in cements used in UK nuclear waste storage and disposal, Euroseminar on Microscopy Applied to Building Materials, Les Diablerets, Switzerland, 2017. (Extended abstract and oral presentation)
3. S. A. Kearney, C. L. Corkhill and J. L. Provis, Gamma irradiation study of cement grouts used for UK nuclear waste encapsulation, 37th Cement and Concrete Science Conference, London, 2017. (Extended abstract and poster presentation)
4. S. A. Kearney, J. L. Provis, The effects of radiation on Portland cement blended grouts used for nuclear waste encapsulation in the UK, International Committee on Irradiated Concrete (ICIC) Prague, 2017. (Oral presentation)
5. S. A. Kearney, C. L. Corkhill and J. L. Provis, Experimental investigation of the effects of radiation on Portland cement blended grouts used for waste encapsulation, Nuclear Frontiers Conference 2017. (Oral presentation)
6. S. A. Kearney, A. S. Yorkshire, C. L. Corkhill, R. Orr, M. Hayes, M. Angus, J. L. Provis, Radiation stability of high volume replacement cements used for nuclear waste disposal, 38th Cement and Concrete Science Conference, Coventry, 2018. (Extended abstract and poster presentation)
7. S. A. Kearney, C. L. Corkhill and J. L. Provis, Radiation damage effects in high volume replacement Portland cements, NUWCEM Cement based materials for Nuclear Wastes conference, 2018. (Extended abstract and oral presentation)
8. S. A. Kearney, J. L. Provis, Radiation effects on the physio-chemical properties of novel and Portland cement based systems for UK waste management, International Committee on Irradiated Concrete (ICIC) Knoxville, Tennessee, 2018. (Oral presentation)

9. S. A. Kearney, C. L. Corkhill and J. L. Provis, Impact of gamma radiation on CeO_2 doped cementitious grouts used for nuclear waste disposal in the UK, Goldschmidt, August 2019 (Abstract and poster presentation)
10. S. A. Kearney, B. Walkley, C. L. Corkhill and J. L. Provis, Radiation damage effects in cementitious grouts used for nuclear waste disposal in the UK, 15th International Congress on the Chemistry of Cement Conference Proceedings, 2019. (Extended abstract and oral presentation)

Abbreviations

AFm	Alumina, ferric oxide, monosulfate; in this thesis includes the phases referred to as monosulfoaluminate, hemicarboaluminate, and monocarboaluminate.
AFt	Ettringite
BFS	Blast furnace slag
BSE	Backscattered electron
C-S-H	Calcium silicate hydrate
dpa	Displacements per atom
EDX	Energy dispersive x-ray spectroscopy
FIB	Focussed ion beam
FTIR	Fourier transform infrared spectroscopy
GDF	Geological disposal facility
GGBS	Ground granulated blast furnace slag
HLW	High level waste
ICP-OES	Inductively coupled plasma – optical emission spectrometry
ILW	Intermediate level waste
LET	Linear energy transfer
LLW	Low level waste
LLWR	Low level waste repository
MAS	Magic angle spinning
MCL	Mean chain length
MIP	Mercury intrusion porosimetry
NMR	Nuclear magnetic resonance

PC	Portland cement
PCM	Plutonium contaminated material
PFA	Pulverised fuel ash
PSD	Particle size distribution
SAED	Selected area electron diffraction
SCM	Supplementary cementitious materials
SEM	Scanning electron microscopy
SL	Sellafield Limited
TEM	Transmission electron microscopy
TGA	Thermogravimetric analysis
UPV	Ultrasonic pulse velocity
w/s	water to solids ratio
XRD	X-ray diffraction
XRF	X-ray fluorescence

Contents

List of Figures

List of Tables

1 Introduction

Management of many types of intermediate level nuclear waste (ILW) in the UK is achieved through encapsulation in cementitious grouts. These wastes contain levels of radioactivity exceeding the threshold values for low-level waste (LLW), but are not heat generating [1]. The cementitious grouts used for encapsulation are therefore subjected to high levels of radiation, which has the potential to alter the physico-chemical properties of the materials. Current UK guidelines for disposal of radioactive waste state that emplacement of a processed wasteform (i.e. cement encapsulated waste) in a geological disposal facility (GDF) should isolate harmful radionuclides from the biosphere for sufficient time to allow decay to non-harmful levels [2]. Given this, it is important to understand how the effects of radiation manifest in the encapsulation cements and what impact this may have on their performance. Only once we understand the interactions and subsequent impact to the wasteform, can these be incorporated into safety case assessments required for GDF construction.

Radiation stability studies of cementitious grouts available in the open literature have focussed on pure Portland cement (PC) systems. However, waste encapsulation grouts in the UK comprise a wide formulation envelope of high volume replacement blends of PC with supplementary cementitious materials (SCM) such as blast furnace slag (BFS) and pulverised fuel ash (PFA). The specification of the powder supplies for the encapsulant grouts are also bespoke to the UK nuclear industry [3], and as such, the impact of high levels of ionising radiation on these cements is not well understood.

In this thesis, the effects of gamma and alpha radiation on commonly used encapsulation grouts were investigated. This was intended to provide a more thorough understanding of how exposure affects the physico-chemical properties of these materials, and what implications this may have for the service life capabilities of cement encapsulants. The findings are provided as support for the GDF safety case moving forward.

The aims of this project are to elucidate the effects of radiation on the cement systems currently used in the UK. This will involve:

- Describing the microstructural and chemical influences of alpha (α) and gamma (γ) radiation on cementitious wasteforms, with a focus on the impact of radiolytic processes at “high” doses (> 10 MGy).
- Developing further understanding of the influence of radiation exposure on the capacity of cements to chemically condition radionuclides.

Chapter 2 presents a literature review outlining an introduction to nuclear waste and current UK waste management policy. A background to the use of cementitious materials for encapsulation purposes is presented. An assessment of relevant literature assessing radiation effects in cementitious materials and natural analogues is outlined, specifically focussing on gamma and alpha sources as they are considered to have a more pervasive effect than beta radiation.

Chapter 3 describes the materials used throughout the thesis, and the experimental methods employed to analyse these materials. Formulations for the four blends of BFS:PC (ratios of 3:1, 3.44:1, 5.67:1, 9:1) and single PFA:PC (ratio of 3:1) blend used throughout this thesis are outlined.

Chapter 4 describes the typical characteristics of the blended cement grouts that are used for nuclear waste encapsulation in the UK. Characterisation of BFS:PC and PFA:PC samples outlined in Chapter 3 was completed to allow a full evaluation of changes due to radiation exposure in subsequent chapters. The impact of SCM replacement on hydration behaviour was also outlined. The development of correlation curves between the ultrasonic pulse velocity (UPV) and compressive strength of BFS:PC samples for the four different BFS blends was outlined, to allow evaluation of the impact of radiation on these samples in later chapters.

Chapter 5 addresses the impact of gamma radiation on cementitious grouts in order to evaluate the impact of radiolysis on the phase assemblage, microstructure and mechanical properties of BFS:PC samples. The four blends of BFS:PC outlined in Chapter 3 were exposed to increasing total absorbed dose (7, 14 and 20 MGy) allowing evaluation of both the increasing dose and increasing level of BFS replacement. Characterisation was completed using thermogravimetric analysis (TGA), X-ray diffraction (XRD), scanning electron microscopy with energy dispersive X-ray spectroscopy (SEM-EDX), UPV, ^{29}Si and ^{27}Al magic angle spinning nuclear magnetic resonance (MAS-NMR)

Chapter 6 presents the findings of a collaborative study with the National Nuclear Laboratory (NNL) investigating the effects of PuO_2 on the physico-chemical behaviour of BFS and PFA blended PC. The presence of cellulose within these cements was also evaluated. The effect of PuO_2 in terms of impact to the phase assemblage and microstructure were assessed using optical microscopy, SEM-EDX, XRD, and TGA.

Chapter 7 outlines the potential impact external exposure to gamma radiation may have had on the PuO_2 containing samples in Chapter 6. Using CeO_2 as a non-radioactive surrogate for PuO_2, samples using the same formulation of BFS:PC as in Chapter 6 were exposed to a total gamma dose of 1.2 MGy. This aimed to assess if the radiation would be attenuated differently from the samples in Chapter 5 when the cement contained surrogate waste materials. In order to assess if increased attenuation

may decrease the ability of the cement encapsulant to effectively retain waste species, leach testing was completed on the samples. The irradiated and control samples were subject to two alternate leaching methodologies; dynamic testing imposed regular sampling and replacement of the leachate, whereas the leachate in static testing was not sampled until the end of the testing period. Characterisation of control and irradiated samples post irradiation and after leachate testing allowed assessment of the phase assemblage and microstructure. Leachate samples were analysed using inductively coupled plasma - optical emission spectroscopy (ICP-OES) to allow investigation of the solution chemistry.

Chapter 8 shows the results of a novel experimental methodology to simulate alpha particle damage in cements. Ion accelerator experiments were used to investigate the interface between encapsulated alpha emitting species (such as PuO_2, as analysed in Chapter 6) and the encapsulant cement. Post irradiation characterisation was completed to assess changes to the phase assemblage and microstructure. Collaboration with Oak Ridge National Lab (ORNL) allowed preparation of SEM focussed ion beam (FIB) sections to be prepared and analysis using transmission electron microscopy (TEM)-EDX to be completed.

Chapter 9 summarises the research findings of the work presented in this thesis, and outlines the recommendations for further work related to this project.

2 Literature Review

2.1 Nuclear power and waste management

The first civil nuclear power station in the UK became operational at Calder Hall in 1956. This was the first “Magnox” type gas cooled reactor, which subsequently were constructed at several sites across the UK [4], [5]. These reactors generated electricity for civil use together with plutonium for military purposes. The reactors were graphite moderated and CO_2 cooled, with unenriched uranium metal fuel clad in a magnesium-aluminium alloy (99.3 wt. % Mg, 0.7 wt. % Al) from which the term ’Magnox’ is derived (Magnesium non-oxidising) [6]. Degradation of the alloy meant that reprocessing of the waste fuel was required prior to disposal. To allow this, Magnox fuel cladding was mechanically decanned and the resulting ‘swarf’ (the remaining cladding) was processed as ILW. The waste fuel underwent reprocessing to separate residual uranium and plutonium in order to manufacture fresh mixed oxide (MOx) fuel using the PUREX (Plutonium Uranium Redox Extraction) process [7]. Further infrastructure was required to allow interim storage and reprocessing to be completed, which, together with the secondary wastes arising from the PUREX process, created additional waste streams that require management [8], [9]. Reprocessing activities are set to cease with the closure of the Thermal Oxide Reprocessing Plant (Thorp) in 2018 and the Magnox reprocessing plant in 2020, after which the UK will move towards an open fuel cycle [8].

Development of different reactor designs over the subsequent decades as nuclear power was used to generate electricity led to different materials being used as fuel, cladding, moderators and coolants [4], [10], [11]. This led to a diversification of wastes generated from both fuel reprocessing and reactor decommissioning, leaving a range of radioactive wastes which require safe disposal [8].

These radioactive wastes are defined as any materials containing levels of radioactivity higher than legislated threshold values [12]. The wastes are classified dependent on the level of activity they contain and potential for heat generation, as outlined in Table 2.1. If materials are classified as radioactive waste, they require management to isolate and contain the hazard.

Civil nuclear power generation produces the largest volume of nuclear waste in the UK inventory, with additional minor contributions from research practices, military developments, medical and industrial activities [8]. Nuclear power generation produces waste at every stage of the fuel cycle, from mining uranium ore to fuel fabrication to decommissioning of power plants. The highest levels of radioactivity are generated from spent nuclear fuel (SNF) and reprocessing of this material, but this represents a small fraction of the total inventory volume at 0.07 vol. % (Table 2.1, Figure 2.1). Larger volumes of

LLW are generated but they contain proportionally smaller radiological burden; estimated as approximately < 0.002 % of the inventory's total radioactivity.

Table 2.1 Radioactive waste category classifications and reported UK waste volumes as of April 2016 including estimated future arisings to 2125. Figures taken from [8]

Waste category	Classification	Reported volume (m^3)
High level waste (HLW)	≥ 4 GBq per tonne α or ≥ 12 GBq per tonne β/γ and generates heat; this is taken into account for design of storage and disposal facilities.	1,150
Intermediate level waste (ILW)	≥ 4 GBq per tonne α or ≥ 12 GBq per tonne β/γ and does not generate heat.	290,000
Low level waste (LLW)*	Radioactive material contained within this is below activity levels stated for ILW and HLW.	1,350,000

*Includes a subcategory of very low level waste which contains levels of radioactivity so low it can be disposed of with municipal, commercial or industrial waste.

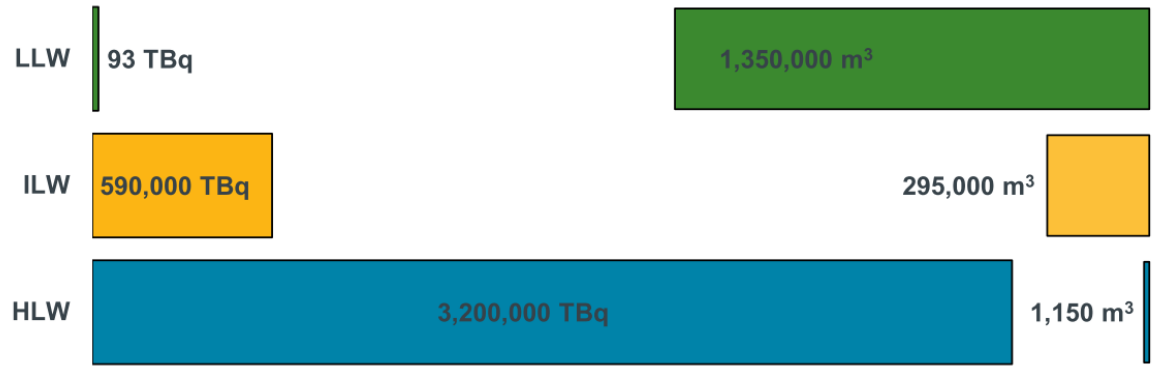

Figure 2.1 The relationship between the volume of each waste category versus the radioactivity it contains. Figure reproduced from [8].

In order to reduce the environmental and biological burden of these materials on future generations, they are managed using a variety of methods dependent on the waste streams. Increased understanding of the detrimental impact of "dilute and disperse" processes historically used to dispose of waste has led to a shift towards "contain and confine" strategies [13]. Central to this has

been the implementation of the 'waste hierarchy'; minimisation of waste production, reuse and recycling central to reduce reliance on disposal [8].

Management of nuclear waste is typically achieved through conditioning of waste to create a wasteform. A wasteform is defined as a solid, stable and passively safe material that is designed and engineered to retain radionuclides in a disposal environment [13], [14]. This can be achieved via immobilisation or encapsulation of the radionuclides, and is dependent on the waste category classification and type material within the waste stream.

LLW generated in the UK often undergoes supercompaction (where suitable) before placement in large containers that are filled with cement grouts prior to disposal at the Low Level Waste Repository (LLWR) facility. Bulk material within these waste streams currently comprises paper, plastics and scrap metal but will likely change dramatically during decommissioning of power stations; construction materials and soil will form the majority of the final volumes in these categories [8], [12].

Management of ILW and HLW is more complex due to the higher levels of radioactivity present (both categories have the same lower thresholds of radioactivity for classification, but are separated by their capacity for heat generation) and the variety of waste streams from which they arise. HLW is a product of the reprocessing of spent fuel and consists of concentrated nitric acid with soluble fission products, insoluble fission product residues, and items of processing plant that have become contaminated. HLW undergoes vitrification, which involves mixing calcined powdered waste with crushed glass and heating this in a furnace to produce a conditioned waste glass product [8]. The glass wasteform immobilises the radionuclides by incorporating them into its structure, reducing the overall waste volume and creating a durable material for disposal. The wasteforms are 150 L stainless steel canisters which are currently stored in temperature controlled vaults to ensure overheating does not occur [12].

ILW incorporates a much wider range of waste materials which are processed in several different ways. The majority of the wastes are metal (mainly steel and magnesium based alloys from fuel cladding and graphite from reactor moderators), ion exchange resins, flocs and sludges (from the treatment of liquid waste and contaminated storage materials), plutonium contaminated materials, and miscellaneous activated materials [8]. The preferred method of management of ILW in the UK is encapsulation in cementitious grouts. The grouts comprise Portland cement (PC) with high volume replacement by supplementary cementitious materials (SCMs) and are tailored for specific suitability to the waste materials by altering the SCM used, and the ratio of SCM:PC [8], [15]. The formation of a physical barrier to restrict the movement of radionuclides is a key objective of encapsulation, but the cement also forms a chemical barrier that can prevent mobilisation of radionuclides through the high

pH promoting insolubility, and through sorption/ionic substitution of radionuclides in hydration products [16], [17].

Wasteforms produced from processing of ILW typically comprise 500 L stainless steel drums or 3 m^3 stainless steel boxes. Encapsulation processes used in the UK fall into three main categories; in-drum mixing of liquids or sludges, in-container grouting of solid waste items, and annular grouting of supercompacted waste pucks, which are demonstrated in Figure 2.2 [18].

Figure 2.2 Examples of encapsulated ILW for solid waste items, liquids and sludges, and annulus grouting of supercompacted pucks. Image from [18]

For certain waste streams (e.g. reactive metals), cementitious grouts have some drawbacks as conditioning materials; high alkalinity in cement pore waters is reactive with certain metals and can cause hazardous gas production, or pyrophoric species [19]. Encapsulation using low pH binders or other alternative cements (e.g. geopolymers) has been investigated for use in these instances [18].

2.2 Geological disposal

UK policy for disposal of ILW and HLW follows the findings outlined by the Committee on Radioactive Waste Management (CoRWM), who in 2006 and 2013 [20], [21] stated that geological disposal together with safe and secure interim storage of higher activity nuclear waste was the best available approach for long term management of nuclear waste [22], [23].

Geological disposal is the internationally favoured option for waste management, as it is deemed the safest long term management solution for highly active wastes [24]. The principle behind geological

disposal is that the construction of an engineered vault several hundred metres below ground will isolate and contain the harmful radionuclides away from the biosphere. This is referred to as the multi-barrier concept, and is designed to prevent the release of hazardous radionuclides to the surface environment until they have undergone decay to near background levels (Figure 2.3) [8], [23]. Once closed, the GDF is designed to be passively safe, avoiding burdens on future generations [23].

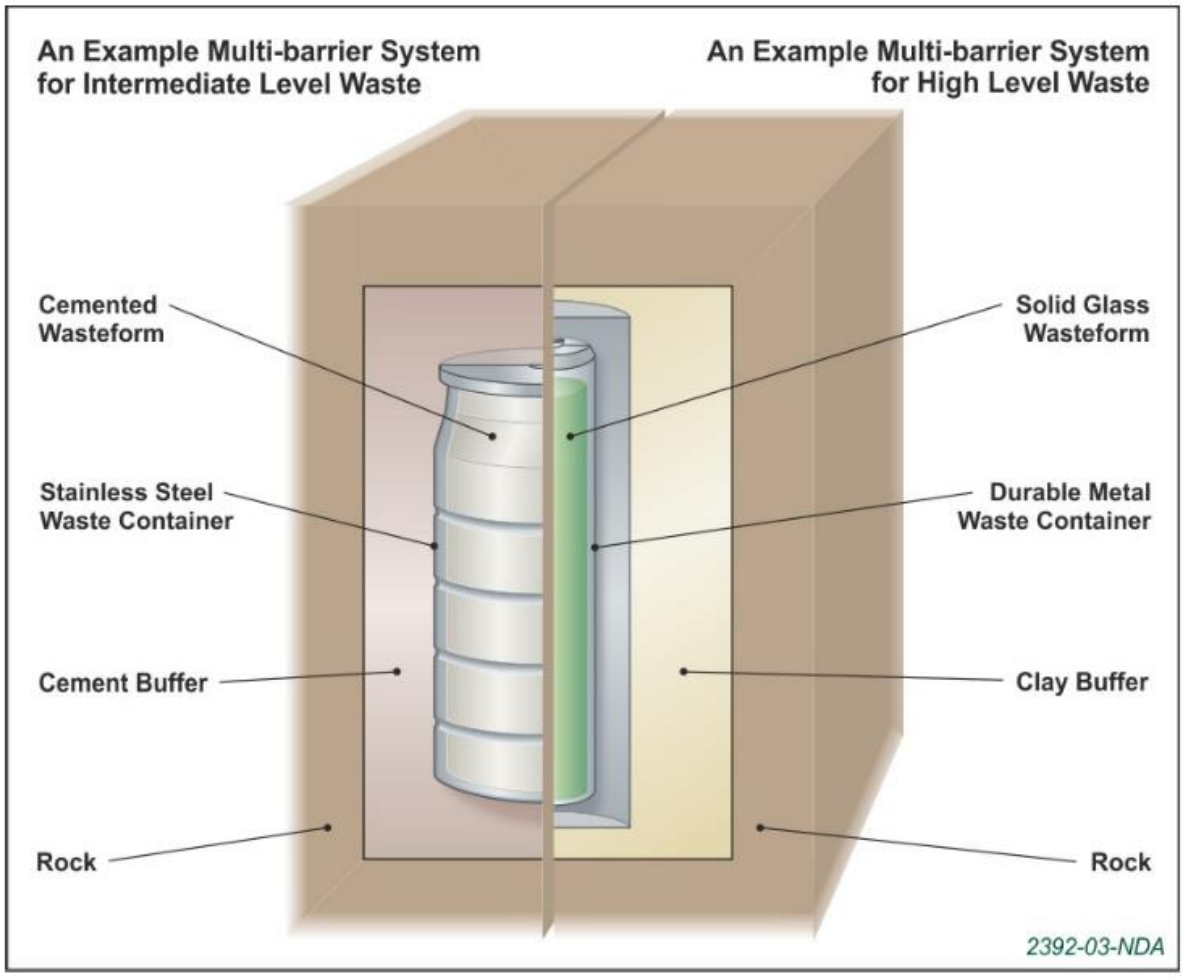

Figure 2.3 Schematic of the multi-barrier system for ILW and HLW. Image taken from [23].

The multi-barrier concept refers to the implementation of physical, chemical and geological containment through carefully designed engineered barriers and placement of the facility in a suitable geological formation. The barriers consist of the waste form, waste container, local backfill / chemical buffer material (adjacent to waste), mass backfill (throughout the whole facility i.e. access tunnels and shafts) together with a tectonically stable, low permeability bedrock that has limited groundwater flow present [25]. Due to the high proportion of cemented wasteforms in the UK inventory, clay backfill materials of the types used in other countries are likely to adversely react [26], [27], and as

such a bespoke cementitious backfill has been designed. Nirex Reference Vault Backfill (NRVB) was developed to provide the high alkalinity and sorption capacity desired for chemical conditioning in a GDF situated in high strength crystalline rock [27], [28].

Construction of a GDF has not yet begun in the UK. Safety and security of the facility are paramount, and unless regulatory bodies can be fully satisfied of the safety, security and environmental protection will be appropriate, construction will not occur. The UK government published a white paper in 2014 titled "Implementing Geological Disposal: A Framework for the long-term management of higher activity radioactive waste", which set out the approach to be taken for siting and construction of a GDF [29]. This was updated in 2018 to include the work completed on national geological screening and working with potential host communities [23]. The voluntarist community approach being used requires that once the regulators are satisfied, a Test of Public Support is conducted to assess if the community within the proposed area is still willing to host the GDF given the proposed siting [23]. Although the layout and design of the GDF will be highly dependent on the host geology, key aspects of the layout are known and are shown in a schematic drawing in Figure 2.4.

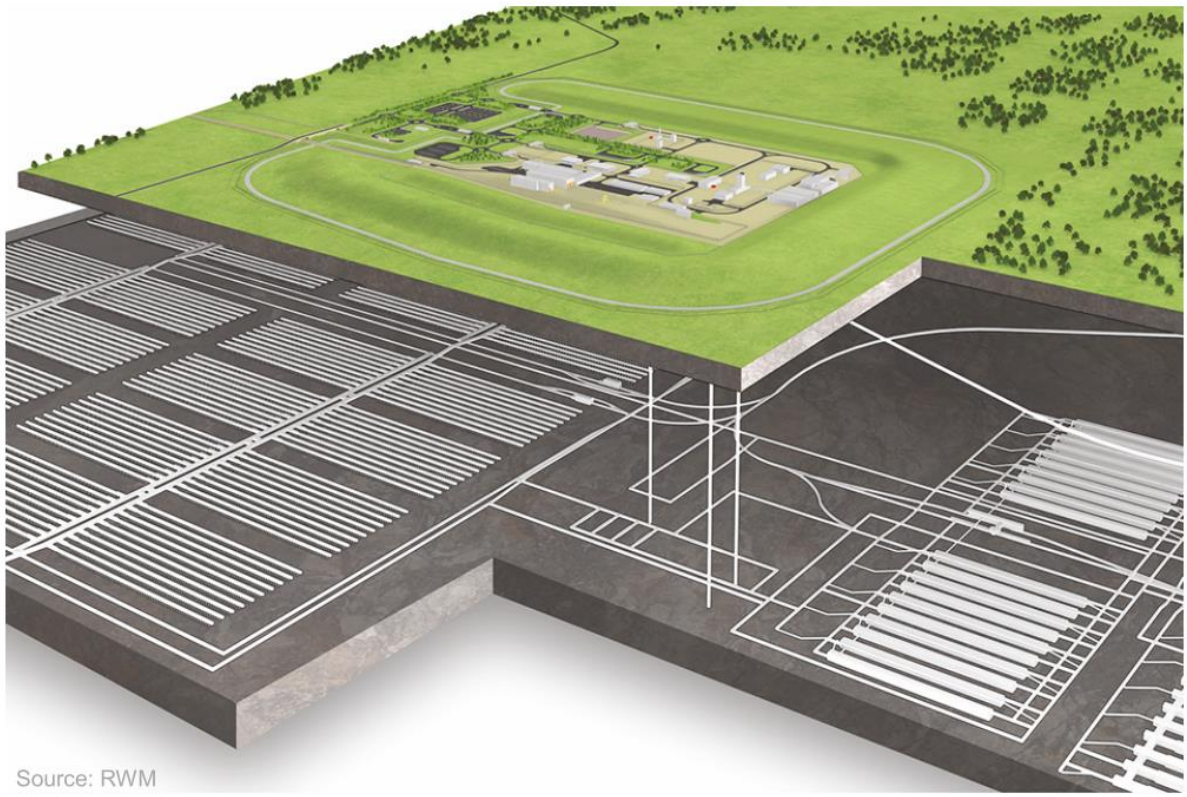

Figure 2.4 Schematic of a potential GDF layout for ILW and HLW. Image taken from [23].

ILW and HLW will be disposed of in separate areas due to the heat generation from HLW. Engineered vaults will be constructed for ILW and a system of tunnels will be used for HLW and SNF disposal [27].

The depth of the GDF will be between 200 – 1000 m, however the final design will be strongly dependent on the local geology of the disposal site and the risk of issues arising from geomorphological processes such as glaciation [23], [27]. Retrievability of the waste once the GDF has ceased its operational phase (i.e. has been closed) is not favoured (although not actively prohibited), with government and regulators agreeing that the purpose of a GDF is to dispose of, not store, waste [23].

The UK Government strongly favours an approach where one GDF will manage higher activity wastes (ILW/HLW) from the national waste inventory (with LLW being disposed of in the LLWR). However, at this stage no site investigations of potential locations have occurred, and as such it is unclear if any host community has a large enough volume of suitable rock to accommodate the whole inventory [23], [29]. The timescale for finding an appropriate site for the GDF is anticipated to be approximately 15 – 20 years. Construction, operation and closure of the facility is estimated to take >100 years [23].

2.3 Cementation of ILW

Cementation was adopted in the UK in the 1980s following investigations into waste conditioning options [30]–[32]. As outlined in Section 2.1, the preferred conditioning route for ILW is via encapsulation in cementitious grouts formed of blends of PC with high levels of replacement by SCMs [15]. Typically the SCMs are either blast furnace slag (BFS) or pulverised fuel ash (PFA), and they are added to improve the material characteristics of the grout, most notably by lowering the heat of hydration of PC which is highly exothermic [33], [34]. This route was adopted due to the widespread availability and understanding of the raw materials, inexpensive and uncomplicated processing, simple remote handling processes, and ease of adaptability for various waste streams [35]. The resulting wasteforms:

- Produce dense products with minimal free liquids, low porosity, voidage and permeability together with adequate compressive strength,
- Are tolerant to a range of chemical constituents, radiation exposure and temperature environments,
- Provide chemical containment to reduce the flow of radionuclides into groundwater; radionuclides can sorb / exchange into cement hydrate phases, and the long-lasting high pH can decrease radionuclide solubility and lead to insoluble phase formation. [18], [33].

The resultant wasteform must comply with specifications relating to radiation dose rates, heat and gas generation, mechanical properties (strength, voidage and homogeneity, mass transport), accident

performance (fire resistance, impact response), as well as performing the physical and chemical containment required [36], [37]. These properties must be maintained for a period of 150 years, with an aim that they should be maintained for 500 years [37]. It is considered that the 150 year timescale will cover interim storage and movement of wasteforms into a GDF facility, and as such the wasteform specifications will ensure safe transport and operation of the GDF [37].

After disposal in a GDF, the wasteform properties will evolve due to external and internal conditions together with aging effects. The impact of dimensional changes, corrosion, radiation, temperature variations and microbial activity need to be considered to assist development of safety cases for long term management.

Waste components including organics (such as cellulose in waste including paper, wood and cotton), sulfates, and nitrates can deleteriously interact with cement, initially causing setting issues and dimensional changes at greater ages. Corrosion of metallic wastes results in a net increase in waste volume and generation of H_2 gas which could cause expansion and cracking within the matrix. Although the effects can be somewhat mitigated through controlling waste loadings, over the timescales for which the wasteforms are required to be operational, the impact on durability requires consideration.

The cemented wasteforms will also be subject to temperature variations through the period of interim storage, transport and different stages of disposal. This will be due to external factors and radiogenic heat generation from radionuclide decay within the waste. The temperature variations will cause changes to hydration rates and phases, pore water content and corrosion rates that will also impact on dimensional stability. The average assumed temperature for above ground ILW storage across the UK is approximately 20 °C [19], [38]. This is anticipated to increase to 35 °C when the waste is first placed in the GDF, followed by a short term peak at 80 °C after the NRVB backfill is emplaced. Post closure of the GDF, temperatures are not expected to exceed 50 °C and are anticipated to continue stabilise at 40 °C, approximately 40 years post closure [19], [38]–[40].

Currently a major problem facing nuclear industry is the security of cementitious powder supplies. Changes in construction needs have led to alteration from historic PC and SCM powder specifications, moving to material characteristics that do not always comply with the nuclear industry's needs. Given this, a bespoke specification for all PC and SCMs used for encapsulation was designed by Sellafield Ltd [15]. However, as the SCMs used are industrial by-products, changes in manufacturing and market demands have limited the availability and consistency of supply [3], [15]. This alteration has partly been driven by the shift to cheaper renewable energy and closure of coal fired power plants in the UK and across Europe, reducing accessibility to PFA. Similarly, the downturn in steel manufacture across

the UK has led to Sellafield having to switch BFS supplies three times since 1990 due to plant closures [15]. A supply shift from a historical, relatively coarse, BFS to a finer product named in the industry as Ground Granulated Blast-furnace Slag (GGBS) in 2003 necessitated the powder to be mixed with a coarse blend BFS product to fulfil the bespoke requirements [3].

2.4 Portland cement and SCMs

2.4.1 Portland cement

PC is a hydraulic binder that was initially advertised as an aesthetically similar alternative to Portland stone, and as such was patented under this name in the 1820s [34], [41]. PC is manufactured from processing limestone ($CaCO_3$) with clay/shale/sand (as sources of Al_2O_3, SiO_2, and Fe_2O_3) in rotary kilns at temperatures of approximately 1400 °C. This forms a product called clinker that contains a specific set of calcium silicate and aluminate minerals [42]. British standards state that the clinker must be composed of "at least two thirds by mass of calcium silicates … the remainder consisting of aluminium and iron containing clinker phases and other compounds" [43]. Alteration of the ratio of clinker phases can allow Portland cement to be tailored for use in specific applications or service environments. To produce Portland cement, clinker is ground to a fine powder along with gypsum; the gypsum aids grinding, and helps to control the initial set and strength gain of the material when mixed with water [42]. Impurities from the fuel used to heat the kiln can be observed as contamination within the clinker, but standardised thresholds for composition together with the ratios of clinker phases in the cement regulate composition [34], [41].

There are four main clinker phases in PC: alite, belite, aluminate and ferrite, details of which are outlined in Table 2.2. As all the phases are oxides, it is common practice in cement chemistry to abbreviate the oxide phases in order to simplify notation, as seen in Table 2.3.

Table 2.2 PC clinker phases, ideal oxide composition of each and oxide abbreviated shorthand form.

Phase	Chemical name	Oxide composition	Abbreviated form
Alite	Tricalcium silicate	$3CaO{\cdot}SiO_2$	C_3S
Belite	Dicalcium silicate	$2CaO{\cdot}SiO_2$	C_2S
Aluminate	Tricalcium aluminate	$3CaO{\cdot}Al_2O_3$	C_3A
Ferrite	Tetracalcium aluminoferrite	$4CaO{\cdot}Al_2O_3{\cdot}Fe_2O_3$	C_4AF

Table 2.3 Cement chemist oxide abbreviated notation

Chemical formula	Abbreviation
CaO	C
SiO_2	S
H_2O	H
Al_2O_3	A
Fe_2O_3	F
SO_3	$\bar{S}$

Mixing of Portland cement with water allows hydration of clinker phases; the powder undergoes dissolution and new solid hydrate phases precipitate from the saturated solution in a series of highly exothermic reactions producing a hardened paste [33], [34], [42]. Alite is the most dominant reacting clinker phase, and is the major contributor to the heat produced during the onset of hydration and the development of initial material properties. The initial set of the cement is controlled by the reaction of aluminate, which undergoes rapid reaction that requires moderating through the addition of gypsum to slow the rate of hydration and avoid flash setting [34]. Belite reacts at a much slower rate comparatively, and contributes to later age strength development. Ferrite is also thought to react slowly in the presence of gypsum, however faster reaction has been observed in some instances, especially in the presence of BFS [44]. Hydration is controlled by the products formed, their rate of formation, and their morphology and growth into available space. Thermodynamics and kinetics are responsible for these factors. The physicochemical characteristics of the clinker material are therefore central to the hydration process of the cement; particle size, morphology and crystallography will dictate the speed at which products form, which in turn will impact on the proportions of products present and their situation and morphology [44].

Dissolution of clinker phases leads to supersaturation of mixing water with respect to hydrous solid minerals, allowing these hydrate phases to form via precipitation, and chemically binding water into their structure. As hydration progresses, the solution becomes less supersaturated but still includes ions from the dissolved clinker. This mixture is termed the pore solution, and is retained in the matrix throughout hydration. This allows lower permeability to be achieved, as later hydration products fill the remaining pore space. Given the formation of later age hydration products requires water, the availability of moisture during the curing process is essential. Curing conditions such as temperature, humidity, and time are critically important and have large implications for the material properties. Hydration of PC results in a characteristic phase assemblage, and the most common reaction products are shown in Table 2.4.

Table 2.4 Typical hydration products of PC

Cement notation	Chemical formula	Phase name
C-S-H	approximately $1.6CaO{\cdot}SiO_2{\cdot}1.8H_2O$	Calcium silicate hydrate
CH	$Ca(OH)_2$	Portlandite
AFt	$Ca_6Al_2(SO_4)_3(OH)_{12}{\cdot}26H_2O$	Ettringite
AFm	$[Ca_2(Al,Fe)(OH)_6]{\cdot}X{\cdot}nH_2O$ where X: OH^-, Cl^-, ½ SO_4^{2-}, or ½ CO_3^{2-}, and $n \geq 2$	Hydrocalumite-like

Hydration of alite and belite leads to the formation of portlandite and a disordered calcium silicate hydrate phase (C-S-H) with variable composition; this makes up the bulk of the hydrate assemblage. The gypsum added to the clinker modifies the reaction of aluminate to ensure the formation of ettringite, a sulfoaluminate hydrate phase. Once sulfate becomes depleted, a secondary stage of ettringite formation is typically observed [45]. As sulfate depletion continues, the ettringite becomes unstable and breaks down, allowing further hydration to form AFm phases which contain at most 1 mole of calcium sulfate per mole of C_3A, instead of the 3 moles per mole of C_3A found in ettringite [34].

2.4.1.1 Calcium silicate hydrate

The C-S-H is the main hydration product and strength giving phase in hydrated PC. It has a poorly crystalline nature which makes determination of its structure difficult. It is typically described as being formed of disordered layers of silicate chains joined to a central calcium oxide sheet. Structural models based on naturally occurring calcium silicate hydrate minerals such as jennite and tobermorite have been proposed as potentially similar, however the highly variable calcium, silicon and water content in cement hydrates can change the structure. Richardson provides a detailed analysis of the different proposed models [46], however classification of structure based on the molar ratio of Ca/Si allows categorisation into two broad structures [42], [47], [48]. It has been postulated that in PC systems where Ca/Si ratios are high (>1.5), a disordered jennite-like phase will form, termed C-S-H(II). Where Ca/Si ratios are reduced, as when blended with SCMs, a tobermorite-like structure is formed, termed C-S-H(I) [47]. However, the structure of C-S-H is still an active research area due to its poorly crystalline nature, and there are also structural models which state a tobermorite-like structure also prevails at Ca/Si ratios >∼1.4 [49]. The change in Ca/Si has been attributed to the presence of interstratified calcium hydroxide, which may be structurally bound to the tobermorite-like layers [49], [50].

The silicate tetrahedra make chains with a repeating kinked pattern, where every third connected tetrahedron is not in contact with the calcium oxide layer forming a typical dreierketten unit (Figure 2.5). Description of chemical environment of the Si tetrahedra is typically expressed using the Q^n notation, where Q represents the Si tetrahedron and n designates the number of bonded tetrahedral units. In the dreierketten unit, the first two tetrahedra are termed paired sites (Q^n_p in Figure 2.5), whereas the kinked tetrahedra are referred to as bridging sites (Q^n_b in Figure 2.5). The length of the silicate chains, and the resulting C-S-H structure, is a function of the Ca/Si ratio, and low calcium systems typically produce longer mean chain lengths (MCLs) as increased silicon is incorporated into the structure [46]. The interlayer space present between the chains permits the pore solution to interact, which allows charge balancing by alkali cations and can cause local differences in the environments of the silicon species [51]–[53].

Cross-linking of the chains across the interlayer can occur via the bridging silicon tetrahedron in each dreierketten unit. This connectivity is reduced at high pH, as is the interaction of the charge balancing alkali ions [52], [54], [55].

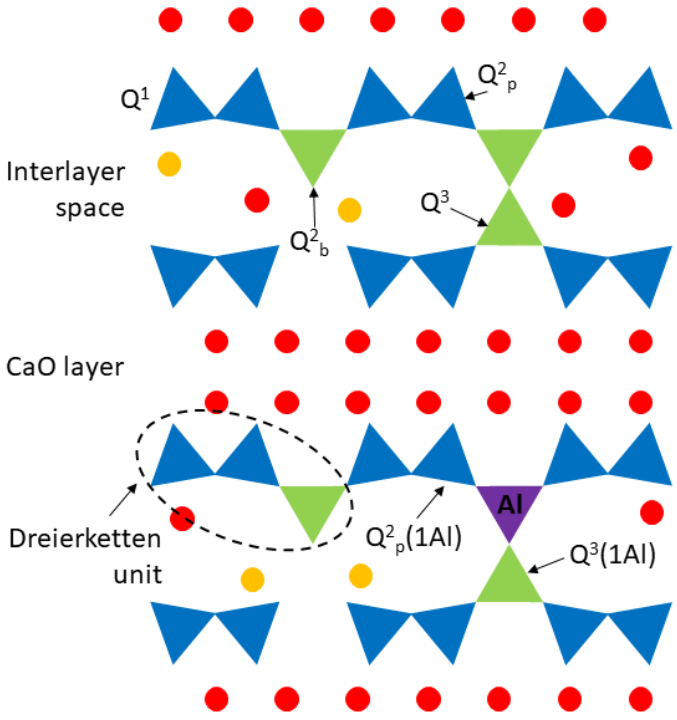

Figure 2.5 Schematic C-S-H structure. Q^n (where n= 1, 2, 3) species relate to chemical environment of the Si nuclei, where Q is the Si tetrahedron and n is the number of bonded tetrahedral units. Paired (Q^n_p) and bridging (Q^n_b) Si tetrahedra are represented by blue and green triangles, Ca is represented by red circles, and orange circles represent charge balancing alkali cations. The purple triangle represents Al substitution in silicate chains, as discussed in Section 2.5. Adapted from [56], [57].

There is a textural difference between areas of C-S-H formed within the space that was originally occupied by dissolved cement grains and the C-S-H formed in the originally water filled space, and these are described as inner product (IP) and outer product (OP) respectively [58]. Formation within hydrating alite and belite grains results in a texturally fine, homogeneous C-S-H product, whereas the morphology of the outer product is much more diffuse and highly dependent on the available space, but often displaying directional, fibrillar textures [58], [59]. The chemical compositions of IP and OP have also been observed to differ, although the difference in composition was observed to reduce over time as degree of hydration increases, and little variation in Ca/Si ratio is anticipated between IP and OP at later age [34], [59], [60].

The water/solid (w/s) ratio used in the cement formulations, and the curing conditions, have a large effect on the microstructural evolution of the C-S-H, especially in the development of outer product morphology. Water which has not been bound into the growing crystal hydrate phases remains present in the system through the pore space. This refers to all space not occupied by hydration product or unreacted solids, however this description does little to illustrate the complexity of cement pore systems, or of the effect the pore system has on both the chemical and physical properties [44]. The different types of porosity within cement pastes can be broadly split in to 3 categories by size:

- Air voids, which can be anything between several μm to a few mm in diameter, and are normally produced through mixing of the paste.
- Capillary porosity refers to the parts of hardened cement paste which are not hydrated phases or unreacted precursor, and are typically on the order of > 10 nm to a few μm.
- Gel porosity is an intrinsic part of C-S-H on the nm scale, and represents the smallest pore population within cement [61].

The capillary porosity is therefore formed through the interconnectivity of the OP, with the spaces between the fibrils constituting the capillary porosity. Given this, the capillary porosity is of major importance for durability as it controls the permeability of the materials [59].

A separate differentiation between types of C-S-H was outlined by Tennis and Jennings [62], separating C-S-H into low density and high density product based on results of nitrogen absorption. These differentiations likely correspond to inner and outer product. Constantinides and Ulm [63] furthered this idea, and using nanoidentation of C-S-H postulated that the dense IP displays different nanomechanical behaviour from low density OP. This was attributed to the differences in particle-to-particle contact forces rather than chemical variations.

2.4.1.2 Portlandite

Portlandite (crystalline $Ca(OH)_2$) has a layered lattice structure where Ca layers are bonded to OH layers, with a hexagonal unit cell and $P\bar{3}m1$ space group. Formation occurs through hydration of alite and belite clinker phases, which react to form C-S-H and portlandite [34]:

$$3\mathrm{CaO}\cdot\mathrm{SiO_2} + (3+m-n)\mathrm{H_2O} \rightarrow n\mathrm{CaO}\cdot\mathrm{SiO_2}\cdot m\mathrm{H_2O} + (3-n)\mathrm{Ca(OH)_2} \quad (2.1)$$

$$2\mathrm{CaO}\cdot\mathrm{SiO_2} + (2+m-n)\mathrm{H_2O} \rightarrow n\mathrm{CaO}\cdot\mathrm{SiO_2}\cdot m\mathrm{H_2O} + (2-n)\mathrm{Ca(OH)_2} \quad (2.2)$$

Ideal crystallization conditions produce hexagonal plates with weak hydrogen bonding and an overall $Ca(OH)_2$ layer composition. Crystals with euhedral habits are observed in young samples, however as hydration increases massive, blocky deposits form [42]. Portlandite is relatively highly soluble compared to other cement hydration products, and is the primary buffer for the high pH of PC pore water, which is typically pH 12.5 [42], [64].

2.4.1.3 Calcium sulfoaluminates (AFt and AFm)

Initial formation of ettringite occurs during hydration of C_3A in the presence of gypsum, which provides an excess of sulfate to the system. Ettringite is the most prominent of the AFt type phases in cement, which have the general form $C_3(A,F)\cdot 3CX\cdot n H_2O$, where X is a double charged ion (e.g. SO_4^{2-}) or two single charged anions (e.g. OH^-) [65]. Hydration of aluminate with gypsum in an idealised system forms ettringite through the reaction described in equation 2.3 [34]:

$$C_3A + 3C\bar{S}H_2 + 26H \rightarrow C_6A\bar{S}_3H_{32} \quad (2.3)$$

The AFt structure consists of hexagonal, prismatic crystals with an acicular habit, composed of column and channel components. The columns are formed of $[Al(OH)_6]^{3-}$ octahedra linked via edge-sharing CaO polyhedra, and the channels contain sulfate to allow charge balance, and water [65], [66]. Naturally occurring ettringite is observed in calcium rich alkaline environments, where iron substitution for the aluminium has been observed [67]. Although this could occur in cement systems through hydration of the ferrite phase in the clinker, the formation of the iron-containing phase is not typically observed as its formation is much slower than for aluminium-containing ettringite [42], [65], [66]. As hydration persists and sulfate depletion occurs, the stability of the ettringite decreases and breakdown occurs [34]:

$$C_6A\bar{S}_3H_{32} + 2C_3A + 4H \rightarrow 3C_4A\bar{S}H_{12} \quad (2.4)$$

allowing formation of AFm type phases, where the m designates mono(sulfate,-hydroxide etc) compared to the tri-sulfate designation of AFt [42].

AFm minerals are structurally related to hydrocalumite, with a base structure similar to the layered lattice of portlandite. However, in this structure every third divalent calcium atom is replaced by a trivalent species (mainly aluminium, with minor iron) which introduces imbalance in the layer charge. Charge balancing of the layers is rectified by the introduction of anions into the interlayer – typically sulfate (SO_4^{2-}), but substitution by carbonates (CO_3^{2-}) and hydroxides (OH^-), among others, can occur [68], [69]. The charge imbalance results in much greater interlayer spacing than is observed in portlandite, with the actual distance dependent on the nature of the interlayer anion and the amount of interlayer water present. The charge balancing anion is initially dictated by the composition of the cement, but can also be influenced by the service environment [68]. The variations in incorporation of both Al^{3+} or Fe^{3+} in the sheet structure and the difference in charge balancing anions can create a solid solution as shown in Table 2.4 [42], [70]. The main AFm phases identified in hydrated PC are monosulfoaluminate, monocarboaluminate and hemicarboaluminate.

2.4.2 Supplementary cementitious materials

SCMs are routinely added to cement clinker and concretes for civil / structural purposes in order to tailor material behaviour and reduce costs; a more recent driver to use SCMs is the effort to reduce CO_2 emissions, which are inherent from the processing of $CaCO_3$ in clinker manufacture [71].

SCMs commonly obtained as industrial by-products are generally at most weakly cementitious; they are cheap, widely available and more acidic than PC. SCMs encompass a large range of materials that have a variety of chemical compositions and physical characteristics, with commonly used materials including limestone, pulverised fuel ash (PFA, also called fly ash), blast furnace slag (BFS), calcined clays, and naturally occurring pozzolans (Figure 2.6 A) [72].

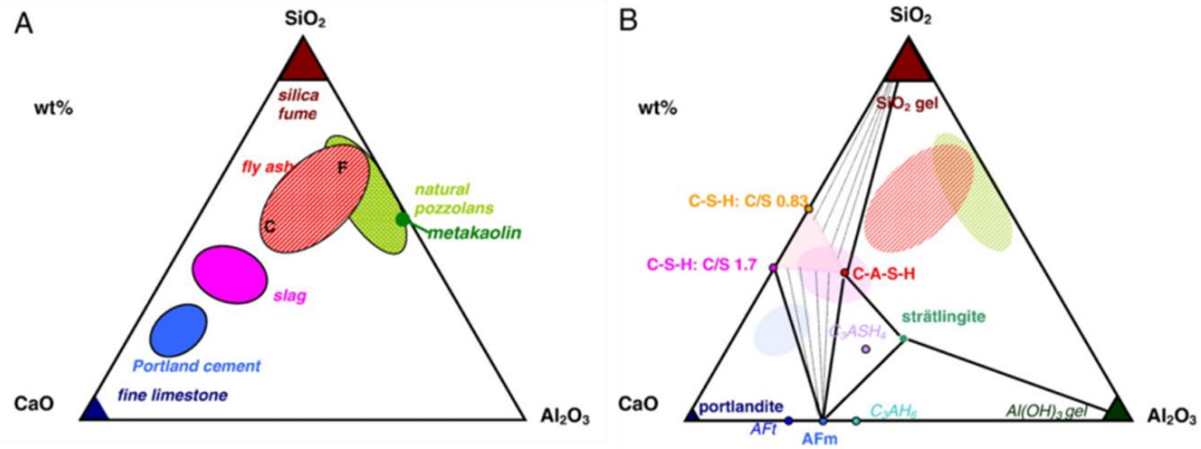

Figure 2.6 CaO-Al_2O_3-SiO_2 ternary diagrams showing A: PC composition and that of different SCMs, and B: hydrate phases formed dependent on composition. Reproduced from [71].

Whilst many SCMs do not readily react with water to form cementitious materials, some are able to do so (e.g. BFS). However, for most SCMs the rate of hydration is much slower than for PC and is largely affected by the chemical composition and physical properties such as fineness. The materials typically require 'activation' by more alkaline compounds, but then undergo the same type of dissolution / precipitation reactions as PC and become part of the matrix. Cements used in nuclear waste encapsulation are generally blends of PC with BFS or PFA to improve the material characteristics; this primarily relates to reduction in the heat of hydration to prevent any cracking of the wasteform that may occur as a result of large thermal excursions [16], [35]. Other factors which make SCM blended cements suitable for ILW encapsulation include a lower amount of water required to achieve a workable grout, and lower porosity in the wasteform. Whilst the pore solution would be less alkaline than in PC, the alkalinity of the pore solution would be sufficient to allow chemical conditioning of radionuclides [35].

2.4.2.1 Blast furnace slag

Blast furnace slag (BFS) is a calcium aluminosilicate glass waste, formed as a by-product of the steel industry (Figure 2.6). Initially formed through high temperature reduction of iron from its ore, the liquid product undergoes rapid quenching to obtain a glassy material containing high levels of Ca, Si, Mg, and Al, although small crystalline fractions are often observed. If slow cooling occurs, the BFS formed is highly crystalline and possesses no cementitious properties. The amorphous phase formed through rapid cooling has a disordered glass structure and relatively high calcium content. This amorphous material is latently hydraulic and so undergoes reaction with water at room temperature, albeit at a very slow rate. The greater the amorphous content of the BFS the greater the reactivity, and so although BS EN 197: 2011 states a requirement for BFS to be composed of at least two thirds glass, typically it contains <10 % crystalline components [17], [43]. It is also specified that the chemical composition should be two thirds CaO, SiO_2 and MgO, with the ratio of (CaO + MgO) / SiO_2 being greater than 1.0 [43]. Chemical composition has been broadly linked to slag reactivity, with higher levels of calcium and magnesium linked to increasing reactivity. However, assessment of performance through calculation of basicity ratios does not show a clear overall correlation [73].

The exact chemical composition of BFS is source-dependent, and will be affected by changes in ore composition and differences in furnace parameters and fuel type over time. Given this, although consistency from a specific source may be achieved over the short term, longer term uniformity is more difficult to achieve [15].

Powder fineness also exerts an important influence on reactivity. Different BFS products with very different particle sizes are formed depending on the cooling method used, and the BFS used in production of ILW grouts is ground granulated blast furnace slag (GGBFS). This is a very fine powder product, and the high surface area allows improved slag reactivity. Whilst this is a desirable property for general construction purposes, it is undesirable for ILW encapsulation as it increases the heat of hydration (which is limited by the Sellafield specification to ≤ 180 kJ/kg after 24 h at 35 °C [3]) and reduces performance in terms of fluidity and bleed [3]. The addition of a coarser BFS fraction with the same chemical composition is undertaken to reduce the reactivity and improve the performance issues [15].

2.4.2.2 Pulverised fuel ash

PFA is a glassy aluminosilicate waste product from coal powered power stations. During the high temperatures reached during burning of coal, the mineral components present melt and form small droplets that form spherical glassy particles under rapid cooling.

The composition of PFA varies greatly dependent on coal type and differences in combustion and collection methods, however two broad categories have been outlined; calcareous (ASTM C618 class C) PFA and siliceous (ASTM C618 class F) PFA [74]. Siliceous materials tend to be more widely used in cements, as they are more abundant and more quality-controlled [34], [71]. For use under BS EN 197-1, the proportion of reactive calcium oxide and silicon dioxide in siliceous PFA must be < 10 % and ≥ 25 % by mass respectively [43]. PFA can also include relatively high levels of alkalis (with more potassium than sodium typically observed), and unburnt carbon [34]. The Sellafield specification states that PFA must also conform with BS EN 450-1, Category S FA [75] and undergo beneficiation processes in order to refine the material through removal of unwanted components including unburnt carbon and magnetite [3]. PFA can contain mineral phases such as quartz, mullite, magnetite and hematite that were present within the coal or formed through thermal conversion. In siliceous PFA, these typically represent an unreactive proportion of the material, and in general, the higher the amorphous fraction the greater the reactivity [34]; calcareous PFA can contain reactive crystalline phases such as free lime and C_3A, and so the same statement is not always applicable [71].

PFA is a pozzolanic material, and so the silicon dioxide and aluminium oxide react with water and calcium hydroxide formed through hydration of the PC. Given that the reaction of the PFA requires calcium hydroxide in order to proceed, initially the PFA acts as an inert filler which provides nucleation sites for the hydration products of PC. The onset of the pozzolanic reaction requires a very alkaline environment, and varies considerably dependent on factors such as temperature and w/s ratio, meaning that the pozzolanic reaction can take many weeks to initiate in some systems [34], [42].

2.4.3 Impact of SCMs on phase assemblage and microstructure

Addition of SCMs to PC clinker changes the chemical system and affects the hydration of the materials and the phases that are formed. Figure 2.6 shows ternary diagrams depicting the characteristic compositions of common SCMs together with PC, and it is clear that both BFS and PFA represent much lower-calcium systems with higher silicon and aluminium contents. As such, hydration results in a different phase assemblage to that seen from pure PC hydration [71].

PFA-containing systems generally contain phase assemblages similar to those of pure PC systems, however portlandite contents are initially higher (per cement mass) and then drop over time as the pozzolanic reaction of PFA proceeds. The hydration of the PFA increases the alumina content of the system; reaction of this with sulfate (from gypsum) forms ettringite and AFm minerals including monosulfoaluminate, and, if sufficient Al_2O_3 is present, strätlingite (a silicate-containing AFm phase, C_2ASH_8) may also form. The relative proportions of ettringite to AFm will decrease as PFA hydration and alumina content increase and sulfate levels become depleted [71], [76], [77].

The high silica and alumina content of SCMs has a distinct effect on the C-S-H formed in PFA- and BFS-containing cements. The Ca/Si ratio decreases compared to pure PC, and the mean chain length increases. The amount of PFA present and the degree of hydration strongly affect the amount of silica that can form chains in C-S-H. The increased presence of alumina leads to partial replacement of silica in the dreierketten unit, creating a C-A-S-H phase. Current understanding indicates that replacement into a paired site is thermodynamically unfavourable, and as such alumina is assumed to be present in bridging sites (Figure 2.5) [49], [53]. Aluminium has been found to substitute into the silicate chains to give Al/Si ≤ 0.1, with concurrent formation of aluminium rich AFm phases such as strätlingite at higher Al/Si ratios [56].

The aluminium incorporated in the silicate chains has been observed to primarily occur as tetrahedrally coordinated species Al(IV). Increased Ca/Si ratios result in a decrease in the proportion of Al(IV), with more octahedrally coordinated Al(VI) present. This is thought to correspond to formation of amorphous aluminium hydroxide or calcium aluminate hydrate at the C-S-H surface [56], [78]–[80]. Pentavalent Al(V) coordinated species are present regardless of the Ca/Si ratio, and act as a charge balancing species in the interlayer [79].

The alkali content of the system can affect the ratio of Al(IV)/Si in the dreierketten units. The substitution of Al(IV) into the silicon site introduces a charge deficit, and this can be balanced through absorption or bonding of alkali cation species such as Na^+ and K^+ in the interlayer. The presence of these charge balancing ions can significantly increase the proportion of Al present within the silicate chains [81].

Cements containing BFS commonly possess lower levels of portlandite than pure PC systems, however unlike in PFA systems, portlandite is anticipated to persist in the phase assemblage due to the higher calcium content in BFS unless very high levels of replacement are used [71], [82].

The increased levels of magnesium and aluminium in BFS-containing cements leads to the formation of a hydrotalcite-like phase, a layered double hydroxide where the generic layer formula is $[(M^{2+}_{1-x}M^{3+}_{x})(OH)_2]^{x+}$. This results in an overall positive charge which is balanced by anions (such as CO_3^{2-}, SO_4^{2-}, Cl^-, and OH^-) between the layers. Although pure hydrotalcite has the formula $Mg_6Al_2(CO_3)(OH)_{18}{\cdot}mH_2O$, cement systems more commonly contain a phase with Mg/Al ratios closer to 2, similar to quintinite ($Mg_4Al_2(OH)_{12}CO_3{\cdot}4H_2O$) [60].

The interdependency between magnesium content and therefore potential formation of hydrotalcite-like phases on the composition of the C-S-H phase has also been investigated, with Ben Haha et al. [83] proposing that the formation of a hydrotalcite-like phase makes incorporation of aluminium in C-A-S-H less likely. Formation of a hydrotalcite-like phase has been observed to occur in alkali-activated slag binders where MgO content is > 5 %, and Bernal et al. [51] proposed that this promoted formation of C-S-H as the hydrotalcite preferentially takes aluminium from the system. The presence of hydrotalcite-like hydrates and the alterations to the C-S-H phase were observed to improve the overall performance with respect to carbonation.

The capacity of Mg-Al layered double hydroxides to immobilise radionuclides within cements has yet to be fully investigated, although it is established that these phases contribute to retention of Cl^- and CO_3^{2-} [84]. Sorption of various actinides to hydrotalcite was investigated by Altenhein-Haese et al. [85], and results were found to be highly dependent on the ionic concentration and speciation. The high affinity of hydrotalcite for CO_3^{2-} has been stated as a limiting factor for its use as an anion absorber, and studies by Angus and Glasser found that low sorption rates were found in batch trials with I^-, likely for this reason [16], [86].

BFS contains sulfide which is released into the pore solution as hydration occurs. This will not readily form hydrate phases, but can exert influence on the poising (redox buffering) capacity of the cement if present in sufficient concentrations, i.e. the presence of BFS containing 1 % sulfide may reduce the redox potential from +200 mV in PC pore solutions to -300 mV, creating a poising reserve [87]. This can result in a decrease in the redox potential of the system via complex interactions of sulfate (from gypsum) reacting with sulfide and thiosulfate (from reaction of sufate and sulfide in an alkaline environment), which may have the capacity to reduce specific radionuclides into less soluble species [17].

The degree of hydration and level of replacement by the SCM will have a distinct impact on the differences observed in the microstructure, as the extent of the modification to the C-S-H is controlled by the Ca/Si and Al/Si ratios. However, lower Ca/Si ratios and higher Al/Si are typical, resulting in longer silicate chains with some aluminium substitution. Although lower Ca/Si ratios were observed with increasing levels of SCM replacement, no difference in the Ca/Si ratio was observed between inner and outer product for BFS/PFA systems [60], [77], [88], [89].

There were strong differences in the morphologies of inner and outer product formed dependent on Ca/Si, however, as increased replacement by SCM causes the fine fibrillar morphologies to convert to less directional foil-like textures. The coarseness of the foils appears initially dependent on space constraints, however over time as hydration progresses the textures become increasingly fine as capillary porosity is reduced [60], [88].

Refinement of the pore structure over time leads to improved material properties such as compressive strength and a reduction in diffusion potential, which decreases the potential ingress of species such as chloride, sulfate and carbonate that could deleteriously affect the cement [34], [44], [71].

As outlined in Section 2.1, encapsulant grouts used by the nuclear industry in the UK are tailored for use with specific waste streams. This means the cements vary in terms of the level of SCM replacement and w/s ratio dependent on the type of waste being managed, creating a diverse formulation envelope. For example, the Magnox Encapsulation Plant (MEP) at Sellafield uses 3.44:1 BFS:PC formulation with 0.35 w/s ratio to manage waste streams such as 2D24: Magnox Cladding and Miscellaneous Waste [90], which are predominantly solid materials. However, the Waste Encapsulation Plant (WEP) uses higher volume replacement blends (4.5:1 – 9:1 BFS:PC) to treat solid waste and sludges [3]. The impact of the range of formulations on the cements and their response to radiation will be further discussed throughout this thesis.

2.5 Radiation damage in ILW

ILW contains significant levels of radioactivity as a result of nuclear fission and waste processing; threshold levels of activity within these waste streams are by definition the same as for HLW. Some examples of the average activity and radionuclides in UK ILW waste streams are shown in Table 2.5.

Table 2.5 Examples of UK ILW waste streams, average specific activity levels and key radionuclides present. Data modified from [90], [91]

Waste Stream Identifier	Average specific activity (TBq/m^3)		Key radionuclides within waste
	Total α	Total β/γ	
Waste Stream 2D24: Magnox cladding and miscellaneous solid waste	3.79	1.79×10^2	^{60}Co, ^{63}Ni, ^{85}Kr, ^{90}Sr, ^{137}Cs, ^{147}Pm, ^{238}Pu, ^{239}Pu, ^{240}Pu, ^{241}Pu, ^{241}Am
Waste Stream 2D03: Plutonium Contaminated Materials; Drums	1.00	1.21×10^1	^{238}Pu, ^{239}Pu, ^{240}Pu, ^{241}Pu, ^{242}Pu, ^{241}Am

Radioactive species have a higher number of neutrons than their stable isotopes, and as such undergo decay through emission of alpha, beta and gamma radiation to lower the N:Z ratio, promoting increased stability [92]. The process of decay is dependent on the radionuclides present within the waste, and will affect the surrounding materials in different ways.

Alpha (α) decay involves the parent nucleus emitting a particle comprising two protons and two neutrons, resulting in formation of a daughter species. Alpha recoil particles have high mass and low velocities, and can be stopped by several centimetres of air [92]. In the cemented wasteform examples given in Table 2.5, the radionuclides are which contribute the most alpha activity are residual fuel fragments composed of plutonium (with some residual uranium) and decay products related to this, including ^{241}Am.

Beta (β) decay results in a change of charge through the emission of electrons or positrons, and less commonly through electron capture. Beta radiation is more penetrative than alpha, but can be stopped with e.g. 3 mm of aluminium plating [92]. Significant proportions of beta emitting species (such as ^{137}Cs and ^{90}Sr) are present in some ILW waste streams, as they are fission products from uranium and plutonium decay. Emission of alpha and beta particles can leave the nucleus energetically excited, and gamma (γ) radiation dissipates this energy through the emission of high energy photons, which requires several centimetres of lead, or up to several metres of concrete, for shielding [92]. Gamma emitting species in the ILW waste streams previously outlined include a ^{60}Co, ^{137}Cs, ^{240}Pu, and ^{241}Am; these are also some of the highest contributors to radiogenic heating in the ILW packages [36]. The highly penetrative nature of gamma radiation means that wasteforms have the potential to be exposed to the decay products of adjacent waste packages, dependent on GDF design, package spacing and backfill material [18].

Cement wasteforms can be affected by radiation through: 1) radiolysis of the aqueous phase or of the waste components, 2) atomic displacements, and 3) heating from absorbed radiation energy [36]. Radiolytic effects arise from alpha, beta and gamma radiation, and as gamma is the most penetrative, the bulk of studies focus on this. However, the impact of the >10,000 ionisation events per cm of travel of alpha particles [93] is of particular interest in this thesis (for comparison, beta particles produce >100 ionisation events per cm travel [93]). Likewise, atomic displacements are most likely to result from interactions of alpha decay, rather than gamma or beta. Given this thesis aims to investigate radiolytic impact and radiation damage associated with this, the effect of gamma and alpha radiation will be focused on.

Much of the existing research on these areas has focussed on pure PC used in concretes, as these are used for structural and biological shielding purposes [94]–[96]. The cements used for encapsulation of ILW comprise SCM blends which have very different chemical and microstructural characteristics from more calcium-rich pure PC matrices. The alterations to the chemical and physical properties of the cement are expected to alter the response to radiation exposure. These waste-encapsulating grouts are subject to high levels of ionising radiation throughout their service life, and although some investigation of how these systems react to radiation exposure has been published, the effects are not currently well understood.

2.5.1 Radiolytic degradation

Due to the high water content of cementitious materials, a primary concern related to their use as encapsulation materials is that the water present is liable to undergo decomposition through radiolysis. This could cause increased internal pressure through gas production, which may result in cracking that reduces wasteform durability.

Radiolysis will occur from exposure to all ionising radiation, however highly energetic gamma radiation has the greatest penetrating strength and as such it will have a significant radiolytic effect on the cement. Although gamma irradiation studies have been the focus of several studies since the 1980's to support waste management, these were often on pure PC systems. Also, few of the findings are published in open literature, and where they are, limited characterisation of the cement post-irradiation had been completed [30]–[32]. The effects of alpha radiolysis have not received as much attention, likely due to the more demanding experimental requirements (requirement of alpha-containing gloveboxes) and licensing requirements to hold radionuclides appropriate for testing (i.e. uranium or plutonium).

Interaction of gamma radiation with materials can result in Compton scattering, photoelectric effects or pair production; regardless of the mode of interaction, electrons are ejected which go on to interact with more material [97]. This cycle continues until the energy of the ejected electron is below the ionisation energy of the material. The collisions of the emitted electrons create electronic excitations which can destroy covalent bonds due to an increase in their vibrational energies, which has been observed to cause decomposition of the Si—O bonds present in the Si-tetrahedra of the C-S-H phase in cement [94], [98].

Radiolysis of water in an alkaline medium generates H_2, e^-_{aq}, $H^\bullet$, OH^-, H_2O, H^+, OH and H_2O_2 as primary products, which can react with solutes in the interstitial liquid producing further reactive intermediates [99]. These can participate in additional reactions within the pore fluid or interact with the cement hydrates [99]. These secondary reactions should in principle lead to the production of O_2, however Bouniol and Aspart reported disappearance of oxygen from the gaseous phase in gamma irradiated samples [100]. This was attributed to the primary yield of H_2O_2 reacting with calcium present in the cement hydrates, leading to the formation of calcium peroxide octahydrate ($CaO_2{\cdot}8H_2O$) which preferentially carbonated to form $CaCO_3$ in the grout. This mechanism for O_2 removal was later queried by Bouniol and Bjergbakke [101] whose simulations showed that formation of $CaO_2{\cdot}8H_2O$ was not systematic, but that the phase must be present if oxygenated species are present. Oxidation of organic additives or iron from the cement grinding process were highlighted as potential causes [101], [102].

Comparatively, the effects of alpha radiolysis may be anticipated to be lesser than those of gamma radiolysis due to the limited zone of influence, as emitted alpha particles have much shorter ranges in material. However, the emitted alpha particle has high linear energy transfer and will initially lose energy through electronic interactions, creating overlapping ‘spurs’ containing ionised and excited species along its path, resulting in formation of a residual column of densely packed ionisation events [103]. This can lead to the proportion of molecular products formed being proportionally higher, as the formation of many radicals in close proximity could result in more reactions forming molecular products [103]. Should an increase in molecular products occur in the zone in which the alpha particle has deposited its energy, this may cause localised increased pressure as the surrounding matrix may not allow efficient removal of the gaseous products [104]. Due to the overlapping ‘spurs’ that result from the alpha particles as they travel through the material, the resulting molecular gas yields (thought to cause higher localised pressure) may be greater than those observed from an equivalent dose of gamma exposure where the ionisation events occur over a greater distance, i.e. the gas generation from a 4 MGy alpha dose would be greater than from a 4 MGy gamma dose. This would be exacerbated in materials with high levels of closed porosity as there would be no preferential

pathway for the gas to be removed, and so may lead to cracking, chipping, spallation and reduction in compressive strength becoming more prevalent.

Only a handful of gas evolution measurements of hydrogen yields from alpha radiolysis of cements have been reported in the open literature. Bibler reported values of $G(H_2)$= 0.63 molecules 100 ev^{-1} for an PC/gypsum cement at w/s = 0.7 [104]. Crapse et al. reported hydrogen yields from a cement sample (of unspecified composition) containing 1 wt. % PuO_2 and 16.5 wt. % water to be 0.15 molecules 100 ev^{-1} [105]. The impact of radiolytically generated species interacting with the cement hydrates, and the creation of a potentially chemically distinct region, has not been investigated in the open literature.

The presence of metastable calcium peroxide octahydrate has been linked to an increase in carbonation and alteration to pore size distributions in gamma irradiated cement [100], [106]–[108]. Vodak et al. [109] speculated that microcracking due to radiolytic dehydration provided a mechanism for ingress of CO_2, which consequently reacted to form $CaCO_3$ in PC systems. Mobasher et al. [110] also observed microcracking in gamma irradiated BFS:PC blended grouts, attributed to the combined effect of radiolysis and heating caused by irradiation exposure. Irradiation-induced carbonation was not observed in the samples analysed in that study; it was speculated that the reduced proportion of $Ca(OH)_2$ in the system may have minimised formation of calcium peroxide octahydrate, inhibiting the carbonation process.

Drying of the grout via radiolytic dehydration has been linked to a reduction in compressive strength. However, there have been limited studies specifically looking at the compressive strength of irradiated concrete and cement, and the available data show no specific trends [94], [110]–[113]. Soo and Milan stated that in PC samples using dose rates of 31 Gy/hr, a threshold dose of 10^5 Gy was required to enable this effect, however the concurrent impacts of carbonation and hydration were not assessed and may impact the findings [112].

Robira et al. [114] investigated the impact of low dose gamma irradiation on PC systems, where marked differences in irradiated samples were found. Reduced compressive and bending strength was observed for dry, humid and carbonated samples, although the effect was smaller in carbonated samples. Changes in the pore size distribution were also seen, and correlations between decreased median pore diameter and decreased strength made, speculated to be the result of changes in the C-S-H.

Maruyama et al. [115] completed a comprehensive study investigating the effects of gamma exposure on the carbonation behaviour of PC pastes. They found that while control samples predominantly

contained the calcite polymorph of $CaCO_3$, production of vaterite and aragonite was observed in the irradiated samples. This was mainly attributed to the rapid drying under gamma exposure artificially preserving the less stable carbonate phases, but precipitation of calcium peroxide octahydrate was thought to have formed additional vaterite. The distribution of the carbonate phases was found to affect the bending strength of the samples, with vaterite formation in the small pores around the C-S-H preserving the structure and increasing strength compared to the non-irradiated carbonated sample.

It should be noted that the carbonation process will vary depending on the atmospheric conditions to which the samples are exposed, and the initial chemistry of the system. In the above scenario, based on previous studies the anticipated process of atmospheric carbonation is as follows. Initially, $Ca(OH)_2$ is decalcified in the presence of carbonate (present as CO_3^{2-} in the pore solution of undamaged cements) forming amorphous calcium carbonate on surface of crystals. Concurrent carbonation of the C-S-H occurs, although more rapid dissolution of portlandite results in faster carbonation of this phase [55]. Although it is metastable, vaterite formation is favoured in the presence of imperfectly crystalline portlandite [116], [117]. Similarities between the calcium oxide layers in calcium rich C-S-H and the calcium octahedral sheets of portlandite have been outlined as a potential reason for the formation of vaterite on their surfaces [49], [115], [116]. As carbonation progresses, decalcified C-S-H produces amorphous hydrated silica which undergoes co-precipitation more easily with aragonite than calcite [115], [118]. If carbonation were to progress in hydrated systems, as vaterite and aragonite are metastable, they would evolve to calcite according to a dissolution-precipitation process [119]. The carbonation products formed are highly dependent on the initial Ca/Si ratio of the system, relative humidity, water content, and pH of the cement [116], [118].

Changes in the C-S-H due to dehydration (reducing the interlayer water) and carbonation (potentially altering the structure of the C-S-H) are likely to reduce the viscous response of the material under sustained load. This change in creep behaviour is key to understanding how the mechanical behaviour of cements and concretes is altered under irradiation. Gamma irradiation has been observed to reduce the creep response in PC systems, with significant decrease observed after exposure to 257 kGy using a low dose rate of 8.5 Gy/hr [120], [121].

Gamma exposure studies of PC pastes that have undergone pre-drying show that radiolytic breakdown of chemically bound water can occur, albeit to a low extent (1.5 % at 200 MGy) [111], [122]. The progressive breakdown of hydrates and decomposition of clinker phases was observed at <130 MGy in PC systems containing PFA and silica fume. Distinct changes in microstructure indicative of phase transformations and densification were observed when the dose reached 290 MGy [107].

Bouniol et al. [123] recently investigated the impact of sulfide species on radiolytic H_2 production using a combination of experimental and simulation based techniques. The sulfide present in the pore solution from hydration of BFS was expected to increase the lifetime of reducing radicals such as e^-_{aq} and $H^\bullet$, which at high pH can react to form H_2. The findings showed an initial increase in H_2 production in cements containing high levels of replacement of PC by BFS. However, this was found to be a temporary increase due to initial oxidation of the sulfide and increase in pH, which allowed reaction of $H^\bullet$ with H_2S. Over time, the anoxic conditions in the system and high liquid saturation within the porosity allow very efficient recycling of H_2, leading to the net production of H_2 reducing towards zero [123].

Richardson et al. [124] investigated the effects of gamma radiation on the microstructure of BFS:PC grouts containing 75 – 90 % replacement of PC by BFS, and observed increased ettringite formation after gamma exposure. This was considered to be due to an increased rate of oxidation in the sulfide present within the BFS. Such a reaction would be analogous to external sulfate attack on cement due to formation of ettringite at the expense of monosulfate and portlandite, which is widely believed to be the cause of physical damage due to the expansive nature of the reaction [125]. However, post irradiation characterisation of samples containing 80 % replacement of PC by BFS in the Bouniol et al. study showed no alteration to the phase assemblage, despite oxidation of the sulfide [123].

2.5.2 Atomic displacements

As outlined in Section 2.5, cement wasteforms can be affected by radiolysis and atomic displacements. Atomic displacements refer to damage to the crystal structure of hydrates and unreacted solids in materials, which can result from elastic scattering interactions with the incoming particles. Beta/gamma radiation is typically too low in energy to produce displacement of atoms from their lattice positions, however alpha decay is sufficiently energetic to create displacements. Alpha decay of actinides produces a high energy (4.5 – 5.5 MeV) helium nucleus which is emitted from the radionuclide, and a resulting daughter recoil nucleus with energy of approximately 70 – 100 keV [92], [126]. As the particles travel through materials, they will slow down by losing energy to the surroundings interacting via elastic and inelastic stopping. Elastic interactions refer to nuclear stopping, where energy is removed from the incident atom via ballistic impact. Inelastic interactions refer to electronic stopping, where energy is removed from the incident atom through transfer to the electronic structure.

The stopping type that predominates is mainly dependent on the energy of the particle, however mass does also have an effect. Electronic stopping dominates for high energy particles, whereas nuclear stopping is more prevalent for low energy particles. In alpha decay, the high-energy emitted helium

nuclei (hereafter referred to as alpha particles) will have contributions from both electronic and nuclear stopping powers. Initially, electronic stopping will be dominant, but once enough energy is lost to ionisation events nuclear stopping will prevail and cause knock-on displacement at the limit of the particle range, creating Frenkel defects (vacancy-interstitial pairs) [126]. The loss of energy through electronic interactions is referred to as the linear energy transfer (LET). The daughter recoil nucleus, having a high mass and low energy, will interact via nuclear stopping, creating thousands of atomic displacements along its path [126].

The amount of damage caused to the structure is typically expressed in terms of displacements per atom (dpa). This is a calculated value estimating the number of times each atom has been moved from its lattice site on average for every atom in the system, so a dpa of 1 indicates every atom in the system has, on average, moved once [126], [127]

Sources of alpha radiation in UK ILW include isotopes of uranium and plutonium including ^{236}U, ^{241}Pu, together with decay products of these radionuclides such as ^{241}Am [128]. These are found in wastes handled through Sellafield's Magnox Encapsulation Plant (MEP) and Waste Treatment Complex (WTC), which process waste streams for Magnox cladding (i.e. waste stream 2D22) and plutonium contaminated materials (i.e. waste stream 2D03) respectively [128], [129]. During initial product evaluation testing for cementitious encapsulant grouts, the dimensional stability of cement wasteforms after exposure to alpha radiation was evaluated by doping BFS and PFA systems with plutonium dioxide or radioactive PCM incinerator ash [32], [130]. The compressive strength decreased with increased alpha dose, however the dimensional stability was observed to vary between studies, with zero change and breakdown of monolithic samples recorded [32]. This variation is likely a product of the different total doses and dose rates used in the various testing campaigns. No characterisation of the phase assemblage or microstructure was published as part of these investigations.

There is currently a gap in knowledge relating to the effects of alpha radiation on cementitious materials, specifically on the interactions of alpha particles with the hydrate assemblage. The mechanisms by which they interact and the resulting effect on the chemistry and phase assemblage of the system is of great interest with regard to nuclear waste disposal.

In cemented wasteforms, the alpha containing waste will likely be present as fuel fragments or within other material (supercompacted drums for PCM) which will then be surrounded by cement [18]. This is different from glass or ceramic wasteforms, where alpha-emitting species are directly incorporated into the host crystal structure. It is considered that radioactive inclusions in minerals may provide a natural analogue for the potential interactions of alpha species with cement encapsulants, especially given that there are similarities in structure between phyllosilicates with layered TOT structures

(tetrahedral-octahedral-tetrahedral, where sheets of silica tetrahedra enclose metal rich octahedral layers) and cement hydrates [42], [88], [131]. However, it is important to note that whilst these similarities exist the structural and chemical differences in cement hydrates, together with the heterogeneous nature of cement paste, mean that the exact response will be different. Rather, it is intended that natural minerals may give examples of the types of processes which will occur in cements and how these effects may manifest.

The development of radiohaloes around actinide-bearing inclusions (e.g zircon, monazite) has long been observed as a petrographic feature of phyllosilicates [132]. Formation of radiohaloes is attributed to the interaction of alpha particles emitted from the inclusion, with little impact from the recoil nucleus which predominantly effects the host lattice. Radiohaloes refer to concentric rings of discolouration surrounding alpha emitting inclusions, with the radius of each ring representative of a discrete alpha particle energy. As such, in well-defined radiohaloes it is possible to infer the isotopes responsible for formation of the feature [132], [133].

The mechanisms responsible for the discolouration are debated in the literature. Radiation-induced point defects have been outlined as a potential cause by Nasdala et al. [134] who attributed limited impact from ionisation and saw no variations in colour centres across the radiohalo. However, the impact of ionisation was found to be more significant by Pattrick et al. [135], where reduction of iron across the radius of the radiohalo was interpreted to be a result of radiolytic breakdown of OH groups producing reductive species. Bower et al. [136] found that structural damage did not correspond directly with discolouration in a range of silicate minerals, and suggested that ionisation mechanisms may be predominantly responsible, also noting that dark radiohaloes appear only in hydrated mineral phases.

The structural damage within radiohaloes is of interest as they represent changes to physical properties and chemical reactivity [137]. Radiohaloes represent the onset of metamictisation, the process through which crystalline materials become amorphous [138]. Despite contradictory literature on chemical variation within the features at time of analysis, there is agreement that structural damage in these areas increases susceptibility to later chemical alteration [136], [138].

2.6 Summary

It has been displayed that cementitious grouts are a suitable option for encapsulation of several varied waste streams, especially when formed from mixtures of SCMs and PC. The addition of BFS and/or PFA successfully lowers the heat generated through hydration of PC and improves fluidity and bleed

issues, allowing formation of a monolithic wasteform with good stability that provides physical and chemical containment of radionuclides. There are distinct differences between pure PC systems and SCM-blended systems, with key differences in the phase assemblage in blended cements clearly impacting the chemical and structural properties.

The anticipated service life for these materials in nuclear waste immobilisation is extraordinarily long by the standards of applications for cements. The duration of integrity of the wasteform itself must exceed 500 years, and there is a requirement to retain radionuclides until decay to levels similar to those of normal background is achieved. The grouts will be exposed to ionising radiation throughout this time. Although bulk response to radiation appears tolerant for these materials, there are many unknowns specifically related to ageing and degradation through radiation exposure which require further investigation.

Although significant research has been completed on the impact of gamma radiation on cementitious systems, these have predominantly focussed on pure PC and/or concrete materials, which are not representative of the encapsulant grouts used in the UK. Currently there is little open literature addressing systematic characterisation of the effect gamma exposure has on the bespoke cementitious grouts used by the UK nuclear industry, which include formulations with very high levels of replacement by SCMs. As such, there is a research gap investigating the impact of “lifetime doses” of gamma exposure on the phase assemblage, microstructure and mechanical properties of these materials.

There is also currently a gap in knowledge relating to the effects of alpha radiation on cementitious materials, specifically on the interactions of alpha particles with the hydrate assemblage. The mechanisms by which they interact, and the resulting effect on the chemistry and phase assemblage of the system, are of great interest with regard to nuclear waste disposal. Radiolysis and atomic displacement may impact the chemistry of the system through redox alterations and charge balancing, or through structural impacts causing defect formation (vacancies, interstitials and creation and migration of these). This work aims to elucidate on the impacts of these processes in terms of long term nuclear waste management.

3 Materials and methods

3.1 Materials

The cement used in this study was Portland cement conforming to Sellafield Ltd (SL) specification [15], supplied by Hanson Cement as Ketton coarse ground PC. BFS conforming to UK nuclear specifications was also obtained from Hanson Cement, as Scunthorpe GGBS blended with Calumite (a coarse ground material produced from granulated blast furnace slag) in a 70:30 weight ratio [139]. PFA was from the CEMEX Drax plant and conformed to BS EN 450-1 [75] as well as the SL specification regarding performance in a pre-prepared grout mix. The oxide compositions of the powders used throughout this study are provided in Table 3.1, together with a summary of the Blaine fineness [140], and particle size distribution (PSD) obtained through laser diffraction.

Table 3.1 Composition of raw materials determined by X-ray fluorescence (XRF) and represented as oxides, Blaine fineness, and PSD analysis.

Oxide	PC (wt. %)	BFS (wt. %)	PFA (wt. %)
SiO_2	21.6	36.1	52.9
Al_2O_3	5.1	11.4	24.8
Fe_2O_3	2.6	0.4	8.4
CaO	64.9	39.4	2.5
K_2O	0.8	0.7	3.1
MgO	1.0	8.4	1.6
Na_2O	0.2	0.4	1.2
TiO_2	0.4	0.9	0.9
Mn_2O_3		0.6	0.1
MnO	0.1	0.6	
SO_3	2.6	-	0.1
S^{2-}	-	0.8	
Cl^-	0.1	0.0	0.1
$SiO_2+Al_2O_3+Fe_2O_3$	-	-	84.6
Glass count	-	97	
Blaine fineness	436 $m^2 \cdot kg^{-1}$	357 $m^2 \cdot kg^{-1}$	
Residue on 0.045 mm sieve (%)			9.1
PSD D_{10}/µm	2.4	3.5	-
PSD D_{50}/µm	18.7	130	-
PSD D_{90}/µm	59.2	1288	-

Figure 3.1 shows the particle size distribution plots for the BFS and PC materials. The PC contains a monomodal particle size distribution, whereas the BFS data clearly show a bimodal distribution due to the intermixing of finely-ground slag (termed GGBS by the UK nuclear industry) with Calumite. The GGBS particle size fraction is all lower than 90 µm, whereas the Calumite particle size range is between

100-3000 µm. The coarser grained Calumite fraction has the same chemical composition as GGBS, and was introduced in order to regulate the heat of hydration and bleed of the grouts as generic GGBS specifications have progressively reduced the particle size to suit construction industry needs [15].

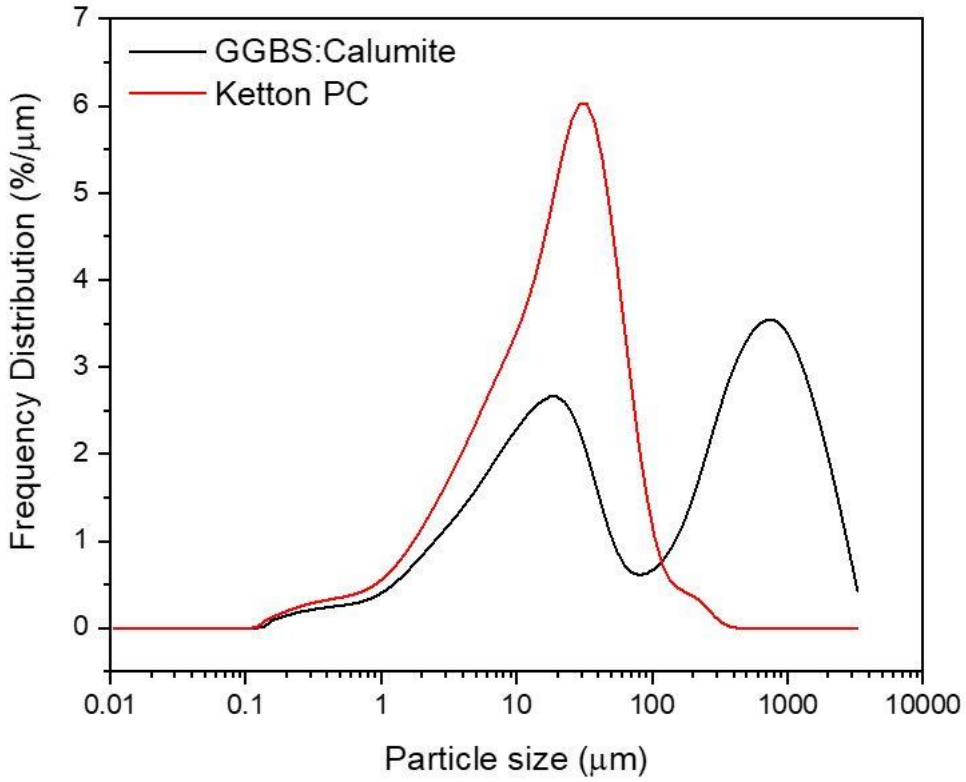

Figure 3.1 PSD data for GGBS:Calumite mix, and Ketton PC, demonstrating the bimodal and monomodal distributions respectively.

3.2 Formulations

Cement blends were identified for analysis by reference to the published Sellafield upper and lower replacement limits of PC by SCM, together with the most commonly used blend ratios [15]. Details of the precise grout formulations used are outlined in Table 3.2.

Table 3.2 Blend ratios of the grout formulations used throughout this study.

SCM:PC	w/s	BFS (g)	PFA (g)	PC (g)	H_2O (g)
3:1	0.35	375.0	-	125.0	175.0
	0.43	-	375.0	125.0	215.0
3.44:1	0.35	387.4	-	112.6	175.0
5.67:1	0.35	425.0	-	75.0	175.0
9:1	0.35	450.0	-	50.0	175.0

Small volumes (<200 g) of cement were manufactured using the following method. Dry powders were initially hand mixed to combine them prior to water addition, after which they were stirred by hand for 3-6 minutes to ensure full incorporation of the dry powders. The pastes then underwent 10 minutes of machine mixing using a Heidolph RZR2020 overhead stirrer, or a Kenwood benchtop mixer for larger volume samples. Combination of the dry powders was completed on low power for 2 minutes, water was added whilst mixing continued for a further 2 minutes, followed by mixing on high power for 4 minutes. Samples were poured into centrifuge tubes or 50 x 50 x 50 mm steel cube moulds, sealed, and placed in a controlled environmental chamber at 20°C and 95 % relative humidity. A vibration plate was used to remove air bubbles from centrifuge tube samples prior to sealing, and cube moulds were repeatedly tapped on a hard surface to replicate this effect. Cube samples were demoulded after 24 hours and cured in sealed plastic bags under the same conditions. These curing conditions were selected to provide baseline characterisation. Temperature variations during irradiation exposure were unavoidable, and for each experiment control samples were cured in similar heating environments where possible. These conditions are detailed in the relevant results chapters.

Where analysis was required at a specific curing age, and the quantity of free water was not of interest in the analysis, hydration was halted on samples by removing unbound water from the capillary pores of the paste. Solvent exchange was utilised for all hydration stoppage, as this has been shown to cause less damage to the microstructure than direct drying techniques [141]. Acetone was used for solvent exchange in this study. Acetone has been shown to interact with hydrate phases, causing increased weight loss in TGA due to aldol condensation. This process forms mesityl oxide, which can react with $Ca(OH)_2$ to form $CaCO_3$, causing under- and overestimation of these phases respectively [142]. No significant impact on other analytical methods were noted from acetone usage, and as hydration was not commonly stopped prior to testing by TGA here, this method was deemed suitable for this study.

3.3 Analytical methods

3.3.1 Particle size distribution

Particle size variation can alter the kinetics of hydration of PC and BFS, and may thus result in different reaction rates and microstructural alterations which are undesirable in terms of process control (e.g. shorter setting times causing blockages in piping infrastructure) and the anticipated properties [44]. Differences in porosity, heat generation, and strength development may be caused by particle size distribution variations. The particle size distribution of the powders was assessed using a dry dispersal method in order to prevent dissolution of the particles in a liquid suspension. The analysis was completed using a Mastersizer 3000 PSA and Malvern instruments analytical software with the

following parameters: 2 bar pressure, 30 % feed rate, 1.25 aperture, and refractive indexes of 1.73 and 1.63 for PC and BFS respectively [139], [143].

3.3.2 Isothermal calorimetry

Isothermal calorimetry is used to monitor the hydration of the cement through measurement of heat evolution. As hydration of cement is a highly exothermic reaction, the heat evolution from a sample that is held under isothermal conditions can be recorded, and compared to a reference (or 'blank') sample running in parallel that has a similar heat capacity [144]. The measurements were obtained using dual channel TAM Air equipment from TA Instruments, with water used as the reference. Cement pastes were hand mixed before 20 g was placed into the glass testing ampoule, which was sealed and placed in the calorimeter. Testing was completed at 20 °C for 14 days.

3.3.3 Selective dissolution via EDTA solution

The degree of hydration of the BFS fraction in blended cements is commonly determined through selective dissolution, as the amorphous nature of BFS means that methods used for evaluating crystalline PC systems such as Rietveld refinement are unsuitable [145], [146]. There are disadvantages to using the selective dissolution method, including ineffective dissolution of hydrate phases (outlined by Kocaba et al. [147], [148]) which can lead to underestimation of the degree of reaction. That being said, a recent round robin study comparing inter-laboratory results for techniques used to assess SCM degree of hydration found problems relating to all commonly used techniques [149]. The main advantages of using the selective dissolution method is that it is a simpler, less analytically intensive and a well- documented technique. The widespread use of selective dissolution using EDTA solution in the literature demonstrates that the method provides sufficiently reliable results [82], [145], [146], [149], [150], which together with the simple methodology meant this technique was determined suitable for the needs of this study.

This study used the selective dissolution method outlined by Luke and Glasser [146], which provides quantitative evaluation of the degree of hydration of BFS by dissolving hydration products and residual anhydrous PC. The remaining residue is considered to be the unreacted BFS fraction. The solution required for this method was made via dissolution of 93.0 g of EDTA·$2H_2O$ in a solution of 250 mL of triethanolamine and 500 mL of water. This mixture was transferred to a volumetric flask, where 173 mL of diethylamine was added. Water was then added to make the solution up to 1000 mL.

For each dissolution test, 50 mL of the solution was pipetted into a beaker and diluted to 800 mL with water. This solution was brought to a temperature of 20 ± 2 °C and 0.5 g of dried sample, ground to a particle size < 63 µm and weighed to the nearest 0.1 mg, was sprinkled over the surface of the solution. The mixture of the solution and the ground sample was stirred at constant temperature using a magnetic stirrer for 120 ± 5 minutes. After this, the solution was filtered under vacuum through a 90 mm diameter Whatman GF/C filter which previously had been washed with 100 mL of water, dried at 105 °C for 1 hour and weighed to the nearest 0.1 mg. The residue was washed 5 times with 10 mL of water, dried at 105 °C for 1 hour and then weighed to the nearest 0.1 mg.

Testing was completed on the anhydrous precursors in order to account for the small levels of BFS which undergo dissolution, and the residual levels of PC which do not dissolve. The residual amounts were found to be 85.3 % and 0.3 % for BFS and PC respectively. Corrections were applied to the results from hydrated samples to reflect these values. A correction was also applied to account for hydrotalcite-group minerals, assuming all MgO from the BFS hydration forms quintinite-like $Mg_4Al_2(OH)_{12}CO_3{\cdot}4H_2O$, which does not readily dissolve in the EDTA solution [82], [146], [150]. This process is outlined in equations 3.1 to 3.4:

$$\mathrm{HT}_m = \frac{m_{\mathrm{MgO}}}{m_{\mathrm{MgO/HT}}/100} \tag{3.1}$$

$$\mathrm{HT}_s = R \times \mathrm{HT}_m \tag{3.2}$$

$$D = \frac{R\left(100 + m_{\mathrm{MgO/HT}}\right)}{100} \tag{3.3}$$

$$I = D - \mathrm{HT}_s \tag{3.4}$$

Where HT_m is the maximum amount of hydrotalcite-group mineral formed from complete hydration of the BFS (25.34 g), m_{MgO} is the mass of MgO in the BFS, $m_{MgO/HT}$ is the mass percentage of MgO within $Mg_4Al_2(OH)_{12}CO_3{\cdot}4H_2O$ (33.14 wt.%), HT_s is the mass of $Mg_4Al_2(OH)_{12}CO_3{\cdot}4H_2O$ created based on the amount of slag reacted, *R* is the residue after dissolution including corrections for PC and BFS, *D* is the corrected degree of hydration, and *I* is the calculated initial residue. Equations 3.2 – 3.4 were solved iteratively, replacing R with D each time. The actual degree of hydration of the slag was determined through minimisation of the sum of squared errors between the iterated initial residue and calculated initial residue.

3.3.4 Compressive strength testing

Cement strength was tested at 28 days, then at 4 or 8 weekly intervals on triplicate 50 mm (± 0.5 mm) cube samples [151]. Each cube was placed between two parallel planes (but not the uppermost cast face) in a Controls Automax 5.0 machine and compressed under a loading rate of 0.25 MPa/s until failure occurred. The reported results correspond to the average of the triplicate tests, and the standard deviation of these was used to display errors.

3.3.5 Ultrasonic pulse velocity testing

Ultrasonic pulse velocity (UPV) is a commonly used non-destructive testing technique which allows information on the homogeneity of a material to be gained through the generation, transmission and detection of longitudinal P-waves over a known path transit length. The pulse velocity is calculated using the following equation:

$$V = \frac{L}{t} \tag{3.5}$$

Where *V* is the pulse velocity in m/s, *L* is the path length in m, and *t* is the time taken to traverse the path length in s. Defects within the material (cracks or voids) cause retardation of the pulse [32], [152], allowing estimation of relative material quality and changes in properties [153]. Changes in pulse velocity can be caused by the presence of aggregates (if present), changes in temperature, and moisture content. No aggregates were used in this study. Changes in moisture content causing different curing environments may lead to chemical variations within the cement leading to variation in pulse velocity. Shorter duration changes in ambient humidity or temperature may lead to the removal of free water from voids which could also impact the pulse velocity; saturated concrete is reported to increase pulse velocity by 5% [154], [155]. It should also be noted that the orientation of defects within material may affect the pulse velocity results [155]. These factors need to be considered when interpreting the results of pulse velocity to provide material properties.

Pulse velocity is independent of the test object dimensions provided that no reflection of waves interferes with arrival time measurements. ASTM C567-16 states that “The least dimension of the test object must exceed the wavelength of the ultrasonic vibration” [153]. Testing was completed using a Pundit Lab instrument equipped with 150 kHz transducers, designed to investigate fine grained materials with a maximum grain size of approximately 12 mm [156]. The wavelength generated from the transducers is 24.7 mm and therefore a minimum lateral path length of 25 mm is required. Zeroing of the equipment was completed before each use using the provided calibration rod (Figure 3.2 B). Testing was completed using the ‘direct’ method, where the transducers are aligned on opposite ends of the specimen (Figure 3.2 C & D). Measurement of the specimen path length was completed to ± 1

mm using digital callipers. Transducers were coupled onto surface of the samples using Proceq coupling gel.

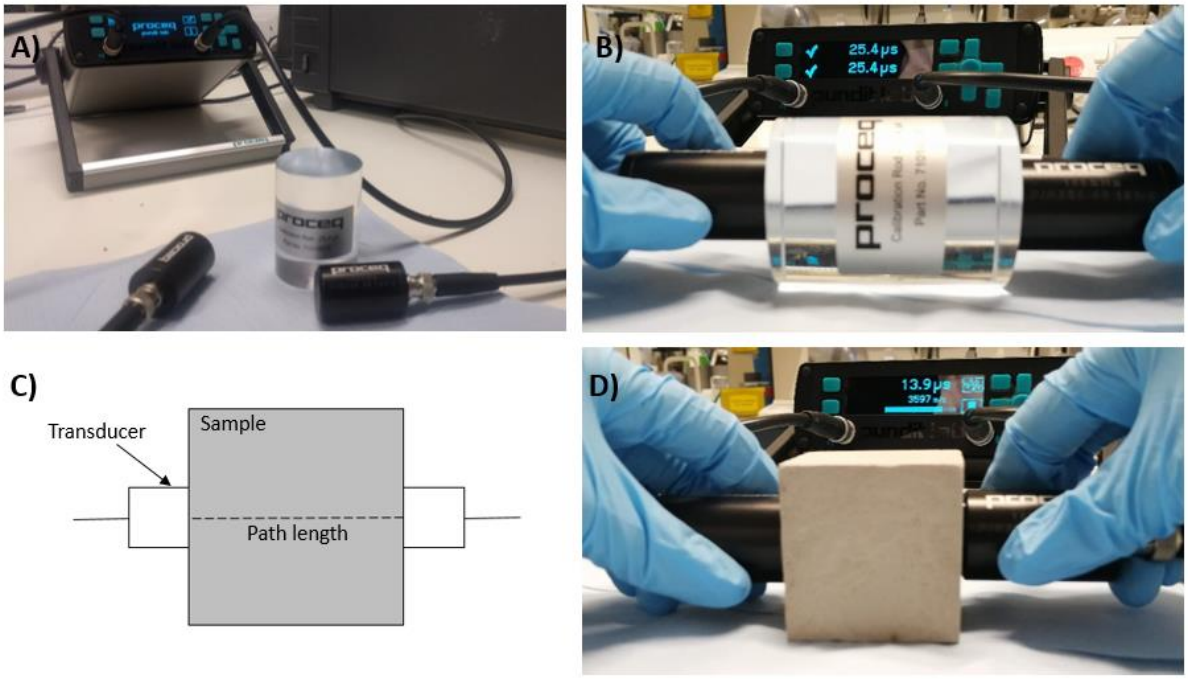

Figure 3.2 UPV testing equipment and procedure A) Testing equipment and calibration bar, B) calibration of transducers, C) schematic of direct transmission testing setup, D) setup for testing of sample.

Assessment of UPV and compressive strength will be completed to clarify if UPV measurements can provide approximate compressive strength estimations in Chapter 4, and these relationships will be used to provide assessment of the impact of gamma radiation on grouts in Chapter 5.

3.3.6 Mercury intrusion porosimetry

Mercury intrusion porosimetry (MIP) analysis allows investigation of the pore structure of cement based materials, with pores broadly defined in three categories dependent on their size and situation. Air voids resulting from poor placement are mm – µm in scale, capillary pores represent areas which are not occupied by hydration product or unreacted raw material and are µm – nm in scale, and gel pores are the nanoscale (nm) porosity present within C-S-H gel [157]. Characterisation using MIP involves the intrusion of mercury into samples of cement. As mercury is a non-wetting liquid, the surface angle is not favourable for liquid intrusion [158]. External pressure is required to achieve infiltration into the pore network; this is termed the pore pressure (P) and is related to the pore radius using the Washburn equation:

$$P = -\frac{2\gamma \cos(\theta)}{r} \tag{3.6}$$

where γ = surface tension of the mercury, θ = contact angle and r = meniscus curvature (i.e. pore entry) radius [42], [159]. This technique measures pore entry size and not pore volume, and an 'ink bottle' effect can lead to under-representation of the pore volume; high volume pores and interconnected networks may only be accessible through narrow openings. Information relating to the total percolated pore volume, the critical pore entry radius and the threshold pore entry radius can be identified from this analysis. The threshold pore entry radius is interpreted to be the minimum geometrically continuous radius throughout the sample; this threshold marks the change between very minor mercury intrusion, and the highest levels of mercury intrusion. The threshold pore entry radius corresponds to the intersection between two tangents of the cumulative intrusion curve (Figure 3.3). The critical pore entry radius represents the steepest slope of the cumulative intrusion curve, and is mathematically defined by the inflection point of main intrusions derivative curve (Figure 3.3) [158].

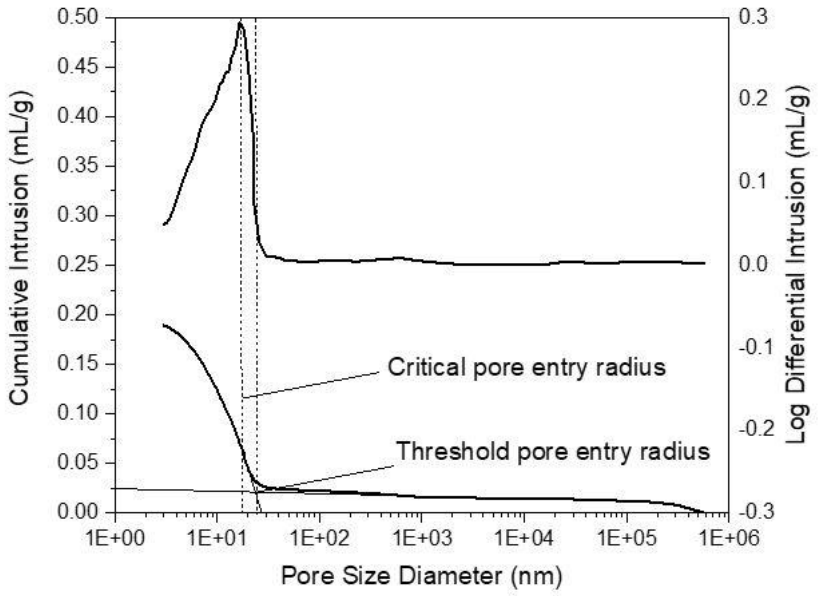

Figure 3.3 Example of MIP cumulative and derivative curves indicating how critical pore entry radius and threshold pore entry radius are calculated.

Samples for MIP consisted of material with a total mass of 0.9 – 1.1 g and analysis was completed using Micrometrics Autopore V equipment. A contact angle of 130 ° and surface tension of 0.485 N/m was applied [160], [161], and the analysis mode was continuous.

3.3.7 Thermogravimetric analysis with mass spectrometry

TGA analyses the phase assemblage of systems through monitoring of sample weight during progressive heating, either in an inert atmosphere or air. Decomposition of mineral phases will occur at characteristic temperatures (dependent on the crystal structure), allowing identification of the assemblage [162]. It should be noted that decomposition and dehydration of different mineral phases can occur at similar temperatures, and may overlap dependent on the testing parameters (heating rate, gas flow), so often TGA is used in combination with mass spectrometry (MS) or X-ray diffraction (XRD) [163].

Analysis was completed using a Perkin Elmer Pyris 1 TGA 4000 in conjunction with a HPR-20 QIC Benchtop Gas Analyser System. Hydration was not stopped on material intended for TGA. Specimens were ground using an agate pestle and mortar and passed through a 63 µm sieve, prior to 40 mg samples undergoing testing. Samples were heated from 30 – 1000 °C in an alumina crucible at a rate of 10 °C/minute, under a nitrogen atmosphere with a flow rate of 40 mL/min.

Weight loss due to the decomposition of $Ca(OH)_2$ and $CaCO_3$ occur over distinct temperature ranges which do not overlap with other phases, allowing quantification of the amounts of portlandite and $CaCO_3$. Free water loss was assessed as the percentage weight loss between 30 – 105 °C. The amounts of portlandite and carbonate in the pastes were quantified from the weight loss between 400 to 500 °C, and 550 to 800 °C, respectively, using the tangential method [163] and calculated according to Eqns. (3.7) and (3.8):

$$Ca(OH)_2 = \ weight\ loss\ (Ca(OH)_2) \times \frac{M_{Ca(OH)_2}}{M_{H_2O}} \tag{3.7}$$

$$CaCO_3 = \ weight\ loss\ (CaCO_3) \times \frac{M_{CaCO_3}}{M_{CO_2}} \tag{3.8}$$

where the portlandite and carbonate wt .% are expressed relative to starting mass, and M is the molar mass. The relative error of these measurements is ± 5-10% [77], [163].

3.3.8 X-ray diffraction

X-ray diffraction (XRD) allows identification of crystalline phases through diffraction of incident X-rays by the crystal structure of the material in accordance with Bragg's Law (equation 3.9). Generation of a monochromatic X-rays is achieved by bombardment of a metal target (e.g. Cu or Mo) with high energy electrons. This excites inner shell electrons, which causes a higher energy electron to be demoted into the vacancy, and the excess energy is emitted as a characteristic X-ray [164]. When the X-rays interact with a sample, the X-rays are scattered by the atoms present in the lattice planes, which

are defined by Miller indices, *hkl*. Constructive interference occurs when the X-rays reflected from different lattices are in phase, and this produces a characteristic diffraction intensity which can be used for identification [165], [166]. This can be seen in diffraction patterns, where the reflection location (diffraction angle) is determined by the wavelength of the X-ray (λ), the incident angle of this (θ) and the spacing between the crystallographic planes (*d*) (equation 3.9, Figure 3.4):

$$n\lambda = 2d \sin\theta \tag{3.9}$$

Identification of phases from diffraction patterns is completed by reference to databases containing known patterns for specific phases [42], [165].

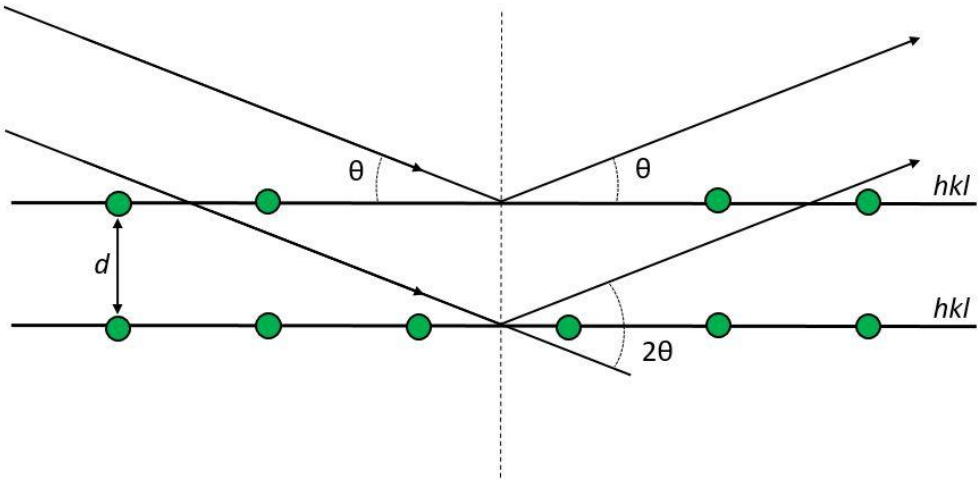

Figure 3.4 Derivation of Bragg's Law (equation 3.9)

Diffraction patterns for anhydrous PC, BFS and PFA are shown in Figure 3.5. Hydration was arrested on samples for XRD, which were ground using an agate pestle and mortar and passed through a 63 µm sieve prior to analysis. Data collection was completed using a Bruker D2 Phaser with Cu (λ = 1.54184 Å) radiation, and scan parameters comprised a step size of 0.02 °2θ with a 2 s dwell per step. Low background sample holders were used for powder samples and front loading of these was completed. Care was taken not to press the sample into the holder during sample loading, which is known to induce preferred orientation of platy and acicular crystals. In hydrated cements this can particularly affect the peak intensities observed for portlandite, hydrotalcite, AFm, and AFt phases [165]. The distinct reflections in the PC pattern represent the crystalline phases present within the clinker, together with the additional cement constituent materials gypsum and calcite. The PFA diffractogram shows diffuse scattering between 7 – 50° 2θ representing the amorphous glassy phase, with inclusions of quartz, mullite and magnetite creating strong crystalline peaks. The BFS diffraction

pattern shows predominantly diffuse scattering between 18 – 37° 2θ due to the disordered structure, but small crystalline inclusions of calcite, melilite and merwinite were observed.

For data in Chapter 8, polished monoliths were analysed after ion implantation using the same equipment and parameters as described above.

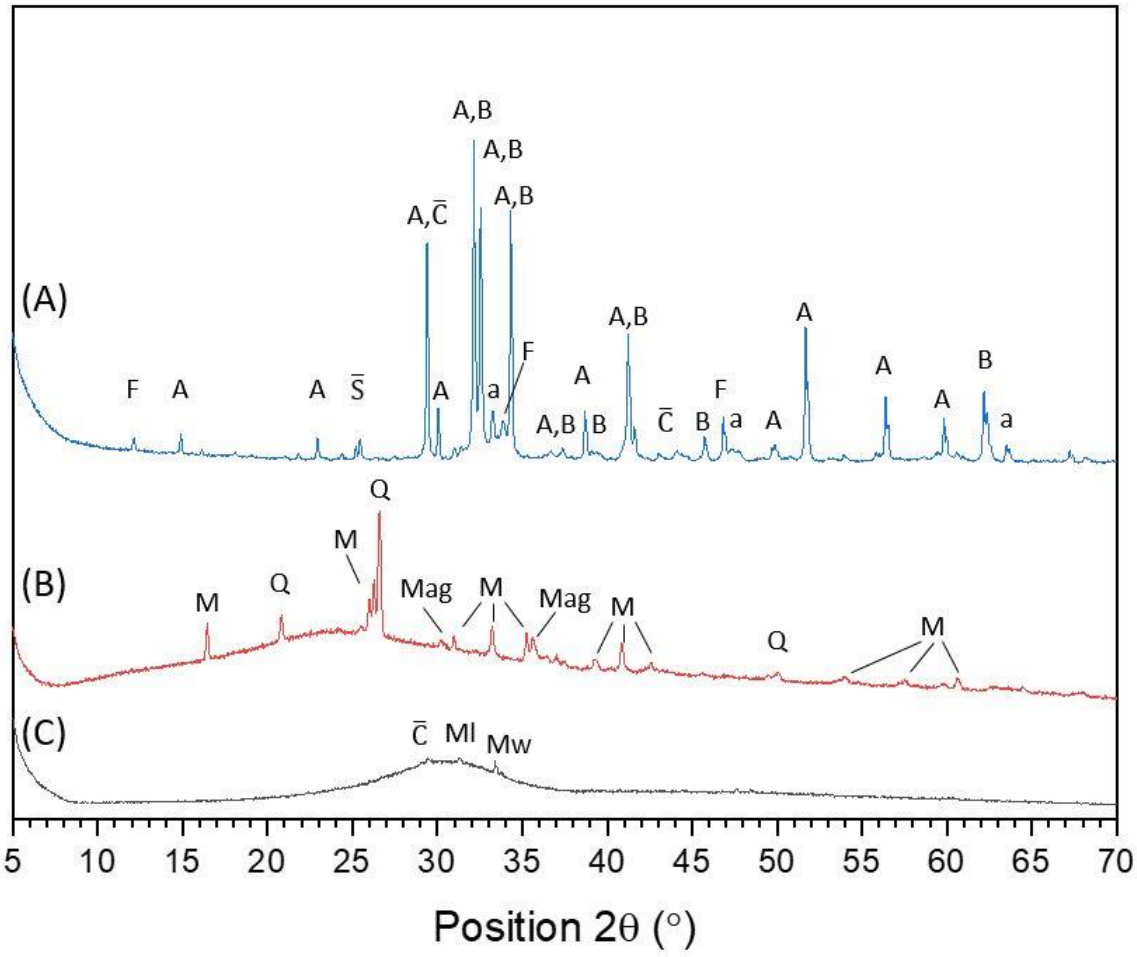

Figure 3.5 X-ray diffraction patterns for a) PC, b) PFA and c) BFS. A: alite, B: belite, F: ferrite, a: aluminate, $\bar{C}$: calcite, $\bar{S}$: gypsum M: mullite, Q: quartz, Mag: magnetite, Ml: melilite, Mw: merwinite

3.3.9 Fourier-transform infrared spectroscopy

Fourier transform infrared (FTIR) spectroscopy provides information relating to the structure of a compound by creating a vibrational response in a molecule, which when absorbed causes stretching or bending of the covalent bonds. The molecules absorb the infrared radiation generated (between 4000 – 500 cm^{-1}) at characteristic frequencies, allowing identification of the same bonds in a range of materials [167]. As the technique does not require the sample to possess long range order, it is particularly useful for cement analysis.

An infrared beam is generated and passed through a beam splitter to create two perpendicular beams. The deflected beam is reflected off a mirror at a fixed distance, whereas the incident beam is reflected off a moving mirror creating many different wavelengths within the beam. Both beams converge at the beam splitter creating a single beam termed the interferogram, containing constructive and destructive interferences. The beam then passes through the sample, the wavelengths corresponding to the frequencies characteristic of the sample are absorbed, and the remaining beam continues to the detector. The signal is processed using a Fourier transform and the absorbed frequencies are extracted, creating the FTIR spectrum. This spectrum plots the transmittance (%), which describes how much infrared radiation was transmitted by the sample, as a function of wavenumber [167].

FTIR data were obtained using a Perkin Elmer Frontier FTIR spectrometer equipped with a deuterated triglycine sulfate detector and KBr beam splitter optical system. Samples underwent scanning 16 times at a resolution of 4 cm^{-1} between 4000 – 400 cm^{-1}. Samples were prepared using the KBr pressed pellet method, where 2 mg of ground sample is mixed with 200 mg of KBr powder. Prior to measurement of the samples a background reading was taken to remove contributions from atmospheric CO_2 and water vapour.

3.3.10 Optical microscopy

Optical microscopy allows evaluation of textural and microstructural development of materials, together with evaluation of characteristics such as colour variations which may not be visible at hand specimen scale or through SEM analysis [168]. Reflected light microscopy was completed using an Olympus CH-2 binocular microscope with 50, 100 and 200× magnification. Samples were mounted in epoxy resin and were prepared for analysis by successive grinding using 240-1200 SiC grit papers before polishing on cashmere cloth coated with progressively finer (6 µm – 0.25 µm) diamond suspensions, with isopropanol as a lubricant.

3.3.11 Scanning electron microscopy

Examination of cementitious materials using scanning electron microscopy (SEM) provides valuable information regarding the microstructural development of cementitious systems. Micrographs are produced through elastic and inelastic interactions that occur when an electron beam collides with the sample surface.

The initial electron stream is generated from an ‘electron gun’ and undergoes focussing to form a beam by acceleration through a series of electromagnetic lenses; condenser lenses demagnify the

electrons forming a beam, and the objective lens focusses the beam on the sample surface. Scan coils then move the beam across the sample [58], [168]. The region within which the electron beam penetrates the sample is termed the interaction volume, and many electron interactions happen within this zone. Different signals are generated depending on the type of interaction, including generation of secondary electrons, back scattered electrons (BSE) and characteristic energy dispersive X-rays (EDX) (Figure 3.6) [168]. Examination of BSE and characteristic X-rays are used for characterisation of materials in this project.

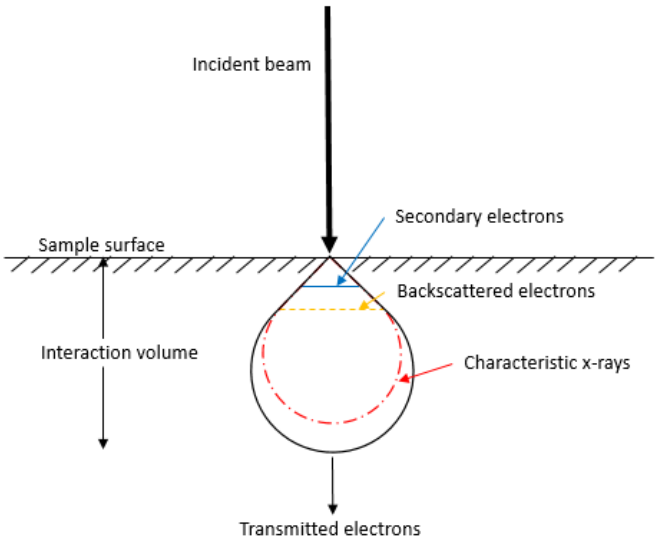

Figure 3.6 Schematic of the interaction volume of an incident beam in a sample, and the zones from which the signals are generated: secondary electrons, backscattered electrons and characteristic X-rays. Adapted from [168].

BSE signals can distinguish materials by atomic number. BSE are the result of elastic collisions and typically have energies similar to the incident beam. Brightness in BSE images is a product of the intensity of electrons, therefore higher numbers of electrons result in brighter images. This is proportional to atomic number and material density; higher density and larger atomic mass mean an increased chance of electron interaction. The interaction volume size can prove a limiting factor with this technique, and it is important to note this will change dependent on the beam energy. At higher energies contrast differences may result from interaction with a sub-surface phase that is not visible. Suitable sample preparation is imperative to obtain good compositional contrast, and inadequate surface preparation can lead to erroneous results, especially if the surface of the sample is rough [58], [168].

3.3.11.1 Energy dispersive X-ray spectroscopy

Evaluation of characteristic EDX energies can provide semi-quantitative compositional analysis that is typically used in conjunction with BSE micrographs. When an incident electron displaces an electron from the inner shell of an atom, movement of higher energy electrons to fill the vacancies produces X-rays with characteristic energies for different atomic species. The resulting spectra can be displayed as elemental maps, linescans, or point analysis data. Because these X-rays can travel much greater distances through the sample than electrons, the sampling volume is of the same order as the interaction volume, as highlighted in Figure 3.6 [168].

SEM samples were mounted in epoxy resin and prepared using the same method used for optical microscopy outlined in section 3.3.10. Samples were carbon coated and the sides were painted with silver conductive paint to prevent charging.

Data displayed in Chapters 4, 5, and 7 were collected using a FEI Inspect F50 SEM and a 15 kV accelerating voltage at a working distance of 8.5 to 9 mm. EDX was completed using an Oxford X-Max 80 mm^2 SSD-EDX detector, with elemental maps collected for 600 s and point analysis for 60 s.

Data displayed in Chapters 6 and 8 were collected using a Hitachi TM3030 SEM and a 15 kV accelerating voltage at a working distance of 8.5 to 9 mm. EDX was completed using a Bruker Quantax 70 detector and software to provide elemental maps that were collected for 600 s. Point analyses were taken from the mapped data.

3.3.12 Solid state magic angle spinning nuclear magnetic resonance spectroscopy

Solid state nuclear magnetic resonance (NMR) spectroscopy allows investigation of the local chemical environment of specific nuclei, allowing information on the local structure of crystalline and disordered materials to be determined. Given the complex nature of cement systems and the presence of poorly crystalline phases, such as C-A-S-H, this is an especially useful analytical technique.

NMR can only be used to probe specific nuclei, as they must have intrinsic magnetic moments, i.e. an odd number of protons, neutrons, or protons plus neutrons, such as ^{27}Al and ^{29}Si. Suitable nuclei are exposed to a strong static magnetic field which orients the magnetic moment either parallel or anti-parallel to the magnetic field. This brings about Zeeman splitting, which is a difference in energy levels of a nucleus. A pulse of radiofrequency radiation is then applied to the nucleus and causes precession of the spin, inducing transition of the spin states to higher energy states. The electromagnetic signal that is produced as the nuclei relax back to the equilibrium spin state is recorded, and this is converted

to a spectrum using a Fourier transform. The results are reported as a chemical shift (δ) that relates to the local structural environment of the nuclei [169].

Line broadening effects can be observed in recorded spectra, a result of interactions of the spin nuclei due to dipolar broadening, quadrupolar interactions and chemical shielding anisotropy. These effects are more significant in solid samples than in liquids, and so solid state NMR uses magic angle spinning (MAS) to reduce this. The sample is rotated around a fixed axis relative to the static magnetic field. Due to the geometric dependence of the internal spin interactions, the line broadening can be reduced by spinning the samples at the magic angle of 54.74° [53], [169]. The presence of paramagnetic species such as Fe within cements can cause further complications, as they will influence the relaxation and chemical shift of nearby nuclei, altering and dampening the NMR signal.

^{29}Si and ^{27}Al SS MAS NMR have been used in this study to provide information relating to the chemical composition of the disordered C-A-S-H phase, together with information on the degree of hydration of PC and BFS. All spectra were acquired on a Bruker Avance III HD 500 spectrometer at 11.7 T with a 4.0 mm dual resonance CP/MAS probe, producing Larmor frequencies of 99.35 MHz and 130.32 MHz for ^{29}Si and ^{27}Al, respectively. During initial experimental setup, measurement of the appropriate delay for full relaxation of both ^{29}Si and ^{27}Al was completed during optimisation. The ^{29}Si spectra were collected at a spinning speed of 12.5 kHz, with a minimum of 256 scans, a pulse width of 4 µs and a relaxation delay of 40 s. ^{27}Al spectra were collected at a spinning speed of 12.5 kHz, with a minimum of 512 scans, a pulse width of 1.7 µs and a relaxation delay of 5 s. The chemical shifts of the ^{29}Si and ^{27}Al nuclei were referenced to external samples of pure tetramethylsilane (TMS) and 1.0 M aqueous $Al(NO_3)_3$ respectively. All data were processed using Bruker TopSpin 4.0.6 software [170]

Deconvolution of the ^{29}Si MAS NMR spectra allows quantitative information on the structure of the sample to be established. Deconvolutions were completed using Gaussian curve fitting to generate a best fit relationship that allowed comparison of the experimental data with the fitted model. Analysis of the anhydrous PC and BFS material was undertaken, and the spectra together with the deconvolutions are shown in Figure 3.7. The spectra for the anhydrous PC used 8 fitted peaks corresponding to alite, with a single peak for belite identified at -71.3 ppm [171]. The BFS spectrum shows a broad resonance from -57 to -95 ppm.

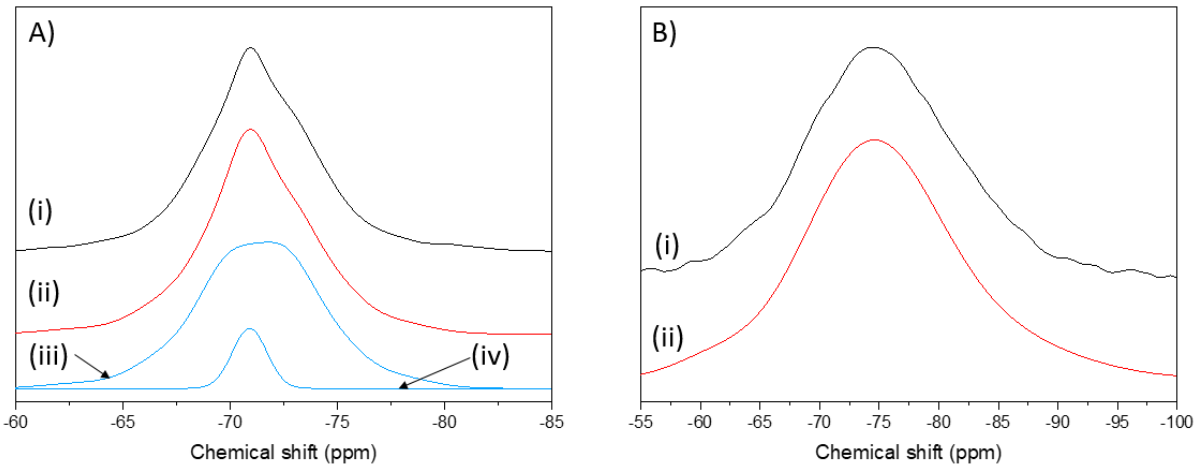

Figure 3.7 Deconvolutions of ^{29}Si MAS NMR spectra for A) PC: i) experimental data, ii) deconvoluted fit, iii) alite spectrum, iv) belite spectrum; and B) BFS: i) experimental data, ii) deconvoluted fit.

In the deconvoluted spectra, the chemical environments of the Si nuclei are generally expressed using the Q^n notation where $0 \leq n \leq 4$, Q represents the Si tetrahedron and n designates the number of bonded tetrahedral units. Al incorporation into the silicate chains is shown by $Q^n(m\text{Al})$, where m indicates the number of bonded Al tetrahedra and therefore $m \leq n$ (See Figure 2.5 in Chapter 2 for diagram illustrating Q^n notation). Using this notation, Q^0 represents isolated tetrahedra and Q^1 represents dimers or the ends of silicate chains. Q^2 are mid chain species in the C-A-S-H product, and Q^2(1Al) indicates that one of the adjacent tetrahedral sites is occupied by Al. Q^3 and Q^4 species indicate that cross linking of the silicate chains has occurred, and this is commonly associated with lower Ca content in the C-A-S-H chains and formation of an amorphous Si phase, often as a product of carbonation [53], [54]. In cementitious materials, resonances between -60 and -120 ppm for Si sites are expected. Chemical shifts determined from previous literature were used to guide the assignment of Q species in this work and are outlined in the relevant chapters. The ^{29}Si spectral deconvolutions were used to calculate the structural characteristics of the C-A-S-H, including the MCL (equation 3.10), Si/Ca (equation 3.11) and Al/Ca (equation 3.12) using equations 3.10-3.12 [46], [82]:

$$MCL = \frac{2}{\left(\frac{Q^1}{Q^1 + Q^2(0Al) + \frac{3}{2}Q^2(1Al) + Q^3(0Al) + Q^3(1Al)}\right)} \tag{3.10}$$

$$\frac{Ca}{Si} = \frac{\frac{3}{2}Q^1 + \frac{2}{3}Q^2}{Q^1 + Q^2} \tag{3.11}$$

$$\frac{Al}{Si} = \frac{\frac{1}{2}Q^2(1Al)}{Q^1 + Q^2(0Al) + Q^2(1Al) + Q^3(0Al) + Q^3(1Al)} \quad (3.12)$$

In the ^{27}Al spectra, resonances at chemical shifts >50 ppm are typical of tetravalent coordinated Al(IV), at 20-50 ppm of pentavalent Al(V), and at <20 ppm of octahedral Al(VI) [53]. Al incorporated in the C-A-S-H chains resonates in the tetrahedral region, as does Al present in BFS and C_3A [53], [82], [172]. AFt and AFm produce resonances in the octahedral region, together with TAH and the hydrotalcite-like phase [42], [53], [80]. Interlayer charge balancing Al resonates in the pentavalent region [53], [82].

3.3.13 Gamma irradiation facilities

Gamma irradiations were completed at the University of Manchester's (UoM) Dalton Cumbrian Facility (DCF) using a Foss Therapy Services Inc. model 812 self-contained irradiation facility with ^{60}Co source (Figure 3.8). Dual rod assemblies each containing 3 sources generated activity of approximately 535.4 TBq. Samples were required to be below 27 mm in diameter, in order to fit the sample holders within the equipment [173]. All samples, regardless of dimensions, were demoulded from curing centrifuge tubes and wrapped in aluminium foil prior to irradiation in order to minimise moisture loss.

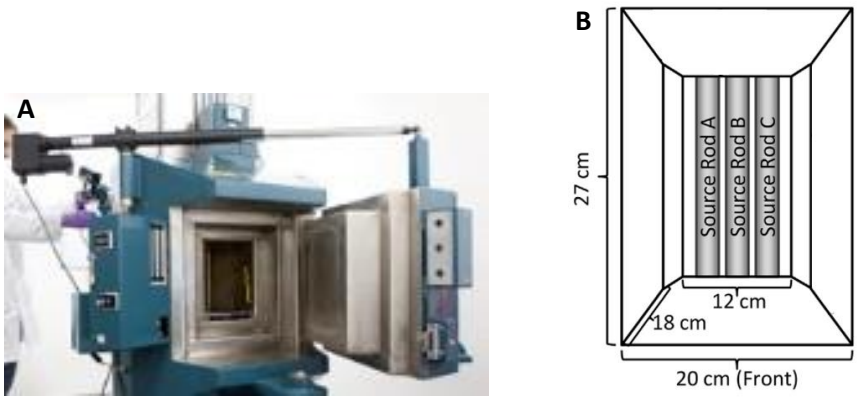

Figure 3.8 A) Photograph of ^{60}Co irradiator and B) schematic showing dimensions of the irradiation chamber. Adapted from [173]

Due to the long nature of the testing required to reach the desired total dose, irradiations were completed in non-continuous batch sessions. Typically, this comprised placing the samples in the irradiator overnight and on weekends until the required dose was met. Temperature within the irradiator was regulated to approximately 35 °C by using an air pump for the data presented in Chapter 5, but this was not possible for the data presented in Chapter 7.

Experiment-specific parameters such as sample dimensions, total dose, average dose and irradiation temperature will be outlined in the relevant chapters.

3.4 Concluding remarks

This chapter outlines the main experimental and analytical techniques used by the author throughout this thesis, however, additional specific analytical techniques used by collaborators are outlined in the relevant chapters. The following chapters utilise these methods to characterise the cementitious materials, referencing back to this chapter for further information when required.

4 Characterisation of nuclear specification Portland cement blends

This chapter describes the typical characteristics of blended cements that are used for nuclear waste encapsulation in the UK. The majority of cement encapsulated waste is contained within BFS:PC blends, however as PFA:PC blends are specifically used for annulus grouting of PCM and are investigated in Chapter 6, an overview of both grout types is provided below. This serves to provide an overview of the hydration, phase assemblage and microstructure of the pastes that are produced using UK nuclear industry specified precursor materials and to enable full evaluation of radiation-exposed samples in Chapters 5, 6, 7 and 8. As the powder specifications for use in nuclear encapsulation applications vary from those of construction industry standards, evaluation of the potential differences from previous literature is required.

4.1 BFS:PC

The bulk of UK cemented nuclear waste is encapsulated in BFS:PC materials. Although this is a well characterised material system, the large formulation envelope used and changes in material supplies over time have led to the creation of a product quality envelope to ensure acceptability. As such, baseline characterisation of the blends currently being used was completed. The formulations used are representative of the range used by Sellafield Limited in their waste encapsulation plants and full details of the mix formulations are provided in Chapter 3, Section 3.2.

4.1.1 Hydration

The heat flow from all blends of BFS:PC was recorded using isothermal calorimetry at 20 °C. The measurements were taken for 14 days and results from the initial period are shown in Figure 4.1. The isothermal calorimetry trace shows the major thermal events of hydration. Initially, the rapid dissolution of ions and reaction of C_3A is observed at < 1 hour, followed by a period of low heat evolution (dormant phase, 1 – 2.5 hours). The main hydration begins as the acceleration period is entered after 1.7 – 2.5 hours, where the heat flow increase is associated with the reaction of C_3S [45], [174], [175]. Formation of both C-S-H and portlandite begin during this phase, reaching a maximum at the peak. Between 6.5 and 9.5 hours, the formation of a sharp shoulder to the main hydration peak indicates that secondary ettringite formation occurred in all the blends [176]. A broad peak of low heat flow was observed between 15 – 25 hours corresponding to AFm formation [42]. Hydration continues at later ages as shown by the slow, continuous heat output after 25 hours, indicative of belite and BFS reaction. There are few studies investigating the kinetics and mechanisms of later age hydration, although the decreasing amount of space available for hydrates to occupy as hydration continues is well established [177].

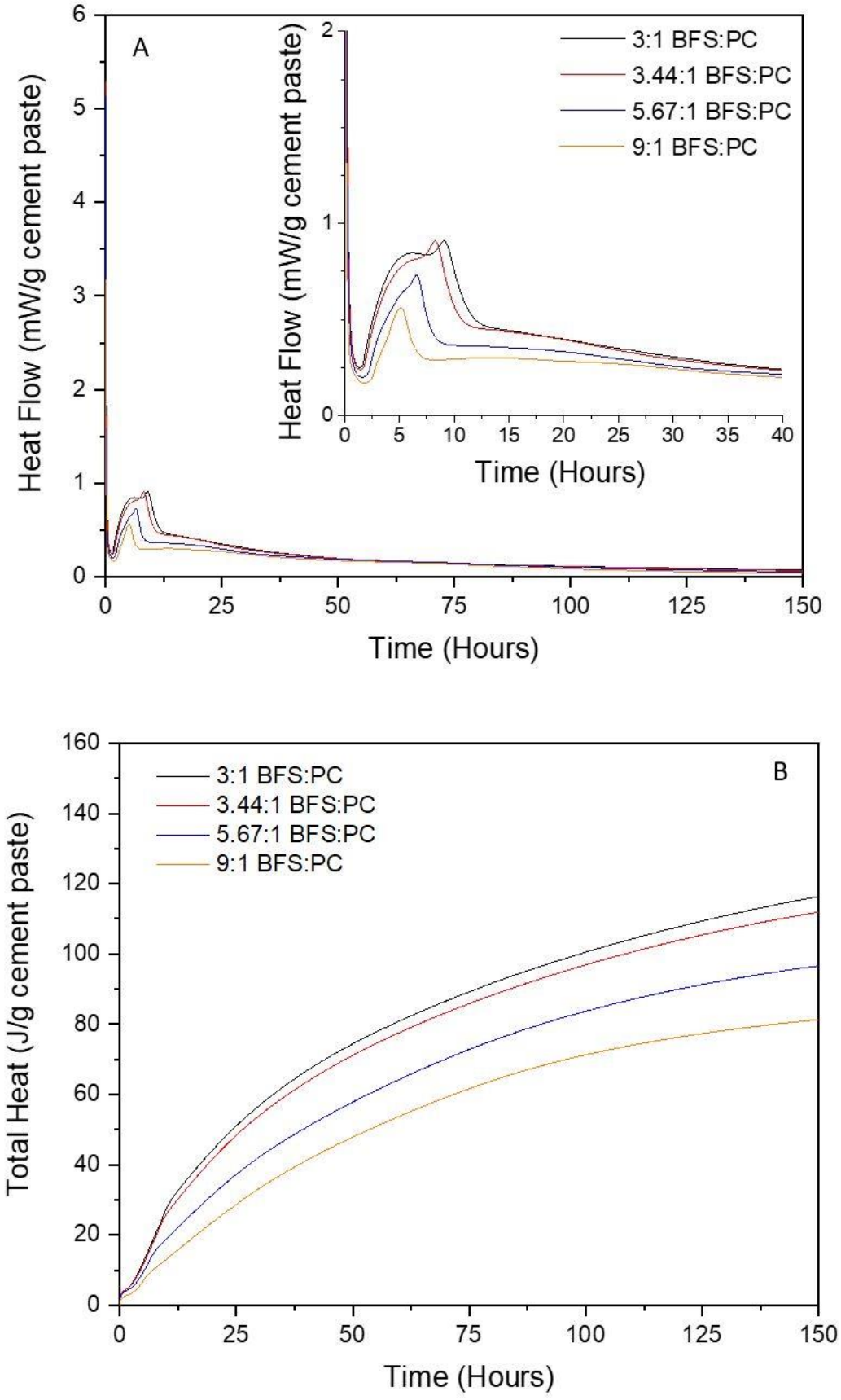

Figure 4.1 A: Isothermal calorimetry and B: total heat evolution of BFS:PC systems with varying BFS content.

All the cements analysed can be considered very low heat cements under European standard classifications, which reports a value of 220 J/g as low heat cement [178]. All blends were within the limits of the Sellafield Ltd. specification, which state that blended cement pastes should not exceed a cumulative heat flow of 180 kJ/kg in the first 24 hours of hydration at 35°C (Figure 4.1 B) [3]. The maximum heat flow recorded was 0.9 mW/g (3:1 BFS:PC), which is lower than pure Portland cement by a factor of ~5.5 [175], [179]. It might have been anticipated that the reduction in maximum heat flow would mirror the replacement level i.e. the maximum heat flow for 3:1 BFS:PC would be 3x lower than for pure PC samples. However, this was not the case, which is postulated to be a product of the relative coarseness of the Sellafield specification PC used [15]. As the BFS fraction increases the maximum heat flow falls, with a 40 % reduction observed between the 3:1 and 9:1 systems from 0.9 mW/g to 0.5 mW/g respectively. The maximum heat of hydration observed in all blends was lower than for equivalent systems using only GGBS, which can range between 1.5 – 3.6 mW/g [175], [180], [181]. This is due to the distinct bimodal PSD of the BFS:Calumite blend used here, as discussed in Chapter 3, which results in a lower reactivity of the total BFS fraction compared to using only GGBS [176], [181]. The overall reaction of the BFS fraction was investigated by Sanderson et al. [181] who found that the Calumite behaved as an inert filler with little contribution to the initial reaction, whereas reaction of the fine grained GGBS fraction contributed to the peak heat of hydration.

Figure 4.1 shows that increased replacement of PC by BFS results in the maximum heat of hydration being reached earlier (observed by a shift to lower time values as the BFS fraction increases). An increase and acceleration of the peak attributed to secondary ettringite formation was also observed as the BFS fraction increased. The presence of SCMs has been shown to enhance the hydration of clinker components, with the particle size of the SCM impacting the rate of reaction, due to a process termed the ‘filler effect’ (where the SCM acts as the ‘filler’). The overall enhancement of hydration due to the ‘filler effect’ is widely accepted to be a result of the increase in potential nucleation sites together with an effective increase in local w/s ratio [157], [182]–[185]. Berodier and Scrivener demonstrated that the increase in surface area resulted in fairly low levels of nucleation comparative to the available area, however they showed a clear link between the interparticle distance and hydration kinetics, attributed to shearing between particles which increases as interparticle distance decreases [186].

It has been stated that the reactivity of the SCM material itself has often been overlooked when addressing the contribution to the filler effect [175], [187], and studies have shown that the SCMs provide an increase in potential nucleation sites for hydrates which in effect cause the acceleration of

hydration [185], [186]. However, in these samples the high proportions of BFS is considered to cause the 'filler effect', providing conditions conducive to enhance nucleation and allowing extra space for hydration of the clinker phase. The limited reaction of the BFS fraction (particularly the Calumite component) at these early ages (as stated above) is not considered to have a significant contribution.

The broad peak attributed to AFm formation also appears to have an earlier onset in blends with higher levels of slag replacement. The conversion of AFt to AFm is likely to occur earlier in systems containing less sulfate, as sulfate depletion will occur more rapidly. This is therefore to be expected with decreasing levels of gypsum [34], [69] , which is added as part of the PC but is not present in this BFS. The slag replacement resulting in earlier onset of the main hydration peak would also support the earlier conversion of AFt, as increasing the rate of reaction of the PC will hasten the sulfate depletion.

4.1.2 Phase assemblage

XRD diffractograms of the samples after 28 days are shown in Figure 4.2, and show that the phase assemblage contains ettringite (PDF# 41-1451), hemicarboaluminate (PDF# 014-0221), hydrotalcite (PDF# 14-0191), monocarboaluminate (PDF# 36-0377), portlandite (PDF# 04-0733), and C-A-S-H, together with unreacted belite (C_2S, PDF# 29-0369), and BFS (identifiable from the diffuse scatter at $25° < 2\theta < 35°$ and small melilite reflection at 31.3° 2θ).

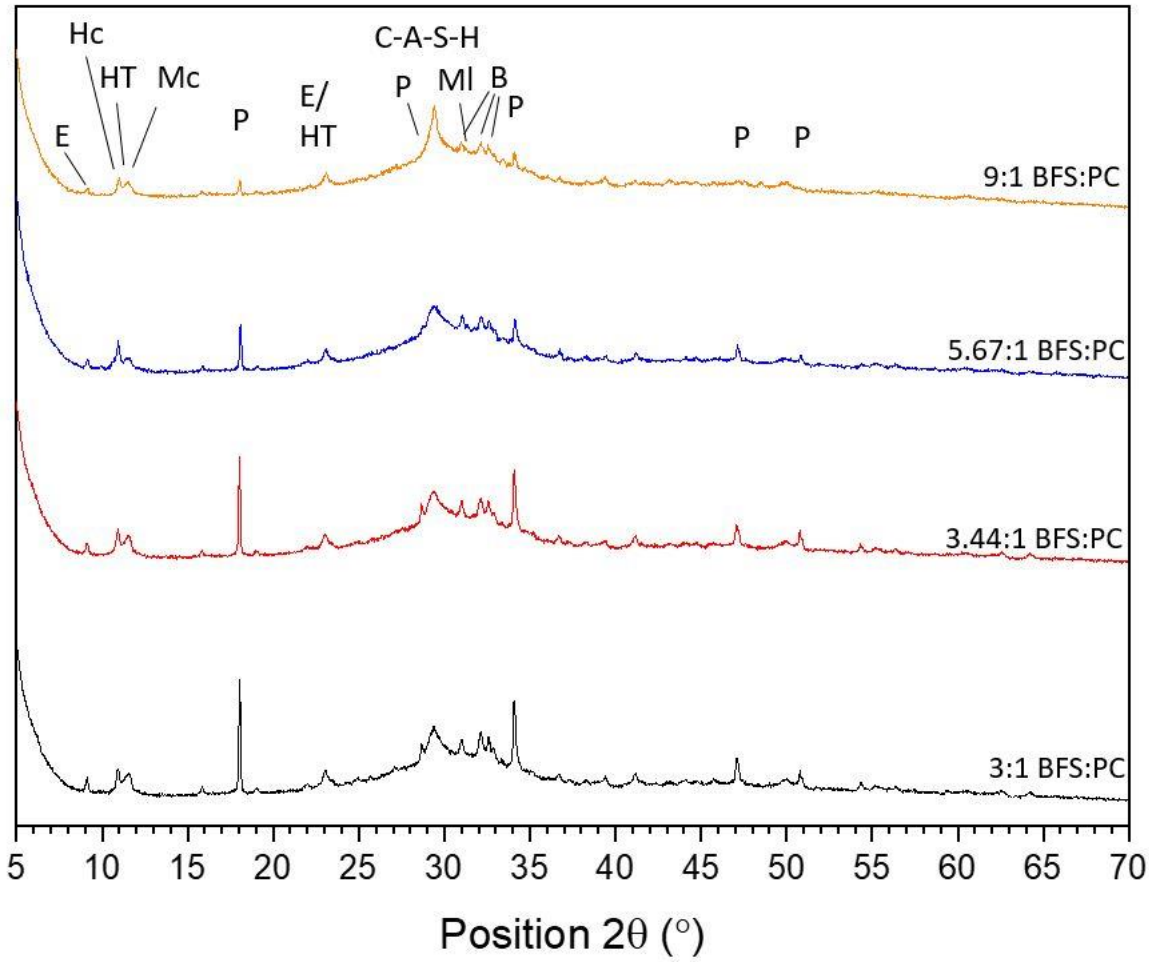

Figure 4.2 XRD diffractograms of hydrated BFS:PC blends at 28 days. E: Ettringite, HC: hemicarboaluminate, HT: hydrotalcite, Mc: monocarboaluminate, P: portlandite, Ml: melilite, B: belite (C_2S).

The varying level of BFS within the blends is seen to have a marked effect on the hydration products in the assemblage. Peak intensities for portlandite and ettringite reduced as BFS content increased. The predominant reflections identified in the 3:1 and 3.44:1 blends are C-A-S-H and portlandite. In the 5.67:1 blend, portlandite reflections were less prominent, and in the 9:1 blend AFm and hydrotalcite-like phases were dominant together with C-A-S-H. Although preferred orientation of the hydrate phases is likely to have occurred to some extent, the overall changes in peak intensities observed for the systems are considered representative of bulk variations caused by the level of BFS replacement [188].

Figure 4.3 shows the distribution of AFm phases in the different blends. Ettringite was identified in all the blend ratios, whilst monosulfoaluminate (PDF #-83-1289) was mostly absent; a small reflection was observed in the 5.67:1 blend at 9.9 °2θ, along with slight broadening of the left shoulder of the hemicarboaluminate reflection at 10.8 °2θ. The formation of monosulfoaluminate or other phases in

the AFm solid solution (AFm_{ss}, discussed in Chapter 2, Section 2.4.1.3) was not observed in the other samples, indicating that the SO_3/Al_2O_3 ratio of the systems had not reduced sufficiently to allow transformation of ettringite, either through hydration of the BFS or depletion of gypsum [69], [82], [125]. The presence of calcite in the precursor materials favours the stabilisation of hemicarboaluminate as the dominant AFm phase, which inhibits monosulfoaluminate formation and indirectly stabilises ettringite [189]. The broad peak between 11.2 – 11.9° 2θ represents overlapping reflections for the hydrotalcite-like phase and monocarboaluminate phases. Given the small volumes of calcite observed in the clinker and BFS (Chapter 3, Figure 3.4) and the strong reflections identified for hemicarboaluminate, it is considered that this peak is predominantly associated with the hydrotalcite-like phase. This phase forms a solid solution where the crystal structure is dependent on the Mg/Al ratio [42]. As such, the basal reflection peak has been observed between 11.2 – 11.6° 2θ [190], with a shift to lower angles when Al incorporation is higher. The MgO content of the BFS is 8.4 wt. % (Chapter 3, Table 3.1) and so the basal reflection is expected to be at higher angles, therefore the reflection position of 11.5° 2θ in all blends is also consistent with a hydrotalcite-like phase rather than monocarboaluminate [191]–[193].

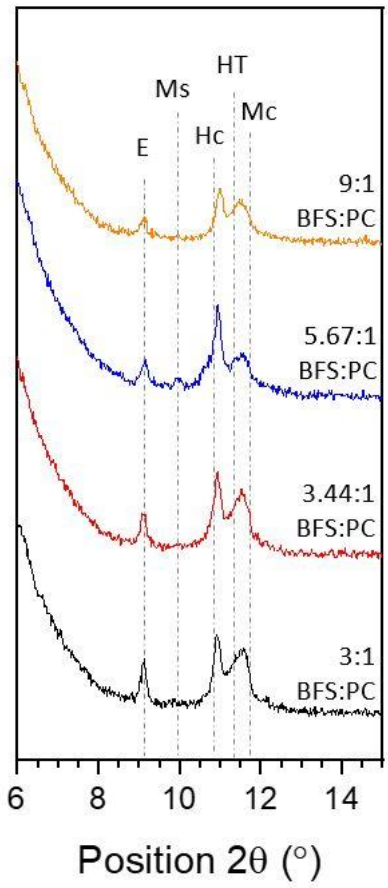

Figure 4.3 XRD diffractograms of hydrated BFS:PC blends at 28 days (subsection of Figure 4.2). E: Ettringite, Ms: monosulfoaluminate, HC: hemicarboaluminate, HT: hydrotalcite, Mc: monocarboaluminate.

The TGA results, together with mass spectrometry data for H_2O and CO_2, are displayed in Figure 4.4. The primary phases identified were: ettringite, C-S-H, AFm phases, hydrotalcite-like phase, portlandite and carbonates, showing good agreement with XRD results. The weight losses associated with free water (> 100 °C) are within 0.5 % of each other for the lower BFS replacement blends, whereas in the 9:1 blend the loss is increased by ∼1.1 %. Given the low levels of PC in this system and the slow hydration kinetics of BFS, a greater proportion of free water is to be expected. The results of the isothermal calorimetry (Figure 4.1) support this, given the prolonged induction period and low thermal maximum recorded. Weight loss below 400°C is due to the decomposition of ettringite, C-S-H, AFm phases, and hydrotalcite-like phases, with weight loss between 400-450°C due to portlandite. Minor carbonate decomposition was observed from ∼550°C [162], [194].

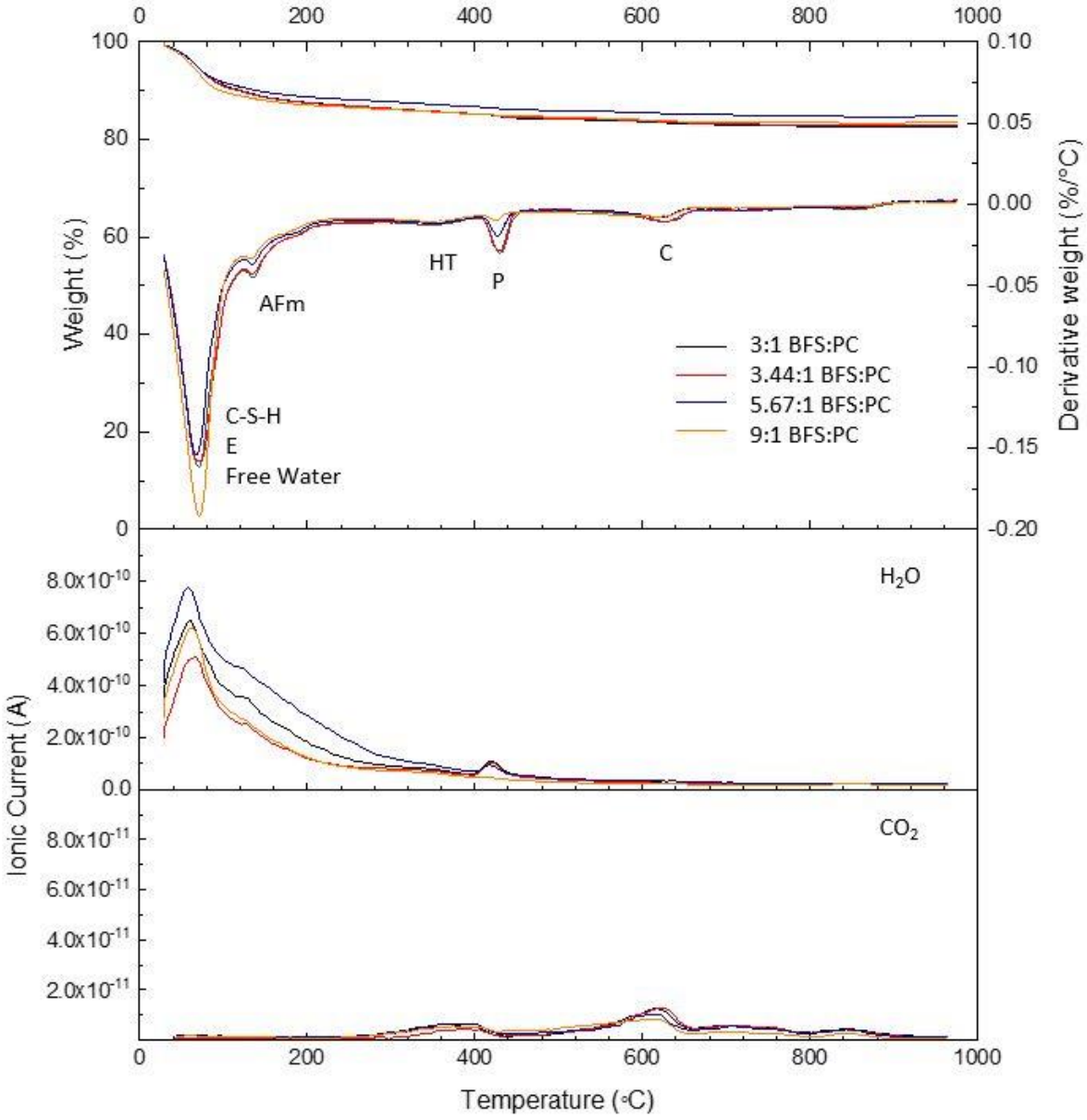

Figure 4.4 TGA and MS results of hydrated BFS:PC blends at 28 days. E: ettringite, HT: hydrotalcite, P: portlandite, C: carbonates.

Quantification of the TGA results is compiled in Table 4.1; see Chapter 3, Section 3.3.7 for details of methodology. The amount of BFS within the blends impacts the proportions of hydrates present within the assemblage, supporting the results from XRD (Figure 4.2). The portlandite content observed in the 9:1 blend was 77 % lower than in the 3:1 sample, due to the reduction of the clinker component, as well as the increased consumption of portlandite formed, via the reaction of BFS. The quantities of portlandite observed are considered representative comparative to similar systems [188]. The CO_2 MS response between 300 – 400 °C is due to the decarbonation of the hydrotalcite-like phase, whilst the peak centred at approximately 620 °C is representative of calcite. However, this weight loss peak

associated with carbonates is fairly broad (between 550 – 700 °C) and so is likely to represent decomposition of a mixture of carbonates of different particle sizes [163], [194], [195].

Table 4.1 Quantification of the free water, portlandite and carbonate content of all BFS:PC blends at 28 days.

BFS:PC	Free water (%)	$Ca(OH)_2$ (%)	$CaCO_3$ (%)
3:1	9.1	3.9	2.6
3.44:1	9.3	3.5	2.3
5.67:1	8.6	2.0	1.7
9:1	10.4	0.9	2.0

SEM-EDX data for all blends is displayed in Figure 4.5. Unreacted BFS was observed in all samples, identifiable by the light grey regions in the backscattered electron images with angular appearance; the larger grained Calumite fraction was observed in Figure 4.5 A and D. Remnant clinker (bright and mottled grey in appearance) was also observed, together with zones of portlandite (light grey) commonly located adjacent to clusters of small BFS or larger BFS particles. Limited hydration rims were noted in the samples but distinct layered darker rims of BFS adjacent to portlandite were observed (label 1 in Figure 4.5 A) and this is considered likely to be a hydrotalcite-rich layer [60]. Distribution of Al through the matrix suggests incorporation within C-S-H, as expected from the level of BFS replacement in these blends [49], [56], [82], [196]. No distinct areas of AFm or AFt were identified at the resolution of these images, with mapping showing the high concentrations within residual clinker and adjacent matrix. Residual iron from BFS was observed within unreacted particles and in the matrix, identifiable through their high relief in BSE images and through EDX mapping (Figure 4.5 B,C,D).

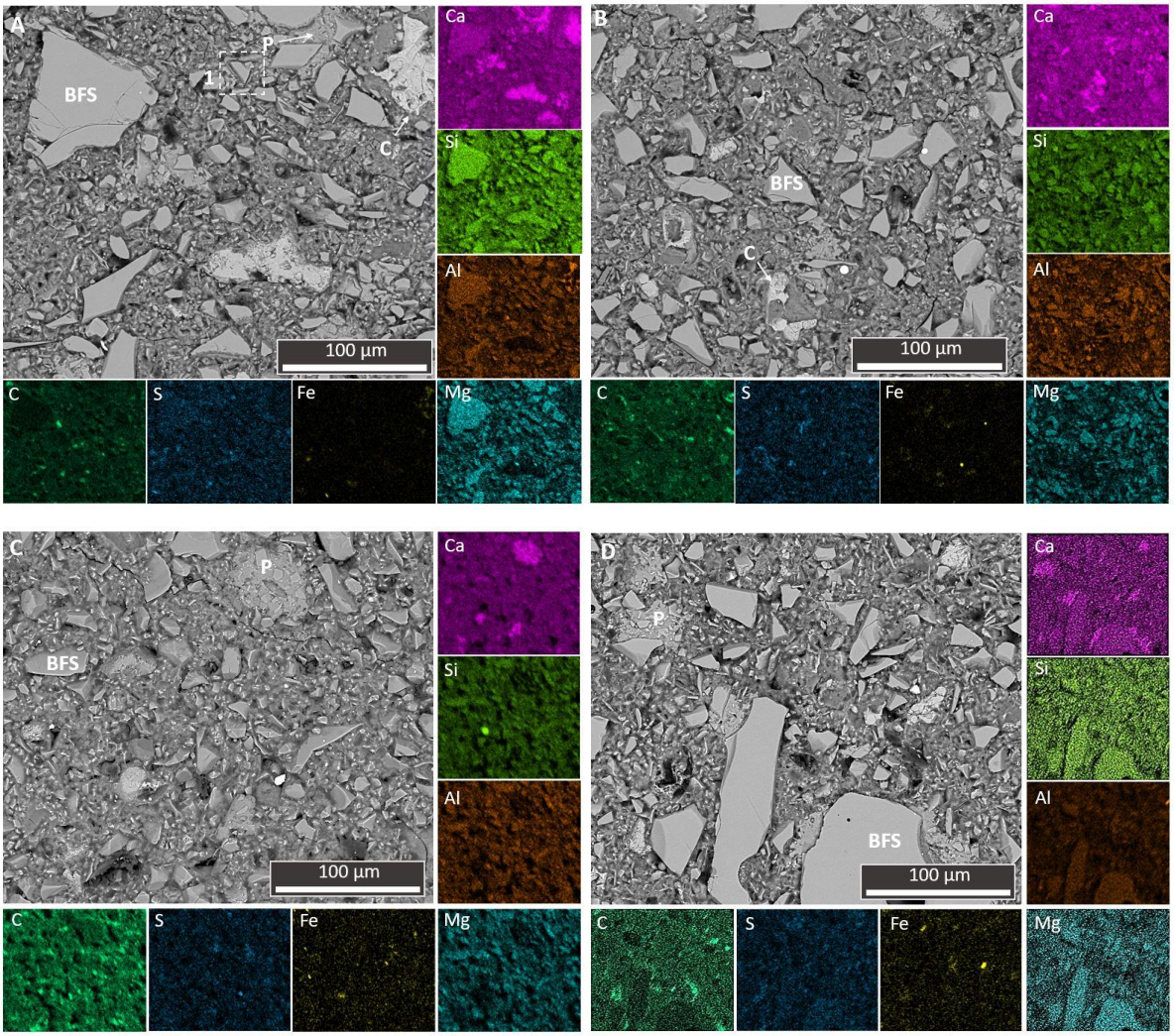

Figure 4.5 Micrographs and EDX maps of BFS:PC blends at 28 days A: 3:1, B: 3.44:1, C: 5.67:1, D: 9:1. BFS: blast furnace slag, C: clinker, P: portlandite. Region 1 in 4.5 A is discussed in text.

Point analysis on the samples further demonstrates the chemical variations in the phase assemblage with the increasing proportion of BFS in the system. Figure 4.6 A shows the variation in C-A-S-H chemistry between the samples. The average Ca/Si ratio was observed to be similar for the 3:1 and 3.44:1 blends (Ca/Si ~1.4-1.5) but appeared to increase slightly in the 5.67:1 sample (Ca/Si ~1.7) and was significantly higher in the 9:1 blend (Ca/Si ~1.9). These levels are comparable with pure PC systems, where Ca/Si ratios tend to sit in the 1.5 – 2.1 range [42], [168]. This increase in Ca/Si with increased BFS replacement can be seen in Figure 4.6 A as the data points for 5.67:1 and 9:1 samples shift to the left of the plot compared to the 3:1 and 3.44: sample data.

Higher levels of replacement by SCMs have typically been identified to lead to a decrease in the Ca/Si ratio of C-S-H, as the hydration of the SCM leads to an increase in the available Si content [71]. Given that the reverse trend is seen here, it appears that in the blends with the highest proportions of BFS,

limited reaction of this material has occurred at 28 days, so the hydration products are dominated by PC reaction at this age. The dominance of PC related hydration products may be a result of the filler effect (as discussed in Section 4.1.1) and limited reaction of the BFS fraction at 28 days.

Prentice et al. found the degree of hydration of BFS to be between 15 % and 20 % for 9:1 and 3:1 BFS:PC grouts respectively [82], for systems that contained no Calumite, and so those values are likely to be higher than achieved in this study. Estimations of Ca/Si ratios from deconvolutions of ^{29}Si MAS NMR spectra produced values significantly lower [82] than observed from point analysis completed here. However, it is acknowledged that estimation of Ca/Si ratios using this method has inherent limitations [49]. The variations observed between this study and those in the literature are considered to be a product of the difference in degree of hydration of the BFS fraction and the methods used to calculate the Ca/Si ratio. Higher proportions of portlandite were observed by Herterich [197] to indicate a reduced degree of hydration of BFS in systems with lower w/s ratios. Lower reactivity of SCM with increasing replacement level was observed by several studies [82], [145], [188], [197], [198], as was reduced reactivity of SCM with lower w/b ratios [145], [198], [199]. The lower reactivity of BFS is supported by the lower Mg/Ca ratios observed as the BFS fraction increases (Figure 4.6 B). Where Mg/Ca ratios are below 0.06, the relationship to Al/Ca ratio appears different; the Al/Ca increases more rapidly. This is likely due to the level of intermixing with C-A-S-H as opposed to analysis of less intermixed hydration rims [148].

No large variation in the sulfate balance of the systems was apparent with increasing BFS fraction (Figure 4.6 C). Despite the presence of ettringite in XRD results for all samples, little supporting evidence was found from the EDX analysis. This may be a product of the level of intermixing of the hydrates within the matrix.

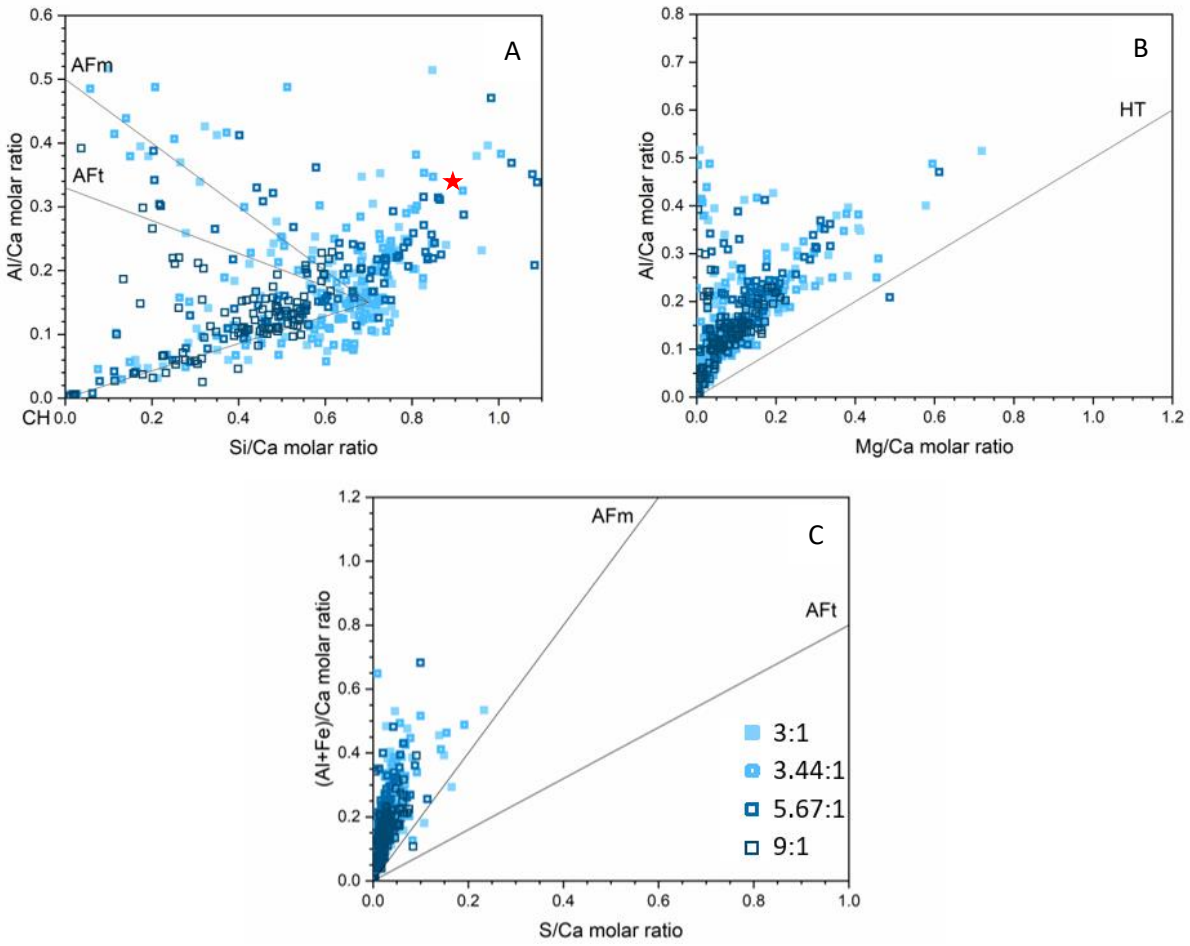

Figure 4.6 EDX point analysis from BFS:PC blend samples at 28 days. Each point sample was taken from a region that visually appeared to be binder rather than residual anhydrous phases. Composition of anhydrous BFS shown in A by ★ symbol. Tie lines link to the other prominent hydrate phases; CH: portlandite; AFm: monosulfoaluminate; AFt: ettringite; and HT: hydrotalcite.

As hydration continues with extended curing time, variations to the phase assemblage will occur. However, this analysis serves to show how the initial hydration of the system is affected by the proportion of BFS within the system.

4.1.3 Microstructure

The microstructure of the grout is altered depending on the level of replacement by BFS. This provides beneficial properties such as reduced accessible porosity compared to pure PC systems at later age [42], [157]. As hydration continues over time, the microstructure densifies due to additional hydration formation and the overall porosity drops (as was outlined in Chapter 2, Section 2.4.1.1).

Examples of the visible variation in microstructure over time for a 3:1 BFS:PC system are shown in Figure 4.7. At 28 days (Figure 4.7 A,B) regions of sparse outer matrix can be observed (Figure 4.7 B,

region 2) and limited reaction of the BFS fraction was seen (Figure 4.7 B, region 1). Unreacted BFS and clinker are observed and cracking of the sample was noted – this is likely a product of sample preparation on a low strength material. The matrix was much denser in the 24 week samples (Figure 4.7 C,D) and no cracking was observed. Almost full hydration of clinker grains was observed in region 2 in Figure 4.7 C, and region 1 shows hydration of small BFS particles. Zones 1, 2 and 3 in Figure 4.7 D indicate BFS grains which have undergone varying degrees of hydration; angular dark zones of the matrix are fully hydrated BFS grains, whilst the dark rims present on remaining slag grains show the hydration front. Portlandite was present at both ages, forming discrete zones in the matrix. These are often adjacent to BFS particles. However, as hydration of the BFS increases, the portlandite is separated by the BFS reaction rim.

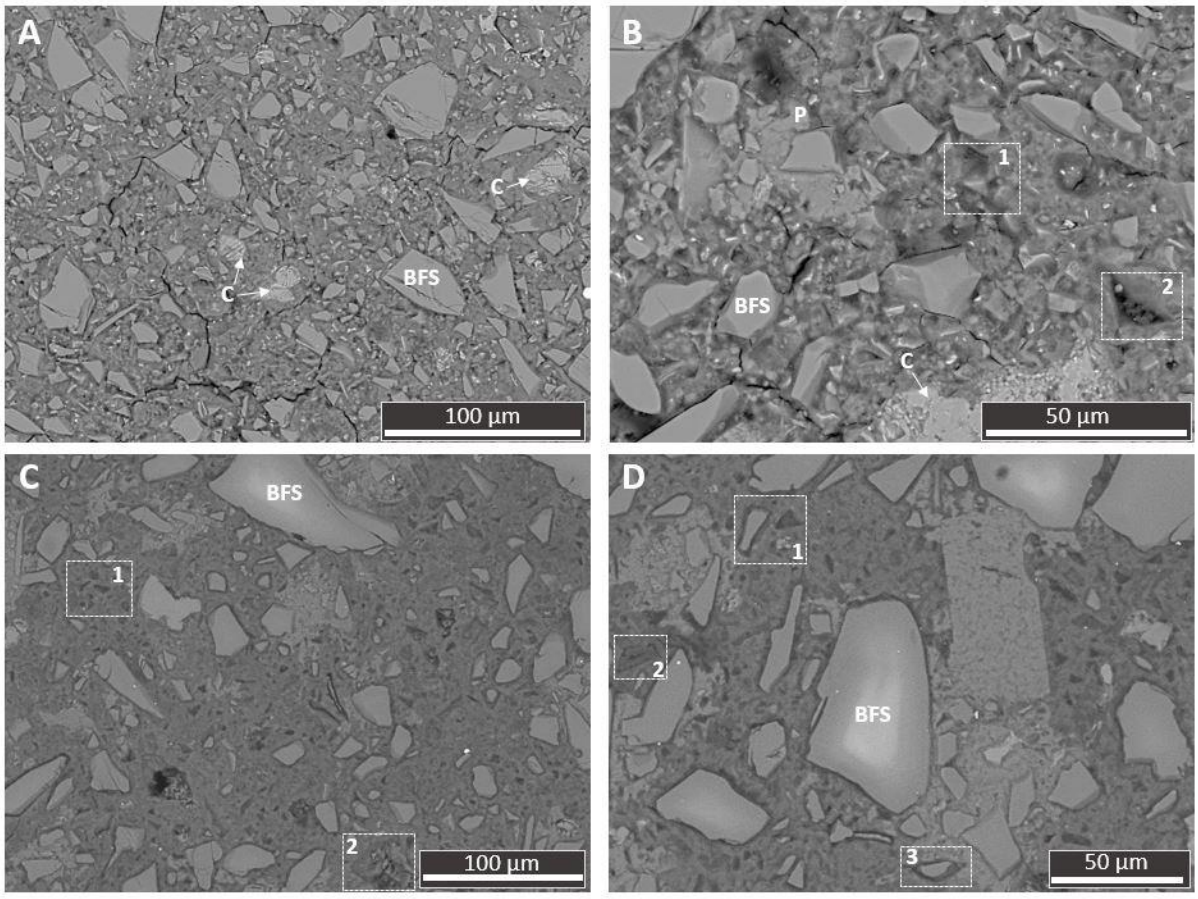

Figure 4.7 BSE micrographs of 3:1 BFS:PC A, B: 28 days, C, D: 24 weeks. C: clinker, P: portlandite. Labels 1, 2, 3 discussed in text.

The effect of the proportion of BFS on the microstructure can be assessed by comparison of Figure 4.7 and Figure 4.8, which shows 9:1 BFS:PC at the same ages. The matrix was less dense initially in the higher replacement blend, with large amounts of porosity apparent (black in the BSE images). Region 1 in Figure 4.8 B represents porosity created by a removed BFS particle which acted as a nucleation

site for the remaining matrix products. The matrix texture in the 9:1 at 24 weeks has many similarities to the 3:1 blend at 28 days: a dense matrix has formed, small BFS particles have undergone hydration (region 1, Figure 4.8 D) and small amounts of unreacted clinker are present in the matrix.

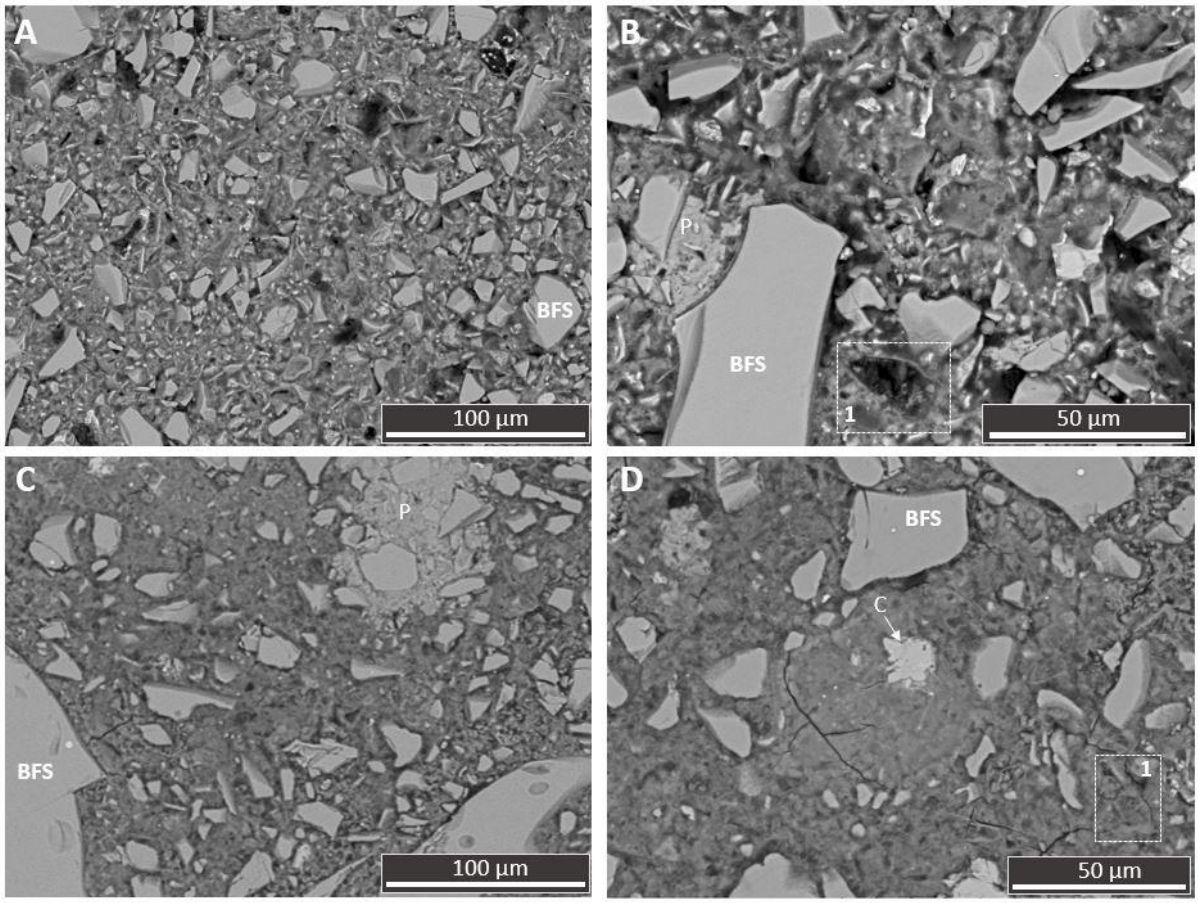

Figure 4.8 BSE micrographs of 9:1 BFS:PC A, B: 28 days, C, D: 24 weeks. Labels in figure are discussed in text.

The analysis of MIP results (Table 4.2) indicates that the overall porosity of the system increased as the BFS fraction increases. The critical pore entry and threshold pore entry radii (for definitions see Section 3.3.6) similarly increase as the proportion of BFS increases.

Table 4.2 Summary of porosity of cement samples containing different amounts of BFS at 28 days.

BFS:PC	Total accessible pore volume (%)	Critical pore entry radius (nm)	Threshold pore entry radius (nm)
3:1	29 ± 2	16	25
3.44:1	33 ± 2	18	30
5.67:1	31 ± 2	23	40
9:1	43 ± 2	33	60

The increase in threshold pore entry radius indicates that the minimum pore radius that is continuous throughout the sample is larger as the BFS fraction increases, i.e there are wider continuous pores. The critical pore entry radius shows the fastest rate of mercury intrusion, and so if this shifts to higher pore sizes indicates there is also a higher proportion of larger pores present with increased BFS replacement. The overall increase in porosity and the changes in the pore size distribution are considered to be a product of the limited BFS reaction that has occurred, as supported by the SEM-EDX results (Figure 4.6).

The results of the MIP analysis support the visual findings from SEM. The analysis of pore structures is important for this thesis because the increased porosity observed in higher BFS replacement pastes may result in differences in the response to radiation, specifically in the impact of carbonation on the systems. Carbonation due to radiation exposure has been observed to reduce the overall pore volume in pure PC systems [109]. From current analysis, the interconnectivity of the pore volume is unknown, which may have implications for mass transport in these systems. The interconnectivity of the pore volume may also be impacted by the carbonation of the paste.

4.1.4 Mechanical properties

Gamma radiation has been found to impact on the mechanical properties of cementitious grouts and their components. Whilst the design criteria for cemented wasteforms do not specify empirical requirements for properties such as strength (“adequate” strength for handling purposes must be achieved [18]), it is necessary to know how the materials perform so that in a GDF scenario the separate barriers can be appropriately engineered. Non-destructive testing methods for estimation of compressive strength are well established in the construction industry, with methods for developing ultrasonic pulse velocity – compressive strength relationships outlined in European and American testing standards [153], [200]. UPV was selected as it analyses the bulk properties of the material being tested. Previous investigation of the impact of gamma irradiation on mechanical strength in high volume replacement BFS:PC pastes found increased compressive strength in samples that had been exposed to gamma radiation despite an increase in microcracking and porosity [110]. Due to size constraints of the irradiation facility used in the Mobasher et al. study [110], and in this current work, the testing was completed on small monoliths, leading to a large standard deviation among the triplicate tests completed. The use of UPV testing in this study aims to provide an alternative testing method to further investigate the relationship between irradiation and mechanical properties. It was considered that the non-destructive nature of the testing would enable replicate measurements of

the same test specimen, potentially reducing the inherent error whilst also allowing ageing effects to be investigated.

The relationship between UPV (v) and compressive strength was estimated through the relationship to the elastic modulus as follows:

$$v = \sqrt{\frac{E(1-\mu)}{\rho\,(1+\mu)(1-2\mu)}} \tag{4.1}$$

where *E* = dynamic modulus of elasticity, μ = dynamic Poisson's ratio and ρ = density. This relationship allows estimation of the strength despite the lack of a direct physical relationship between these quantities. This relationship is generally assumed to be non-linear, as the elastic modulus and strength of the material increase at different rates as it ages; the elastic modulus increases more rapidly than strength at early ages, and lower at later ages, leading to an exponential style relationship typical expressed as:

$$C = a * V^b \tag{4.2}$$

where C = compressive strength, *V* = ultrasonic pulse velocity, and *a* and *b* are constants related to the fitted curve. The non-linear nature of the relationship can result in a loss of sensitivity in this technique in older cements [153], [155].

To produce correlation curves for UPV and compressive strength for each of the formulation of BFS:PC outlined in Chapter 3, Section 3.2, multiple sets of triplicate 50 mm cubes were made to allow compressive strength testing in accordance with a modification of ASTM C109 [151]. Testing was completed at 4 or 8 week intervals, dependent on the blend, and continued to 32 weeks for all blends except the 3.44:1 samples which were tested until 65 weeks. At each test point, UPV readings were taken across two transects of each cube (the top surface was not flat enough to permit testing) and underwent destructive testing to measure the compressive strength.

In order to create a correlation of UPV with strength, the procedure outlined in ACI 228.1R-03 was followed [155]. For each test age, the average values for the compressive strength and UPV were taken as a single data pair. Regression analysis was completed on the natural logarithms of the data pairs to ascertain the best fit relationship. Mandel's regression procedure [155], [201] was applied to the data instead of ordinary least squares analysis (OLS). This was to attempt to minimise uncertainty in the strength relationship, as OLS analysis assumes no error in the X value and that the standard deviation of Y remains constant, where neither of these conditions is true for the data analysed here. The results of the fitting for each blend can be seen in Figure 4.9.

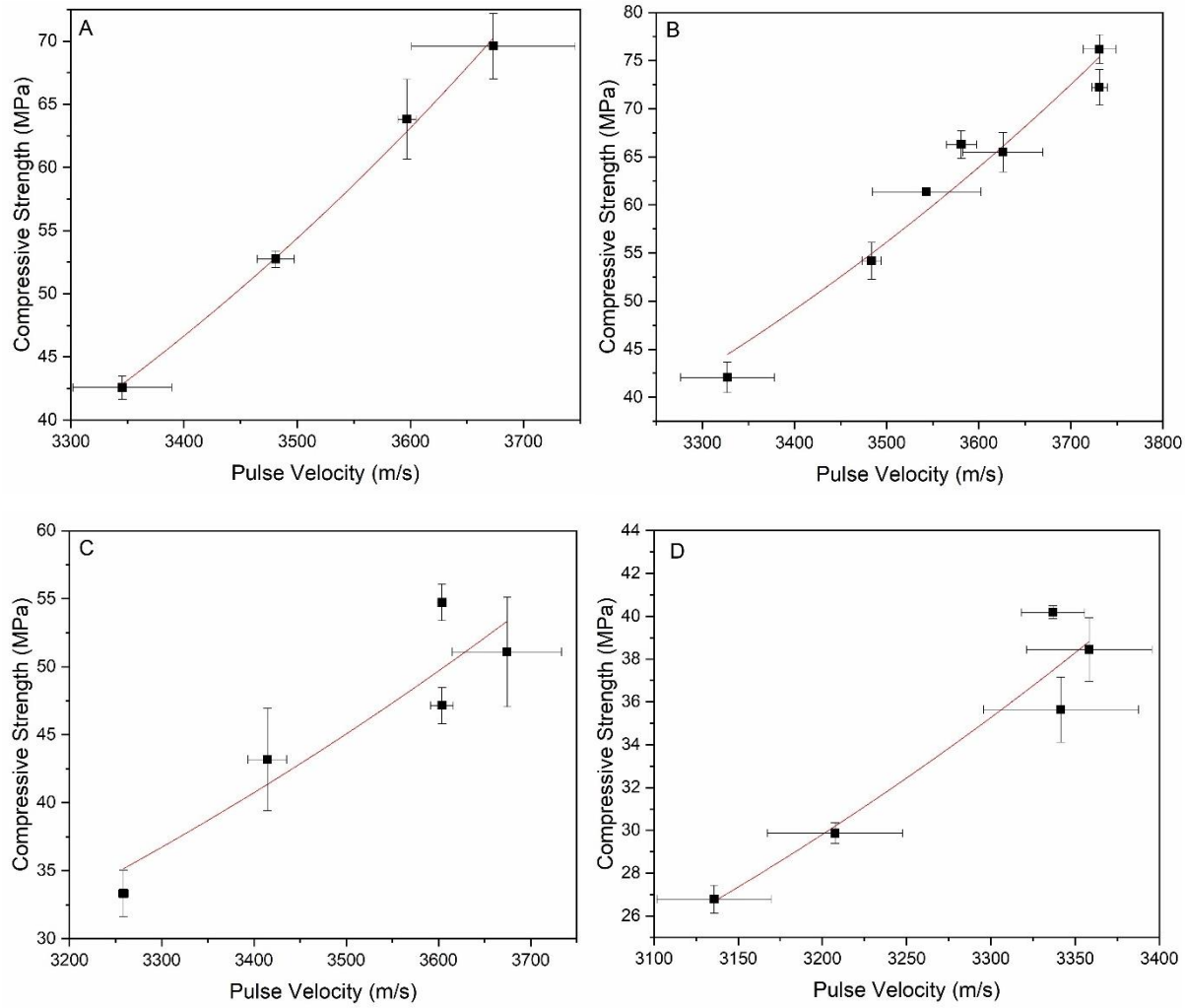

Figure 4.9 Data for UPV-Strength relationship for all BFS:PC blends. A: 3:1 BFS:PC, B: 3.44:1 BFS:PC, C: 5.67:1 BFS:PC, D: 9:1 BFS:PC.

A summary of the defined relationship parameters for the compressive strength – UPV relationship for each blend is provided in Table 4.3.

Table 4.3 Fit parameters for UPV - Compressive strength relationships shown in Figure 4.9

BFS:PC	Identifier in Figure 4.9	Correlation equation	R^2 value
3:1	A	$C = 9.64\times10^{-18}*V^{5.29}$	0.99
3.44:1	B	$C = 2.65\times10^{-15}*V^{4.61}$	0.95
5.67:1	C	$C = 2.22\times10^{-11}*V^{3.47}$	0.85
9:1	D	$C = 2.05\times10^{-18}*V^{5.47}$	0.91

The relationship between compressive strength and UPV for all blends was observed to be good, with R^2 values > 0.85 observed. This is in accordance with the findings of Demirborğa et al. [202], who investigated the relationship between UPV and compressive strength of concretes containing varying levels of PFA and BFS replacing PC. The decrease in UPV and compressive strength that was observed with increasing replacement by BFS in Figure 4.9 agrees with the findings of previous studies [202], [203]. This was unsurprising as increased BFS content in grouts is known to reduce early age strength but can contribute to higher overall later strength compared to PC systems depending on the fineness and reactivity of the BFS fraction [34]. The heat of hydration has also been proposed as a cause for early age low strength of BFS replaced cements, providing another link between the reactivity of BFS and strength development [203]. BFS addition lowers the heat of hydration (Section 4.1.1) because it does not react as rapidly as PC, and so there are less exothermic reactions occurring. This slower rate of reaction is also responsible for the slower strength development, as if the BFS is not reacting, not hydrate phases responsible for strength are forming. The testing of all blends at 32 weeks showed a 42 % reduction in average compressive strength between the 3:1 and 9:1 blend and a fall of 10 % in the recorded UPV. At 4 weeks, the difference was 37 % for strength and 6 % in UPV. The overall rate of increase in compressive strength was 27 % greater in the 3:1 BFS:PC blend compared with the 9:1 blend.

The overall goodness of fit for the strength correlation relationships (Table 4.3) decreased with increasing BFS replacement. This may be due to the increased scatter in the compressive strength data at increased UPV values in the higher replacement blends. Previous research found that the increase in UPV plateaued after 28 days of curing [202]. Although this was not observed to the same extent in this data set, this effect is expected in all compressive strength-UPV correlations due to the elastic modulus and strength increasing at different rates as the material ages [155].

To ascertain the precision of the technique, the standard deviations of the UPV and compressive strength at each testing point were determined. No discernible trends were observed with increasing mean values (Figure 4.10 A,B). To provide a direct comparison, the coefficient of variation (COV) was calculated for each testing point, and the cross plot for this is shown in Figure 4.10 C.

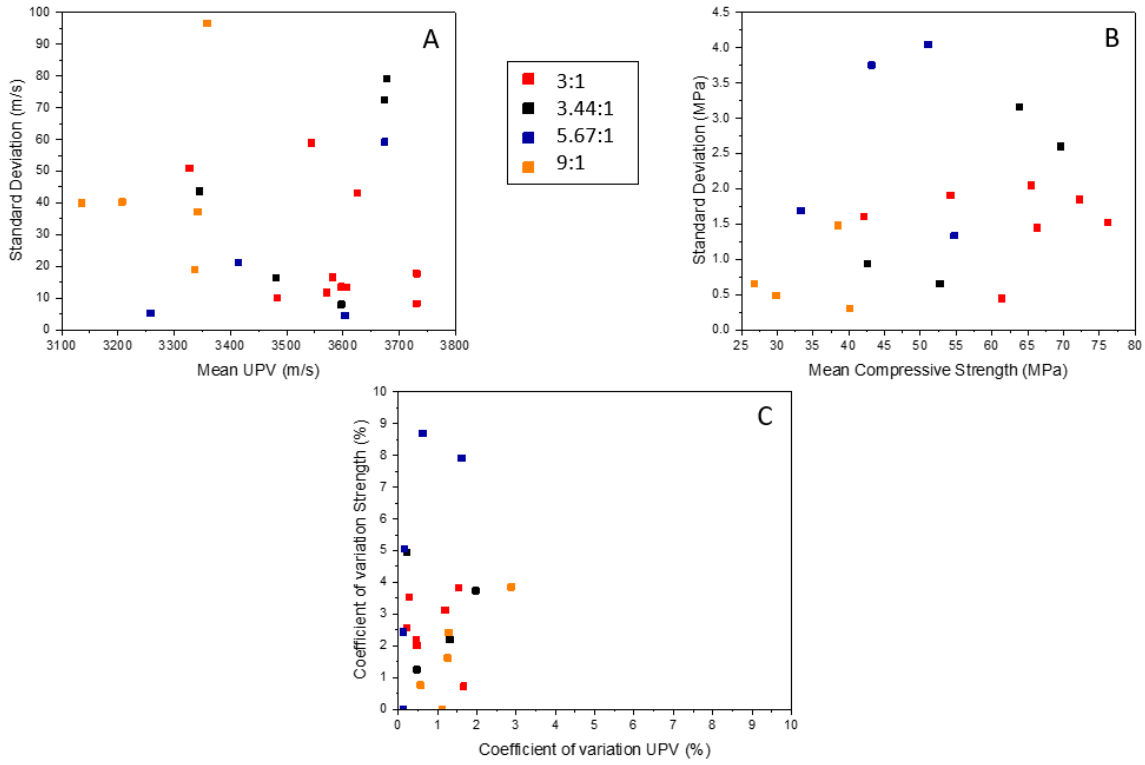

Figure 4.10 Standard deviation at each test point for A) UPV, B) compressive strength and C) coefficient of variation from A and B. Key shows colour variations for each BFS:PC blend.

The COV was observed to be much larger for the compressive strength testing than the UPV, indicating that the reproducibility of UPV testing was much higher. Data from the 5.67:1 blend show very high COV for the compressive strength values, which may be the cause of the low R^2 value observed in the correlation relationship.

For all levels of replacement by BFS, the relationship between compressive strength and UPV appears to fit the exponential style relationship found for similar materials in other studies [152], [155], [202]–[205]. However, the need for separate correlation relationships dependent on the level of BFS replacement within the cement is clear from these data, unlike the work of Demirboğa et al. [202]. The overall correlation relationships determined are considered suitably robust for the assessment of the impact of gamma radiation on the bulk properties of these cements, which will be presented in detail in Chapter 5.

4.2 PFA:PC

Cementitious grouts containing PFA are commonly used as 'capping' materials on the surface of waste which is encapsulated in alternative materials [15]. However, they are also used as the main encapsulant for less common waste streams e.g. ferric flocs [8], [18], and at the Dounreay cementation plant for raffinates and flocs [3]. The formulation envelope used by the UK nuclear industry is fairly limited when compared to formulations based on BFS. Given this, a single formulation of PFA:PC (3:1, 0.43 w/s) was chosen to provide characteristic microstructural and phase assemblage information prior to the initiation of irradiation testing.

4.2.1 Hydration

The isothermal calorimetry data for the initial 150 hours of hydration for the PFA:PC system is shown in Figure 4.11. The isotherm shows the same main thermal events of hydration outlined in Section 4.1.1: initial rapid dissolution with high heat flow, low heat evolution during the dormant phase, and a subsequent increase in heat evolution corresponding to main hydration and sulfate depletion. The dormant period appears extended in this system compared to the 3:1 BFS:PC, which has the same level of replacement, as highlighted in Figure 4.11. This extended dormant period is due to the reaction of PFA in cement being pozzolanic, and as this reaction is very dependent on a highly alkaline environment, in water activated pastes this can be very slow (see Section 2.4.2.2). The rate of heat evolution attributed to the main hydration event also appears to be slower than in the BFS containing systems, although the sharp shoulder representing secondary ettringite formation is much more prominent in the PFA containing system.

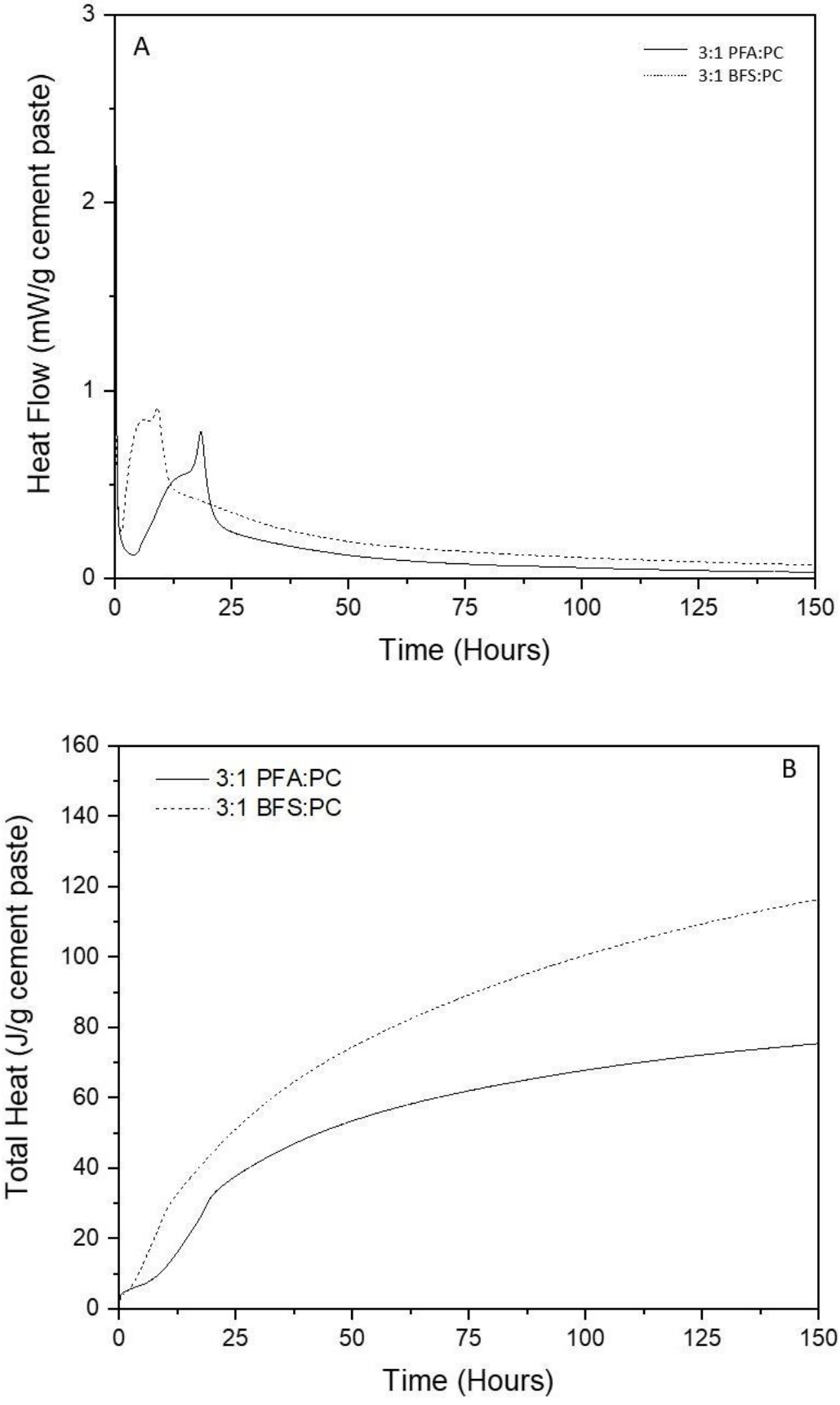

Figure 4.11 A: Isothermal calorimetry and B: total heat evolution data for the 3:1 PFA:PC system. Dashed line shows comparison with same level of replacement by BFS.

The overall heat evolution of the system is lower than the maximum evolved heat from any of the BFS:PC systems as described in Section 4.1.1, therefore complying with the European standards and Sellafield specifications [15], [178].

Differences in early age hydration kinetics for PFA-containing blends have long been noted, with directly opposing results often seen. Richardson et al. [206] investigated the impact of PFA on hydration and compared new results with data from several other studies, finding that the slower initial hydration results in lower cumulative heat evolution. However, it was acknowledged that the impact of PFA on hydration is complex and the variable impact on the silicate and aluminate hydration rates observed in other studies may be attributed to differences such as the physical and chemical nature of the PFA and PC, mix ratio, and the w/s ratio.

The extension of the dormant period (between 2 – 5 hrs) in Figure 4.11 may be a product of the higher w/s ratio (in line with the Sellafield specification [3], [15]) of w/s 0.43 used in the 3:1 PFA:PC blend compared to the 0.35 w/s used for the BFS:PC cements. However, it is considered that the slower rate of heat evolution for main hydration peak is not solely a product of this change in w/s ratio [186]. Deschner et al. [77] observed longer induction periods in systems doped with PFA compared to the same levels of replacement by quartz, showing that the change in kinetics cannot only be due to dilution. An alternative cause for the prolonged induction period and the slower initial rate of hydration suggests that calcium ion adsorption on the PFA particle surface causes retardation of the silicate reaction [77], [207].

There is an increase in heat flow associated with the secondary ettringite formation peak (centred at 18 hrs) in Figure 4.11. This may be a product of the finer particle size of PFA compared to BFS (part comprised of Calumite) creating different seeding effects and increasing the overall filler effect. Dittrich et al. [207] observed an increase in aluminate reaction due to the increased nucleation sites provided by a finer particle size, increasing the reaction of C_3A leading to quicker precipitation of ettringite. The sulfate content of the PFA was also observed to impact the overall kinetics of formation and the total amount of ettringite formed. However, given the low sulfate content of the PFA (0.1 wt.%, Chapter 3, Table 3.1) used in the current study, it is considered that the particle size is the controlling factor.

4.2.2 Phase assemblage

Analysis of the phase assemblage was completed using XRD, TGA and SEM-EDX techniques. The XRD diffractogram of the sample after 28 days is shown in Figure 4.12, and shows the phase assemblage

contains ettringite (PDF# 41-1451), hemicarboaluminate (PDF# 014-0221), portlandite (PDF# 04-0733), and calcite (PDF# 01-0837) along with residual mullite (PDF# 79-1453), quartz (PDF# 85-0335) and belite (PDF# 29-0369). The diffuse scatter observed between 10-35° 2θ is due to the contribution of unreacted PFA. The diffuse peak located between 10.4-11.2° 2θ may indicate an AFm solid solution (AFm_{ss}) of hemicarbonate and highly OH^- substituted monosulfoaluminate [69]. The poor crystallinity of these phases typically produces broad peaks which makes certainty around the presence of solid solution problematic.

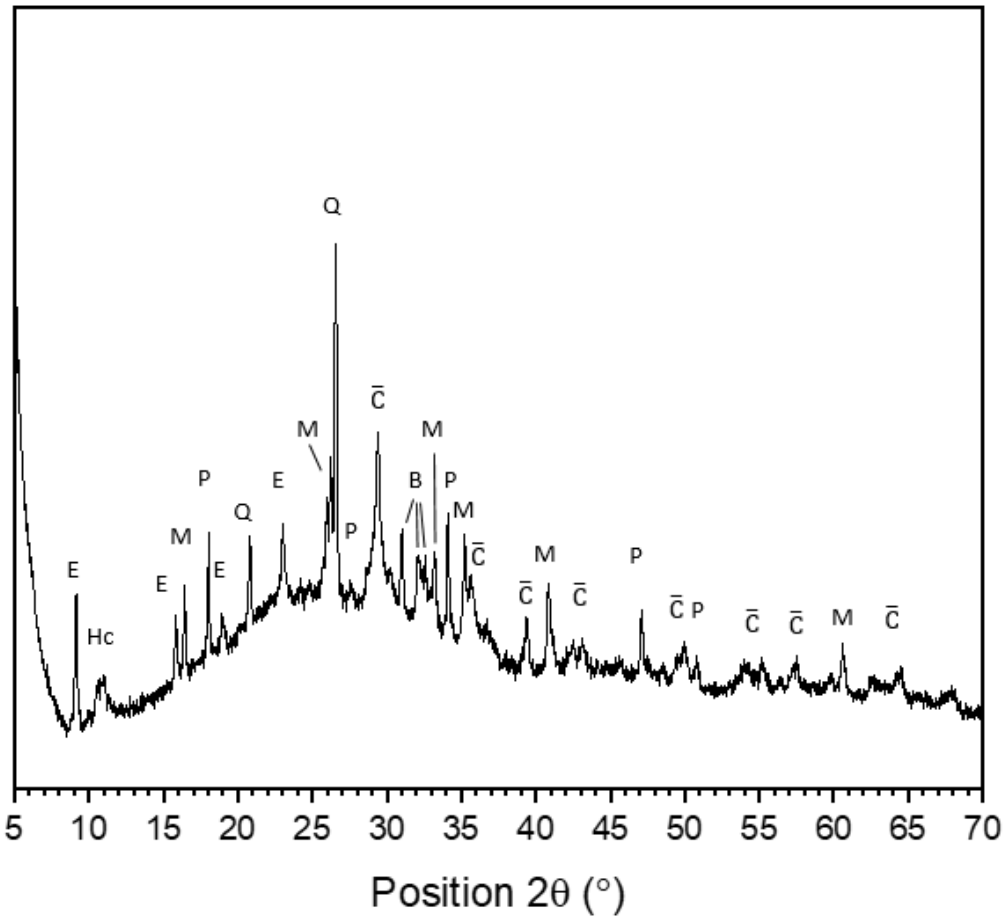

Figure 4.12 XRD diffractograms of hydrated 3:1 PFA:PC at 28 days. E: Ettringite, HC: hemicarboaluminate, M: mullite, P: portlandite, Q: quartz, C: calcite, B: belite (C_2S).

The TGA results from 7 and 28 days are displayed in Figure 4.13, together with mass spectrometry data for H_2O and CO_2. The primary phases identified are ettringite, C-S-H, portlandite and carbonates, showing good agreement with XRD results. The weight loss associated with free water (>100 °C) was significantly reduced in the 28 day sample as hydration had increased and the formation of a distinct shoulder was observed at approximately 100 °C as a result of the water loss and increased ettringite formation [194]. Portlandite presence was confirmed from the weight loss at 420 °C, and carbonate

decomposition was observed between 500 – 700 °C. Increased CO_2 emission from the samples at > 800 °C was thought to be due to oxidation of elemental carbon [77].

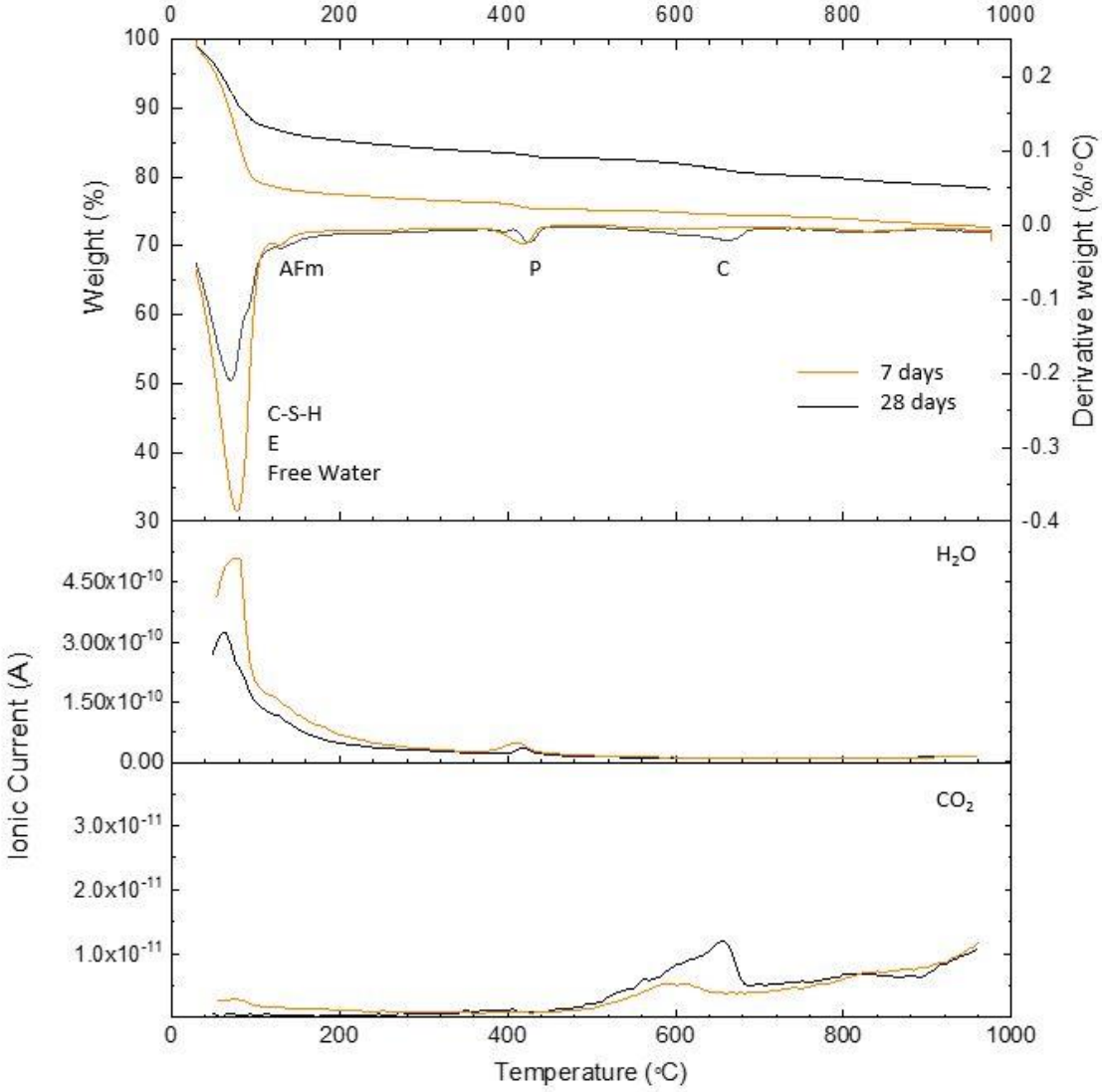

Figure 4.13 TGA and MS response from 3:1 PFA:PC at 7 and 28 days. E: ettringite, P: portlandite, C: carbonates.

Quantification of the proportions of portlandite and carbonate in each sample are shown in Table 4.4 (see Section 3.3.7 for quantification details). The onset of portlandite consumption was observed, with an overall reduction of approximately 48 % in the relative proportion between the 7 and 28 day samples. This was due to the pozzolanic reaction of the PFA as hydration continues [34]. The carbonate content of the 28-day old sample was increased, indicating that carbonation of the system at the expense of portlandite may have occurred, also contributing to the reduction in portlandite content.

Table 4.4 Quantification of free water loss, portlandite and carbonate content from 3:1 PFA:PC at 28 days

Age	Free water (%)	$Ca(OH)_2$ (%)	$CaCO_3$ (%)
7 days	20.8	4.6	2.0
28 days	12.3	2.4	5.8

SEM-EDX showed unreacted Si and Al rich PFA particles, within a hydrate matrix comprised of open textured C-S-H (Figure 4.14). The chemical composition of PFA is highly variable, and Fe content was especially inconsistent, with particles rich in Fe containing little Si and Al [208], [209]. To provide an overview of the hydration of the PFA as a whole, a large representative area was subjected to chemical mapping to show overarching relationships. Zones of portlandite were still present, and unburnt carbon and residual iron were identifiable. Sulfur rich zones were identified through EDX mapping (labelled AFt in Figure 4.14), likely to represent ettringite given the XRD results.

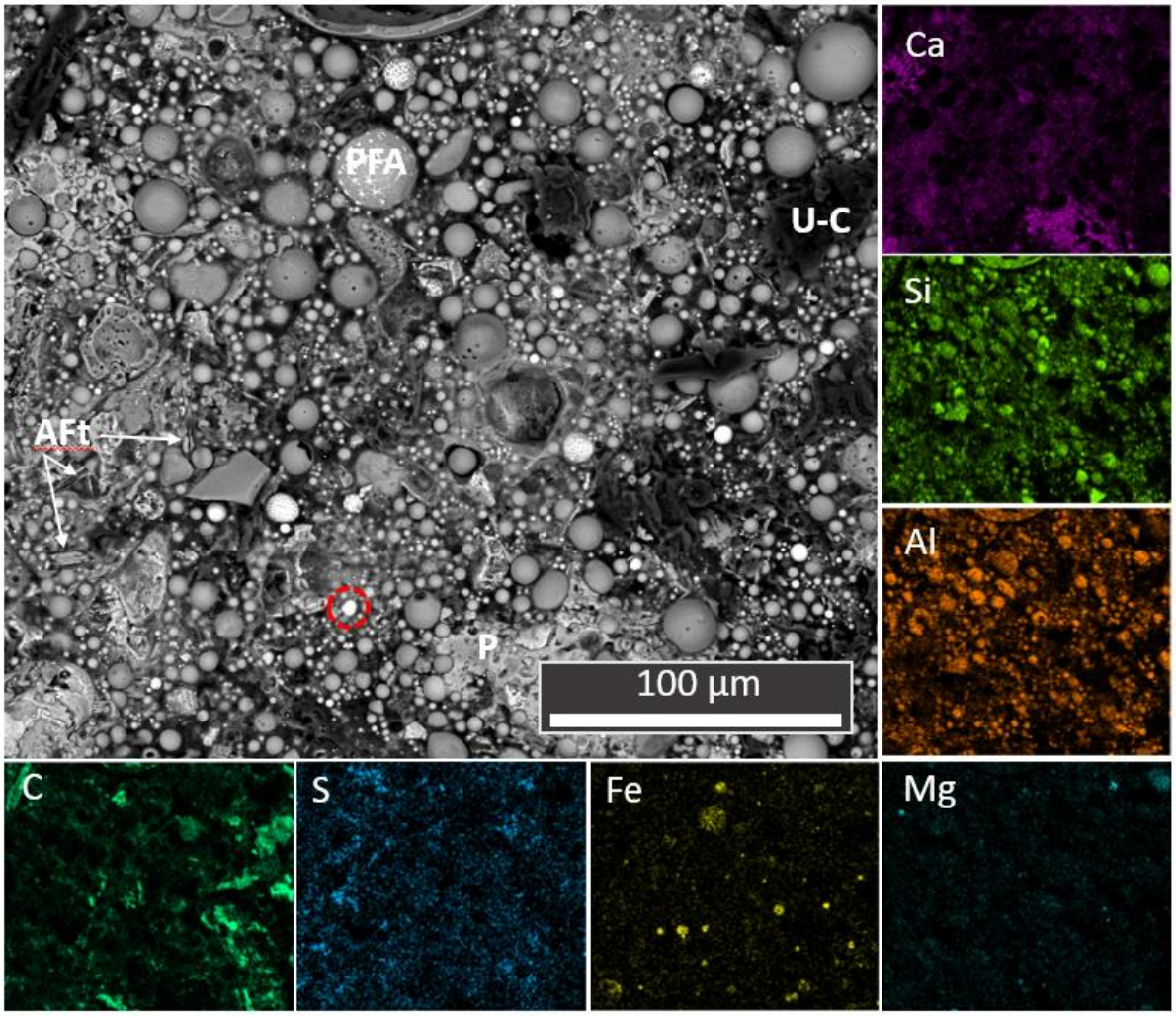

Figure 4.14 SEM EDX of 3:1 PFA:PC at 28 days. Labels mark AFt: ettringite, P: portlandite, U-C: unburnt carbon and PFA. Red dashed circle indicates residual iron.

Point analysis was carried out on zones of the outer matrix product with minor areas of inner product from hydrated clinker grains or PFA rims (Figure 4.15) to allow estimation of the approximate composition of the C-S-H. Ca/Si ratios of between 1.25-1.55 were observed, with a mean value of 1.41 ± 0.3. These are similar to literature values for systems with slightly lower volume replacement by PFA: Deschner et al. [77] observed Ca/Si ratios of 1.3 ± 0.2 for blended systems with 50 % fly ash, and with increased PFA content in the samples in Figure 4.14, the Ca/Si ratio should be reduced [71]. The estimation of chemical composition from SEM should be approached cautiously, as the intimate intermixing of hydrates within the matrix means that the area of the EDX spot size and resulting interaction volume is greater than the length scale of individual hydrates and may include analysis of PFA particles and/or hydrates beneath the sample surface. This is the cause of the distribution of points outside the anticipated C-S-H envelope and hydrate compositional points [168], [210], [211]. The clustering of points around the tie lines in Figure 4.15 A shows that both ettringite and AFm-type phases were present and the fine intermixing of these phases within the matrix results in the spread of points. Figure 4.15 B gives a clearer division of the sulfate balance within the system, and the majority of points lie within the AFm-type region indicating that the diffuse peak identified between 10.4 – 11.2° 2θ in the XRD results (Figure 4.12) is likely representative of an AFm solid solution of hemicarbonate and highly OH^- substituted monosulfoaluminate [69], [77].

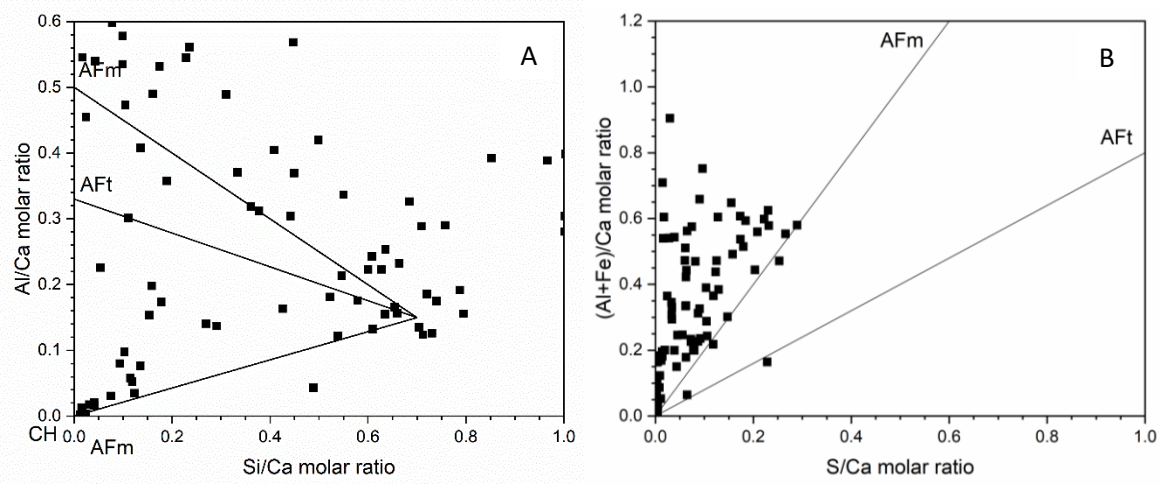

Figure 4.15 EDX point analysis from 3:1 PFA:PC A: Al/Ca versus Si/Ca, B: (Al+Fe)/Ca versus S/Ca. Each point sample was taken from a region that visually appeared to be binder rather than residual anhydrous phases. Tie lines link to the other prominent hydrate phases; CH: portlandite; AFm: monosulfoaluminate; and AFt: ettringite.

Overall, the phase assemblage was found to be consistent with literature findings for systems containing similar levels of replacement of PC by PFA.

4.2.3 Microstructure

To provide an overview of the microstructural characteristics of this paste, SEM micrographs of the 3:1 PFA:PC at 28 days with increasing levels of magnification are shown in Figure 4.16. Open porosity and sparse zones of outer matrix were observed, especially compared to the dense portlandite areas identifiable by the lighter greyscale appearance. The matrix was texturally varied between zones and some rim features were present on the surface of PFA (Figure 4.16 B, C, D). This may indicate initial reaction of the materials, or their role as nucleation sites for hydrates, or may be due to the chemical variation of PFA. Areas of residual clinker (Figure 4.16 B) and hydration rims around the edge of PFA particles (Figure 4.16 B, D) were observed. In Figure 4.16 D region 1, fine fibres assumed to be C-S-H were observed radiating from PFA particles. A thin dark rim was observed between this and the PFA particle, indicating inner product formation through PFA hydration. The more porous structure of the outer product can be seen adjacent to AFm rich zones (labelled 2, Figure 4.16 D). MIP measurements on the sample produced a total accessible pore volume of 43 ± 1 % with threshold pore entry radii of below 0.4 µm.

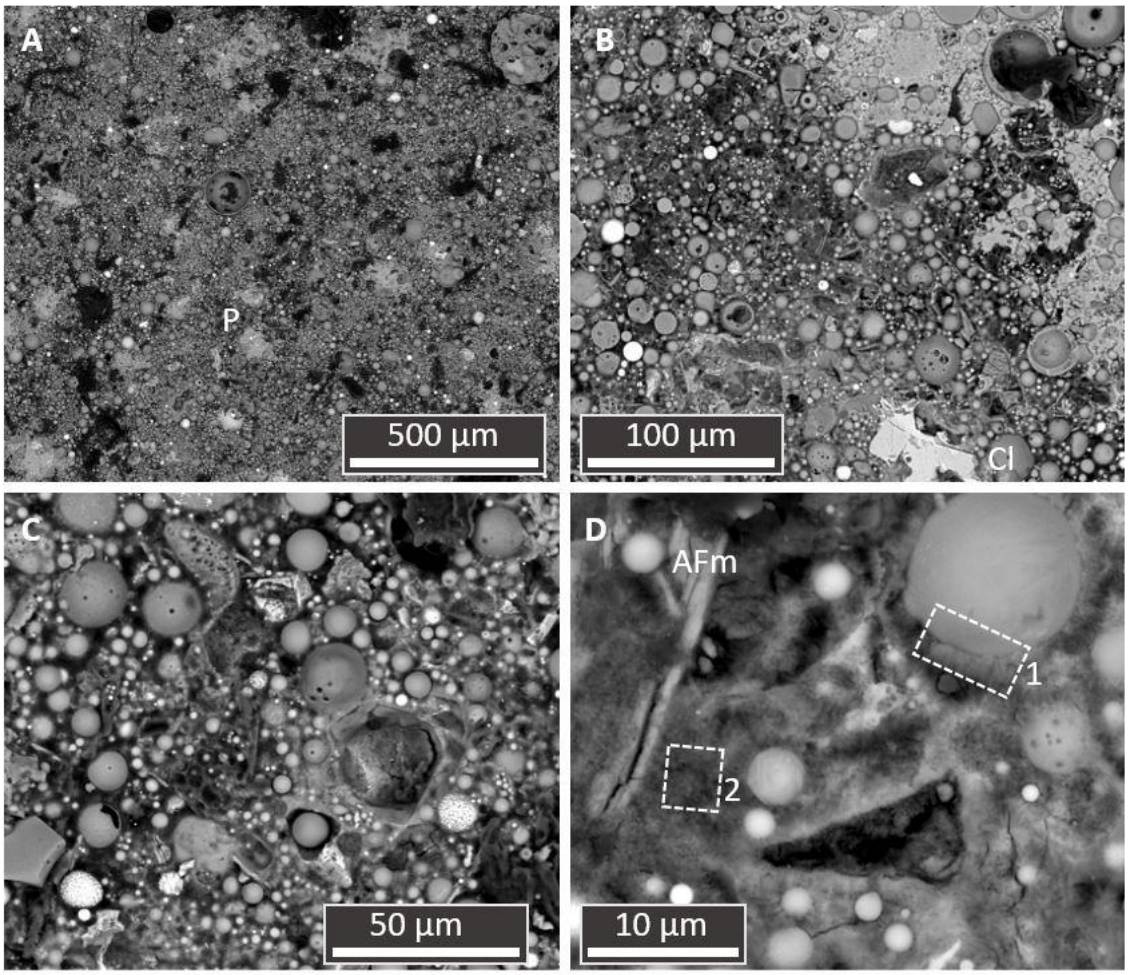

Figure 4.16 SEM micrographs of PFA:PC after curing for 28 days at increasing magnification. P: Portlandite, Cl: clinker. Regions 1 and 2 in 5 D discussed in text.

4.3 Conclusion and discussion of baseline parameters

Addition of Sellafield Ltd. specification SCMs to PC systems causes distinct changes to hydration, phase assemblage and microstructural development dependent on the SCM used and the level of replacement in the grout. These changes are predominantly in line with those observed in systems using generic SCMs, however, variations were noted.

The heat of hydration of BFS cements was lower than observed in literature studies that included similar replacement levels of BFS due to the addition of Calumite to regulate the BFS reactivity. Nevertheless, the phase assemblage and microstructure were not different to those seen in literature where no Calumite fraction was used. In PFA systems, the heat of hydration was lower than in BFS systems and the hydration kinetics were altered due to the fine particle size of the PFA. However, the overall phase assemblage remained comparable to those in literature.

The average Ca/Si ratio for grouts with the same level of replacement by SCM was found to be comparable: approximately 1.4 for both of the 3:1 systems. The Ca/Si ratio increased with increasing SCM replacement i.e. the 9:1 sample Ca/Si = 1.9, whereas in the 3:1 sample Ca/Si = 1.4. The higher Ca/Si ratio indicates very little reaction of the lower-Ca BFS and PFA material at increased replacement level, and so indicates that at 28 days the phase assemblage is primarily composed of PC hydration products. This indicates the slow rate of hydration of the Calumite fraction causes the chemical behaviour to be similar to that of grouts with lower levels of replacement by SCMs. The similar Ca/Si ratio observed in the BFS and PFA cements also indicates a low level of reaction of the SCMs, as PFA tends to react more slowly than BFS; this is because PFA requires a very alkaline environment to initiate the pozzolanic reaction.

In terms of radiation effects at young ages in these systems, this means that work completed on pure PC systems may provide relevant information even given the high levels of replacement in these cements. Despite this, the effects of radiation are still unknown for these materials at increased ages, where increased hydration of the SCM fraction will have occurred, altering the physico-chemical properties. Other factors such as the impact of temperature differences experienced by the wasteform through interim storage and disposal will also impact the hydration products and phase assemblage of the grouts (see Chapter 2, Section 2.3), and although this is not investigated here, it is touched upon in Chapter 7.

PFA systems contained higher porosity than BFS systems with equivalent replacement levels. Increased replacement by BFS resulted in higher total porosity with larger pore entry distribution.

Correlation of UPV with compressive strength was completed for all levels of BFS replacement. Exponential style relationships used in previous studies apply well to these materials. The goodness of fit was observed to be high for all fitted relationships. However, with higher levels of BFS replacement, compressive strength and UPV were reduced and increased variation in the fitted relationship was observed. This variation was likely a product of compressive strength testing, as the UPV results generated highly reproducible data.

It is considered that the UPV testing method is appropriate to generate semi-quantitative data on how radiation impacts compressive strength. This can only be done using the blend-appropriate correlation relationships outlined in Section 4.2.4.

BFS systems have been selected to take forward as the focus of this study, as they are used to encapsulate the bulk of ILW and demonstrate more range in the formulation envelope used.

5 Gamma stability of BFS:PC systems

In this chapter, the range of BFS:PC samples characterised in Chapter 4 were exposed to increasing total doses of gamma radiation. Post irradiation characterisation was completed and the results compared to control samples of the same age that had undergone similar curing conditions. Assessment of the impact of gamma exposure as a function of dose and BFS replacement level on the phase assemblage, microstructure and mechanical properties was completed.

As outlined in Chapter 2, Section 2.5, radiation damage via radiolytic degradation is a primary concern for the evolution of cementitious wasteforms. The formation of hydrogen gas through the radiolytic breakdown of pore water could lead to overpressure within the pore space that could cause cracking of the wasteform [18]. Alterations to the microstructure via changes in pore size distribution have been observed, often linked to increases in carbonation [106], [109], [114]. Irradiation-induced carbonation has been observed, postulated to arise via formation of calcium peroxide octahydrate, $CaO_2{\cdot}8H_2O$ [107]–[109], [115]. In terms of mechanical properties, gamma exposure has been associated with increased and reduced strength compared to control samples [110]–[113]. Drying of the paste through radiolytic dehydration is often linked with decreased compressive strength, whereas increased carbonation has been associated with maintaining or improving strength [115], [212], [213]. The role of sulfur in gamma-irradiated BFS-containing systems is also debated in the literature, with potential oxidation of sulfide proposed as leading to later-age ettringite formation which may be analogous to internal sulfate attack [124].

There are limited available gamma irradiation studies which have investigated the impact of gamma irradiation on cements containing BFS replacement levels representative of Sellafield's encapsulation formulation envelope. Richardson et al. [124] investigated the phase assemblage and microstructure of 3:1 and 9:1 blends and Mobasher et al. [110] assessed the impact on 9:1 samples. However, no systematic assessment of the impact of gamma exposure with increasing gamma dose on samples which include the coarse grained Calumite fraction have been completed. The impact of irradiation at varying levels of BFS content will be assessed here. The use of non-destructive testing methods to assess changes in the mechanical properties of irradiated samples as they age will provide novel insights into radiolytically induced damage and any potential recovery as curing continues. The effect of total absorbed dose on these systems will be evaluated at 7 MGy, 14 MGy, and 20 MGy, far exceeding the anticipated lifetime dose of 10 MGy estimated for ILW packages, to provide contingency for GDF safety case planning [36].

In order to investigate the long term effects of anticipated lifetime doses of gamma irradiation on the materials, accelerated testing methods are required. The dose rates produced by the ^{60}Co irradiator used in this chapter were much higher than the dose rates experienced in wasteforms, allowing the total lifetime dose to be exceeded in the timeframes required for laboratory study. The use of accelerated testing is commonly employed to assess the radiation response of materials in this manner, although it is still a matter of some debate whether accelerated testing can be used to extrapolate degradation effects to lower fluxes [94]. Kontani et al. [214] found that within certain limits the rate of H_2 production scales linearly in gamma-exposed cements, potentially validating the use of accelerated testing. The increased dose rate may induce changes that are more severe than observed in the waste containing materials, however it is considered that this will provide a conservative estimation of the impact on the cementitious materials.

5.1 Experimental setup

The samples were synthesised and cured using the method outlined in Chapter 3, Section 3.2 for small volumes of materials. The grouts were cured in sealed 50 mL centrifuge tubes for 8 days after which the samples were demoulded, sectioned into cylindrical monoliths approximately 25-30 mm in length and wrapped in aluminium foil to minimise moisture loss and atmospheric carbonation. Half the samples were sent to the UoM DCF for testing using the facilities outlined in Chapter 3, Section 3.3.13. Details of the samples and the irradiation conditions are summarised in Table 5.1.

Table 5.1 Summary of gamma irradiation conditions. See Appendix Section 10.1 for dose rate variations with time.

BFS:PC	Average gamma dose (kGy/hr)	Total dose (MGy)	Irradiation temperature (°C)	Sample age at start of irradiation (wks)	Sample age at end of irradiation
3:1	13.2 (± 0.05)	7 (± 0.02)	35 °C*	9	16
	12.9 (± 0.10)	14 (± 0.11)		16	28
	12.3 (± 0.19)	20 (± 0.31)		30	58
3.44:1	13.8 (± 0.08)	7 (± 0.03)		9	16
	13.4 (± 0.27)	14 (± 0.28)		16	28
	12.5 (± 0.56)	20 (± 0.92)		30	58
5.67:1	12.2 (± 0.07)	7 (± 0.03)		9	16
	11.9 (± 0.09)	14 (± 0.10)		16	28
	12.0 (± 0.53)	20 (± 0.88)		30	58
9:1	13.2 (± 0.07)	7 (± 0.03)		9	16
	12.9 (± 0.10)	14 (± 0.12)		16	28
	11.8 (± 0.70)	20 (± 1.18)		30	58

*Temperature was regulated through use of an air pump to minimise heating of samples.

The irradiations were initiated with the 7 MGy samples, after which the 14 and 20 MGy samples underwent irradiation successively. The average dose rate achieved at each subsequent stage of testing is observed to decrease – this is due to the natural decay of the ^{60}Co pellets within the irradiator and could not be altered within the scope of this experiment.

Due to the timescales required for the total doses to be reached, the cement samples were different ages immediately post-irradiation. Initial TG, XRD and SEM analysis were completed as soon as the samples were received back from UoM DCF, with further analysis of all samples completed at 80 weeks to remove variations due to ageing. The data in this chapter are from the characterisation at 80 weeks, with the exception of TGA results; these are taken at 22, 39, and 80 weeks for 7 MGy, 14 MGy, and 20 MGy samples respectively.

5.2 Irradiation to 7 MGy

Irradiation of these samples began 9 weeks after the samples were made. The time taken to reach 7 MGy was approximately 5 weeks, and so the samples were 16 weeks old when exposure ceased.

5.2.1 Phase assemblage

5.2.1.1 XRD

XRD diffractograms of the irradiated and control samples are shown in Figure 5.1. The phase assemblage is broadly as described in Chapter 4, Section 4.1.2, however ettringite is no longer observed and monosulfoaluminate (PDF# 83-1289) is present. The difference patterns indicate a potential increase in the proportion of this phase in all the blends after 7 MGy gamma exposure and also show the disappearance of hemicarboaluminate. The majority of the control samples have greater peak intensities for portlandite; however, in the 3.44:1 blend (Figure 5.1B) the opposite trend is observed. Overall, no large scale alterations to the phase assemblage were observed after irradiation.

The alterations in peak intensities for portlandite and monosulfoaluminate may be a product of preferred orientation, rather than an effect of gamma radiation. If a decrease in the proportion of portlandite had occurred as a result of gamma exposure, an increase in calcium carbonate-containing phases might be anticipated via radiolytically generated formation of metastable calcium peroxide octahydrate (discussed in Chapter 2, Section 2.5.1) [100], [115]. However, no associated increase in carbonate phases was observed in these samples, which calls into question any apparent decrease in portlandite content.

The differences in the AFm phases observed in the irradiated samples compared to the controls indicate destabilisation of hemicarboaluminate. This could be the result of shifts in temperature that

were greater than anticipated/experienced by the control sample, as hemicarboaluminate is not stable at temperatures > 25 °C [69], [82]; given this, it is interesting that this phase persists in any of the samples. Changes in the pH of the pore solution due to radiolysis may also destabilise hemicarboaluminate; SO_4-OH-AFm has been shown to becomes more stable at pH >13.5 [215]. Changes in the carbonate concentration in the pore solution have also been shown to reduce the stability of hemicarboaluminate, with an increase in CO_3^{2-} ions in pore solution stabilising monocarboaluminate [69], [216].

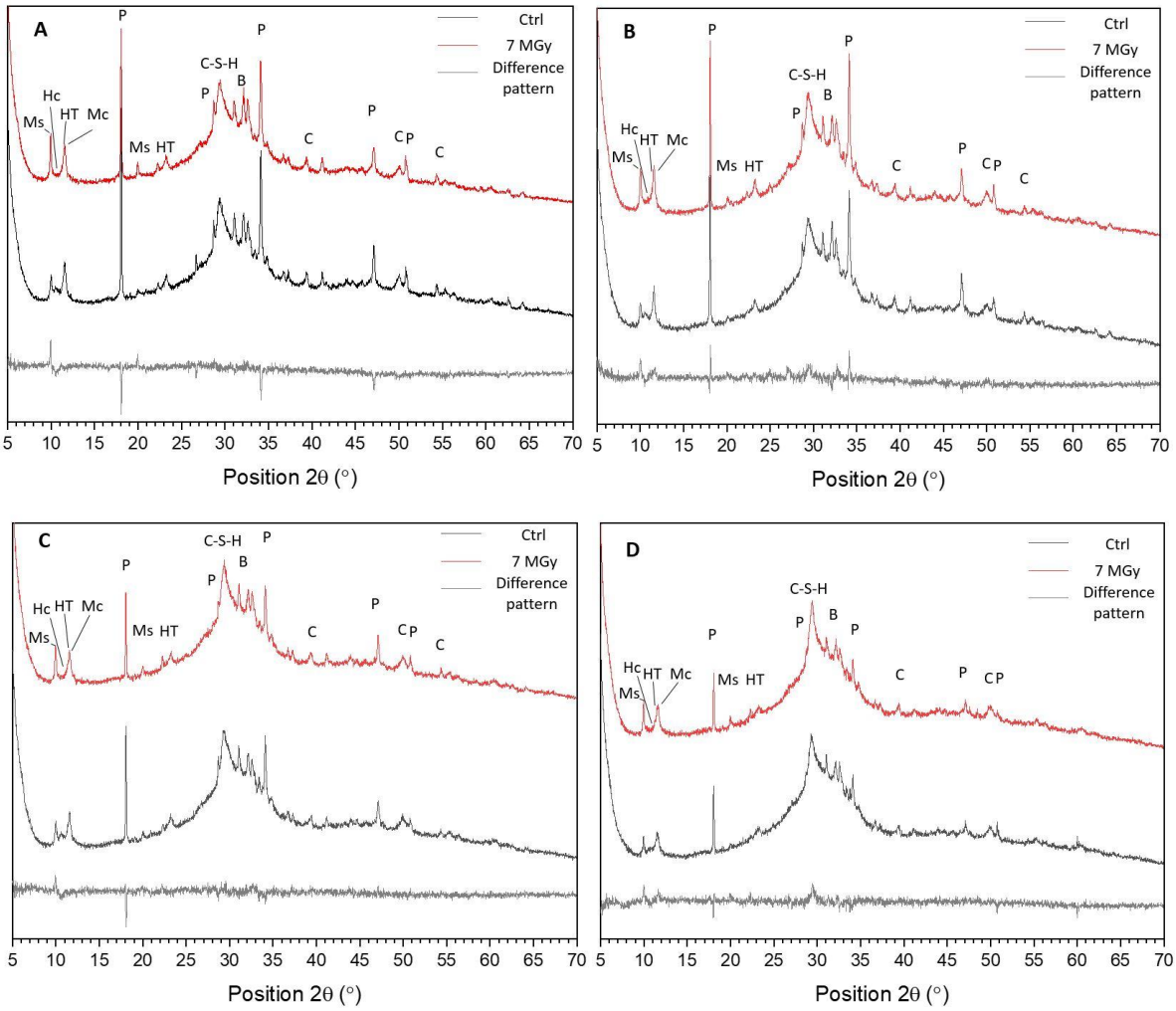

Figure 5.1 X-ray diffractograms of hydrated BFS:PC blends irradiated to 7 MGy and the corresponding control (Ctrl). BFS:PC ratios corresponding to each data set are: A: 3:1; B: 3.44:1; C: 5.67:1; D: 9:1. Ms: monosulfoaluminate, HC: hemicarboaluminate, HT: hydrotalcite, Mc: monocarboaluminate, P: portlandite, B: belite (C_2S), C: calcite.

The increased peak intensities observed for monosulfoaluminate in these samples is to be expected compared to the results shown in Chapter 4, given the increased age of the samples shown in Figure 5.1 (80 weeks versus 28 days in Chapter 4). The results in Chapter 4 showed minor proportions of monosulfoaluminate, with hemicarboaluminate and ettringite noted as primary hydration products.

Formation of ettringite is favourable at young ages due to the initial high concentrations of sulfate; however, as sulfate depletion occurs and dissolved aluminium concentrations increase as hydration continues, monosulfoaluminate increases at the expense of ettringite (Chapter 2, Section 2.4.1.2).

The reduction in hemicarboaluminate over time (compared to the results from Chapter 4) destabilises the ettringite formed at early ages; initially, the formation of hemicarboaluminate stabilises ettringite as it removes aluminium and carbonate from the pore solution, keeping the sulfate content high. As hemicarboaluminate breaks down increased aluminium and carbonate concentrations in the pore solution will reduce the sulfate concentrations [69], [189]. The ongoing hydration of BFS will also lead to a reduction in SO_3/Al_2O_3 ratio over time. Given this, there is potential for the formation of increased amounts of monosulfoaluminate due to hydration of BFS increasing the dissolved aluminium concentration of the pore solution; although not observed in BFS systems, this has been seen in pore solution studies of PFA blended samples [217].

5.2.1.2 TGA

Results from TGA are shown in Figure 5.2, which shows that the major variation between the 7 MGy and control samples is the reduction in free water observed in the irradiated samples (indicated by grey arrows in Figure 5.2). Samples were approximately 22 weeks old when analysed. Quantification of the TGA results is shown in Table 5.2.

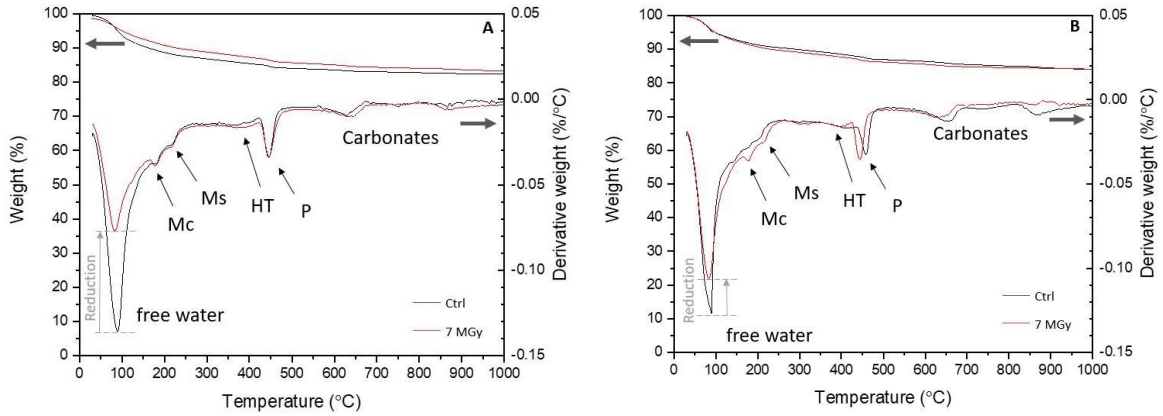

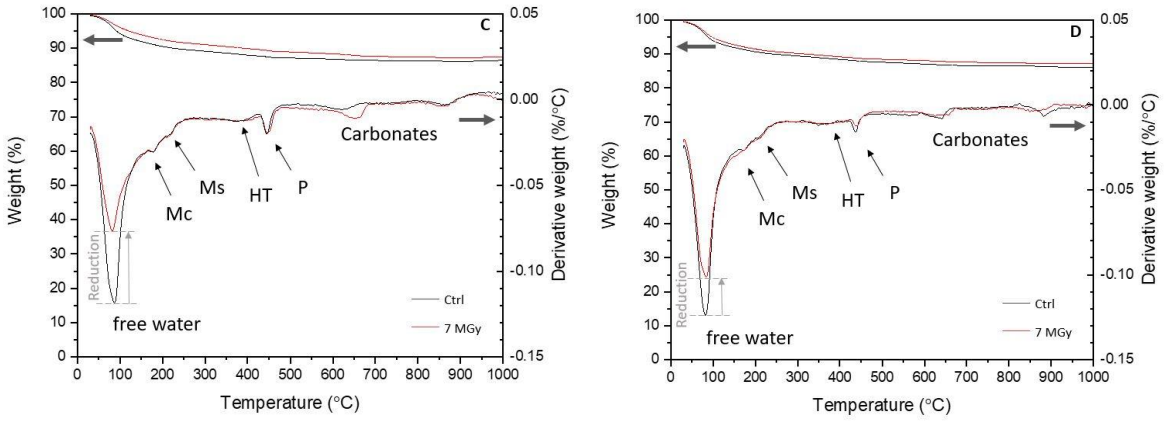

Figure 5.2. TGA data for 7 MGy and control (Ctrl) BFS:PC samples. BFS:PC ratios corresponding to each data set are: A: 3:1; B: 3.44:1; C: 5.67:1; D: 9:1. The apparent shift in the portlandite (P) peak observed in B is due to equipment undergoing repair and recalibration between testing of the two samples shown here. Mc: monocarboaluminate, Ms: monosulfoaluminate, HT: hydrotalcite, P: portlandite.

Table 5.2 Quantification of free water, portlandite, and calcium carbonate content of 7 MGy irradiated and control BFS:PC samples.

BFS:PC	Free water (%)		$Ca(OH)_2$ (%)		$CaCO_3$ (%)	
	7 MGy	Ctrl	7 MGy	Ctrl	7 MGy	Ctrl
3:1	4.5	6.3	6.0	6.3	4.5	3.5
3.44:1	5.1	5.2	6.8	6.2	4.3	6.0
5.67:1	4.0	5.8	3.8	3.3	3.6	2.2
9:1	5.2	6.0	2.4	2.7	2.5	2.6

Irradiation has caused minor changes in the both the free water quantity and phase assemblage proportions. The free water content in the four irradiated samples is reduced by between 10 – 31 % from the amount present in the respective control samples. No overall trend was identified between the quantity of free water identified and the proportion of BFS replacement, indicating that the radiation response is not severely affected by high volume substitution for this dose. The proportion of portlandite was broadly similar in irradiated and control samples. Slight increases in the portlandite quantities in the irradiated samples are considered to be insignificant given the errors associated with quantification [77], [163]. The overall trend in the control samples shows a decreasing portlandite quantity with increasing slag fraction, as observed in Chapter 4, Section 4.1.2.

There is no trend between the portlandite contents and variations in carbonate quantities of the 7 MGy irradiated samples, which, given the small differences observed and errors associated with quantification (discussed above) is to be expected. Carbonate quantities in the 7 MGy samples

decrease with increasing BFS fraction, but this is not observed in the control samples which display more variation. In both instances, carbonate quantities would be anticipated to be lower in the samples with increased BFS replacement. The lower proportions of clinker mean less carbonates from the precursor and the lower calcium content means lower Ca/Si in C-S-H and less portlandite which are thermodynamically favoured routes for carbonation in cements [195].

These minor variations indicate that the radiation response is not significantly affected by the different levels of BFS replacement at a dose of 7 MGy. The findings of the TGA results support the XRD results and indicate that preferred orientation of portlandite is not solely responsible for the reduced peak intensities observed in Figure 5.1, however the variations are minor. The differences in carbonate content observed are not linked to variations in portlandite quantities, perhaps indicating that carbonate products are being formed at the expense of an alternative phase; potentially, some limited decalcification of C-S-H is occurring. However, this may be a result of the heterogeneous nature of the samples. Given that the relative error of quantification measurements between samples has been observed to be between 5 – 10 %, the small variations observed for portlandite and carbonate quantities between samples here do not appear to represent any significant bulk effect caused by exposure to radiation [77], [163].

5.2.1.3 SEM-EDX

SEM-EDX data for all 7 MGy irradiated and control samples are shown in Figure 5.3. Identification of unreacted precursor materials (BFS and clinker) and hydration products (portlandite) from greyscale intensity information shows that similar phases are present to those identified in Chapter 4, Section 4.1.2.

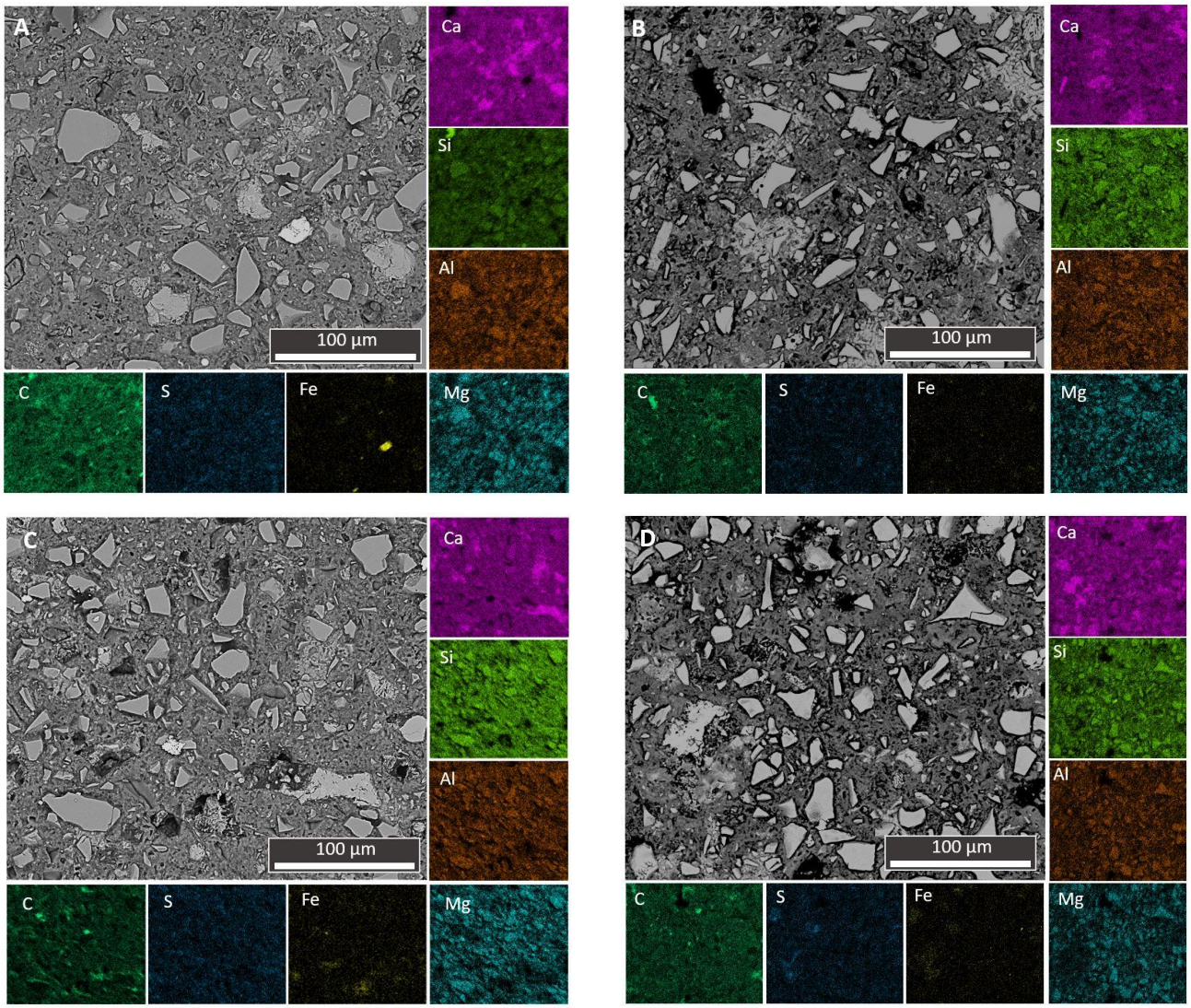

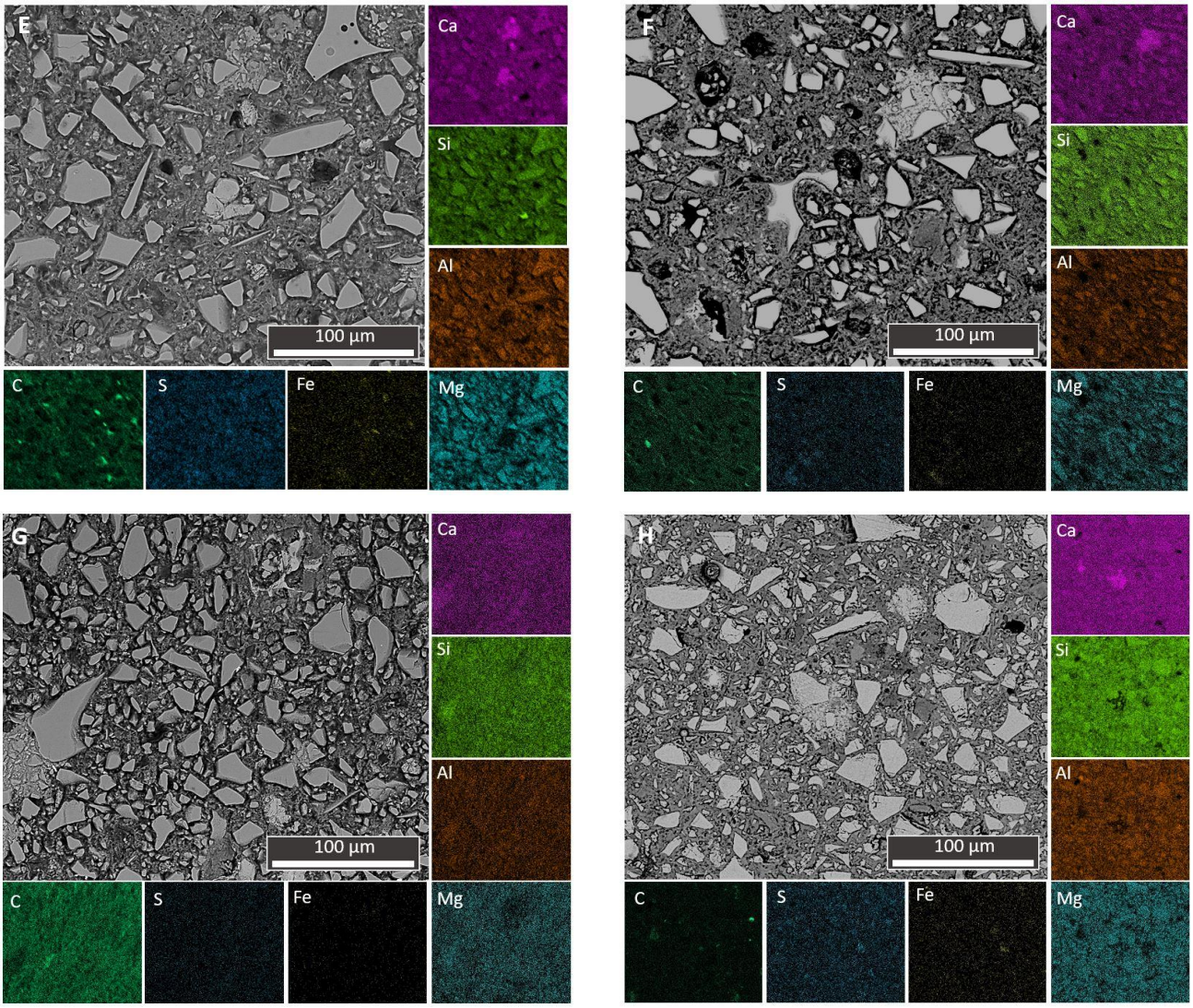

Figure 5.3 SEM images and corresponding EDX elemental maps (for selected elements as marked) for different BFS:PC blends, exposed to 7 MGy and respective control samples: A: 3:1 7 MGy; B: 3:1 control; C: 3.44:1 7 MGy; D: 3.44:1 control; E: 5.67:1 7 MGy; F: 5.67:1 control; G: 9:1 7 MGy; H: 9:1 control.

No significant variations were observed in the distribution of elements from EDX mapping after gamma exposure compared to the respective control samples; areas of portlandite are still stable within the microstructure and aluminium distribution indicates the formation of C-A-S-H. Sulfur is observed at low levels, with higher concentrations observed in hydrated matrix frequently in zones adjacent to unhydrated clinker and BFS. The sulfide that is provided to the system through hydration of BFS does not appear to have caused any variations in the local phase assemblage connected to 7 MGy irradiation and, as seen from the XRD and TGA results, no bulk alterations to the AFm/AFt balance were seen in the phase assemblage.

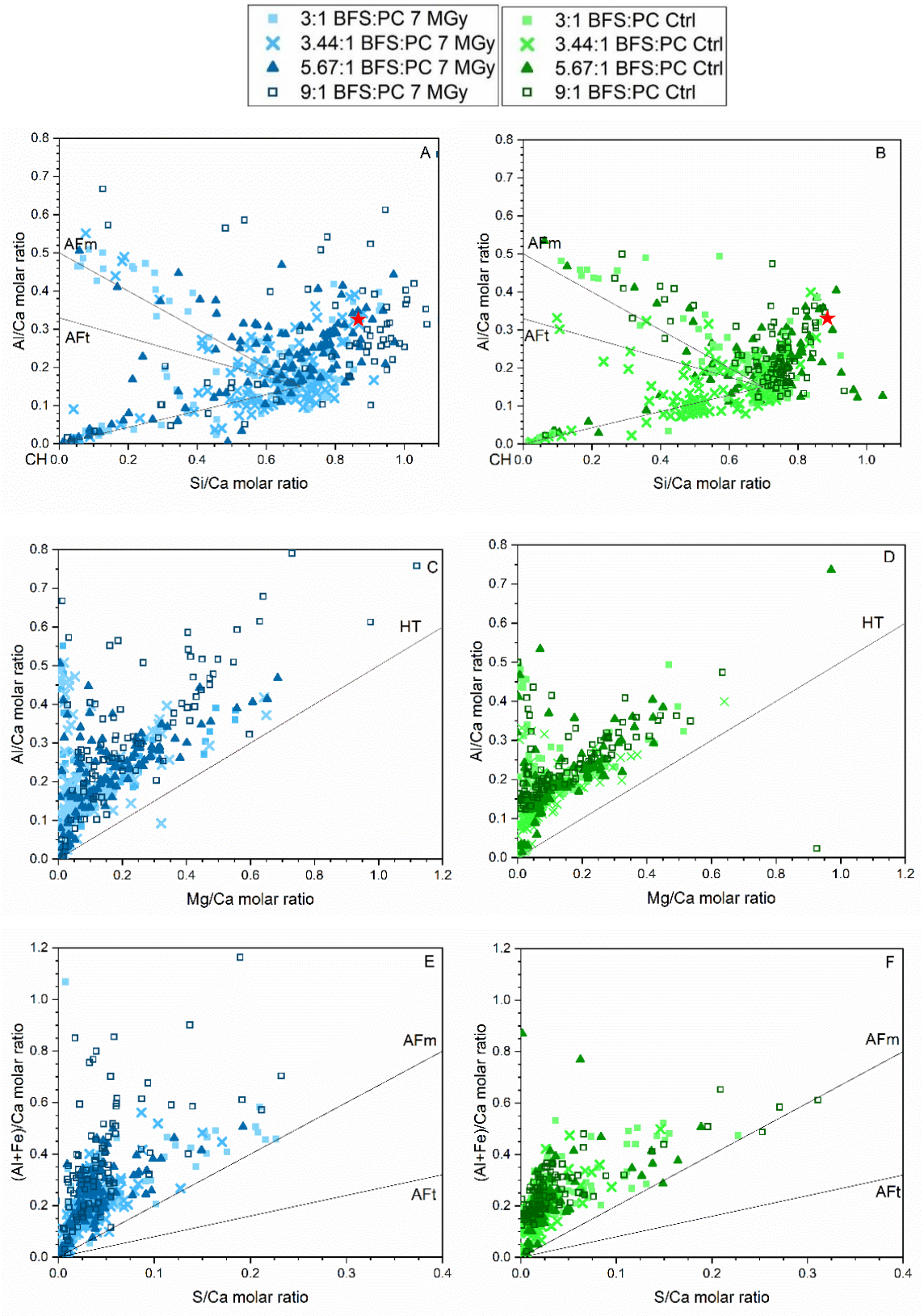

Figure 5.4 EDX point analysis data for all BFS:PC blends, for 7 MGy irradiated and control samples. A, C, E: 7 MGy; B, D, F: control. Each point sample was taken from a region that visually appeared to be binder rather than residual anhydrous phases. Composition of anhydrous BFS shown in A, B by ★ symbol. Tie lines link to the other prominent hydrate phases; CH: portlandite; AFm: monosulfoaluminate; AFt: ettringite; and HT: hydrotalcite.

Point analysis EDX data from the irradiated and control specimens shows that the Ca/Si ratio did not vary in the majority of blends as a result of the gamma exposure (Figure 5.4 A, B). Average Ca/Si ratios of approximately 1.40 (± 0.5) were observed for the 3:1 and 3.44:1 systems regardless of gamma exposure, with lower average values of 1.35 (± 0.2) for the 5.67:1 blend. A shift to lower Ca/Si ratios was observed in the 9:1 7 MGy sample compared to the control, with average values of 1.10 and 1.30 (± 0.2) observed respectively. These Ca/Si values are slightly lower than observed by Prentice et al. [218], where Ca/Si ratios from SEM EDX for 3:1 and 9:1 samples were 1.70 – 2.00 and 1.40 – 1.60 respectively, although the statistically determined Ca/Si ratios of 1.42 and 1.25 for the 3:1 and 9:1 blends from that study are more representative of the data in Figure 5.4. Similar Ca/Si values for 9:1 BFS:PC samples were found by Taylor et al. [88], where TEM analysis provided values of 1.29 (± 0.11) in 14 month old specimens.

Although this is a greater variation than was observed in the lower volume replacement blends, the results are within the error for these samples. Also, these data were more dispersed and did not show a uniform cluster denoting the likely C-S-H composition. This is likely due to the heterogeneity of the sample and the interaction volume therefore including a higher proportion of unreacted BFS [168], [210].

Minor increases in the Al/Ca ratios for the irradiated samples were observed, with the 9:1 7 MGy showing the greatest increase – a difference of 0.04, although this is within the error of the measurements. The Mg/Ca variations in the system follow the same trend as the Al/Ca ratio and are shown in Figure 5.4 C and D; slight magnesium increases are seen in the irradiated blend, with the 9:1 7 MGy sample displaying the highest average molar ratios.

The increased aluminium and magnesium contents in the point analysis of irradiated systems may indicate an increase in the overall degree of hydration of the BFS component. Exposure of cements to radiation has been linked to acceleration of hydration of unreacted components. Potential causes for this include radiation induced heating and the formation of radicals from the decomposition of pore water [98], [111], [115]. The sulfate balance of the systems does not appear to have been altered by the irradiation, as shown in Figure 5.4 E and F, which do not show an evident systematic difference between irradiated and control samples. This means that if increased hydration of the BFS fraction has occurred in the gamma exposed samples, the sulfide released does not appear to have undergone oxidation in large enough proportions to alter the phase assemblage as was found by Richardson et al. [124]; this will be revisited and expanded on in Chapter 6, Section 6.1.2. The potential increased hydration of BFS supports the XRD and TGA findings, which indicate a reduction in portlandite quantities and increased aluminate-containing hydrate phases.

5.2.1.4 MAS NMR

Multinuclear MAS NMR was completed to further investigate potential changes to the binder nanostructure. Results from ^{29}Si MAS NMR for the 3.44:1 and 9:1 blends are shown in Figure 5.7 A and B, where variations between the irradiated and control spectra can be observed for both blends. The spectra were deconvoluted to obtain information relating to the chemical environments of silicon nuclei and this was used to calculate the structural characteristics of the C-A-S-H phase. The chemical shifts for the distinct silicon environments used for the deconvolutions are shown in Table 5.3. Further details, including parameters for the deconvolution of anhydrous clinker and BFS used in this section, can be found in Chapter 3, Section 3.3.12.

Table 5.3 Site allocations used for different silicon environments in ^{29}Si MAS NMR deconvolutions. Peak width was constrained to 3.5 ± 0.2 ppm for Q^1 and Q^2 species, and > 12 ppm for Q^3 species. Based on data from [57], [82], [219].

Silicon site	Q^0	Q^1(I)	Q^1(II)	Q^2(1Al)	Q^2	Q^3(1Al)	Q^3
Chemical shift (ppm)	-74.2	-77.3	-79.4	-81.2	-84.1	-87.0	-97.5

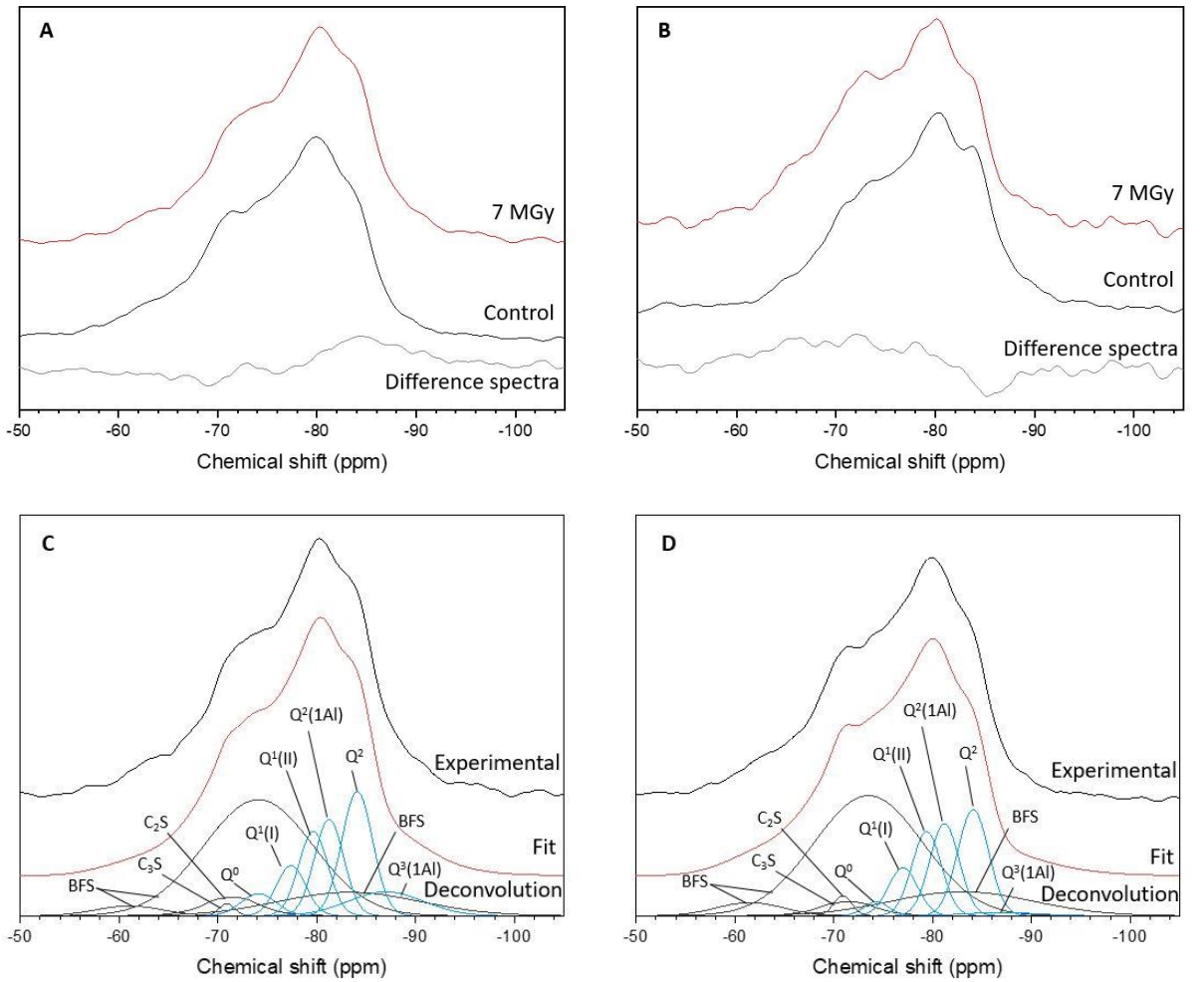

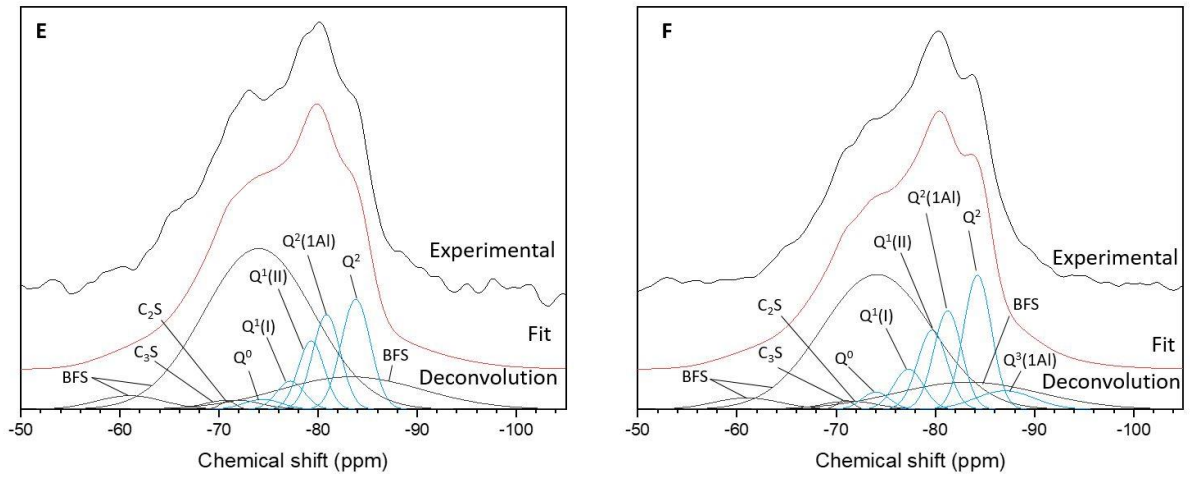

Figure 5.5 ^{29}Si MAS NMR spectra of A: 3.44:1 BFS:PC 7 MGy and control; B: 9:1 BFS:PC 7 MGy and control; and deconvolutions of: C: 7 MGy 3.44:1 BFS:PC; D: control 3.44:1 BFS:PC; E: 7 MGy 9:1 BFS:PC; F: control 9:1 BFS:PC.

When undertaking the deconvolutions, the peak positions were allowed to vary by ± 0.2 ppm of the values provided in Table 5.3. Peak width was constrained to 3.5 ± 0.2 ppm for Q^1 and Q^2 species and > 12 for Q^0 and Q^3 species. Furthermore, it was assumed that congruent reaction of C_2S, C_3S and BFS occurred, resulting in the fitted spectral shape (details provided in Chapter 3, Section 3.3.12) remaining constant but with decreasing intensity as hydration progressed. By scaling the fit of the normalised peak intensities for the anhydrous materials to the fitted hydrated spectra, semi-quantitative estimation of the degree of hydration (DoH) was calculated.

The resonance for BFS and anhydrous clinker overlap significantly, complicating assessment of the degree of hydration. Given this, for BFS hydration, the results from ^{29}Si MAS NMR were compared with independent selective dissolution testing using EDTA solution [146]. The results are shown in Table 5.4; overall agreement between the two techniques is variable. From the ^{29}Si NMR results no distinct increase in BFS DoH after gamma exposure was noted, and the selective dissolution results support this. However, the agreement between techniques for each sample is not consistent, i.e. DoH estimates from NMR are not always higher. It should be noted that the selective dissolution method used here has received criticism regarding the corrections applied (see Chapter 3, Section 3.3.3), especially at later stages of hydration, and the inherent error is at best approximately 10 % [149], [220]. Despite this, the results from selective dissolution are considered to be more representative of likely BFS hydration levels, especially in the control samples where ^{29}Si NMR estimates suggest much lower and higher levels of BFS hydration in the 3.44:1 and 9:1 systems respectively.

With the exception of these anomalous hydration levels, the measured DoH from both techniques is low compared to literature values for similar systems [82], where testing using the EDTA technique

and NMR methods produced values of > 50 % and 20 – 30 % for 3:1 and 9:1 BFS:PC samples respectively at 360 days. This may be a product of the presence of the very coarse Calumite fraction in the BFS for these systems, or the reduction in free water due to radiolytic dehydration/control heating of samples. It does not appear that the minor differences observed in the phase assemblage after irradiation are attributable to large increases in the DoH of the BFS fraction, although minor variations are noted.

Table 5.4 Degree of hydration of BFS fraction after 7 MGy exposure for 3.44:1 and 9:1 blends. Results from both EDTA dissolution method and ^{29}Si MAS NMR deconvolutions.

BFS:PC		BFS DoH (%)	
		EDTA	^{29}Si NMR
3.44:1	**7 MGy**	36 ± 5	31 ± 11
	Control	35 ± 5	22 ± 9
9:1	**7 MGy**	24 ± 6	21 ± 13
	Control	19 ± 6	30 ± 9

Table 5.5 shows the results for the degree of hydration of clinker phases. The results are broadly comparable with figures from previous studies using similar materials, although DoH of C_3S in the 9:1 blend would typically be higher than the 3.44:1 system [82]. A small increase in DoH of belite after radiation exposure was noted.

Table 5.5 Degree of hydration of clinker components after 7 MGy exposure for 3.44:1 and 9:1 blends taken from ^{29}Si MAS NMR deconvolutions.

BFS:PC		Clinker DoH (%)		
		C_3S	C_2S	Total
3.44:1	**7 MGy**	87 ± 5	50 ± 8	83 ± 13
	Control	86 ± 4	40 ± 5	81 ± 9
9:1	**7 MGy**	81 ± 6	59 ± 6	79 ± 12
	Control	83 ± 4	50 ± 4	79 ± 8

The overlapping of resonances for unhydrated material and the Q^0, Q^1 and Q^2(1Al) species complicates the deconvolution of the spectra, especially for Q^1 sites. In these spectra, two separate Q^1 environments (Q^1(I) and Q^1(II)) were identified with distinct resonances caused by the presence of monovalent or divalent charge balancing ions [53], [82], [219]. The silicon environment represented by the resonance assigned to Q^0 is currently not well understood. Previous studies have ascribed it to incongruent reaction of BFS, as the Q^0 resonance was observed to strengthen with increased BFS content and BFS DoH [82], [221], [222]. This was seen in the spectra for these samples to a certain extent: where lower resonances for BFS were observed in ^{29}Si spectra, the Q^0 resonance increased. However, Walkley et al. [223] recently expanded on the potential assignment of this resonance to Q^1(1Al) in C-(N)-A-S-H gels, which necessitates the presence of Al pairing tetrahedra (q^2(P)) in silicate chains. Whilst this is thermodynamically less favoured than the Al being located in bridging tetrahedra, sufficiently high Al concentrations will allow it [223]. This hypothesis would also fit the data observed here, and further complicates the assessment of the structural characteristics of the C-A-S-H phase as additional Q^n species would be required to fully constrain the new silicon environments which are not included in standard C-A-S-H models [49], [221].

The structural characteristics of the C-A-S-H phase were calculated from the deconvoluted spectra, as described in Chapter 3, Section 3.3.12, and the results are shown in Table 5.6. As mentioned previously, the resonances for different Q^n environments overlap which affects the values obtained from the calculations. Given this, whilst estimation of the Ca/Si ratio can be completed using this method, determinations from SEM- or TEM-EDX are considered to give a more accurate value.

Table 5.6 Structural characteristics of C-A-S-H in 7 MGy and control systems from deconvolutions of ^{29}Si MAS NMR.

BFS:PC	Ca/Si		Al/Si		MCL	
	7 MGy	Ctrl	7 MGy	Ctrl	7 MGy	Ctrl
3.44:1	1.1	1.1	0.12	0.14	6.6	5.8
9:1	1.0	1.1	0.16	0.13	7.4	6.9

As anticipated, the Ca/Si values are lower than those obtained from SEM-EDX (3.44:1; 1.4 ± 0.5, 9:1; 1.1-1.3 ± 0.2). The irradiated samples have lower Ca/Si values than the controls, although not by a significant amount. Al/Si ratios are broadly within the anticipated range, although the 9:1 control value was slightly low. No systematic variation was observed for Al/Si between the irradiated samples and the controls. The calculated MCL is higher in the irradiated blends, which suggests an increase in the

Al and Si levels within the irradiated systems. Given the DoH was estimated to have no significant difference as a result of irradiation, this seems somewhat counterintuitive and merits further discussion as follows.

Either the inherent error of the DoH testing methods has produced a false negative result, or the changes are not due to hydration variations. Carbonation of the system could account for the increased MCL through the increased polymerisation of silicate chains. This can be seen in the reduced proportion of Q^1 sites relative to Q^2 sites in the irradiated systems. Potential decalcification of the C-A-S-H tentatively links with the TGA results, where differences in carbonate content were not directly linked to a reduction in portlandite content. The presence of portlandite would likely moderate major decalcification and, as such, the effect would be more extreme in higher BFS content systems; the Q^1:Q^2 values for the 9:1 blend show lower proportions of Q^1 sites than the control sample, supporting this theory.

As carbonation progresses, the C-A-S-H system would become increasingly disordered and an increase in Q^3 sites representing crosslinking of the chains would occur, making it more polymerised. In the 7 MGy samples there was still a high proportion of Q^1 species and limited Q^3 sites, with no correlation between irradiation and Q^3 sites. This indicates that, should carbonation be the cause for the increased MCL post irradiation, it is only the earliest stages of carbonation of C-A-S-H that have occurred, where the Ca is initially removed from interlayer and defect sites [54], [197]. Given the modest differences in Ca/Si and MCL observed, this seems the most plausible scenario.

The proportions of Q species in the hydrated assemblage are shown in Table 5.7. The 9:1 system shows higher proportions of Q^2 sites compared to the 3.44:1 system, likely a product of the increased Si content in the higher replacement blend. There is a similar fraction of Al substituted sites in both the systems.

Table 5.7 Results of ^{29}Si MAS NMR with proportions of Q species shown from deconvolution of the 7 MGy spectra. The estimated uncertainty in absolute site percentages is ± 1 %.

BFS:PC		Q^0	Q^1(I)	Q^1(II)	Q^2(1Al)	Q^2	Q^3(1Al)	Q^3
3.44:1	7 MGy	6	11	19	21	29	14	0
	Control	3	14	24	26	32	2	0
9:1	7 MGy	4	9	20	30	37	0	0
	Control	4	10	20	24	32	9	0

The irradiation does not appear to have induced lasting paramagnetic effects in the samples, according to the results of the NMR analysis. It is considered that this may manifest as either a severe line broadening effect (as caused by Fe^{3+} in PC systems) or a significant increase in noise in the spectra [171], [224]. Although the 9:1 7 MGy system does show an increase in noise, this is relatively minor and no line broadening was observed. Given the samples were tested up to 2 years after radiation exposure had ceased, this is not considered surprising as recovery of any short term effects would have occurred. Having said this, there was increased variation in chemical shift position for Q^n species between 9:1 7 MGy samples and corresponding control, potentially indicating that the irradiation had a lasting effect on the charge balancing ions in the system.

The ^{27}Al MAS NMR spectra for anhydrous PC and BFS are shown in Figure 5.6. BFS contributes a broad resonance centred at 62 ppm due to the presence of Al(IV) with a minor resonance from Al(VI) at 11 ppm. The PC similarly has a strong resonance in the Al(IV) region centred at 82 ppm and the Al(VI) centred at 10 ppm.

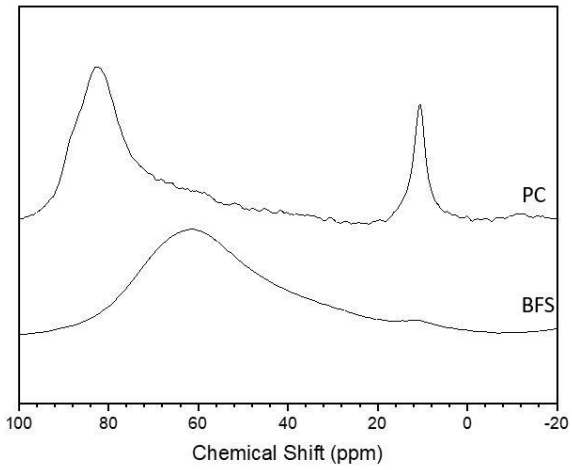

Figure 5.6 ^{27}Al MAS NMR spectra for anhydrous PC and BFS.

The ^{27}Al MAS NMR spectra from hydrated samples are shown in Figure 5.7. The presence of Al substituted into C-S-H silicate chains is shown by the presence of the peak centred at 71 ppm. A slight shoulder is present on this peak centred at approximately 63 ppm, which is considered to be due to the contribution of the unreacted BFS fraction. This peak becomes less defined after irradiation, and is more prominent in the 9:1 system.

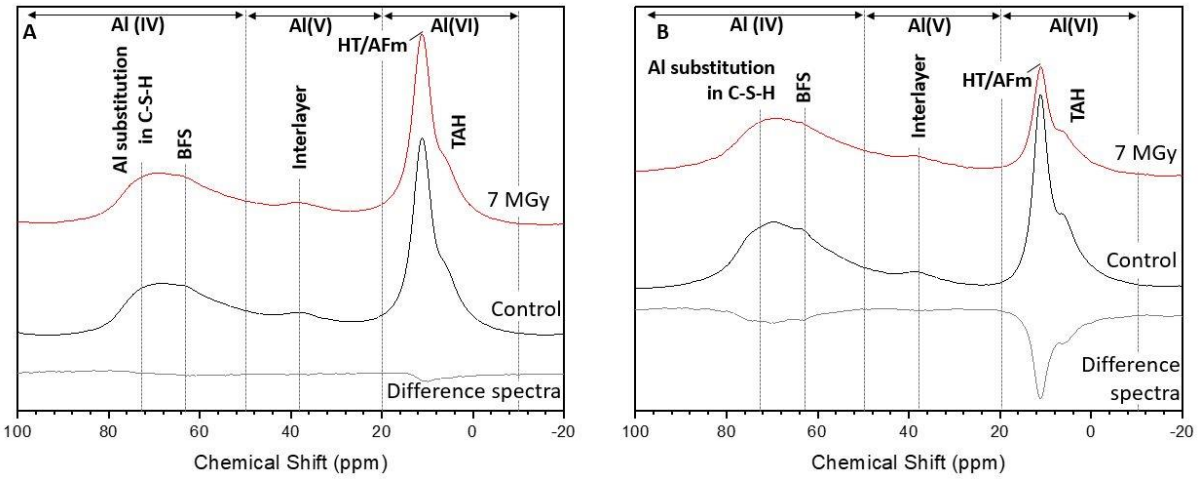

Figure 5.7 ^{27}Al MAS NMR Spectra for A: 3.44:1 BFS:PC 7 MGY and control; B: 9:1 BFS:PC 7 MGy and control.

The cause of this variation could be a reduction in intensity for the BFS resonance, an increase in the intensity for the Al substitution in C-S-H peak or a change in the local environment of the Al(IV) species. However, neither the DoH analysis or deconvolution of the ^{29}Si MAS NMR spectra support these hypotheses. This may further support the findings of Walkley et al. [223] regarding the presence of Al in pairing tetrahedra, as currently no allowance for Q^1(1Al), Q^2(2Al) or Q^3(2Al) sites is made. This limit on the allocation of Q^n(*X*Al) species in the ^{29}Si deconvolutions may mean that increased Al content in C-S-H is not fully reflected in the calculated proportions of Q species.

Interlayer charge-balancing Al is observed in the Al(V) coordination region in all samples. In the Al(VI) region, notably, there is no strong resonance observed at 13 ppm, indicating that ettringite is not present in any of the samples. This supports the findings obtained by SEM-EDX and suggests that oxidation of sulfide released from the BFS has not led to later-age ettringite formation. The resonances associated with AFm phases and hydrotalcite strongly overlap, but identification via XRD indicates that they all contribute to this peak at 11.3 ppm. The shoulder present on the right of this peak represents the third aluminate hydrate (TAH) [80]. The 7 MGy 9:1 blend shows a distinct reduction in peak intensity in the Al(VI) region, indicating a reduction in AFm and hydrotalcite phases which was not observed from any other analysis. A reduction in these phases may provide increased Al levels for substitution into C-S-H, thus increasing resonances in the Al(IV) region.

Overall, XRD, TGA and SEM-EDX have shown at most minor variations in the phase assemblage from 7 MGy gamma irradiation exposure. Minimal variations in proportions of phases have been identified but no large scale alteration to the bulk phase assemblage was observed. Assessment of the degree of hydration of BFS and PC indicates no significant increase due to radiation exposure, although the

results from other analysis may indicate a slight increase post radiation exposure. Changes in the structural characteristics of C-A-S-H were observed in the irradiated samples via ^{29}Si and ^{27}Al MAS-NMR analysis. The irradiated samples had increased MCL, which was attributed to a minor increase in carbonation of the system. An increase in the proportion of Al in C-A-S-H was also tentatively noted.

5.2.2 Microstructure

Variation in the microstructure of the grouts after gamma irradiation was assessed using SEM and MIP techniques.

5.2.2.1 SEM

SEM micrographs of the 3.44:1 and 9:1 systems are shown in Figure 5.8 to provide an overview of radiation response of samples with different BFS contents.

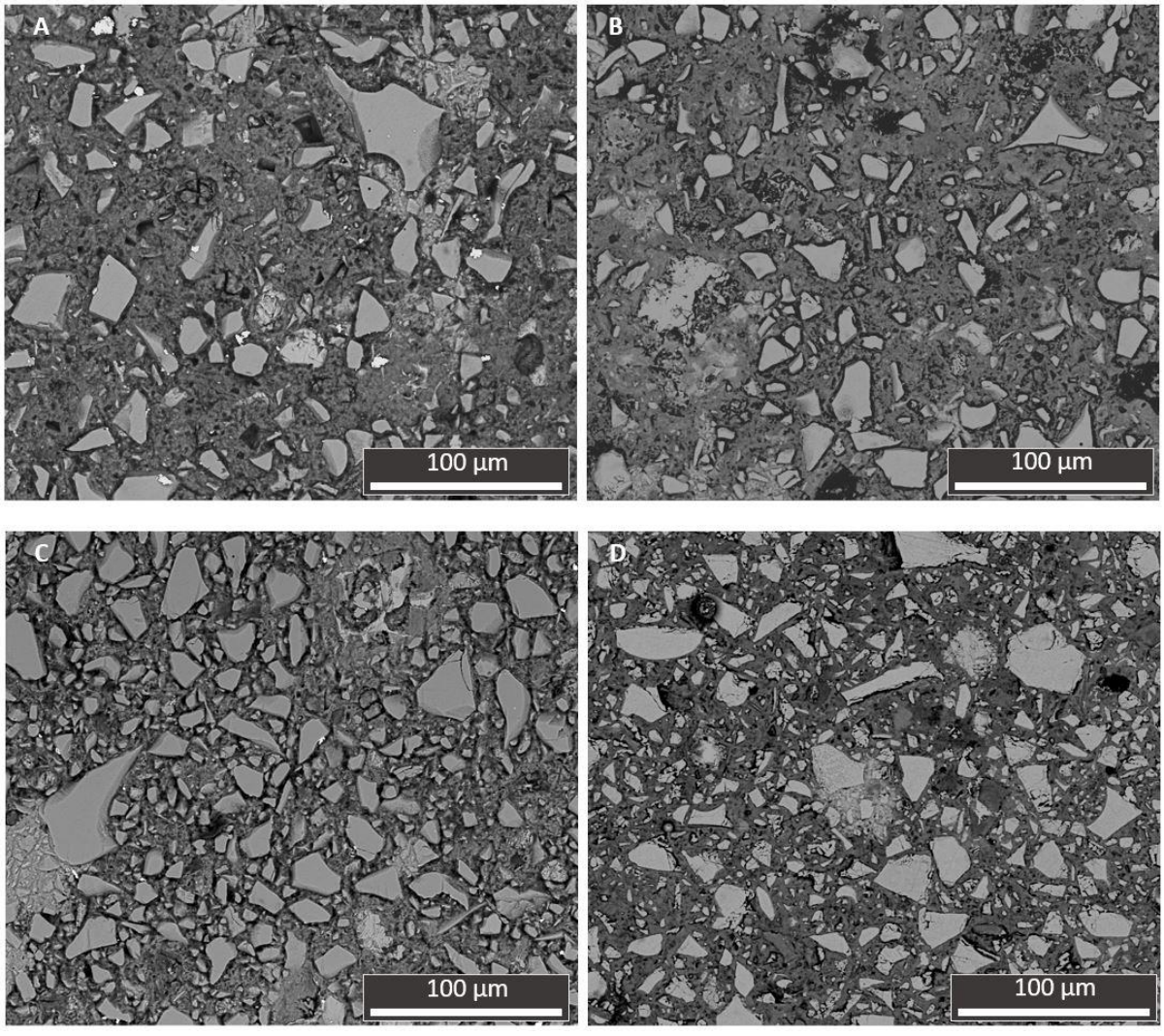

Figure 5.8 SEM micrographs of A: 3.44:1 BFS:PC 7 MGy; B: 3.44:1 BFS:PC control; C: 9:1 BFS:PC 7 MGy; D: 9:1 BFS:PC control

Little variation is observed in the microstructures of the 7 MGy irradiated (Figure 5.8 A,C) and control (Figure 5.8 B,D) samples. Similar textural development to that described in Chapter 4, Section 4.1.3 was observed. No large scale cracking or defects were observed, indicating that the radiolytic decomposition of the pore fluid did not lead to overpressure of closed porosity in the systems.

5.2.2.2 MIP

Changes in the porosity and pore size distribution were assessed using MIP, and the results are shown in Table 5.8. Increased total accessible pore volume was observed in all irradiated samples, which may indicate that cracking has occurred on a micro- or nanoscale within the matrix. Irradiation has been linked with a decrease in overall average porosity in previous studies, where carbonate products have infilled larger pores [95], [106], [109]. However, no large scale carbonation was observed in the phase assemblage for these systems (see Sections 5.2.1.1 and 5.2.1.2) and, as such, no infilling of pores was observed.

Table 5.8 Porosity measurements for all 7 MGy irradiated samples and corresponding controls obtained through MIP analysis

BFS:PC	Total accessible pore volume (%)		Critical pore entry radius (nm)		Threshold pore entry radius (nm)	
	7 MGy	Control	7 MGy	Control	7 MGy	Control
3:1	26 ±2	21 ±2	5	9	14	12
3.44:1	24 ±2	19 ±2	6	9	18	13
5.67:1	36 ±2	26 ±2	11	6	16	12
9:1	26 ±2	25 ±2	15	18	20	22

The changes in critical pore entry radius and the threshold pore entry radius values (see Chapter 3, Section 3.3.6 for definitions) demonstrate that alterations to the pore entry size distribution as a whole have occurred [158]. As the threshold pore entry radius measures the smallest continuous pore entry diameter present throughout the interconnected pore volume, an increase in this value indicates an overall widening of the narrowest pore entry radius in the sample. As it is the measurement of something that is geometrically continuous throughout the sample, this widening is present throughout the sample. Given this, an increase in threshold pore entry radius may represent an increase in features such as crack – these would provide geometrically continuous mercury intrusion pathways that are wider than the pores in the sample. As such, the increase in threshold

pore entry radius shown in Table 5.8 may indicate cracking as a cause for the increased accessible pore volume.

5.2.3 Mechanical properties

Pulse velocity testing was completed on each section of the monolith for all blends which created 3 test sections for each irradiated and control system. Testing was completed from receipt of the irradiated samples to 94 weeks in order to assess if radiation affected the aging characteristic of the materials.

UPV values were higher in the 7 MGy irradiated samples compared to the control samples, which does not support the increased porosity observed from MIP in the Section 5.2.2.2. The magnitude of variation in the UPV ranges was between 0.3 – 4.0 % and this does not scale linearly with the observed increase in porosity either. These discrepancies are likely due to the limitations inherent in the testing techniques, such as the ink bottle effect for MIP and limit of detection for small defects from UPV.

The precision of this technique was discussed in Chapter 4, Section 4.1.4, with average values of ± 2 % for all systems observed which is similar to ASTM values for path lengths > 0.3m. Accuracy of the results relates to how far the results are shifted from the true value, which is unknown in this testing. This is especially true for the accuracy of the estimated compressive strength and material properties. Given this, it was considered that assessment of these quantities could only be completed using comparison to the global mean and by assessing causes for potential over /under-estimation.

Figure 5.9 shows the average UPV values for all irradiated and control monolith sections at each testing point. For the bulk of the data, the global mean values of the irradiated samples have higher UPV values (as discussed above). However, the whiskers (representing the maximum and minimum values obtained from each test section) show that there is no significant difference at most testing points.

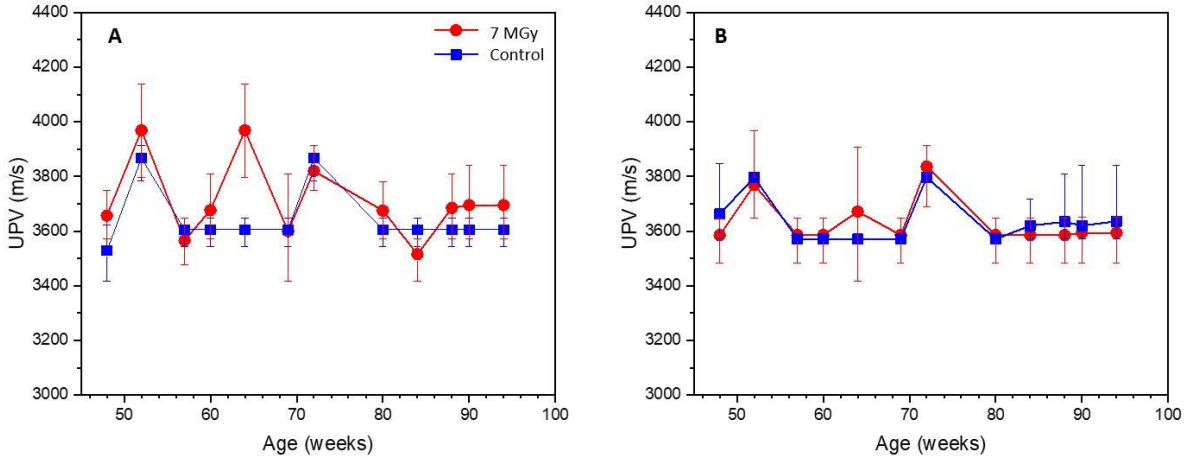

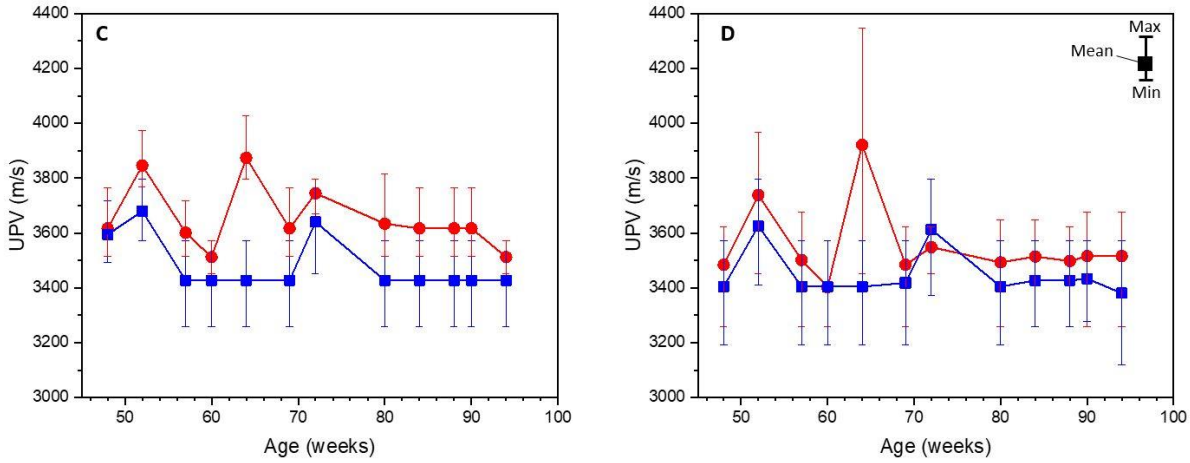

Figure 5.9 Comparison of UPV global mean values for 7 MGy and control systems. A: 3:1 BFS:PC, B: 3.44:1 BFS:PC, C: 5.67:1 BFS:PC, D: 9:1 BFS:PC. Data from 52, 64 and 72 weeks are considered to have been affected by local environmental conditions.

Variations in UPV over time are observed, and these are considered to be due to changes in local humidity and temperature. Samples were stored wrapped in foil and sealed within polythene bags; an environment chamber was not used as initially replication of the conditions of the samples awaiting irradiation (14 and 20 MGy) was desired and after this for continuity purposes. Increases in UPV from median levels at discrete testing points were noted across all systems at 52, 64 and 72 weeks, which may be due to an environmental influence in the laboratory affecting measurements on all samples on those days. The 7 MGy samples appear more susceptible to these deviations. This may be due to radiolytic dehydration making them more sensitive to changes in local conditions.

Systematic variation in UPV over time for each sample was minor, indicating limited change in the elastic modulus during the testing period. Estimation of the compressive strength was completed using the relationships outlined in Chapter 4, Section 4.1.4, and calculation of the stiffness constant (K) and dynamic modulus of elasticity (E_d) was completed using equations (5.1) and (5.2):

$$K = \rho c^2 \tag{5.1}$$

$$E_d = \rho c^2 \frac{(1+v)(1-2v)}{(1-v)} \tag{5.2}$$

where c = pulse velocity (m/s), ρ = density (kg/m^3) and v = Poisson's ratio [225]. Estimation of these material properties was undertaken to try and understand if any alteration to the deformation potential to the material besides compressive strength was caused by irradiation. The results are

shown in Table 5.9, where a density of 2000 kg/m^3 and Poisson's ratio of 0.28 were used for all samples; these are average values taken from [32] and are intended to allow assessment of comparative trends.

Table 5.9 Summary of average change in material properties after 7 MGy exposure from UPV measurement (compared to control sample). Density of 2000 kg/m^3 and Poisson's ratio of 0.28 were assumed [32].

BFS:PC	UPV change (%)	Compressive strength change (%)	K change (%)	E_d change (%)
3:1	+1.7	+10.0	+3.5	+3.5
3.44:1	-0.2	-1.0	-0.6	-0.6
5.67:1	+4.3	+15.4	+8.7	+8.7
9:1	+2.9	+19.0	+6.1	+6.1

Relatively minor changes to the UPV values for the samples compound into higher overall differences for estimated material properties. From these results, none of the changes indicate significant reduction to the material properties. In fact, an overall improvement in material properties is outlined. The highest changes in compressive strength for the 5.67:1 and 9:1 blends equate to maximum increases of 6 and 8 MPa. Given these materials are expected to have compressive strengths > 45 MPa, and for waste management there are currently no specified compressive strength limits for wasteforms in place, these variations are considered interesting but not significant. As such, this level of radiation exposure is not considered to induce meaningful differences in the bulk material.

5.3 Irradiation to 14 MGy

Irradiation of these samples began at 16 weeks and was undertaken for 12 weeks, making the samples 28 weeks old when exposure ceased.

5.3.1 Phase assemblage

5.3.1.1 XRD

Diffraction patterns for all systems after exposure to 14 MGy irradiation are shown in Figure 5.10. Similar tendencies to those outlined in Section Phase assemblage were observed in terms of variable portlandite peak intensities, although no systematic overall trend was observed. Similarly, increased peak intensities for monosulfoaluminate were observed after 14 MGy exposure, although this was not a uniform increase across all systems. The increased radiation dose does not appear to have altered the scale of the differences observed compared to the 7 MGy data presented in Section 5.2.1.

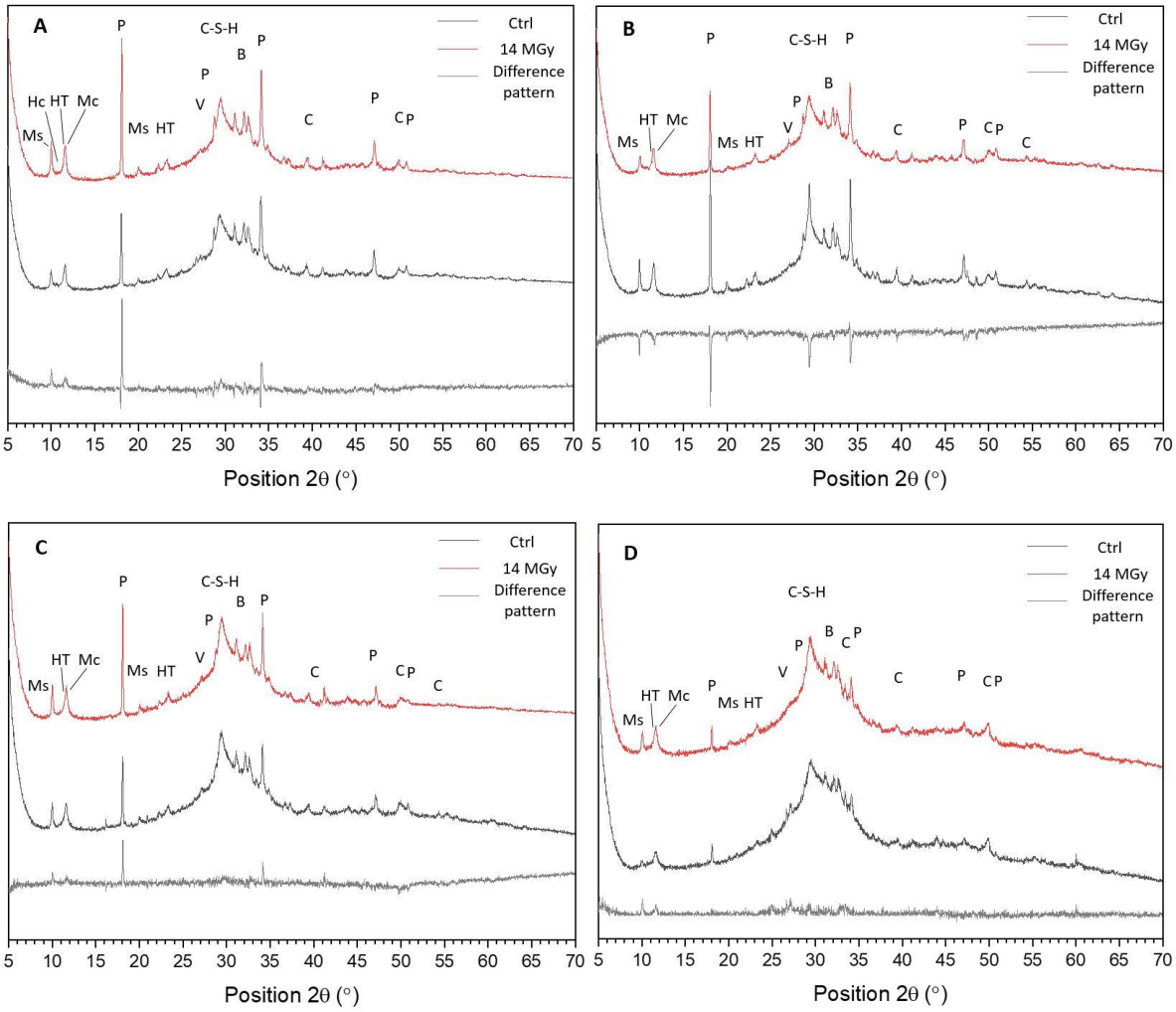

Figure 5.10 X-ray diffractograms of hydrated BFS:PC blends irradiated to 14 MGy and the corresponding control (Ctrl). BFS:PC ratios corresponding to each data set are: A: 3:1; B: 3.44:1; C: 5.67:1; D: 9:1. Ms: monosulfoaluminate, HC: hemicarboaluminate, HT: hydrotalcite, Mc: monocarboaluminate, V: vaterite, P: portlandite, B: belite (C_2S), C: calcite.

Peak intensities for calcite do not appear to have been affected by the radiation exposure. Small reflections associated with the vaterite polymorph of $CaCO_3$ were present in the diffraction patterns for the irradiated and control systems. As outlined in Chapter 2, Section 2.5.1, vaterite persistence in phase assemblages is frequently associated with irradiation-induced drying. However, no distinct trend in peak intensity and irradiation exposure is seen in the results here. Also, the presence of vaterite does not appear to correspond with reduced reflections for calcite. The XRD results do not indicate bulk alterations to the phase assemblage as a result of 14 MGy exposure.

5.3.1.2 TGA

Figure 5.11 shows the TGA results for all 14 MGy and control systems; a clear reduction in the free water content of the irradiated systems was observed, as seen in the 7 MGy samples (see Section 5.2.1.2). Results for the 9:1 system appear to show uncharacteristically low free water contents and an unusual weight loss profile was observed. The reason for this is unknown. Increased heating of these samples would be a likely cause, however all control samples were temperature treated together and, as no other samples show the same trend, this is not easily explained. The 9:1 14 MGy irradiated sample displayed greater weight loss in regions associated with hydrate phases. The increased weight loss does not appear at temperatures > 500 °C, therefore is not the result of radiation-induced carbonation, and so again a potential increase in hydration of BFS and PC components is indicated.

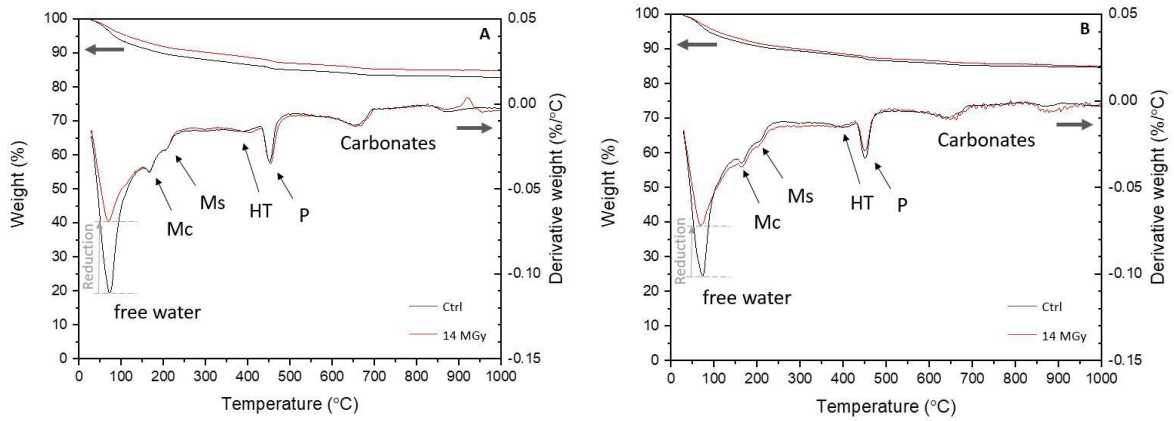

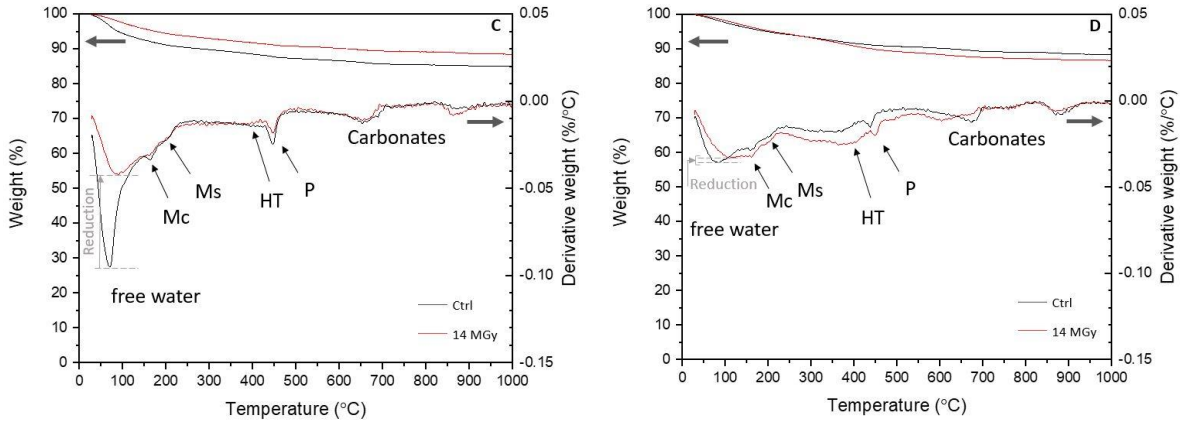

Figure 5.11 TGA data for 14 MGy and control (Ctrl) BFS:PC samples. BFS:PC ratios corresponding to each data set are: A: 3:1; B: 3.44:1; C: 5.67:1; D: 9:1. Mc: monocarboaluminate, Ms: monosulfoaluminate, HT: hydrotalcite, P: portlandite.

Testing of these samples was completed at 39 weeks and quantification of the results is shown in Table 5.10.

Table 5.10 Quantification of free water, portlandite and carbonate content of 14 MGy irradiated and control BFS:PC samples.

BFS:PC	Free water (%)		$Ca(OH)_2$ (%)		$CaCO_3$ (%)	
	14 MGy	Ctrl	14 MGy	Ctrl	14 MGy	Ctrl
3:1	5.0	6.3	6.4	4.8	4.4	4.3
3.44:1	4.6	5.8	4.6	5.9	4.1	3.5
5.67:1	2.5	5.5	4.4	5.3	5.0	4.9
9:1	1.8	2.4	4.7	3.5	5.0	4.9

Overall, the free water contents of the control samples are not significantly different from those for the 7 MGy samples (see Table 5.2) with the exception of the 9:1 system (discussed above). The reduction in free water content (relative to the control samples) is between 20–23 %, although a larger relative reduction of 55 % was observed in the 5.67:1 system. However, no overall trend in the proportion of water loss and increased fraction of BFS was noted.

Portlandite quantities were higher than observed for the 7 MGy exposure (see Table 5.2), which is surprising given the increased age of these samples. This may be a product of the increased curing that occurred prior to irradiation exposure; more free water allowed increased hydration. Indeed, persistence of portlandite in these samples is unusual as significant reduction/disappearance of this

phase due to its consumption in ongoing slag hydration has been noted from experimental studies and is anticipated from thermodynamic modelling [82], [175], [226], [227]. No relationship between variations in portlandite content and radiation exposure were observed after 14 MGy exposure.

Quantified carbonate contents indicate that the 14 MGy irradiated samples (Table 5.10) have increased carbonate levels compared to the controls. This increase does not link with the changes in portlandite quantities, similar to the results from the 7 MGy samples, and so further support the potential decalcification of C-S-H in the irradiated cements. Although the increase in carbonate content in the 14 MGy samples compared to the controls is very small, the impact it may have on the cement properties requires investigation.

5.3.1.3 SEM-EDX

SEM-EDX data for all the 14 MGy systems (Figure 5.12) shows very similar data to the 7 MGy systems (see Section 5.2.1.3). The elemental mapping does not show any variations in the distribution of elements after gamma exposure up to 14 MGy. No increase in the size of BFS reaction rims was observed and residual unhydrated clinker was seen in all systems together with zones of portlandite. Radiation exposure up to 14 MGy does not appear to have had a significant effect on the bulk chemistry of the cementitious matrices, supporting the results from XRD and TGA.

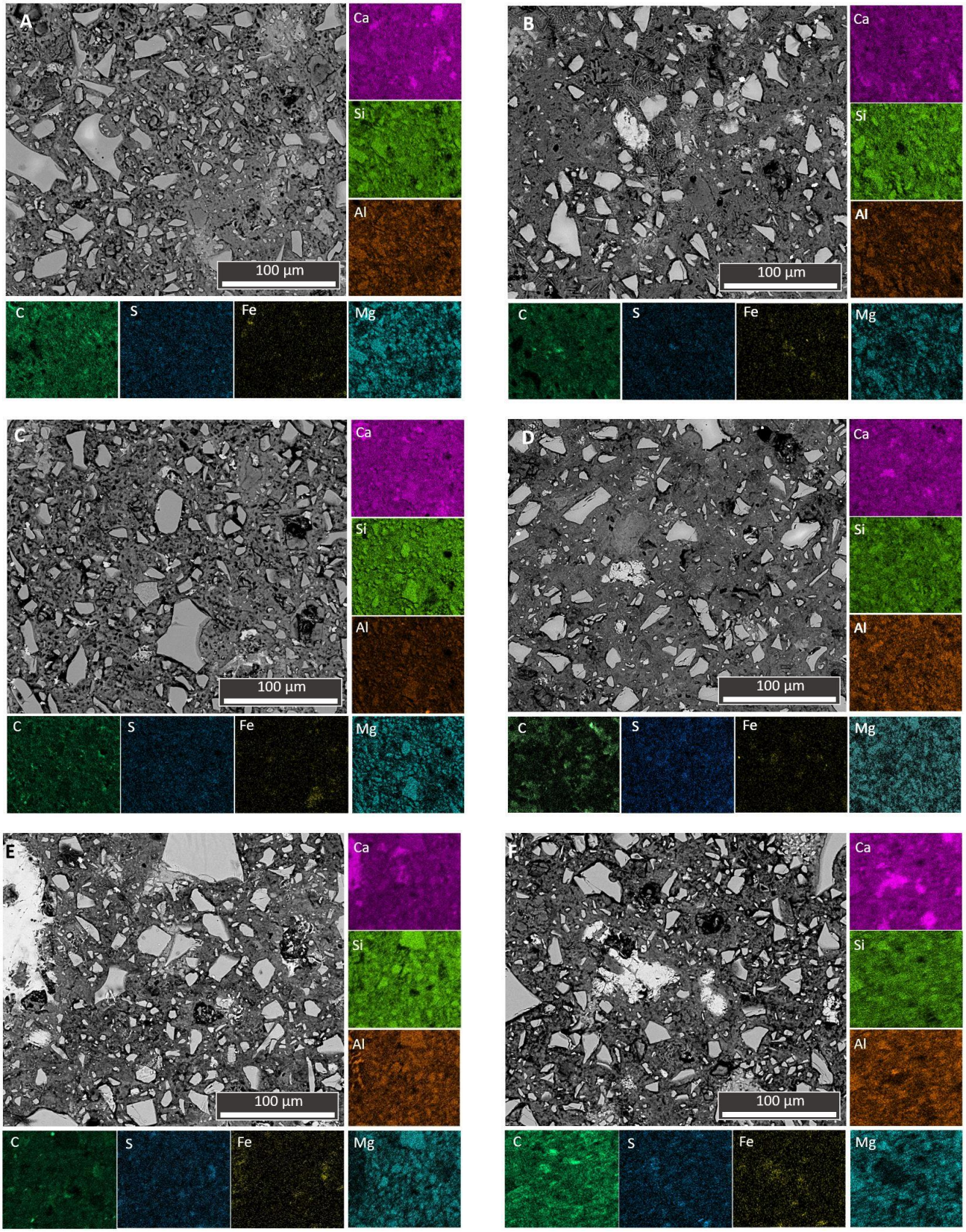
A
Ca
Si
Al
100 µm
C
S
Fe
Mg
B
Ca
Si
Al
100 µm
C
S
Fe
Mg
C
Ca
Si
Al
100 µm
C
S
Fe
Mg
D
Ca
Si
Al
100 µm
C
S
Fe
Mg
E
Ca
Si
Al
100 µm
C
S
Fe
Mg
F
Ca
Si
Al
100 µm
C
S
Fe
Mg

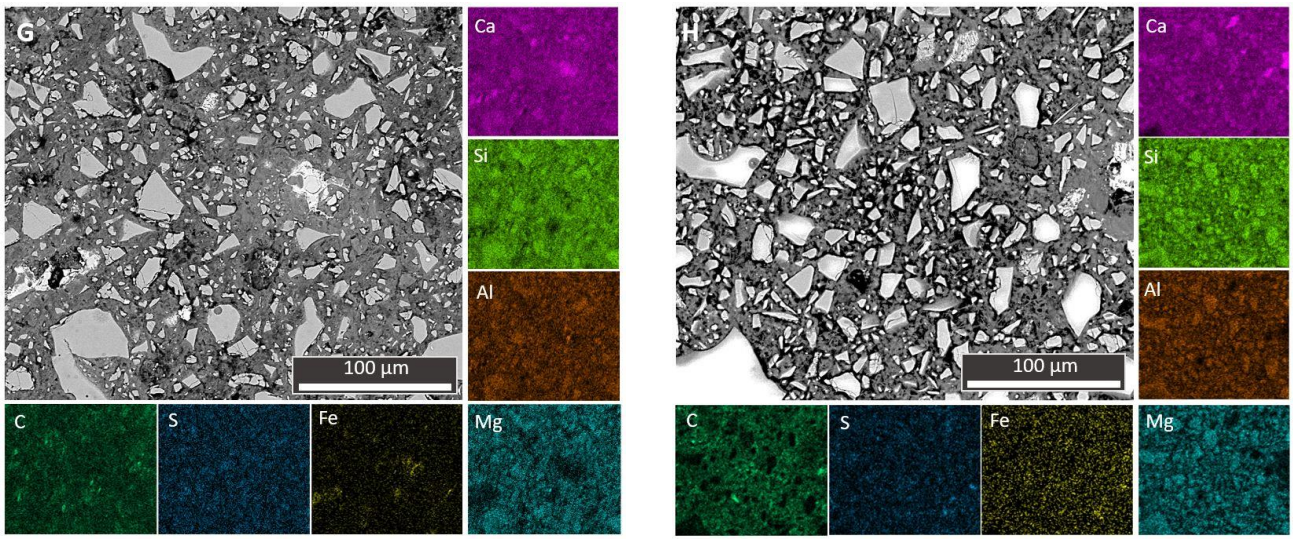

Figure 5.12 SEM images and corresponding EDX elemental maps (for selected elements as marked) for different BFS:PC blends, exposed to 14 MGy and respective control samples: A: 3:1 14 MGy; B: 3:1 control; C: 3.44:1 14 MGy; D: 3.44:1 control; E: 5.67:1 14 MGy; F: 5.67:1 control; G: 9:1 14 MGy; H: 9:1 control.

Point analysis showed that there was little variation in the Ca/Si ratio for all blends after radiation exposure (Figure 5.13 A, B). The average Ca/Si ratios determined for the 3:1, 3.44:1 and 5.67:1 samples were approximately 1.43 ± 0.5, 1.40 ± 0.5 and 1.35 ± 0.3 respectively. The data for the 9:1 system displayed a much more constrained grouping than in the 7 MGy samples (Figure 5.4 A), giving a C-S-H composition with Ca/Si of 1.3 ± 0.2 for irradiated and control samples.

No distinct variations were observed in the Al/Ca or Mg/Ca values post-irradiation at 14 MGy (Figure 5.13 C, D). The sulfate balance similarly appears unaffected, with molar ratio plots showing extremely similar data for all samples (Figure 5.13 E, F). Given this, it appears that the 14 MGy data does not show the increased Al and Mg contents observed after 7 MGy (Figure 5.4 C), despite the increased radiation dose. This could indicate that the trends at lower dose were not significant. Alternatively, the reduced impact on aluminium and magnesium molar contents may be a product of the 14 MGy samples being 7 weeks older (see Table 5.1) when irradiation exposure began and therefore having a higher degree of hydration and lower free water content due to increased curing before irradiation. This would result in lower amounts of unreacted precursor together with less free water available to hydrate. Lower proportions of free water would also limit the amount of radical formation from radiolytic decomposition, which has been linked to accelerated hydration. However, the differences in DoH of the BFS and PC components in this 7 week range (between 9 and 16 weeks) would be < 8 % and < 2 % respectively [82], [198]. This indicates it is likely to be the free water content that drives the potential increased hydration under irradiation, rather than the proportion of unhydrated precursor.

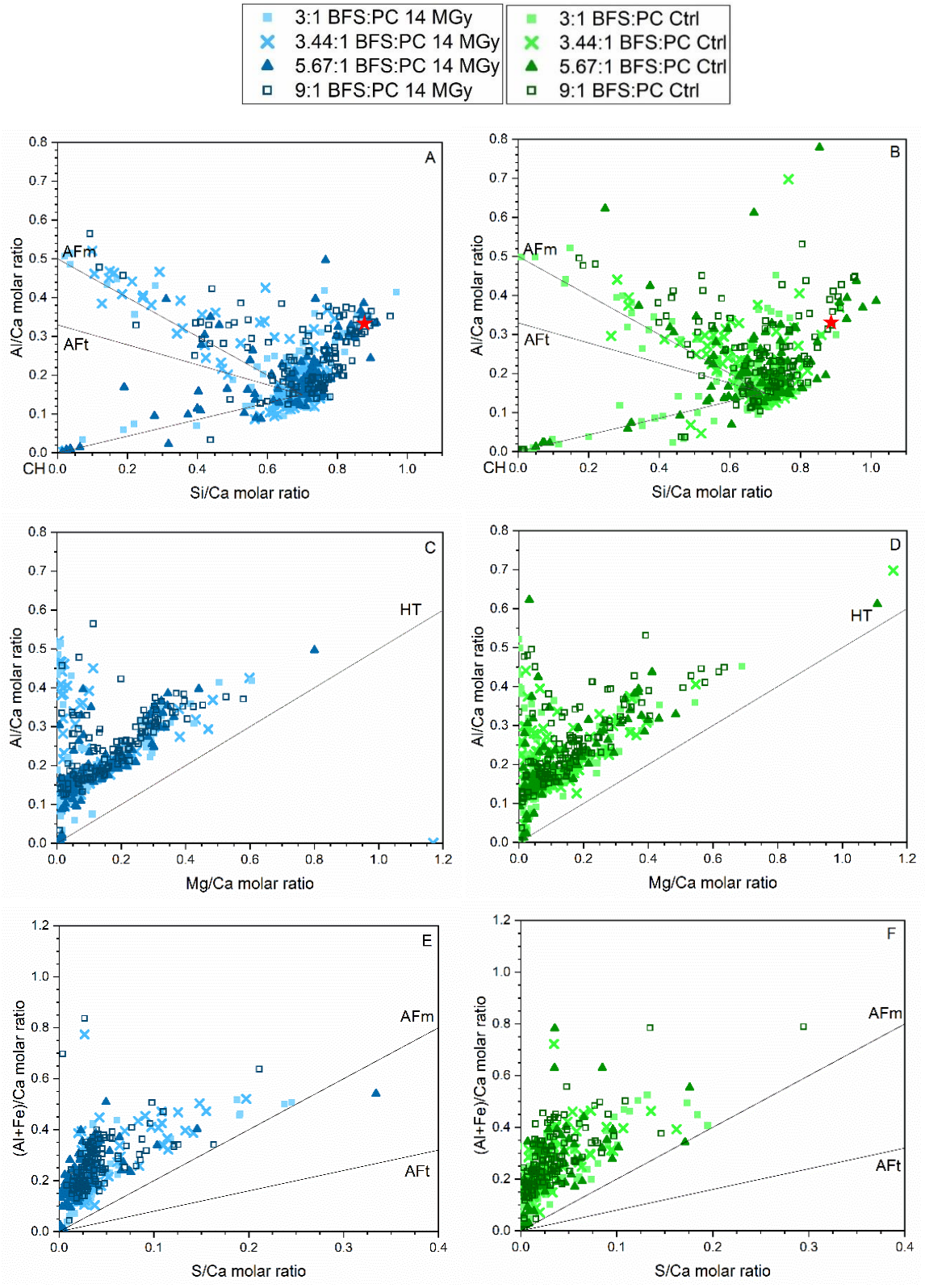

Figure 5.13 EDX point analysis data for all BFS:PC blends, for 14 MGy irradiated and control samples. A, C, E: 7 MGy; B, D, F: control. Each point sample was taken from a region that visually appeared to be binder rather than residual anhydrous phases. Average composition of anhydrous BFS shown in A, B by ★ symbol. Tie lines link to the other prominent hydrate phases; CH: portlandite; AFm: monosulfoaluminate; AFt: ettringite; and HT: hydrotalcite.

5.3.1.4 MAS NMR

The composition of the C-S-H was further probed using ^{29}Si and ^{27}Al MAS NMR. The difference spectra in Figure 5.14A, B show that there is limited variation in the 3.44:1 system after irradiation, with minor differences observed in the 9:1 blend; these are centred around -70 ppm and -80 ppm, so likely relate to BFS content and Q^2 species.

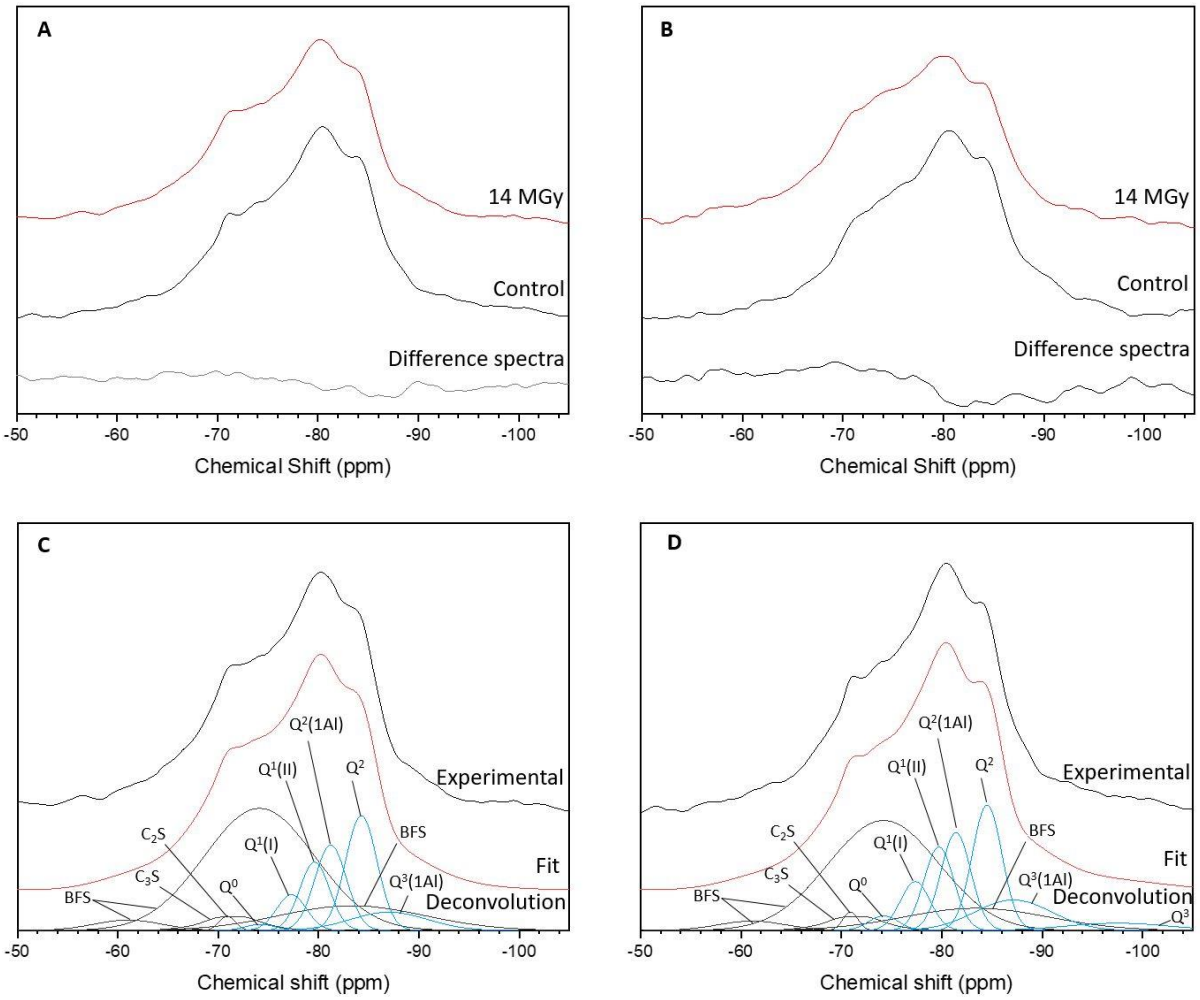

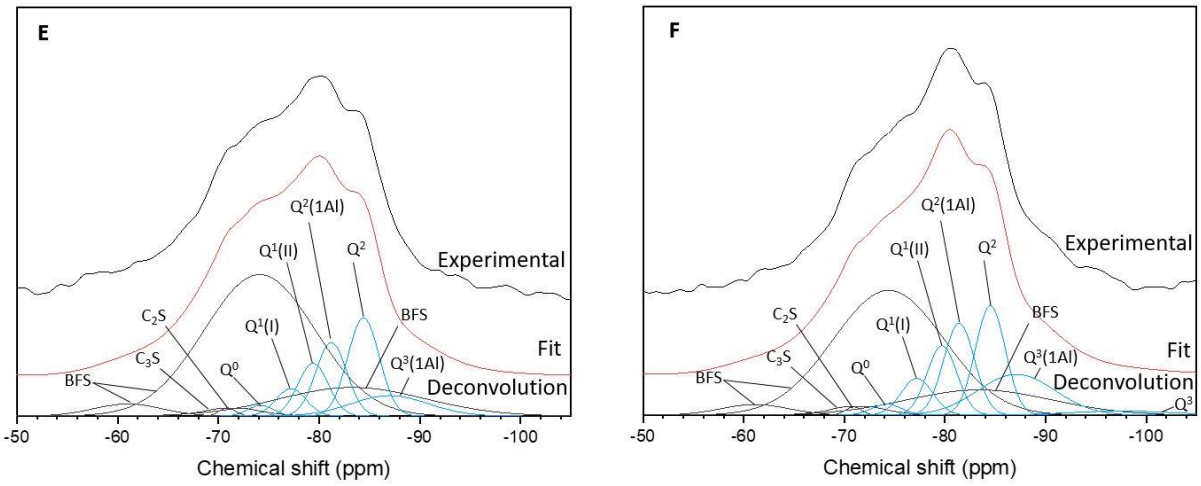

Figure 5.14 ^{29}Si MAS NMR spectra of A: 3.44:1 BFS:PC 14 MGy and control; B: 9:1 BFS:PC 14 MGy and control and deconvolution of C: 14 MGy 3.44:1 BFS:PC; D: control 3.44:1 BFS:PC; E: 14 MGy 9:1 BFS:PC; F: control 9:1 BFS:PC.

Selective dissolution of the control samples produced similar BFS DoH values to those found in the control samples corresponding to the 7 MGy irradiation dose, indicating that the increased duration at elevated temperature did not affect hydration. Comparison of the BFS DoH determinations obtained from the two techniques is shown in Table 5.11. Overall hydration levels were low for the level of BFS replacement, as seen in the 7 MGy samples; however, in the 14 MGy samples, the agreement between DoH values from the two testing methods was poor, likely due to the inherent errors associated with both techniques.

Evaluation of the values obtained using the EDTA method showed no clear trend in DoH after radiation exposure. The results from ^{29}Si MAS NMR are considered suspect, as similar levels of BFS hydration were observed in both systems regardless of BFS replacement level. Given the variability of the data, together with the inherent errors associated with testing methods, and increasing maturity of samples pre-irradiation, the accurate assessment of BFS DoH with increasing radiation dose becomes increasingly troublesome.

The EDTA testing results for the 3.44:1 14 MGy system show an increase in DoH of BFS compared to the control and 7 MGy values; however, this is within the known 10 % error of the testing technique [149], [220]. The 9:1 14 MGy results showed 7 % difference between the control and irradiated samples and a reduction in DoH of 13 % when compared to the 7 MGy data shown in Table 5.4. This determination is therefore considered an unrealistically low value for a sample of this age. From all the previous analysis of the phase assemblage, the results indicate broadly similar BFS DoH in the irradiated and control systems; this would especially support the SEM-EDX results. Given the spread in the data here, no firm conclusions can be reached.

Table 5.11 Degree of hydration of BFS fraction after 14 MGy exposure for 3.44:1 and 9:1 blends. Results from both EDTA dissolution method and ^{29}Si MAS NMR deconvolutions

BFS:PC		BFS DoH (%)	
		EDTA	^{29}Si NMR
3.44:1	14 MGy	42 ± 5	24 ± 5
	Control	36 ± 5	31 ± 5
9:1	14 MGy	11 ± 8	26 ± 8
	Control	18 ± 6	36 ± 7

Analysis of the DoH of clinker within the systems (Table 5.12) shows similar levels of C_3S hydration, and slightly higher belite hydration compared to Table 5.5. This is likely to be due to the extended curing time prior to radiation exposure. No variation was noted when comparing the irradiated samples to their controls, with the exception of increased belite hydration in the 3.44:1 14 MGy sample.

Table 5.12 Degree of hydration of clinker components after 14 MGy exposure for 3.44:1 and 9:1 blends taken from ^{29}Si MAS NMR deconvolutions.

BFS:PC		Clinker DoH (%)		
		C_3S	C_2S	Total
3.44:1	14 MGy	86 ± 2	64 ± 5	84 ± 7
	Control	86 ± 2	57 ± 6	83 ± 8
9:1	14 MGy	83 ± 2	55 ± 4	80 ± 6
	Control	81 ± 3	56 ± 4	78 ± 7

The C-A-S-H structural characteristics were calculated from deconvolution of the ^{29}Si MAS NMR spectra and the results are shown in Table 5.13. Ca/Si ratios are comparable to the values observed for the 7 MGy samples (see Table 5.6) and are similarly lower than those found in the SEM-EDX analysis (Figure 5.13) for reasons previously discussed. Al/Si ratios are broadly consistent for all the samples after 14 MGy irradiation, regardless of BFS replacement fraction. Irradiation exposure has not impacted the molar ratio values for either of the systems explored here. A minor increase in MCL was observed, however, this was not as significant as seen previously in the 7 MGy samples. This supports

results of the DoH testing being broadly similar for both systems, as similar levels of DoH would cause similar MCL.

Table 5.13 Structural characteristics of C-A-S-H in 14 MGy and control systems from deconvolutions of ^{29}Si MAS NMR.

BFS:PC	Ca/Si		Al/Si		MCL	
	14 MGy	Ctrl	14 MGy	Ctrl	14 MGy	Ctrl
3.44:1	1.1	1.1	0.13	0.12	7.1	7.1
9:1	1.0	1.1	0.13	0.12	8.1	7.9

The onset of minor carbonation (as discussed in Section 5.2.1.4) may also be the cause of the observed differences in MCL. The same reduction in the Q^1:Q^2 ratio was observed, and higher proportions of carbonate were seen from the TGA data for the irradiated systems. However, the control samples possess higher proportions of Q^3 sites, indicating an increased degree of polymerisation.

Similar trends to the 7 MGy systems were observed (MAS NMR), with an apparent decrease in the BFS resonance and increased Q^0 proportions, however the cause for this cannot be elucidated upon further from the current data.

The proportions of Q species in the hydrated assemblage are shown in Table 5.14. An increase in Q^2 quantities was observed after 14 MGy irradiation for both 3.44:1 and 9:1 samples. The proportion of Al linked tetrahedra was the same in the 3.44:1 irradiated and control sample. A higher proportion of Al sites was observed in the 9:1 blend; however, the quantity was reduced in the irradiated systems.

Table 5.14 Results of ^{29}Si MAS NMR with proportions of Q species shown from deconvolution of the 14 MGy spectra. The estimated uncertainty in absolute site percentages is ± 1 %.

BFS:PC		Q^0	Q^1(I)	Q^1(II)	Q^2(1Al)	Q^2	Q^3(1Al)	Q^3
3.44:1	14 MGy	2	10	19	25	33	13	0
	Control	3	11	18	21	27	17	4
9:1	14 MGy	3	9	17	24	32	16	0
	Control	3	9	16	22	25	24	2

The ^{27}Al MAS NMR spectra of the 14 MGy samples are shown in Figure 5.15. The shoulder present on the peak assigned to Al-substitution in C-S-H (centred at 63 ppm) is considered to be residual BFS. As

seen in the 7 MGy samples, this peak becomes less defined after irradiation. As discussed in Section 5.2.1.4, this variation may indicate an increase in the proportion of Al present in crosslinking sites (i.e. $Q^3(1Al)$); however, this is not supported by the ^{29}Si spectral deconvolutions. As such, it may further support the possibility of additional $Q^n(XAl)$ sites.

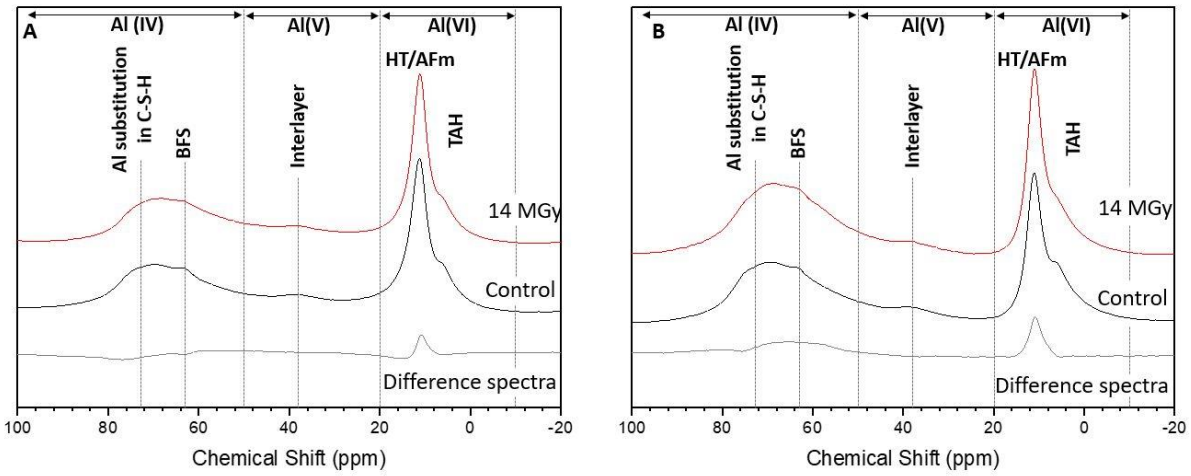

Figure 5.15 ^{27}Al MAS NMR Spectra for A: 3.44:1 BFS:PC 14 MGY and control; B: 9:1 BFS:PC 14 MGy and control.

Unlike the 7 MGy samples, a strong increase in intensity for the resonance associated with AFm and hydrotalcite phases was observed after irradiation. This supports the TGA results for the 9:1 14 MGy sample and suggests increased hydration of the irradiated cements. The shoulder associated with TAH is also noticeably reduced in the 9:1 14 MGy sample. Anderson et al. [80] found that the stability of TAH was affected by temperatures >70 °C and the presence of sulfate ions, which may form ettringite with the Al at the expense of TAH; however, neither of these factors provides an appropriate mechanism for the TAH reduction observed here. It is considered that reduction in TAH is either the result of pH variations or interaction with CO_3^{2-}. A similar decrease in TAH intensity has been observed with increasing carbonation levels in white PC systems [115].

5.3.2 Microstructure

5.3.2.1 SEM

SEM micrographs of the 3.44:1 and 9:1 systems (Figure 5.16) show the textural development of the samples after irradiation. The matrix of the 3.4:1 14 MGy samples appears less dense than the corresponding control, with a higher proportion of porosity (black in the BSE image). Dark striations (labelled 1 in Figure 5.16A) may indicate micro-cracking, although this may be a product of sample preparation. Also, smaller BFS particles have a tendency to fall out during preparation, creating small

black features that may be conflated with defects. This is not observed in the 9:1 sample, where the main distinctions are between regions of inner product and outer matrix. he outer matrix appears to comprise the majority of the control sample micrograph shown (Figure 5.16D). Overall, no large scale defects are noted in either system which was representative of the samples containing different replacement levels of BFS.

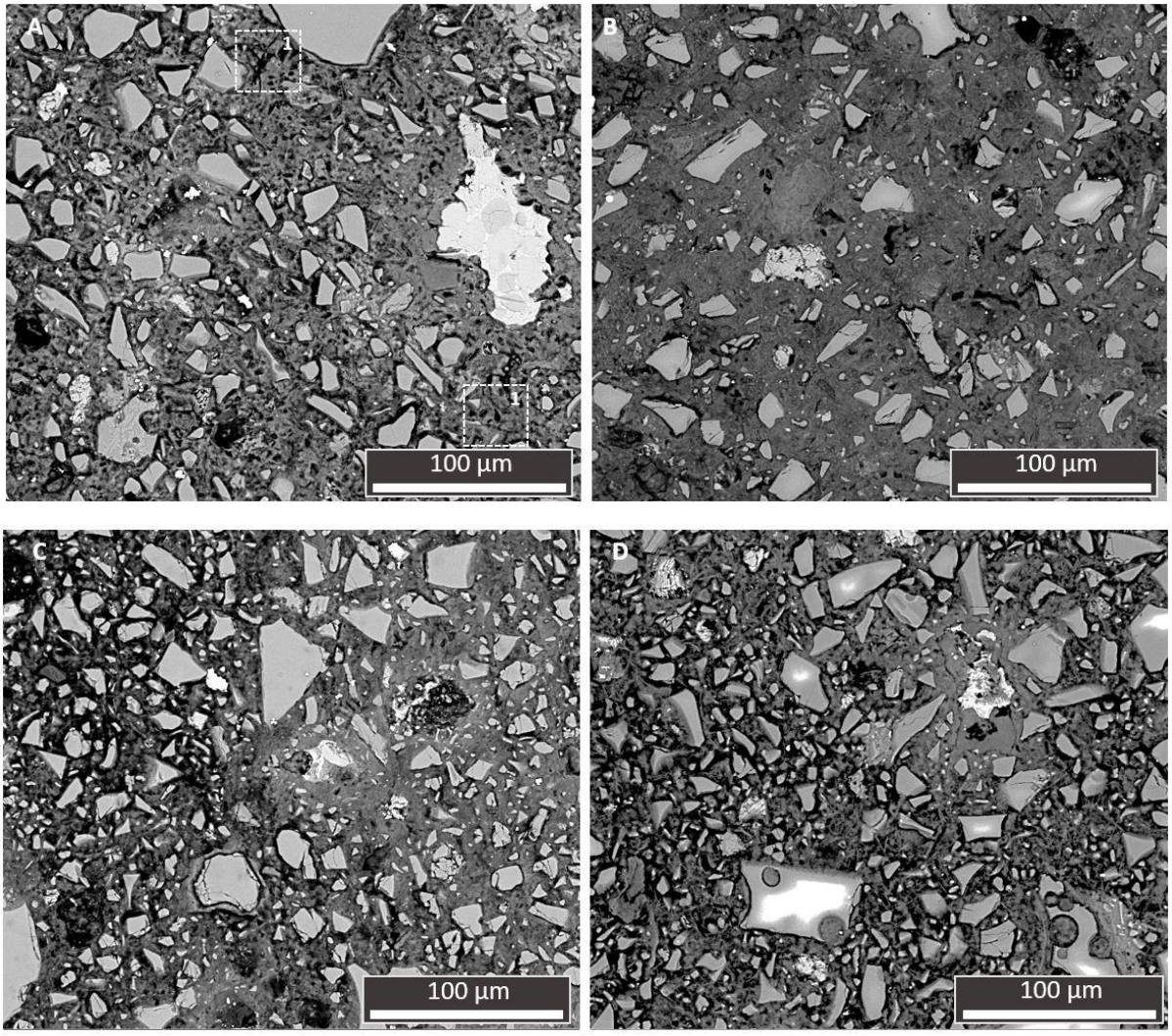

Figure 5.16 SEM micrographs of A: 3.44:1 BFS:PC 14 MGy; B: 3.44:1 BFS:PC control; C: 9:1 BFS:PC 14 MGy; D: 9:1 BFS:PC control. Box 1 discussed in text.

5.3.2.2 MIP

The MIP results for the 14 MGy samples show less definitive trends than the 7 MGy samples in terms of total accessible pore volume; however, the majority of samples show an increase in total pore volume which would be consistent with micro- or nano-cracking occurring after irradiation. The threshold pore entry radius has increased significantly after 14 MGy irradiation, which also supports the cracking hypothesis.

The critical pore entry radius is also affected by the irradiation and decreases as a result of exposure. Given that increased carbonation was observed in these samples (Table 5.10), an increase in critical pore entry radius might have been expected, as infilling of pores by carbonate products occurred. This process of small pore infilling has been linked with vaterite formation, where it has been observed to effectively fill pores formed in C-S-H agglomerations [115]. This was attributed to the low density of vaterite when compared to calcite – 2.54 g/cm^3 and 2.71 g/cm^3 respectively. Although vaterite was identified in the phase assemblage of these samples (Figure 5.10), the data shown in Table 5.15 indicate this pore infilling did not occur. This may be due to the quantities of carbonates formed and where they are located in the matrix.

Table 5.15 Porosity measurements for all 14 MGy irradiated samples and corresponding controls obtained through MIP analysis.

BFS:PC	Total accessible pore volume (%)		Critical pore entry radius (nm)		Threshold pore entry radius (nm)	
	14 MGy	Control	14 MGy	Control	14 MGy	Control
3:1	31 ±2	25 ±2	4	8	24	13
3.44:1	20 ±2	29 ±2	8	11	20	13
5.67:1	25 ±2	24 ±2	9	6	15	11
9:1	33 ±2	25 ±2	12	14	39	15

UPV values were reduced in the 14 MGy systems comparable to their respective controls, supporting the increased porosity observed in most samples. When compared to the control values, UPV values decreased by between 0.6 – 4.0 %. Once again, this did not scale linearly with the observed MIP values.

5.3.3 Mechanical properties

UPV testing showed a reduction in average values as a result of 14 MGy irradiation, indicating that irradiation resulted in an increase in discontinuities within the bulk. The scale of the reduction varies as a function of BFS fraction; the difference in UPV comparable to the control reduces by a greater extent as BFS replacement increases. The 5.67:1 system is the exception to this trend, with only minor change noted.

Variations in UPV at discrete testing points was observed as seen in the 7 MGy samples (see Section 5.2.3). Testing was completed on the same day, and so the differences at 52 and 72 weeks are as seen

in Figure 5.9, further supporting these being the result of local environmental conditions. However, the variation seen at 64 weeks is not observed for all the 14 MGy samples and so the cause for this is not as clear. The change in UPV over time was also observed to be negligible in each sample.

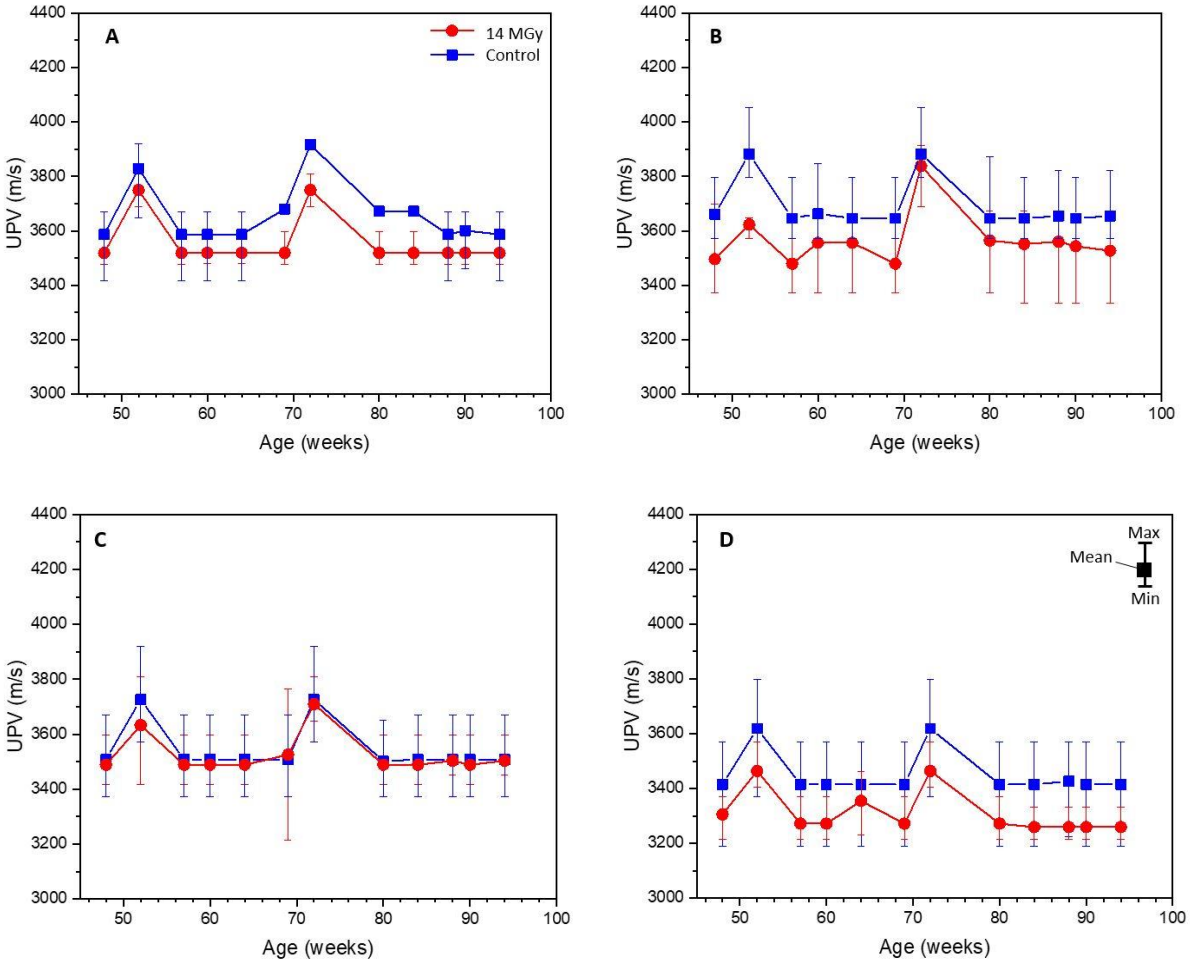

Figure 5.17 Comparison of UPV global mean values for 14 MGy and control systems. A: 3:1 BFS:PC, B: 3.44:1 BFS:PC, C: 5.67:1 BFS:PC, D: 9:1 BFS:PC. Data from 52 and 72 weeks are considered to have been affected by local environmental conditions.

The calculated material properties shown in Table 5.16 indicate an overall reduction as a result of 14 MGy exposure. However, as was seen for the 7 MGy samples, the scale of these variations is not considered to be significant given current wasteform property requirements.

Table 5.16 Summary of average change in material properties after 14 MGy exposure from UPV measurement (comparative to control sample). Density of 2000 kg/m³ and Poisson's ratio of 0.28 were assumed [32].

BFS:PC	UPV change (%)	Compressive strength change (%)	K change (%)	E_d change (%)
3:1	-2.7	-14.3	-5.4	-5.4
3.44:1	-3.4	-14.3	-6.6	-6.6
5.67:1	-0.6	-2.1	-1.1	-1.1
9:1	-4.1	-22.0	-7.9	-7.9

5.4 Irradiation to 20 MGy

Sample irradiation began when the cements were 30 weeks old and was undertaken for 28 weeks, making them 58 weeks when exposure ended.

5.4.1 Phase assemblage

5.4.1.1 XRD

Results from XRD analysis are shown in Figure 5.18. The difference patterns show very little variation from control samples after 20 MGy exposure and, although some variation in portlandite peak intensities is still observed, no increase in the monosulfoaluminate reflection was seen post-irradiation. Vaterite was observed in the majority of samples. These reflections were quite weak for 5.67:1 and 9:1 samples but were much stronger in the 3.44:1 irradiated sample.

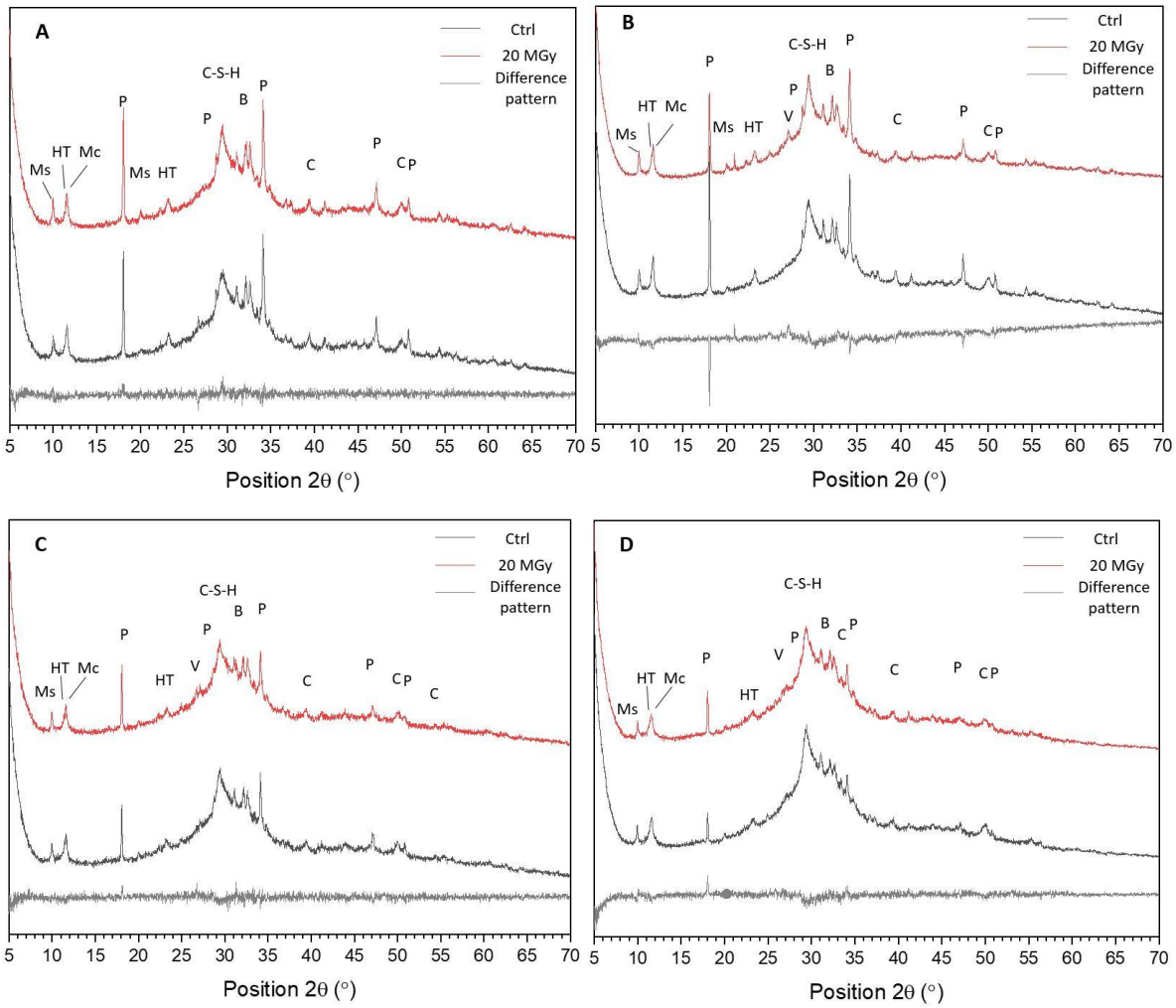

Figure 5.18 X-ray diffractograms of hydrated BFS:PC blends irradiated to 20 MGy and the corresponding control (Ctrl). BFS:PC ratios corresponding to each data set are: A: 3:1; B: 3.44:1; C: 5.67:1; D: 9:1. Ms: monosulfoaluminate, HT: hydrotalcite, Mc: monocarboaluminate, V: vaterite, P: portlandite, B: belite (C_2S), C: calcite.

The irradiation appears to have either enabled increased proportions of vaterite to form or preserved this metastable phase to a greater extent. No variations in calcite reflections were observed and it is notable that vaterite presence did not impact on the peak intensities for calcite. Given this, it is considered that vaterite formation is assisted by gamma exposure. This supports the findings of Maruyama et al. [115], where higher amounts of vaterite were attributed to the drying of the sample and the precipitation of calcium peroxide octahydrate, which then carbonated to form vaterite. This fits with less intense vaterite reflections being observed with increasing BFS fraction, where less calcium is present. Mobasher et al. [110] found limited carbonation after irradiation of a 9:1 BFS:PC cement and speculated that this was due to the limited proportion of calcium hydroxide present, which supports the overall trend observed in the data presented here.

5.4.1.2 TGA

The results from TGA are shown in Figure 5.19 and again, a clear reduction in the free water after irradiation is apparent. Increased weight loss in regions associated with hydrates was observed for the 3.44:1, 5.67:1, and 9:1 irradiated samples. This was in part due to increased levels of carbonation for the majority, but there appears to be a driving weight loss at 200 – 400 °C in the 3.44:1 sample. A distinct increase in weight loss at 375 °C was noted in the 5.67:1 and 9:1 samples. This may be a product of increased hydrotalcite formation [194], which would require an increase in BFS hydration. Testing was completed at 80 weeks and quantification of these results is shown in Table 5.17.

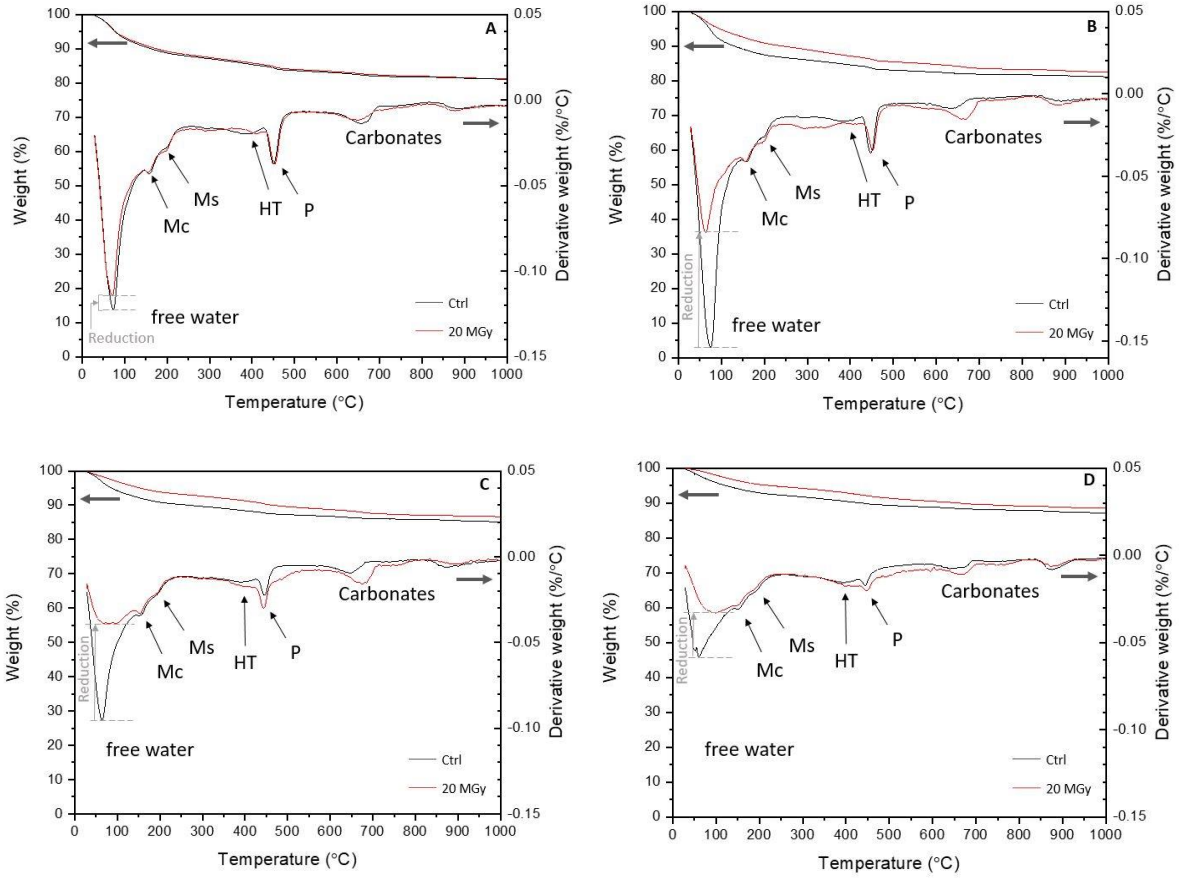

Figure 5.19 TGA data for 20 MGy and control (Ctrl) BFS:PC samples. BFS:PC ratios corresponding to each data set are: A: 3:1; B: 3.44:1; C: 5.67:1; D: 9:1. Mc: monocarboaluminate, Ms: monosulfoaluminate, HT: hydrotalcite, P: portlandite.

Table 5.17 Quantification of free water, portlandite and carbonate content of 20 MGy irradiated and control BFS:PC samples.

BFS:PC	Free water (%)		$Ca(OH)_2$ (%)		$CaCO_3$ (%)	
	20 MGy	Ctrl	20 MGy	Ctrl	20 MGy	Ctrl
3:1	6.7	7.1	5.8	5.4	5.7	5.2
3.44:1	5.2	8.3	4.3	4.2	6.3	4.2
5.67:1	3.1	5.8	6.4	3.1	5.7	4.4
9:1	2.0	4.1	5.2	3.9	4.8	3.9

The free water content in the control samples was higher than in the 14 MGy counterparts for 3:1, 3.44:1 and 9:1 samples (see Section 5.3.1.2, Table 5.10). Whilst this is a minor difference in the case of the 3:1 sample and the erroneous results for the 9:1 14 MGy sample were discussed previously, the result for the 3.44:1 20 MGy control is considered slightly high. Nevertheless, the reductions in free water after irradiation (relative to the control sample) showed a monotonic increase from 5.4 % at 3:1 to 50.7 % at 9:1, showing the magnitude of water loss is greater with increasing BFS content.

Portlandite contents in the 20 MGy irradiated samples are similar to those observed after 14 MGy testing for 3:1, 3.44:1 and 9:1 samples (Table 5.10), although slightly more variable for 5.67:1. An increase in portlandite content was observed at higher BFS replacement levels. This is counterintuitive, as it would be expected that the limited amount of portlandite that is formed from initial hydration of PC in these cements would be consumed by the slower reaction of the BFS given the extended curing time these samples experienced.

Portlandite and carbonate quantities were elevated in the 20 MGy irradiated samples, further indicating that carbonation during irradiation does not proceed purely at the expense of portlandite. Carbonate quantities were more significantly increased in systems with lower BFS fractions. This supports the findings from the XRD analysis and the hypothesis regarding Ca content being a limiting factor for radiation induced carbonation.

The scale of the changes in free water loss and carbonation observed through TGA increased for the 20 MGy samples in comparison to the 14 MGy samples (Table 5.10). However, the overall impact on the phase assemblage is still very minor and unlikely to impart significant detrimental effects to the bulk.

5.4.1.3 SEM-EDX

SEM-EDX maps are shown in Figure 5.20 and display much the same trends with irradiation as observed at lower irradiation doses; that is, no significant variations in the distribution of elements were observed after gamma exposure (see Figure 5.4, Figure 5.12). Despite the increased weight loss associated with hydrotalcite in the TGA of 20 MGy samples, the reaction rims of BFS were not significantly increased in thickness.

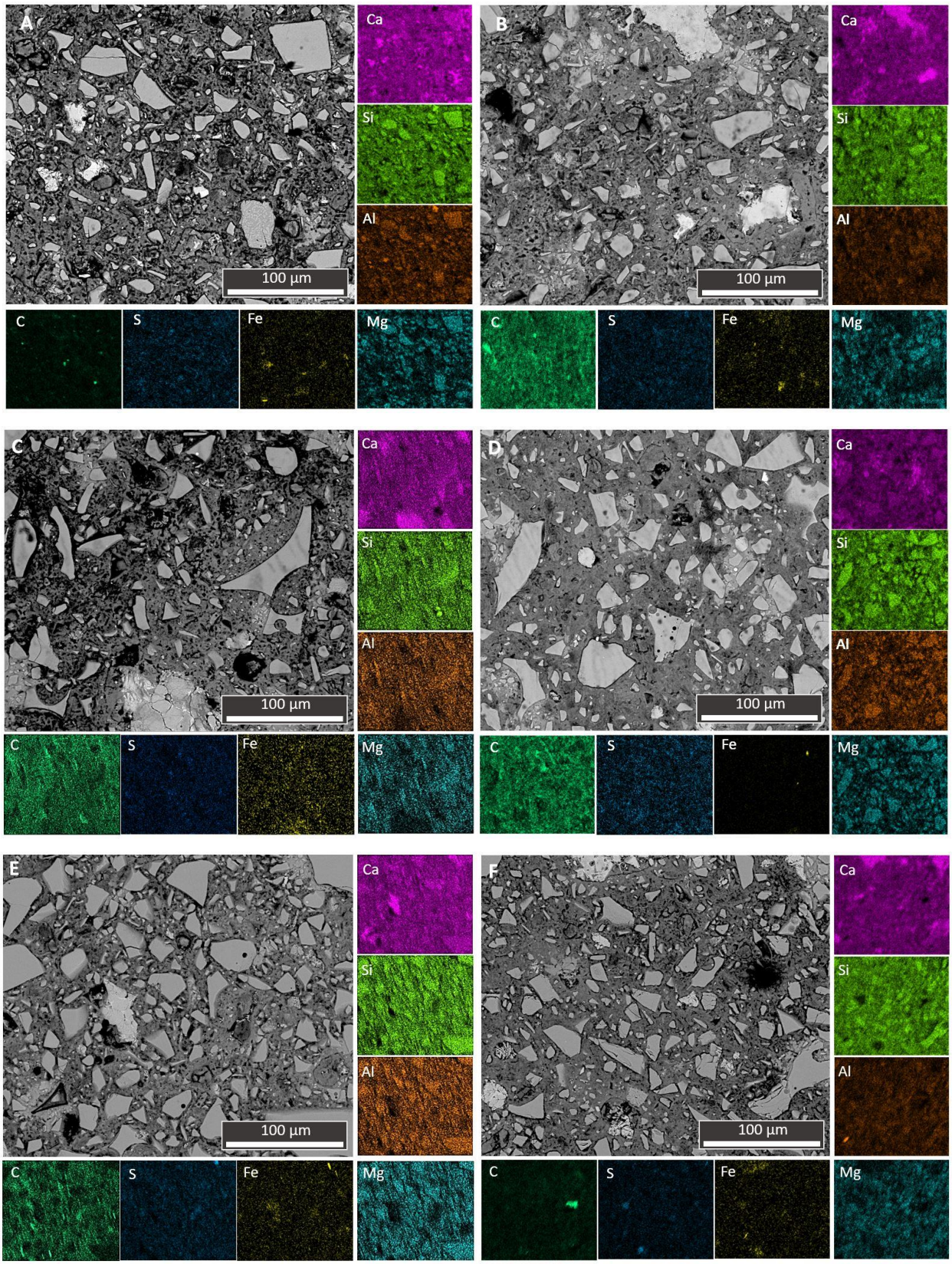
A
Ca
Si
Al
100 µm
C
S
Fe
Mg
B
Ca
Si
Al
100 µm
C
S
Fe
Mg
C
Ca
Si
Al
100 µm
C
S
Fe
Mg
D
Ca
Si
Al
100 µm
C
S
Fe
Mg
E
Ca
Si
Al
100 µm
C
S
Fe
Mg
F
Ca
Si
Al
100 µm
C
S
Fe
Mg

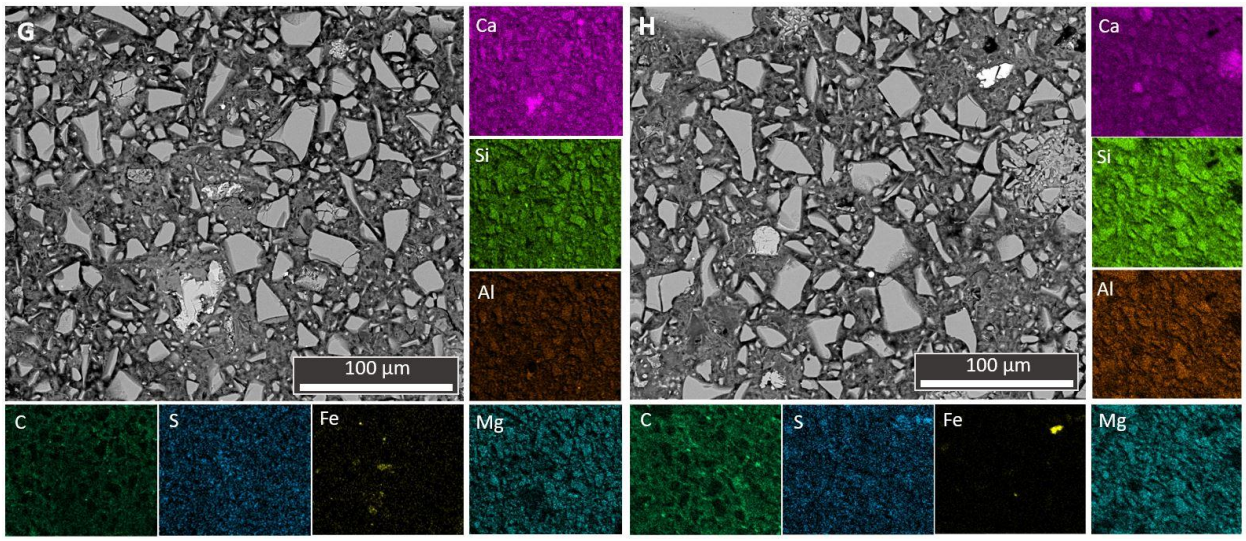

Figure 5.20 SEM images and corresponding EDX elemental maps (for selected elements as marked) for different BFS:PC blends, exposed to 20 MGy and respective control samples: A: 3:1 20 MGy; B: 3:1 control; C: 3.44:1 20 MGy; D: 3.44:1 control; E: 5.67:1 20 MGy; F: 5.67:1 control; G: 9:1 20 MGy; H: 9:1 control.

Point analysis data for the 20 MGy samples is shown in Figure 5.21 and very little variation is seen between the irradiated and control samples. The average Ca/Si ratios were the same as observed after 14 MGy: Ca/Si = 1.4 ± 0.5 for the 3:1 and 3.44:1 samples, and 1.3 ± 0.3 for the 5.67:1 and 9:1 samples. No variation in the Al/Ca or Mg/Ca ratios was observed and the sulfate balance did not appear to be affected by 20 MGy irradiation exposure.

The limited change in the aluminium and magnesium balance does not support the increased weight loss observed in TGA being attributed to an increase in hydrotalcite formation. However, the point analysis conducted under SEM primarily targeted the C-S-H matrix (the bulk of the grey matrix, avoiding very light grey areas which are portlandite (see Figure 4.5 for example), and as hydrotalcite will primarily be found in the reaction rims of BFS particles (darker rims adjacent to bright angular BFS particles), this may be a product of measurement statistics. Nonetheless, as stated above, the scale of BFS hydration rims was not visibly increased in the irradiated samples. The EDX data indicates that 20 MGy gamma exposure has not significantly altered the bulk chemistry of the system, as limited variation was observed.

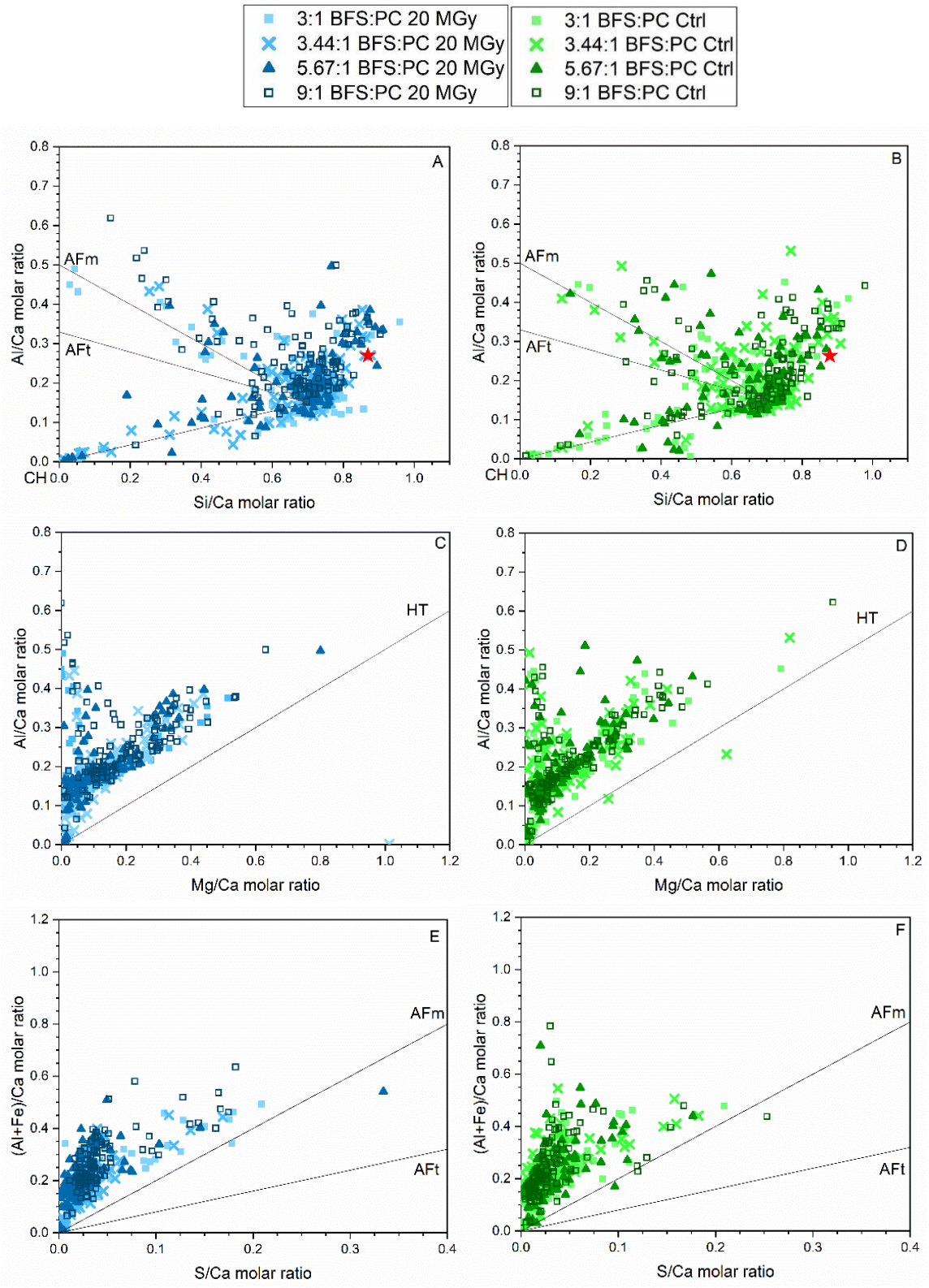

Figure 5.21 EDX point analysis data for all BFS:PC blends, for 20 MGy irradiated and control samples. A, C, E: 7 MGy; B, D, F: control. Each point sample was taken from a region that visually appeared to be binder rather than residual anhydrous phases. Composition of anhydrous BFS shown in A, B by ★ symbol. Tie lines link to the other prominent hydrate phases; CH: portlandite; AFm: monosulfoaluminate; AFt: ettringite; and HT: hydrotalcite.

5.4.1.4 MAS NMR

The results obtained from ^{29}Si MAS NMR spectroscopy of the 20 MGy samples are shown in Figure 5.22, and the difference spectra indicate minor changes to the 3.44:1 system but greater differences in the 9:1 sample. The difference in the 9:1 spectra compared to the control is similar to those observed in the 14 MGy samples (Figure 5.14); relating to Q^2 species and BFS resonances.

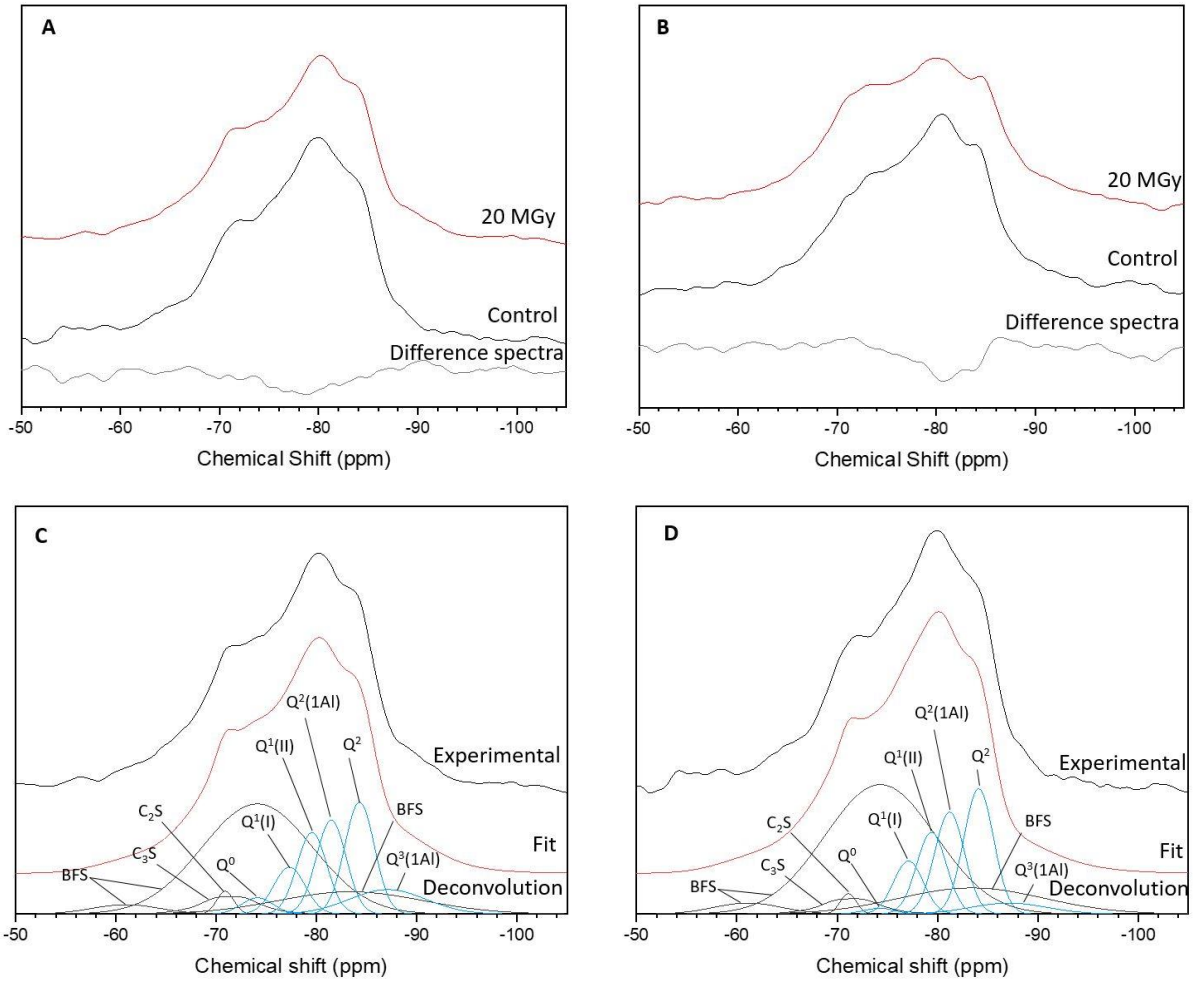

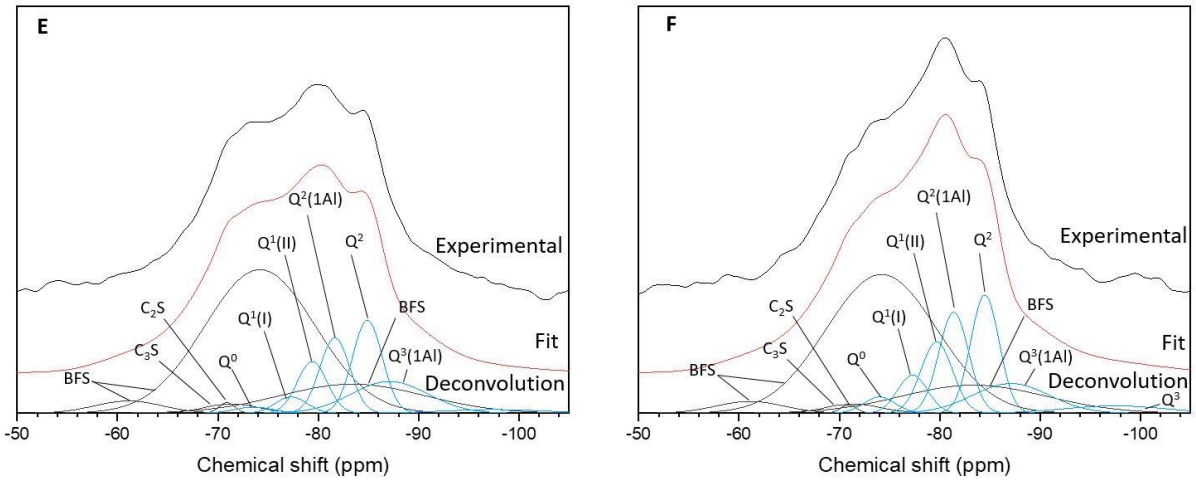

Figure 5.22 ^{29}Si MAS NMR spectra of A: 3.44:1 BFS:PC 20 MGy and control; B: 9:1 BFS:PC 20 MGy and control and deconvolution of C: 20 MGy 3.44:1 BFS:PC; D: control 3.44:1 BFS:PC; E: 20 MGy 9:1 BFS:PC; F: control 9:1 BFS:PC.

Selective dissolution using EDTA indicated that BFS hydration was similar to the levels found in the 14 MGy samples for the 3.44:1 blend (Section 5.2.1.4, Table 5.18) and no difference was observed between the 20 MGy and control samples. The results from the 9:1 samples indicate overall BFS DoH values similar to the 7 MGy samples of this blend; however, the relationship between the samples was the same as at 14 MGy. The control was observed to have a higher DoH than the irradiated sample. This does not support the increased weight loss observed in the TGA results associated with hydrotalcite decomposition.

Estimates from deconvolution of the ^{29}Si MAS NMR spectra show low DoH values for the 3.44:1 system; however, considering the errors on these estimates, they are broadly similar to the EDTA values. An increase in DoH in the irradiated blend is indicated. For the 9:1 sample, the DoH is high compared to the EDTA results but again, when considering the errors, the results are comparable. Also, the difference in DoH is similar between the irradiated and control samples according to both methods. The overall agreement between techniques was better than for the 14 MGy samples (Table 5.11); however, the results are still variable and should be treated tentatively. No trend was observed between irradiation exposure and increased BFS hydration, although the NMR results for the 3.44:1 20 MGy sample indicate that this may have occurred. This is considering both the known errors of the techniques used and the results from other analytical methods.

Table 5.18 Degree of hydration of BFS fraction after 20 MGy exposure for 3.44:1 and 9:1 blends. Results from both EDTA dissolution method and ^{29}Si MAS NMR deconvolutions.

BFS:PC		BFS DoH (%)	
		EDTA	^{29}Si NMR
3.44:1	**20 MGy**	37 ± 5	33 ± 5
	Control	38 ± 5	25 ± 6
9:1	**20 MGy**	20 ± 7	25 ± 5
	Control	26 ± 6	31 ± 5

Similar DoH values for C_3S hydration were observed in both the 3.44:1 and 9:1 systems (Table 5.19); however, a reduction in belite hydration was observed in the irradiated systems. This is the opposite of the results for the 7 and 14 MGy, where increased or similar levels of belite hydration were observed (Sections 5.2.1.4, 5.3.1.4). Given the extended curing time these samples encountered prior to irradiation, it would be assumed that belite hydration would be increased. It is considered that the variations may be due to the limited resolution achieved in the spectral deconvolutions due to the overlapping nature of the resonances.

Table 5.19 Degree of hydration of clinker components after 20 MGy exposure for 3.44:1 and 9:1 blends taken from ^{29}Si MAS NMR deconvolutions.

BFS:PC		Clinker DoH (%)		
		C_3S	C_2S	Total
3.44:1	**20 MGy**	83 ± 4	42 ± 7	79 ± 11
	Control	85 ± 2	53 ± 4	82 ± 6
9:1	**20 MGy**	80 ± 2	42 ± 5	77 ± 7
	Control	81 ± 2	58 ± 3	79 ± 5

C-A-S-H structural characteristics determined from these NMR results are shown in Table 5.20. The Ca/Si ratios do not indicate any major variation as a result of radiation, although a slight decrease was noted in the 9:1 20 MGy irradiated sample. No differences in the Al/Si ratios were observed in any of the 20 MGy samples. Increased MCLs were observed for the irradiated cements, although the MCL values for the 3.44:1 samples are lower than seen at 14 MGy (see Section 5.3.1.4, Table 5.13). This

shift in MCL does not appear to be the result of increased hydration and so it is considered likely that removal of Ca by carbonation is responsible for the increased chain length identified.

Table 5.20 Structural characteristics of C-A-S-H in 20 MGy and control systems from deconvolutions of ^{29}Si MAS NMR spectra.

BFS:PC	Ca/Si		Al/Si		MCL	
	20 MGy	Ctrl	20 MGy	Ctrl	20 MGy	Ctrl
3.44:1	1.1	1.1	0.13	0.13	6.5	6.0
9:1	1.0	1.1	0.13	0.13	9.5	7.6

From quantification via TGA (Table 5.17), the 9:1 irradiated system appeared to have a modest increase in carbonate content of 0.9 %, compared to 2.1 % seen in the 3.44:1 systems. If carbonation is the cause of the increased MCL, this does not match the differences observed.

Given the minor increase in MCL observed (despite the increase in carbonation seen in the 3.44:1 sample) it would appear that carbonation is decalcifying a phase other than C-S-H; portlandite is typically assumed to initially be consumed by carbonation [228]. However, portlandite quantities observed for the 3.44:1 20 MGy sample were similar to the control sample. This increase in carbonate content, maintained portlandite content, and increase in MCL, indicates that gamma exposure is promoting decalcification of both portlandite and C-S-H phases concurrently. C-S-H with higher Ca/Si ratio has been observed to be more resilient to carbonation induced effects [54], which supports the differences in response between the 9:1 and 3.44:1 cements.

Table 5.21 Results of ^{29}Si MAS NMR with proportions of Q species shown from deconvolution of the20 MGy spectra. The estimated uncertainty in absolute site percentages is ± 1 %.

BFS:PC		Q^0	Q^1(I)	Q^1(II)	Q^2(1Al)	Q^2	Q^3(1Al)	Q^3
3.44:1	20 MGy	4	12	20	23	27	15	0
	Control	2	13	21	26	32	7	0
9:1	20 MGy	2	5	15	23	28	24	3
	Control	4	9	17	23	26	17	4

The 20 MGy irradiated samples have a greater proportion of Al-linked tetrahedral sites, which further supports the identification of decalcification of the C-A-S-H as a result of gamma exposure. However,

the ratio of Q^1:Q^2 sites is higher in the 3.44:1 irradiated sample due to a decreased proportion of Q^2 sites relative to the control. This reduction is mainly in the Q^2(1Al) sites and an accompanying increase in the proportion of Q^3(1Al) site was observed. This shift has been observed as a product of carbonation in BFS:PC blended cements, where Al was removed from bridging sites and incorporated in an amorphous silica phase [197]. This trend is also seen in the 9:1 irradiated sample. The Q^0 proportions show the same trend as identified previously: the resonance increases when there is decreased response from the BFS.

The ^{27}Al MAS NMR spectra from the 20 MGy samples are shown in Figure 5.23. Similar trends to those seen from the 14 MGy samples were observed, such as the decreased resonance related to residual BFS in the irradiated samples. The difference spectra show an increase in the intensity of the resonances in the 20 MGy irradiated samples between 50 – 75 ppm. This is indicative of an increase in the proportion of Al(IV) in cross linking tetrahedra, which is seen in the deconvolutions of the ^{29}Si spectra by the increased proportion of Q^3(1Al) sites. This increase does not appear to have significantly diminished the resonance associated with Al located in bridging sites, despite the minor reduction for Q^2(1Al) sites identified from the ^{29}Si spectra.

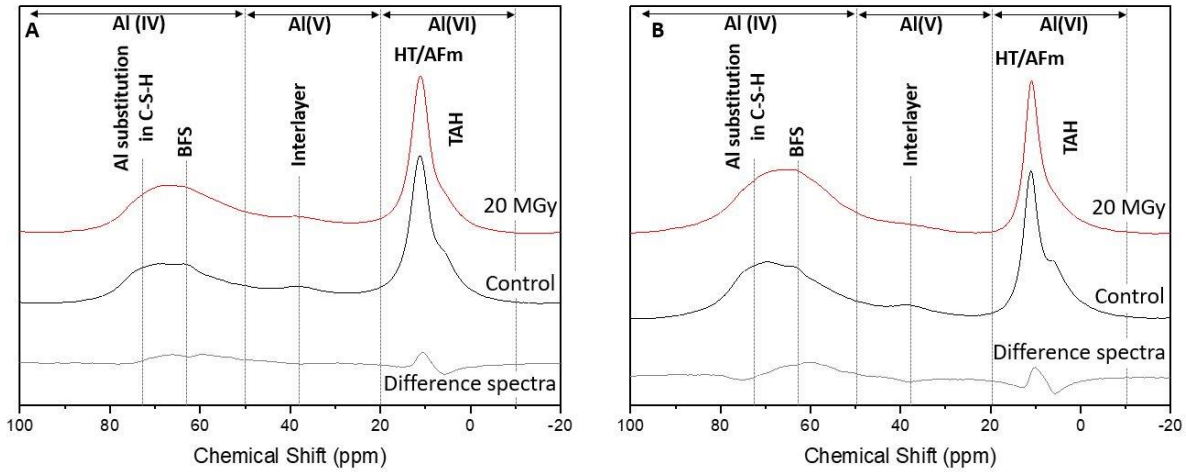

Figure 5.23 ^{27}Al MAS NMR Spectra for A: 3.44:1 BFS:PC 20 MGY and control; B: 9:1 BFS:PC 20 MGy and control.

A strong increase in intensity for the resonance associated with AFm and hydrotalcite was observed after irradiation, as was seen for the 14 MGy samples (see Figure 5.15). Larger proportions of hydrotalcite were tentatively identified by an increase in weight loss observed from TGA results (Figure 5.19) for these cements, supporting the results shown here. The increased resonances associated with Al(IV) and Al(VI) in the irradiated samples again link to an increase in the DoH of the BFS in these systems. This further calls into question the validity of the results of DoH testing completed for these samples as reported in Table 5.18.

The shoulder associated with TAH is noticeably reduced in the 20 MGy samples, as was observed in the 14 MGy samples but to a greater extent here. This indicates that the TAH stability is negatively affected by the irradiation, with greater instability as dose increases. As outlined in Section 5.3.1.4, the stability is known to be negatively affected by temperatures >70 °C and the presence of sulfate ions, which may form ettringite with the Al at the expense of TAH. As neither of these are applicable to the current samples, and given the findings of the ^{29}Si spectral deconvolutions, it is considered that the reduction is likely due to interaction with CO_3^{2-}. However, as this process may also have caused pH variations, the direct mechanism is not known.

5.4.2 Microstructure

5.4.2.1 SEM

SEM micrographs of the 3.44:1 and 9:1 systems (Figure 5.24) show the microstructures of the samples after irradiation. The matrix of the 3.44:1 20 MGy samples appears less dense than the control, with a higher proportion of porosity (black in BSE image). This is also observed in the 9:1 irradiated sample: however, no large scale defects are noted in either system which was representative of the samples containing different replacement levels of BFS. Increased magnification images of zones (i, ii) are shown in Figure 5.24 E, F and the development of micro-cracks is shown by boxes labelled 1. These features are very small and limited in scale, unlike the macroscopic cracking identified by Mobasher et al. [110] in similar materials exposed to much lower total gamma doses. However, that study focussed on irradiation response at early age, whereas these samples were 30 weeks old before irradiation was initiated and, as such, the differences in observations may be a product of the increased curing age prior to irradiation. Regions of poorly consolidated matrix and / or increased porosity were observed (box 2) with increased frequency in the irradiated samples.

The differences in microstructure observed after 20 MGy exposure are similar to those seen in 14 MGy samples (see Section 5.3.2.1). It is considered that the differences in degree of hydration of the precursor materials at 16 weeks (when 14 MGy irradiations began) and 30 weeks (initiation of 20 MGy exposure) would be negligible. This assumption is based on both literature studies [82], [198] and the DoH testing completed in previous sections. Given this, the differences in microstructural textures at the initiation of irradiation are assumed to be minimal.

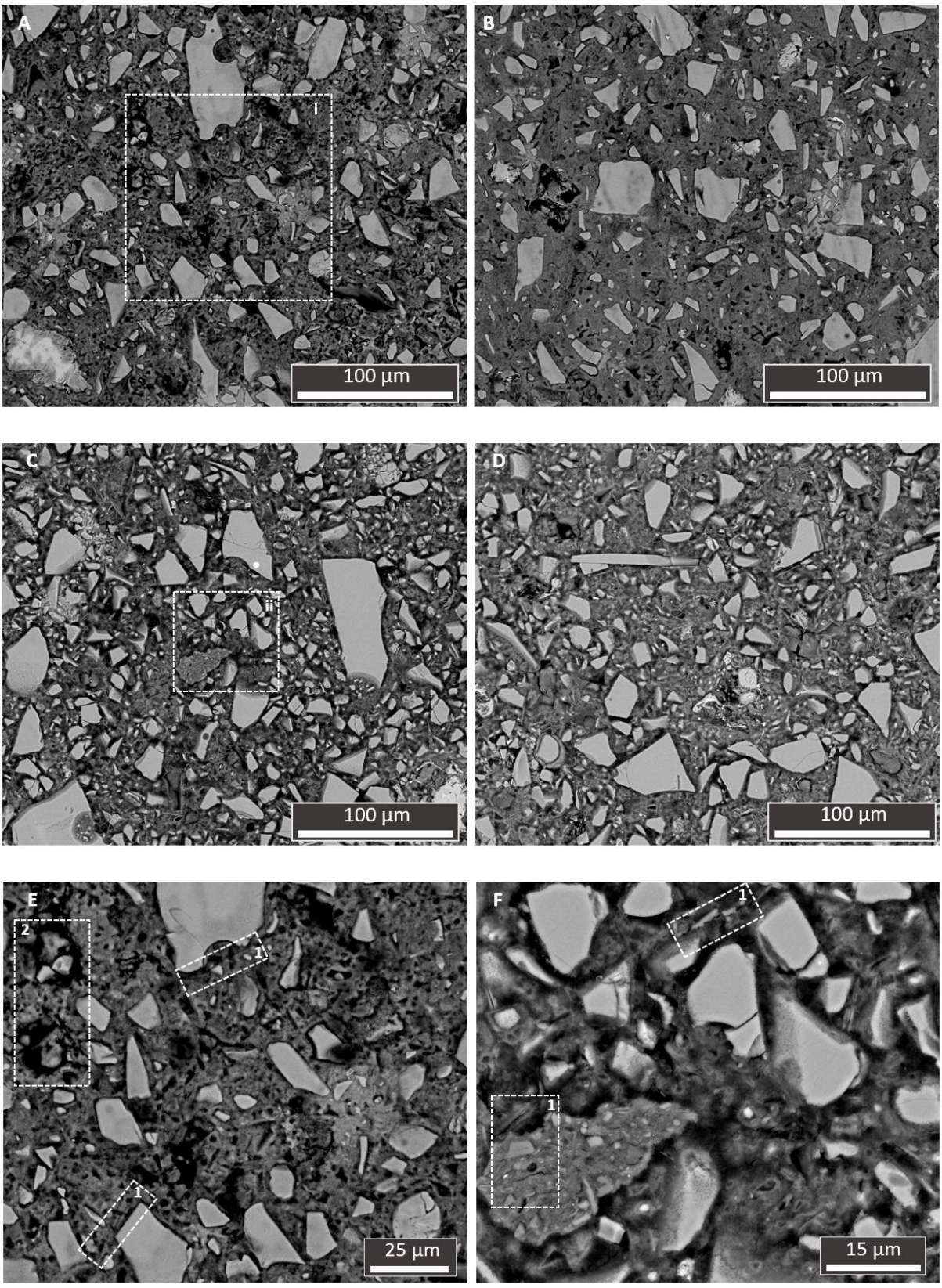

Figure 5.24 SEM micrographs of A: 3.44:1 BFS:PC 20 MGy; B: 3.44:1 BFS:PC control; C: 9:1 BFS:PC 20 MGy; D: 9:1 BFS:PC control; E: Increased magnification of area (i) in A; F: increased magnification of area (ii) in C . Boxes 1, 2 discussed in text.

5.4.2.2 MIP

MIP results are shown in Table 5.22 and show that the differences observed in total accessible pore volume for irradiated / control samples were limited after 20 MGy exposure. However, alteration to the pore size distribution was observed as a result of irradiation. The critical pore entry radius was observed to increase in the majority of the irradiated samples. This effect was greater in samples with higher BFS fractions. This is the opposite of what was observed in the data for the 7 MGy and 14 MGy irradiated samples (see Table 5.8, Table 5.15), which showed a decrease in critical pore entry radius. The threshold pore entry radius was also increased in the irradiated samples, as observed in the 7MGy and 14 MGy samples (see Table 5.8, Table 5.15), indicating that nano- or micro-cracking had occurred.

Table 5.22 Porosity measurements for all 20 MGy irradiated samples and corresponding controls obtained through MIP analysis.

BFS:PC	Total accessible pore volume (%)		Critical pore entry radius (nm)		Threshold pore entry radius (nm)	
	20 MGy	Control	20 MGy	Control	20 MGy	Control
3:1	26	23	4	3	20	11
3.44:1	21	24	4	6	22	12
5.67:1	30	30	32	10	58	15
9:1	31	29	26	18	50	23

A reduction in critical pore entry radius supports the hypothesis of vaterite effectively filling pores formed in C-S-H agglomerations (outlined in Section 5.3.2.2), indicating refinement of the critical pore entry radius. XRD results (see Figure 5.18) indicated that the proportion of vaterite was higher in the 3.44:1 blend exposed to 20 MGy, and this sample also shows a reduction in critical pore entry radius compared to the control sample. This observation supports the vaterite formation – pore infilling hypothesis observed by Maruyama et al. [115].

UPV values were reduced in the 20 MGy irradiated samples compared to their respective controls, indicating an increase in discontinuities in the bulk. When compared to control values, UPV values decreased by between 1.4 – 6.3 %. This decrease did not correlate with the observed MIP values for total accessible porosity.

5.4.3 Mechanical properties

UPV testing showed a reduction in average values as a result of 20 MGy irradiation, indicating that this resulted in an increase in discontinuities within the bulk. The scale of the reduction was not dependent on the BFS fraction; there was no clear trend observed in the difference in UPV as BFS replacement increases.

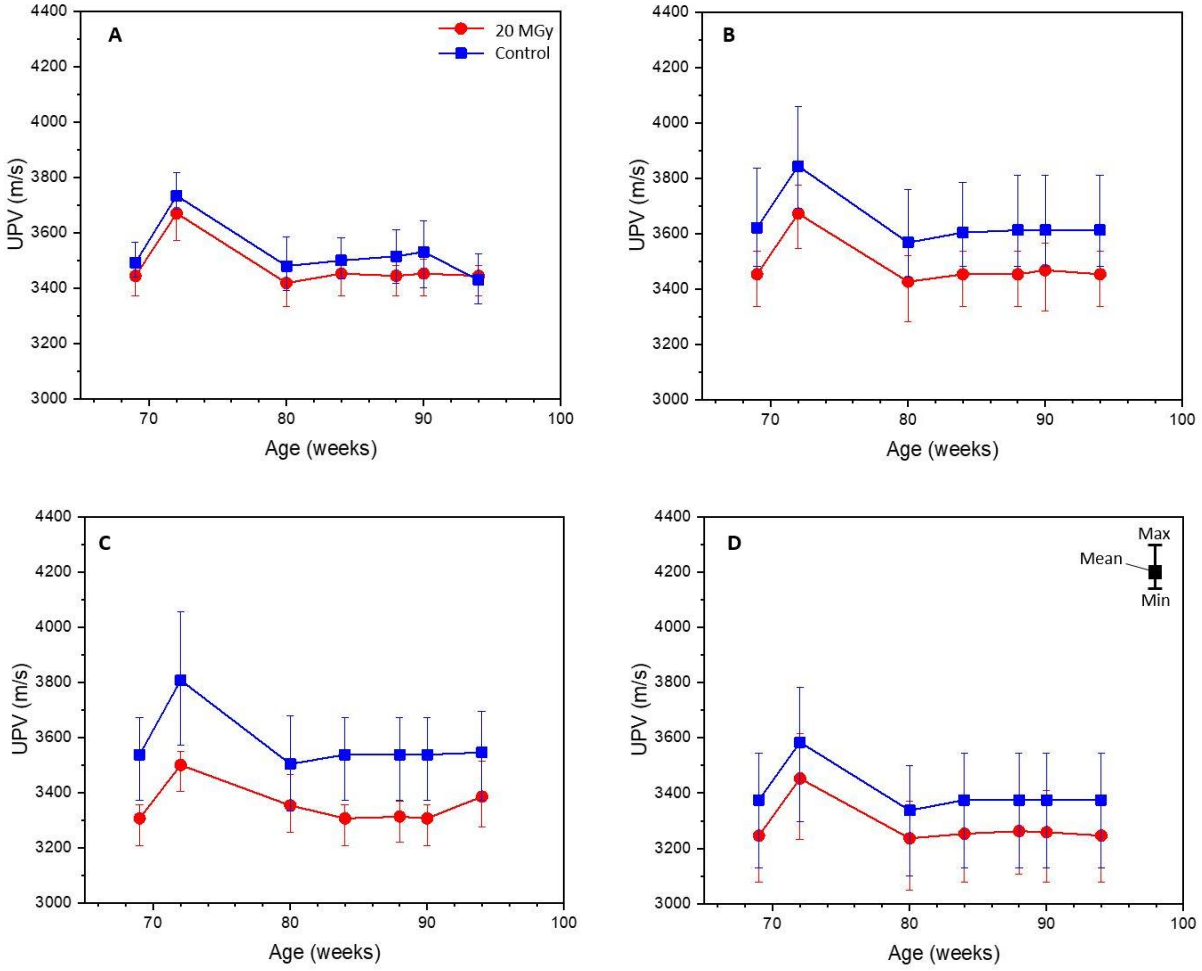

Figure 5.25 Comparison of UPV global mean values for 20 MGy and control systems. A: 3:1 BFS:PC, B: 3.44:1 BFS:PC, C: 5.67:1 BFS:PC, D: 9:1 BFS:PC. Data from 72 weeks are considered to have been affected by local environmental conditions.

Due to the time taken for the irradiation to be completed, testing on these samples was undertaken for a shorter time period. As a result of this, a single variation in UPV at 72 weeks (corresponding with the 72 week variation seen for the 7 and 14 MGy samples (see Figure 5.9, Figure 5.17)), was observed which is considered the result of local environmental conditions. Other than this, the change in UPV over time was also observed to be negligible.

Table 5.23 Summary of average change in material properties after 20 MGy exposure from UPV measurement (comparative to control sample). Density of 2000 kg/m³ and Poisson's ratio of 0.28 were assumed [32].

BFS:PC	UPV change (%)	Compressive strength change (%)	K change (%)	E_d change (%)
3:1	-1.4	-7.6	-2.9	-2.9
3.44:1	-4.3	-18.9	-8.4	-8.4
5.67:1	-6.1	-20.2	-11.9	-11.9
9:1	-3.5	-19.0	-6.9	-6.9

Calculated material properties indicate an overall reduction as a result of 20 MGy irradiation exposure. The overall response does not appear to be affected by the BFS fraction in the cement. The changes in values from the controls are considered minor. As such, the scale of these variations is not considered to be significant given current wasteform property requirements.

5.5 Effect of increased total gamma dose

Although the samples were different ages and therefore cured to a different extent before irradiations began, it is considered that the differences in DoH of BFS and PC components between 9 and 30 weeks would be < 12 % and < 2 % respectively [82], [198]. Although minor variations in hydration would be present, it is considered that the overall effect of increasing gamma dose can be evaluated despite this.

The overall dose rate was also variable as a result of ^{60}Co decay over the time taken for testing to be completed (Appendix 10.1). Given this, the effect of dose rate cannot be evaluated from the current data.

A summary of data from 3.44:1 and 9:1 BFS:PC blends are presented in the following section.

5.5.1 Phase assemblage

5.5.1.1 XRD

Diffractograms for both BFS:PC replacement levels are shown as a function of gamma dose in Figure 5.26.

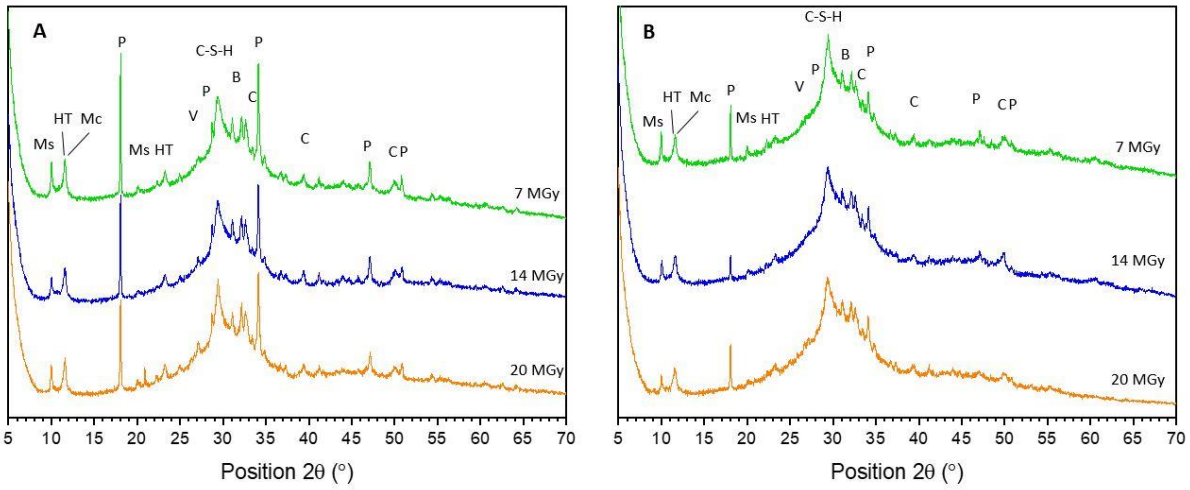

Figure 5.26 X-ray diffractograms showing effect of increasing total gamma dose on hydrated BFS:PC blends for A: 3.44:1; B: 9:1 systems. Ms: monosulfoaluminate, HT: hydrotalcite, Mc: monocarboaluminate, V: vaterite, P: portlandite, B: belite (C_2S), C: calcite.

In the 3.44:1 blend, no overall trend was observed in the peak intensities for AFm phases such as monosulfoaluminate. A reduction in peak intensity was observed for portlandite with increasing gamma dose. Despite this reduction, no significant increase in calcite peak intensities was observed. However, it was possible to observe the development of a reflection associated with vaterite which strengthens with increasing dose as portlandite decreases.

The 9:1 blend shows a reduction in peak intensity associated with monosulfoaluminate as the total dose increases. This may be a product of carbonation, as an increase in molar bulk CO_2/Al_2O_3 ratio would decrease the stability of this phase. Carbonation of monosulfoaluminate has been observed to proceed by initially transforming to monocarboaluminate before decalcification occurs [69], [215]. However, no increase in peak intensity for monocarboaluminate was observed from the XRD data; as this peak overlaps with the hydrotalcite reflection, this is difficult to ascertain. Variable peak intensities for portlandite were observed; however, variations were not linked to increases in calcite peak intensities. Minor reflections associated with vaterite formation were noted and these increased slightly with total gamma dose.

Overall, there is not a significant change to the phase assemblage as a result of the increased total dose in either system. The changes observed are primarily a product of carbonation. Various

polymorphs of $CaCO_3$ are identified, and these are related to the increased calcium content of the blend with lower BFS content.

5.5.1.2 TGA

The TGA results, Figure 5.27, indicate that there is more variability in the phase assemblage as a function of increasing dose. Although the overall mineralogy identified is the same, the proportions of the phases changed after different gamma exposure levels.

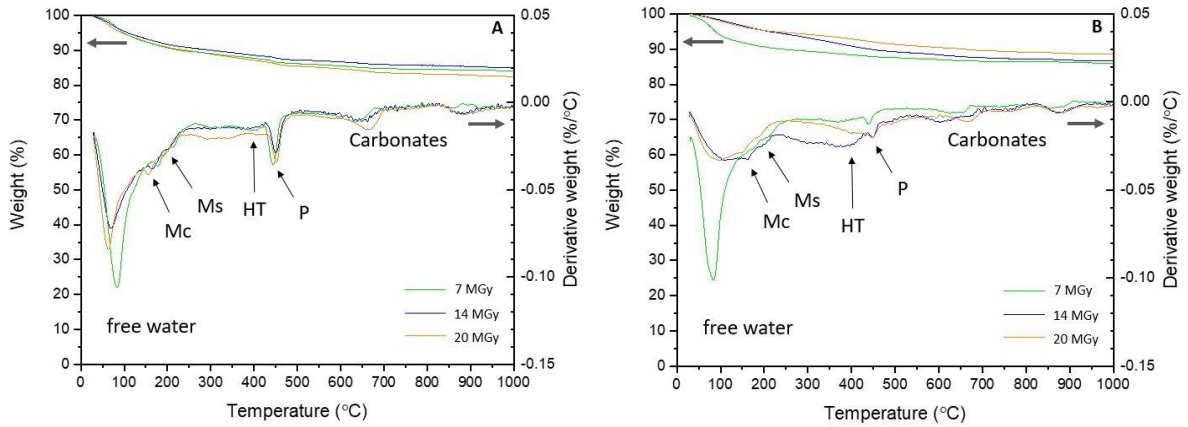

Figure 5.27 TGA results showing effect of increasing total gamma dose on hydrated BFS:PC blends for A: 3.44:1; B: 9:1 systems. Mc: monocarboaluminate, Ms: monosulfoaluminate, HT: hydrotalcite, P: portlandite.

Results for the 3.44:1 blend (Figure 5.27 A) show that although free water is reduced as a product of irradiation, this was not proportional to the total absorbed dose. Increased weight loss associated with monosulfoaluminate, monocarboaluminate, and hydrotalcite phase decomposition was observed up to 400 °C with increasing total dose. No distinct trend was observed in portlandite content with increasing dose and the carbonate content was greater with increased gamma dose for both blends.

The 9:1 samples did show an overall reduction in free water that was more notable with total gamma dose, indicating that higher BFS fractions make the sample more susceptible to water loss from irradiation. Increased weight loss associated with monosulfoaluminate, monocarboaluminate and hydrotalcite is observed with increased radiation exposure, although not linearly. Analysis of the off-gas from the TGA via a coupled mass spectrometer indicated an increase in CO_2 emissions from approximately 300 °C, peaking at 400 °C, that must be due to hydrotalcite decomposition (see Appendix 10.2).

Table 5.24 Quantification of free water, portlandite and carbonate content of 3.44:1 BFS:PC and 9:1 BFS:PC samples with increasing total gamma dose.

BFS:PC	Free water (%)		$Ca(OH)_2$ (%)		$CaCO_3$ (%)	
	3.44:1	**9:1**	**3.44:1**	**9:1**	**3.44:1**	**9:1**
7 MGy	5.1	5.2	6.8	2.4	4.3	2.5
14 MGy	4.6	1.8	4.6	4.7	4.1	5.0
20 MGy	5.2	2.0	4.3	5.2	6.3	4.8

Radiation exposure has a more significant effect on the free water content of the 9:1 system, indicating that the radiation response is altered by the BFS replacement level. The increased curing time for 14 MGy and 20 MGy samples prior to irradiation is not considered to have impacted the radiation response; as discussed in Section 5.5 the changes in DoH and water content resulting from the pre-irradiation curing are anticipated to have been small. This is further supported by the 9:1 20 MGy overall weight loss results, which are lower than for the 7 MGy and 14 MGy samples.

Measured portlandite quantities appear to decrease with increasing irradiation dose in 3.44:1 but increase in the 9:1 blend. It is postulated that this may be due to an overlap in the decomposition temperature ranges of portlandite and hydrotalcite [194]. If increased hydrotalcite quantities were present, could the overlap of the end of decomposition of this phase with the onset of portlandite decomposition in the same temperature range cause an artificial inflation of the portlandite quantity? This might account for the surprising trend in portlandite quantities observed. However, the results from the XRD data (Figure 5.26) do not show significant variations in peak intensities associated with hydrotalcite and so does not clearly support this hypothesis.

Greater carbonate quantities were observed with increasing gamma exposure, indicating that this is a radiation-induced effect. However, as the testing took place at 22, 39 and 80 weeks, atmospheric carbonation effects will have contributed to this increase, even though samples were handled carefully and wrapped to minimise carbonation effects. The results of the control samples taken at the same ages show maximum carbonate increases of 1.2 %, whereas the irradiated samples increase by > 2.0 %. Increased carbonate quantities were also observed in the irradiated samples compared to the controls at 14 MGy and 20 MGy for all levels of BFS replacement, further indicating that this is an effect of radiation.

5.5.1.3 SEM-EDX

Point analysis showing the impact of the different gamma doses for the separate blends is shown in Figure 5.28. Very little difference is observed with increasing dose in any of the figures, indicating large

changes to the bulk matrix compositions have not occurred. Data points for the 9:1 system are much more scattered as a result of the interaction volumes inevitably containing unreacted BFS particles.

In analysis of the 7 MGy samples in Section 5.2.1.3, it was speculated that increased Al/Ca and Mg/Ca molar ratios were observed for the irradiated samples. From Figure 5.28, it is clear that no increase is observed with increasing gamma dose. The scatter in the 7 MGy 9:1 data is a product of the interaction volume and high BFS content.

The increased curing time prior to irradiation was suggested as a potential cause for the resistance to gamma-induced alterations. However, as outlined previously, the overall DoH of the precursors should barely change between 14 – 20 MGy and only change by a maximum of 12 % between 7 – 20 MGy. In terms of free water in the system, this varied but not linearly with increased curing time; the 20 MGy samples had higher free water than the 14 MGy. Even given these variations, the overwhelming similarity observed for all the systems in Figure 5.28 indicates that the pre-irradiation curing conditions and duration had little impact on the results.

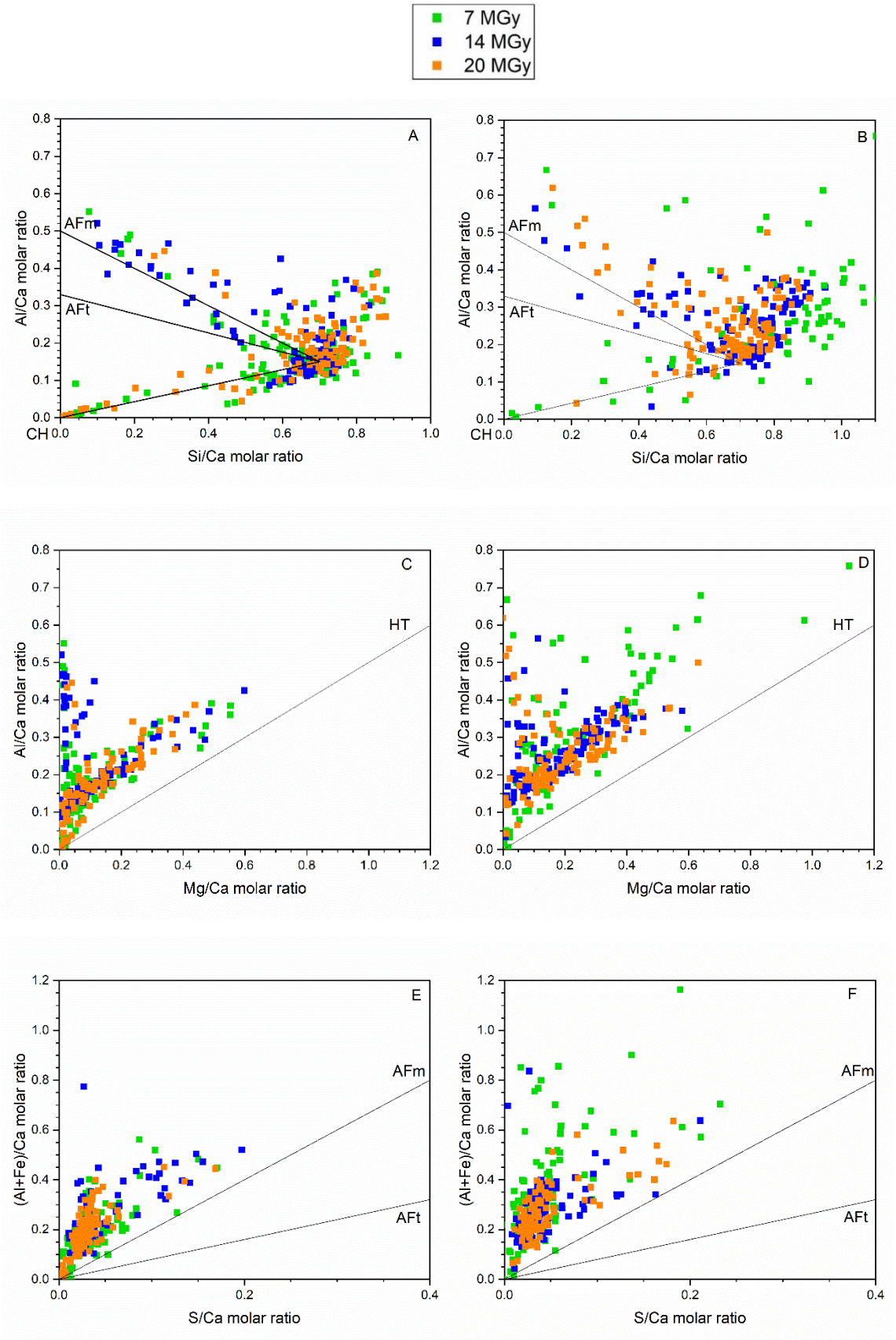

Figure 5.28 EDX point analysis showing effect of increasing total gamma dose for A,C,E: 3.44:1 BFS:PC; B,D,F: 9:1 BFS:PC systems. Each point sample was taken from a region that visually appeared to be binder rather than residual anhydrous phases. Tie lines link to the other prominent hydrate phases; CH: portlandite; AFm: monosulfoaluminate; AFt: ettringite; and HT: hydrotalcite.

A minor shift to lower Ca/Si ratios is seen in Figure 5.28A for the 20 MGy samples but this equates to a change of <0.05, which is much smaller than the error of these measurements. No distinct variation to the Mg or Al balance is observed despite the TGA results indicating an increase in hydrotalcite content. Sulfur-containing phases appear to remain stable at all doses of gamma, eliminating the possibility for radiolytic formation of ettringite from these BFS-containing grouts.

5.5.1.4 MAS NMR

The ^{29}Si MAS NMR spectra as a function of total dose are shown in Figure 5.29 and it is clear that the radiation exposure has caused variations in the C-A-S-H composition and structure. The changes appear more distinct in the 9:1 blend, again indicating that the higher replacement level increases the susceptibility to radiation.

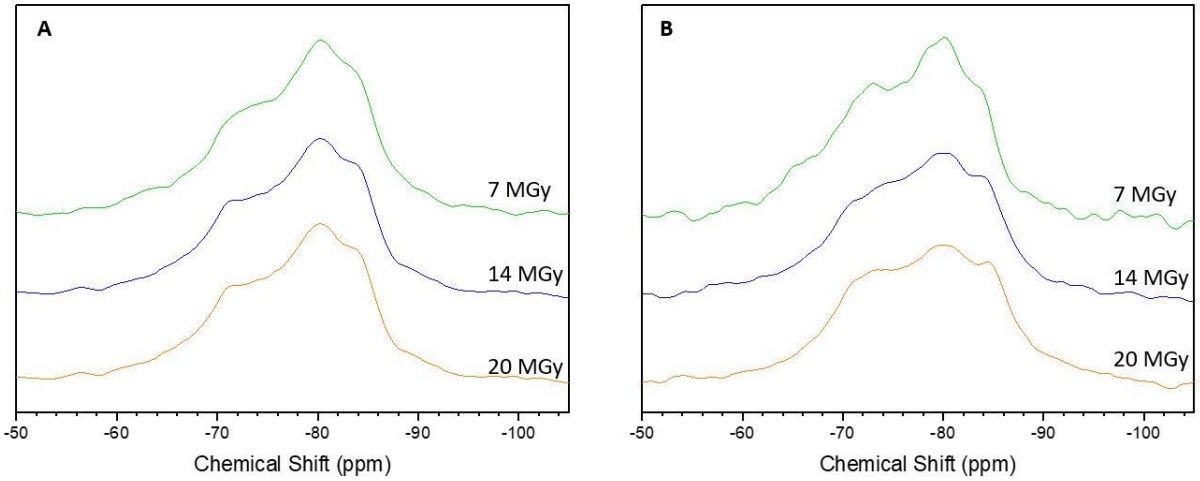

Figure 5.29 ^{29}Si MAS NMR spectra of A: 3.44:1 BFS:PC; B: 9:1 BFS:PC with increasing total gamma dose.

Estimation of the DoH of the BFS from complementary methods provided variable results, as seen in Table 5.25. However, given the intrinsic errors known to exist for both testing methods [149], [171], [220], the data are considered to display moderate agreement with the exception of the 14 MGy data. Estimation of clinker hydration provided figures that are considered realistic when compared to studies on similar systems for the 3.44:1 system; however, values are slightly low for the 9:1 blend [82].

Table 5.25 Degree of hydration of anhydrous components for 3.44:1 and 9: BFS:PC systems with increasing total gamma dose.

		BFS DoH (%)		Clinker DoH (%)					
				C_3S		C_2S		Total	
		3.44:1	**9:1**	**3.44:1**	**9:1**	**3.44:1**	**9:1**	**3.44:1**	**9:1**
7	**EDTA**	36 ± 5	24 ± 6	-	-	-	-	-	-
MGy	**^{29}Si NMR**	31 ± 11	21 ± 13	87 ± 5	81 ± 6	50 ± 8	59 ± 6	83 ± 13	79 ± 12
14	**EDTA**	42 ± 5	11 ± 8	-	-	-	-	-	-
MGy	**^{29}Si NMR**	24 ± 5	26 ± 8	86 ± 2	83 ± 2	64 ± 5	55 ± 4	84 ± 7	80 ± 6
20	**EDTA**	37 ± 5	20 ± 7	-	-	-	-	-	-
MGy	**^{29}Si NMR**	33 ± 5	25 ± 5	83 ± 4	80 ± 2	42 ± 7	42 ± 5	79 ± 11	77 ± 7

The BFS DoH from EDTA testing indicates fairly similar levels of hydration in the samples (within 5 %) with increasing total dose, suggesting that there is limited acceleration of hydration as a result of radiation exposure. Given this, the interaction of radiolytically-generated peroxide radicals with unreacted precursors is considered minor. This is in agreement with the lack of change observed in the SEM-EDX data but does not fit with the TGA results. The results for clinker hydration also show little variation with increased radiation dose.

Structural characteristics for the C-A-S-H show little variation in terms of molar ratios (Table 5.26), with minor reductions in 9:1 with increasing dose observed and no trend in the 3.44:1 sample. No overall alteration to bulk chemistry is indicated from this, supporting the finding of SEM-EDX. However, it is worth remembering the inherent errors that are involved with the deconvolution process and use of structural models to calculate these parameters [82], [229]. Variations may be masked by the assumptions of the deconvolutions.

Table 5.26 Structural characteristics of C-A-S-H at each total gamma dose. Calculated from deconvoluted ^{29}Si MAS NMR spectra.

	Ca/Si		Al/Si		MCL	
	3.44:1	**9:1**	**3.44:1**	**9:1**	**3.44:1**	**9:1**
7 MGy	1.1	1.0	0.12	0.16	6.6	7.4
14 MGy	1.1	1.0	0.13	0.13	7.1	8.1
20 MGy	1.1	1.0	0.13	0.13	6.5	9.5

The increase in MCL observed is considered to be due to the onset of carbonation. The impact of this is greater in the 9:1 blend, as the lower Ca/Si ratio makes it more susceptible to decalcification. However, only a slight change in Ca/Si was observed, from both deconvoluted spectra and SEM-EDX. Given the increase in MCL observed in the 9:1 system, a decrease in Ca/Si ratio of ~0.05 would be anticipated from C-A-S-H structural models [49]. To accurately assess a change of this magnitude, TEM-EDX of the C-A-S-H phase without intermixing from other phases within the interaction volume would be required. However, given that such a small change in Ca/Si ratio is anticipated, it is considered that limited decalcification of the systems has occurred and this is supported by the SEM-EDX results. Decalcification of C-S-H under ambient atmospheric conditions has been observed to be a slow process [197], [230] and these results indicate that radiation exposure does not significantly increase the carbonation rate. This may be impacted by the dose rate to which the samples are exposed but, as the rates used in this study are extremely high compared to those prevailing within wasteforms, this is considered a worst case scenario.

A summary of the proportions of Q^n species in each sample with increasing total gamma dose is shown in Table 5.27. No overall relationship was observed between total gamma dose and the proportion of Q^0 species; however, as was outlined in each section above, the overall intensity of this resonance increases as BFS intensity drops. Currently, it is not clear whether this is due to incongruent dissolution of BFS or the presence of aluminium in Q^1(1Al) sites. DoH estimation from scaling of the BFS peak provided variable results but the ^{27}Al NMR spectra indicate an increase in aluminium in the system that is not accounted for from the ^{29}Si spectra. Additional investigation using different methods would be required to resolve this.

Table 5.27 Results of ^{29}Si MAS NMR showing proportions of Q species with increasing total gamma dose from deconvolutions. The estimated uncertainty in absolute site percentages is ± 1 %.

		Q^0	Q^1(I)	Q^1(II)	Q^2(1Al)	Q^2	Q^3(1Al)	Q^3
3.44:1	**7 MGy**	6	11	19	21	29	14	0
	14 MGy	2	10	19	25	33	13	0
	20 MGy	4	12	20	23	27	15	0
9:1	**7 MGy**	4	9	20	30	37	0	0
	14 MGy	3	9	17	24	32	16	0
	20 MGy	4	12	20	23	27	15	0

There is an overall increase in the total proportion of Q^1 and Q^3 sites with irradiation and a decrease in the total number of Q^2 sites. This increase in polymerisation is expected to occur as a result of

carbonation but is somewhat contradictory with an increase in Q^1 (dimer/chain end) species. Carbonation usually reduces the total amount of Q^1 and Q^2 sites and this is seen in the 9:1 samples but is less clear in the 3.44:1 blend. Once again, this indicates that higher levels of BFS replacement increase the susceptibility to irradiation-induced carbonation. Estimation of the amount of decalcification as a function of gamma total dose was completed using the proportions of Q^1 and Q^2 species at 7 MGy and 20 MGy; values of 0.5 % and 15.6 % were observed for 3.44:1 and 9:1 systems respectively.

There was an increased proportion of aluminium linked sites in the ^{29}Si spectral deconvolutions of the irradiated samples, indicating an increased DoH of the BFS. Despite the estimations of DoH showing no significant increase as a result of irradiation, there are clear indications that there is some alteration to the aluminium balance in these cements as a result of gamma exposure. It is hypothesised that the small increase in Q^1 sites might be due to potential $Q^n(X\text{Al})$ sites not being accounted for in deconvolutions.

The ^{27}Al spectra support the hypothesis of gamma irradiation increasing the aluminium content/proportion of aluminium containing phases (i.e. Al within C-S-H and increased hydrotalcite and AFm) of the hydrated assemblage in these samples (Figure 5.30). For both blends, there was an increase in resonances associated with Al(IV) and Al(VI) environments with increasing dose. This suggests more hydration causing elevated aluminium concentrations in the systems. However, as this was not observed from the DoH analysis outlined in Table 5.25, it is unclear what is causing the observed behaviour in these samples.

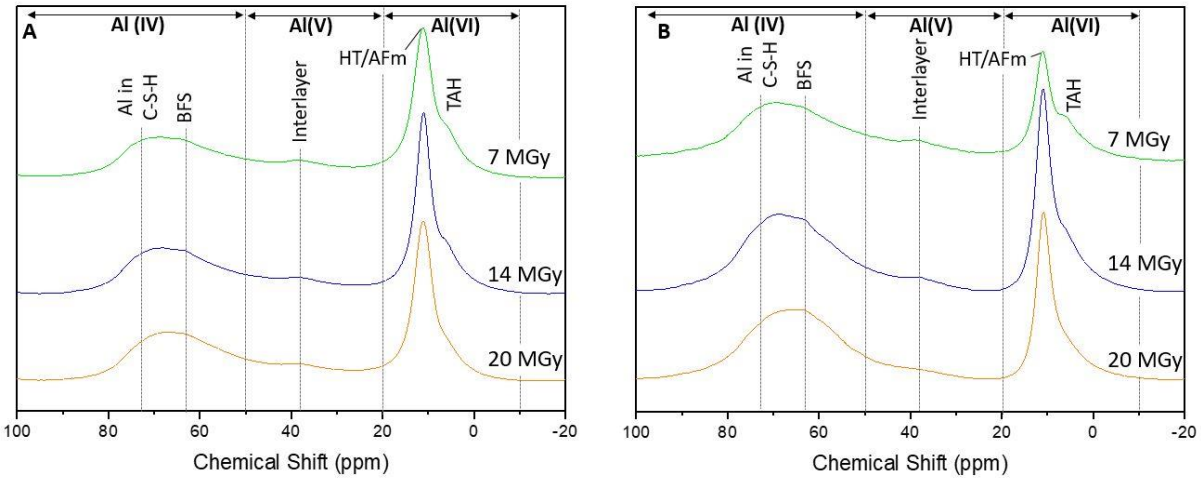

Figure 5.30 ^{27}Al MAS NMR spectra of A: 3.44:1 BFS:PC; B: 9:1 BFS:PC with increasing total gamma dose.

The increased resonance at lower chemical shift in the Al(IV) region was partly due to an increase in cross linking species, which may be why there appears to be such a marked reduction in the BFS peak with increasing gamma dose. The resonance associated with interlayer aluminium also appeared reduced with increasing gamma exposure.

The resonance attributed to TAH in the Al(VI) region significantly reduces as the radiation dose increases. This effect was not observed to the same extent in the control samples. The reduction in peak intensity is more significant at lower dose in the 9:1 blend, although the response in both systems after 20 MGy is similar. It is considered that the decrease in resonance associated with TAH is a product of carbonation; specifically, interaction of carbonates on the surface of C-A-S-H where both TAH and vaterite tend to form, leads to the destruction of TAH [80], [115].

5.5.2 Microstructure

SEM micrographs indicated very limited alteration to the microstructure as a result of irradiation exposure. No large scale cracking was evident in any of the cements, at any level of BFS replacement.

Analysis of the total porosity and pore size distribution via MIP indicates irradiation causes variations which were not observed from SEM analysis because the scale of pores undergoing changes was below the resolution of the SEM (Table 5.28). The response of the materials varied dependent on the level of BFS replacement; the 9:1 samples showed greater variation.

Table 5.28 Porosity measurements for irradiated samples from 3.44:1 and 9:1 BFS:PC systems obtained through MIP analysis.

	Total accessible pore volume (%)		**Critical pore entry radius (nm)**		**Threshold pore entry radius (nm)**	
	3.44:1	**9:1**	**3.44:1**	**9:1**	**3.44:1**	**9:1**
7 MGy	24	26	6	15	18	20
14 MGy	20	33	8	12	20	39
20 MGy	21	31	4	26	22	50

Increased total accessible pore volume was seen at higher total dose in the 9:1 sample, although an overall reduction was observed in the 3.44:1 sample. However, these differences were minor and may represent the error margins of the technique together with the variability of the samples. Given the

comparisons with control samples in the 3.44:1 blend, it is not considered that the reduced pore volume is a product of large scale pore filling from carbonation.

Critical pore entry radius increased by a minor amount in the 9:1 sample, although this was not observed in the 3.44:1 sample. Vaterite, which was identified in both samples, was assumed to have increased efficacy at pore filling in C-S-H agglomerations due to its lower density compared to calcite. This was speculated to cause a reduction in the proportion of small pores, shifting the pore size distribution and resulting in elevated critical pore entry radius. However, the 3.44:1 sample had a higher proportion of vaterite identified from XRD, and so this hypothesis is not appropriate for the 3.44:1 system. Although only minor reflections for vaterite were identified for the 9:1 sample, the ^{29}Si NMR results indicate an increased level of decalcification in the sample, showing that carbonation had occurred. Given that no increase in reflections for any polymorph of crystalline carbonate was observed from XRD analysis, perhaps the presence of amorphous or microcrystalline carbonation products caused the observed shift in pore size distribution. The reduced free water from irradiation may have prevented the recrystallisation of $CaCO_3$ to more stable forms.

For all samples, the threshold pore entry radius increases with total gamma dose. This means that the minimum radius that is geometrically continuous throughout the test volume is larger as a result of irradiation i.e. the increase in porosity is likely due to wider diameter, continuous features, such as cracks.

UPV values decreased by 4.0 % and 7.5 % in the 3.44:1 and 9:1 samples respectively. The increase in difference between the blends supports the variations observed in total accessible pore volume, further indicating that the higher BFS fractions increase the effects of radiation.

5.5.3 Mechanical properties

UPV results, Figure 5.31, show that increased exposure to radiation caused a reduction in the pulse velocity response, indicating an increase in the presence of discontinuities in the bulk. The reduction is smaller in the 3.44:1 blend and the global average decreases by small amounts successively after exposure to 14 MGy and 20 MGy. The results for the 9:1 sample show an initial large reduction after 14 MGy exposure; however, no further increase was observed at 20 MGy. No corresponding trend with heating is seen in the control samples, where reductions of 0.06 % and 1 % indicate that heating effects are unlikely to be responsible for the increase in discontinuities observed.

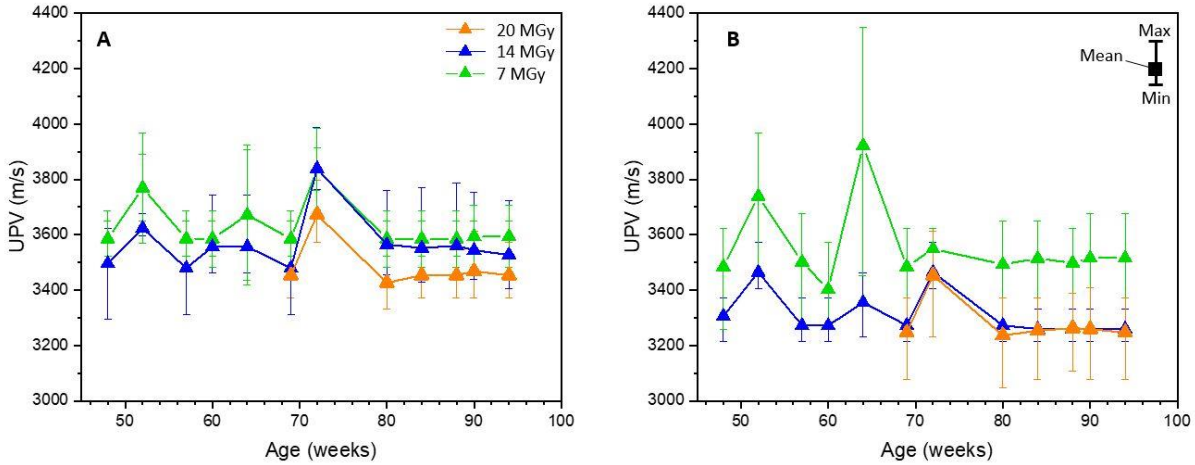

Figure 5.31 Comparison of UPV global mean values with increasing total gamma dose. A: 3.44:1 BFS:PC; B: 9:1 BFS:PC.

It must be noted that drying of the samples will reduce the transit time of the UPV. However, excess drying on top of that experienced by the controls is a product of irradiation, therefore the results of the testing are still valid. As outlined, the control samples were heated to remove the worst of this effect; however, the decrease in UPV may be a direct response to the radiolytic drying. Saturation of concrete is known to increase pulse velocity by 5 % [155]. Given that none of the irradiated or control samples are remotely close to saturation (the highest free water content was 5.2 %), it is considered that comparison between the systems is valid. In order to assess the change in UPV as a function of dose without drying effects, the variations in the free water content of the irradiated samples are considered together with the UPV reductions. The variation in the proportion of free water in the 3.44:1 sample from 7 MGy to 20 MGy is + 0.1 %, whereas the change in UPV is -4.1 %. For the 9:1 sample the change in free water is 3 %, whereas the change in UPV is + 7.4 %. This shows that, although the loss of free water is contributing to the reduction in UPV, it is not solely responsible.

Given this, the calculated stiffness constant and dynamic modulus of elasticity indicate an overall decrease as total absorbed gamma dose increases (Table 5.29). This indicates an increase in the potential capacity for deformation within the material.

Table 5.29 Summary of average change in material properties after 7, 14 and 20 MGy exposure from UPV measurement (comparative to control samples). Density of 2000 kg/m³ and Poisson's ratio of 0.28 were assumed [32].

BFS:PC	UPV change (%)		Compressive strength change (%)		K change (%)		E_d change (%)	
	3.44:1	**9:1**	**3.44:1**	**9:1**	**3.44:1**	**9:1**	**3.44:1**	**9:1**
7 MGy	-0.2	+2.9	-1.0	+19.0	-0.6	+6.1	-0.6	+6.1
14 MGy	-3.4	-4.1	-14.3	-22.0	-6.6	-7.9	-6.6	-7.9
20 MGy	-4.3	-3.5	-18.9	-19.0	-8.4	-6.9	-8.4	-6.9

The change in UPV, and therefore also in the material properties calculated from these values, does not linearly increase with increasing dose. Little variation indicated that minor initial strengthening may have occurred after 7 MGy exposure, despite the reduction in free water.

Estimation of compressive strength from the UPV results indicates a reduction of roughly 19 % in 20 MGy samples for both blends. This suggests that the overall impact of the irradiation does not vary significantly depending on the fraction of BFS replacement. However, the impact of radiation exposure in the 9:1 system appears to be greater at lower total dose; large deterioration was observed after 14 MGy but results after 20 MGy were similar.

Given that there are currently no specified compressive strength limits for waste management purposes in the UK, nor are threshold values for materials properties for wasteforms in place, these variations are considered interesting but not significant. As such, this level of radiation exposure is not considered to induce significantly detrimental differences in the bulk material. From this testing, the mechanical integrity of the wasteforms appears sufficient in radiation environments in excess of those they are planned to experience.

5.6 Conclusions

The impact of gamma irradiation on BFS:PC cements representative of the formulation envelope used by Sellafield Limited for encapsulation of nuclear waste was investigated. Assessment of changes to the phase assemblage, microstructure and mechanical properties was completed at 7, 14 and 20 MGy total gamma doses, with irradiated samples compared to controls of appropriate age and thermal history in each case.

Analysis of the phase assemblage post irradiation indicated no bulk alterations to the assemblage had occurred; however, limited variations in the proportions of the phases present were noted. Progressive radiolytic dehydration was observed which was linearly associated with total dose in higher replacement BFS samples but variable at lower replacement levels.

The variations observed in the phase assemblage were attributed to carbonation effects in the irradiated samples. The increased presence of vaterite in the irradiated samples indicates that irradiation assists formation of this phase, likely via the formation of calcium peroxide octahydrate, although no peroxide phases were detected in this study. The increase in vaterite content was greatest in the lower BFS replacement samples, where there were also reduced quantities of portlandite. In the higher BFS content samples, an increase in the carbonation of C-A-S-H and AFm rather than portlandite happened which resulted in a shift in the pore size distribution due to a reduced proportion of small pores. Analysis of ^{29}Si MAS NMR data was consistent with the identification of irradiation-induced carbonation, and again showed more changes in the C-A-S-H at higher BFS content.

The destruction of TAH was seen in the ^{27}Al MAS NMR spectra, and attributed to the interaction of carbonates on the surface of C-A-S-H where TAH is known to form. Irradiation was also observed to increase the resonances associated with aluminium inclusion in C-A-S-H and in AFm/hydrotalcite phases.

DoH analysis of the irradiated systems provided mixed results and is considered an area that requires further investigation. There were several indications that DoH of BFS had increased in the irradiated samples. In BFS-rich binders, a greater proportion of aluminium was observed in the Al(IV) and Al(VI) regions, indicating a shift in the chemistry of the system that was not observed through SEM-EDX.

Irradiation was observed to cause minor variations to the microstructure, with a shift in the pore size distribution indicating nano- or micro-cracking of the samples had occurred. This is in agreement with an overall reduction in compressive strength and an increase in potential deformation as a result of irradiation, as determined from UPV measurements. Due to the increased susceptibility to carbonation, the 9:1 sample showed a greater decrease in properties at lower total dose; however, the exposure to higher dose did not further decrease the measured UPV.

The scale of these changes in binder characteristics is considered minor, given that there are currently no threshold strength requirements for wasteforms. However, given the analysis here, it is suggested that the radiation stability of these materials was moderate to good and this should be considered in GDF safety case planning. However, the impact of α-radioysis on these cements is currently not well

understood and may cause more variation to the cement – albeit within more localised regions. In order to better understand how radiolytic effects within cements differ dependent on radiation type, Chapter 6 will investigate the impact of alpha emitting species on blended cement grouts.

6 Effects of plutonium dioxide encapsulation on the physico-chemical development of BFS and PFA blended Portland cement grouts.

Note: This chapter is based on the published paper entitled "Effects of plutonium dioxide encapsulation on the physico-chemical development of Portland cement blended grouts", *Journal of Nuclear Materials*, vol. 530, Article #151960, by Kearney et al. [231]. However, the section of the paper describing gas evolution measurements, conducted and drafted by collaborators at NNL, has been removed for presentation in this thesis.

Synthesis and laboratory analysis of the PuO_2 containing grouts was completed at NNL by Bliss McLuckie, Kevin Webb, Ian Vatter and Robin Orr, as outlined in Section 6.2.2.

6.1 Introduction

Plutonium contaminated materials (PCM) are a subcategory of ILW that includes process equipment and materials used in Pu finishing and mixed oxide (MOX) fuel pellets production, in addition to Pu-contaminated high efficiency particulate in air (HEPA) filters [232]. PCM waste is initially stored in 200 L drums prior to high force compaction, creating a puck that is encapsulated within a 500 L drum using a PFA:PC grout. These drums may contain up to 260 g Pu and ^{235}U, combined. The initial mean specific activity of PCM drums produced up to 2016 is ~1 TBq/m^3 alpha and 12.1 TBq/m^3 beta / gamma [91]. Over time, alpha decay leads to the ingrowth of actinide daughters, including isotopes of americium and uranium. Plutonium, within fuel residues, is also expected to reside in BFS:PC grouts used to encapsulate Magnox fuel swarf. These canisters, 500 L in size, have a mean specific activity of ~175 TBq/m^3, of which ~18 TBq/m^3 is from Pu isotopes [90], [128]. The interface between radionuclide species and cement materials, which may be highly localised, is of specific interest, since these areas can be subjected to high levels of ionising radiation throughout their service life. As such, it is important to build an understanding of how Pu, ranging from soluble nitrates to solid oxides, interacts with cement minerals.

Firstly, one must consider the role of radiation within the Pu-cement system. Two key processes are likely to induce reactions within cement materials upon irradiation: (i) radiolysis of pore fluid; and (ii) direct impact of alpha and alpha-recoil particles. Radiolytic decomposition of water generates H_2, e^-_{aq}, H, OH^-, H_2O, H^+, OH and H_2O_2 as primary products [99]; generation of $H_{2(g)}$ may pressurise the wasteform, leading to cracking of the cement and creation of a potential explosion risk [36], [233]. In grout systems containing BFS, the oxidation of sulfide to sulfate is of particular concern since internal sulfate attack may occur [124], [234]. This is analogous to external sulfate attack, where ettringite

forms at the expense of monosulfate and portlandite in an expansive nature, causing damage [125], [192].

Volumetric expansion is widely reported to result from direct impact of alpha- and alpha-recoil particles within crystalline phases [18], [235]. The production of damage zones, typically highly localised, will affect cement microstructure and cause expansion, which may impact physico-chemical properties; hypothetically, this may manifest as a layer of altered hydrates in alpha deposition zones, similar to radiohaloes seen in natural minerals [132], [133], [136], [137]. The localised absorption of energy around alpha emitting species could hypothetically increase pressurisation within closed porosity compared to gamma exposure to similar total dose and as such, cracking, chipping, spallation and reduction in compressive strength may be more prevalent.

One further consideration is the potential influence of radiolytic effects on degradation of the wasteform itself. For example, the degradation of organic materials such as cellulose, which was a significant component of PCM wastes prior to the 1980s, can produce gaseous products and soluble organic compounds that may result in swelling of the cement and increased radionuclide solubility, respectively [236], [237].

Given the potential for radiation effects in Pu-containing cement grouts, the aim of this chapter is to assess the impacts of alpha radiation, arising from PuO_2, on the hydration and physico-chemical properties of BFS and PFA:PC blended cement systems relevant to nuclear waste encapsulation. These results can be used to enhance understanding of ageing processes for existing encapsulated products and to support development of waste storage and disposal safety cases.

6.2 Materials and Methods

6.2.1 Materials

Portland cement conforming to Sellafield Ltd (SL) specification was supplied by Hanson Cement as Ketton coarse ground PC. BFS conforming to SL specification was also obtained from Hanson Cement as Scunthorpe GGBS blended with Calumite (a coarse ground material produced from blast furnace slag) in a 70:30 weight ratio. PFA was from the CEMEX Drax plant and conformed to BS EN 450-1 as well as the SL specification regarding performance in a pre-prepared grout mix [15]. Oxide composition and other available details of the powders are given in Chapter 3, Table 3.1.

Plutonium dioxide (PuO_2) was obtained from the Sellafield Ltd. Magnox reprocessing plant. PuO_2 is manufactured by precipitation of plutonium(IV)oxalate from plutonium nitrate, which is washed and calcined at 650 °C. The specific surface area of the PuO_2, determined by BET analysis using nitrogen as the adsorbate, was 11.8 $m^2 g^{-1}$. The isotopic composition is given in Table 6.1. The α particle dose rate

was $2.8x10^{10}$ MeV s^{-1} $g(Pu)^{-1}$. At the PuO_2 loading used in these experiments (0.5 wt.%) the dose rate to the sample was ~72 Gy h^{-1}.

Table 6.1 Plutonium and americium isotopic composition of PuO_2 accounting for ^{241}Am in-growth.

	^{238}Pu	^{239}Pu	^{240}Pu	^{241}Pu	^{242}Pu	^{241}Am
Wt. fraction heavy metal	0.0027	0.72	0.23	0.032	0.0011	$4.90x10^{-3}$

Selected samples were prepared with 5 wt.% microgranular cellulose to simulate organic containing waste streams, as degradation products can form soluble actinide complexes. Grout formulations representative of those used for encapsulation of ILW were prepared according to Table 6.2.

Table 6.2 Grout formulations.

Samples	Powder blend	Powder ratio	*w/s* ratio	Cellulose* (wt.%)	PuO_2* (wt.%)
BFS:PC	BFS:PC	3.44:1	0.35	-	-
BFS:PC + Pu	BFS:PC	3.44:1	0.35	-	0.50
BFS:PC + C	BFS:PC	3.44:1	0.35	5.0	-
BFS:PC + C + Pu	BFS:PC	3.44:1	0.35	5.0	0.50
PFA:PC	PFA:PC	3:1	0.43	-	-
PFA:PC + Pu	PFA:PC	3:1	0.43	-	0.51
PFA:PC + C	PFA:PC	3:1	0.43	5.0	-
PFA:PC + C + Pu	PFA:PC	3:1	0.43	5.0	0.49

*Expressed as a weight percentage of the grout mix mass

6.2.2 Sample synthesis

Grouts were first prepared in a non-radioactive laboratory using a method developed to assess powder properties for current intermediate level waste (ILW) encapsulation plant processes [15]. Cement precursors were added to deionised water while mixing (3L low-shear) over a period of 5 minutes, with PC added first, followed by another 5 minutes of mixing at low shear and then 10 minutes at 6000 rpm in a high shear mixer. Non-radioactive reference samples were prepared in ~1 cm^3 moulds. For formulations containing cellulose, cellulose powder was added by hand mixing to 100 g of cement paste. Within an α-radioactive glovebox, approximately 0.5 g PuO_2 was added to

100 g of cement paste (with or without cellulose) prior to mixing by hand and placing within ~1 cm^3 moulds. All samples were cured for 28 days in sealed bags with water to maintain high relative humidity, after which time they were de-moulded and cured in $Ca(OH)_2$-saturated water.

6.2.3 Sample characterisation

Characterisation of samples was performed after approximately one year of curing. Control samples were provided to the University of Sheffield to enable characterisation of the phase assemblage and microstructure, whilst the PuO_2 containing samples remained at the NNL active facilities to allow concurrent analysis. Analytical protocols were dictated by the constraints imposed of handling PuO_2 samples under local health and safety requirements. As a result, some variation from typical preparation methods was required. Hydration of the samples was not halted prior to any analysis, powders were crushed several days prior to analysis and stored under vacuum in a desiccator, and the materials did not undergo sieving before XRD and TGA testing.

6.2.3.1 Non-radioactive Reference Samples

Upon receipt from NNL, non-radioactive reference samples were stored in a controlled environmental chamber at 20 °C and 95 % relative humidity. After removal from the curing solution, slices were cut and mounted in epoxy resin or crushed into a fine powder. Sample preparation and analysis was co-ordinated with NNL, and the samples were stored in a Parafilm sealed jar inside a desiccator at room temperature until analysis was completed.

Sample preparation and SEM analysis were completed as outlined in Chapter 3, Section 3.3.11. Minor variations in sample preparation of powders were made; no sieving of the samples was completed, to align with the procedure used at NNL. Otherwise, TGA and XRD analysis were completed as outlined in Chapter 3, Sections 3.3.7 and 3.3.8 respectively.

6.2.3.2 PuO_2 Containing Samples

The PuO_2-containing samples were stored in glovebox facilities. No temperature controls were implemented in the glovebox. Samples were cut from the 1 cm^3 cubes for grinding and mounting for microscopy. Samples underwent successive grinding using 220 – 3 µm diamond suspensions with resin bonded diamond discs, followed by polishing using 1 µm – 0.25 µm diamond suspensions with alcohol based lubricant. Due to alpha handling protocols and equipment location, movement of the samples between laboratories was required for several of these stages increasing the overall preparation time. During this period the samples were stored in a glovebox.

TGA used 40 mg of sample, which underwent heating using the same parameters as the control sample in an alumina crucible. The raw TG data were processed to produce the derivative weight loss

using a Mathematica script based on Tikhonov regularization that calculates the first derivative via the second derivative [238], and a correction for the formation of condensation in equipment tubing during the initial hold temperature was applied. Quantities of $Ca(OH)_2$ and $CaCO_3$ were calculated using equations (3.7), (3.8). Variations in peak width and position are present between the PuO_2 containing and control results for all samples; this is likely the result of equipment differences.

XRD analysis was completed using a Bruker D8 ADVANCE with Cu Kα radiation operating between 5° < 2θ < 60° with a step size of 0.02 °2θ. The samples were mixed with Epofix resin (due to alpha handling protocols at NNL) and loaded into a polymethylmethacrylate (plexiglass) puck, giving rise to intense diffuse scattering in the background of all diffractograms. This was sealed using an additional layer of resin. The results were processed to subtract this background, and this has removed diffuse scatter associated with poorly crystalline hydrate phases and unreacted SCM. The data were subject to an overall plot offset of -0.25 °2θ to correct for equipment drift. Whilst this was effective for 2θ > 23°, peak positions at low angles are slightly more variable, potentially due to the data processing to remove the background scatter. SEM-BSE imaging was carried out using a Phenom ProX desktop instrument.

6.3 Characterisation results and discussion

6.3.1 Influence of PuO_2 on BFS:PC

6.3.1.1 3.1.1 Microstructural development

Figure 6.1 shows the development of a characteristic microstructure for BFS:PC grouts, displaying unhydrated cement clinker and BFS together with hydrate products including portlandite and AFm-type phases; these results are similar to the findings of Chapter 4 however the increased age of these samples has resulted in a much denser microstructure. Figure 6.2 shows a hydrated cement clinker grain and the surrounding matrix; textural differences between the denser appearing inner product and the surrounding outer product forming the remaining matrix can be seen. EDX analysis shows distribution of aluminium throughout the matrix indicating substitution into C-S-H to form C-A-S-H [56], [227]. Dark rims surrounding the BFS indicate hydration of the particle, forming a hydrotalcite-like product [196], [239]. Residual iron from the BFS can be seen in the Fe mapping [240]. High concentrations of sulfur are shown in Figure 6.2 which together with low Si content indicates high proportions of AFm-type phases in this region. Cracking was observed at a range of scales, thought to be the product of sample preparation rather than of curing.

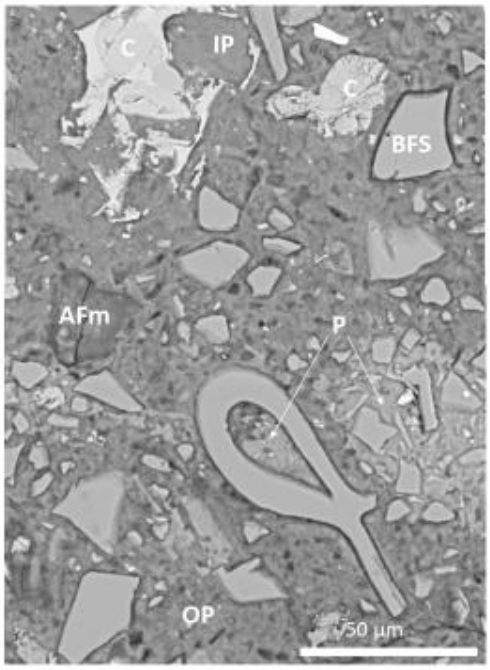

Figure 6.1 BSE micrograph of BFS:PC showing characteristic microstructural development and some identifiable phases: C: unreacted cement clinker, BFS: unreacted BFS (larger grains are Calumite), AFm: monosulfoaluminate-type phase, P: Portlandite (lighter grey area s of matrix), IP: matrix inner product, OP: matrix outer product.

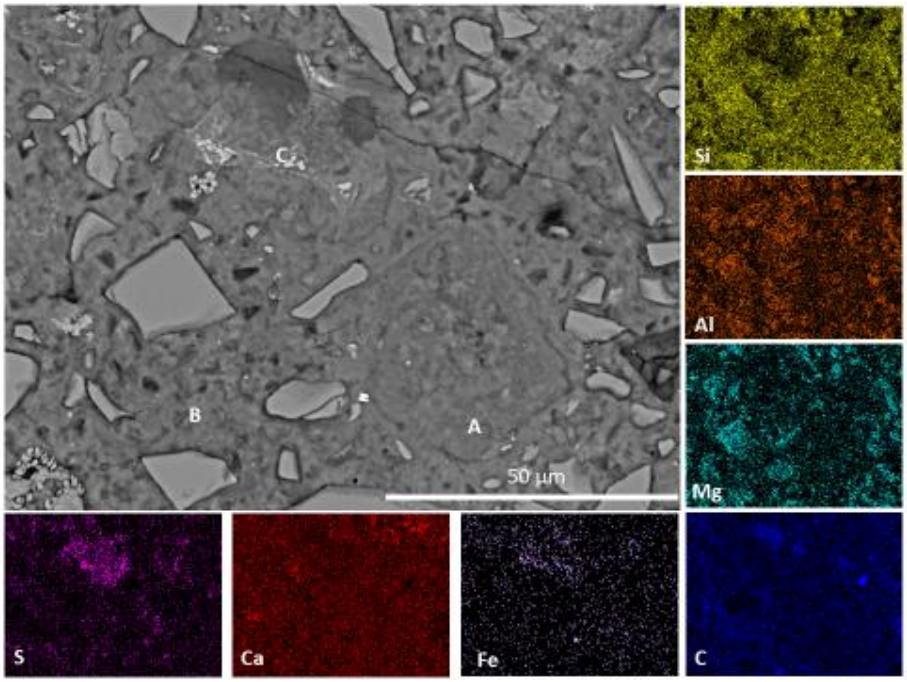

Figure 6.2 BSE micrograph and EDX analysis of BFS:PC grout showing a clinker grain which is almost fully hydrated. A: inner product C-A-S-H, B: outer product C-A-S-H and C: S rich inner product – potential AFm formation.

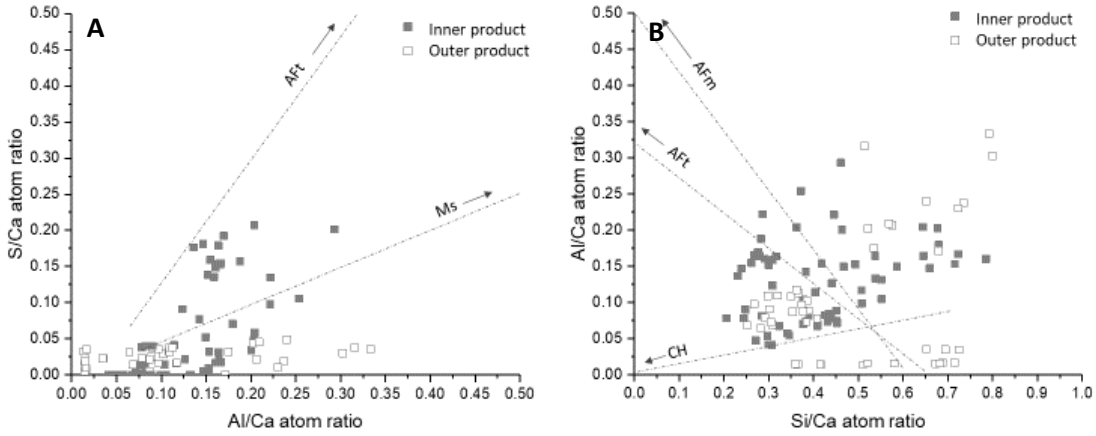

Figure 6.3 Atomic ratio plots from EDX spot analysis of areas A, B and C from Figure 2 demonstrating the variations in A: S/Ca and Al/Ca, and B: Al/Ca and Si/Ca across the matrix. Each point sample was taken from a region that visually appeared to be binder rather than residual anhydrous phases. Tie lines link to the other prominent hydrate phases; CH: portlandite; AFm: monosulfoaluminate; and AFt: ettringite..

Spot analyses from the BFS:PC samples were taken and ratio plots are shown in Figure 6.3. Due to intermixing of the hydrate phases results should not be treated as quantitative, but broad trends are provided such as lower Si/Ca ratio for the outer matrix product, and inner product areas containing higher proportions of sulfate containing phases. The Ca/Si ratio is higher than observed in Chapter 4; this is a product of the $Ca(OH)_2$ curing solution used for these samples.

The BFS:PC + Pu grouts display similar microstructural development, with no large scale defects present in the matrix (Figure 6.4). Large unreacted Calumite particles are identifiable in the hydrate matrix and areas of red-brown coloration were noted, thought to represent ferrite rich hydrate zones although no SEM EDX has been completed. Porosity estimations from the thresholding of the dark field images using ImageJ was 3.63%.

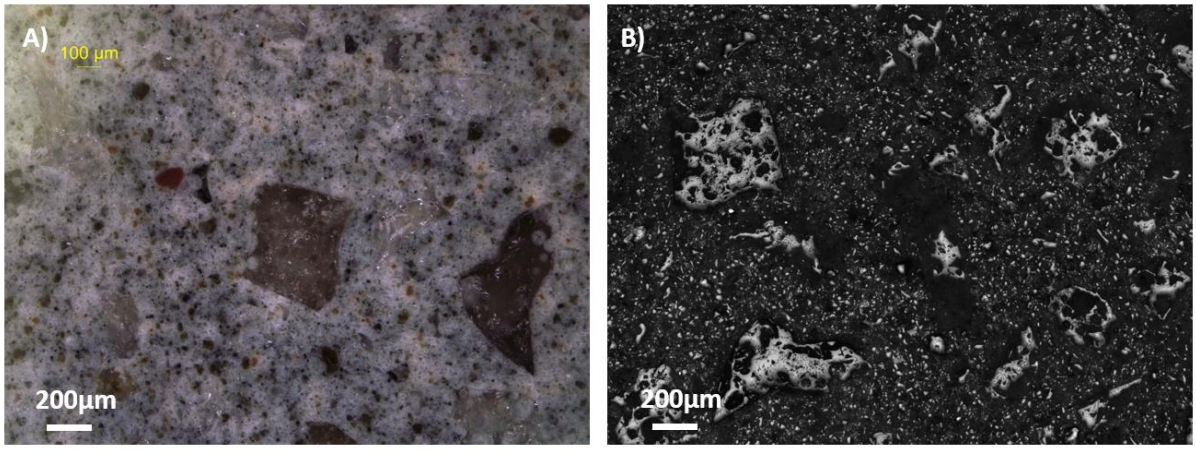

Figure 6.4 Optical images of BFS:PC + Pu cements. A) Bright field image, B) Dark field image

6.3.1.1.1 Effects of cellulose addition

The incorporation of cellulose powder does not appear to have had a significant impact on the microstructural development of the grout in the BFS:PC + C sample (Figure 6.5). Cracking in the cellulose is present, which may be due to sample preparation techniques together with cellulose degradation. There is some smudging evident at the outer boundaries of the encapsulated cellulose that may indicate greater decomposition of the cellulose material.

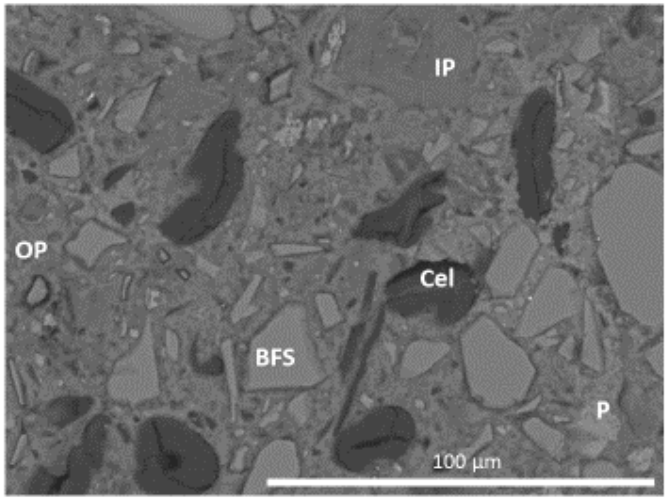

Figure 6.5 BSE micrograph of BFS:PC + C grout. Cel: cellulose powder, BFS: unreacted BFS (larger grains are Calumite), P: Portlandite (lighter grey areas of matrix), IP: matrix inner product, OP: matrix outer product.

BFS:PC + C + Pu samples show no significant microstructural alteration, with no large scale cracking observed in the bulk matrix (Figure 6.6). Porosity was estimated to be 3.1%, using thresholding of the greyscale histogram of the dark field images.

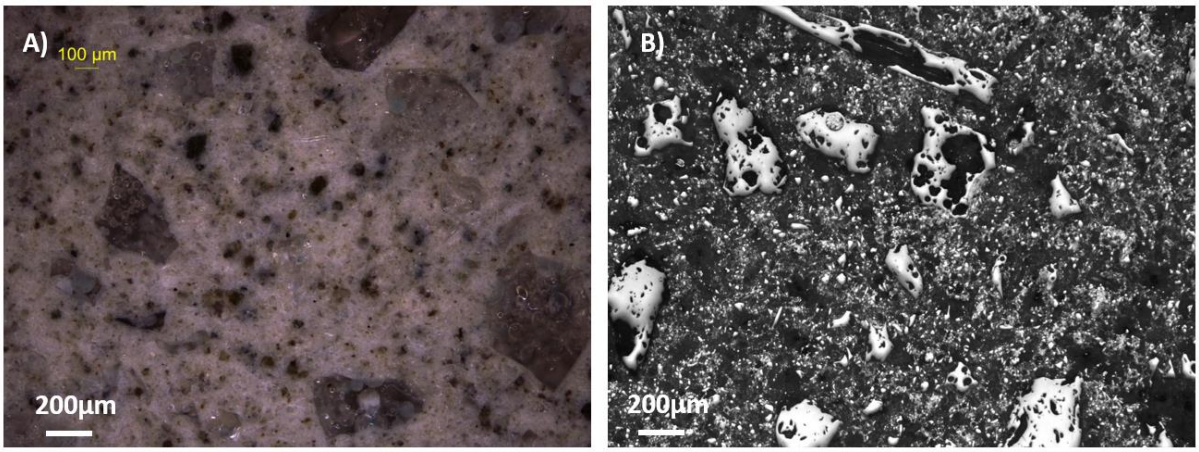

Figure 6.6 Optical images of BFS:PC + C + Pu cements. A) Bright field image, B) Dark field image

SEM investigation of the BFS:PC + C + Pu also showed no large scale defects in the matrix surrounding the PuO_2 particles, which appear to have been well encapsulated in the matrix (Figure 6.7). Limited investigation of the interface between the PuO_2 and the grout has been completed, however Figure 6.7 C) shows this area is of interest; label 1 indicates that good infilling of PuO_2 by the grout has been achieved around most of the particle, whilst label 2 shows a low contrast backscatter area which may be due to cellulose particles, or topographic differences that might be a result of a damaged zone [137]. Pervasive cracking was also not observed, indicating overpressure of the matrix through gas generation did not occur.

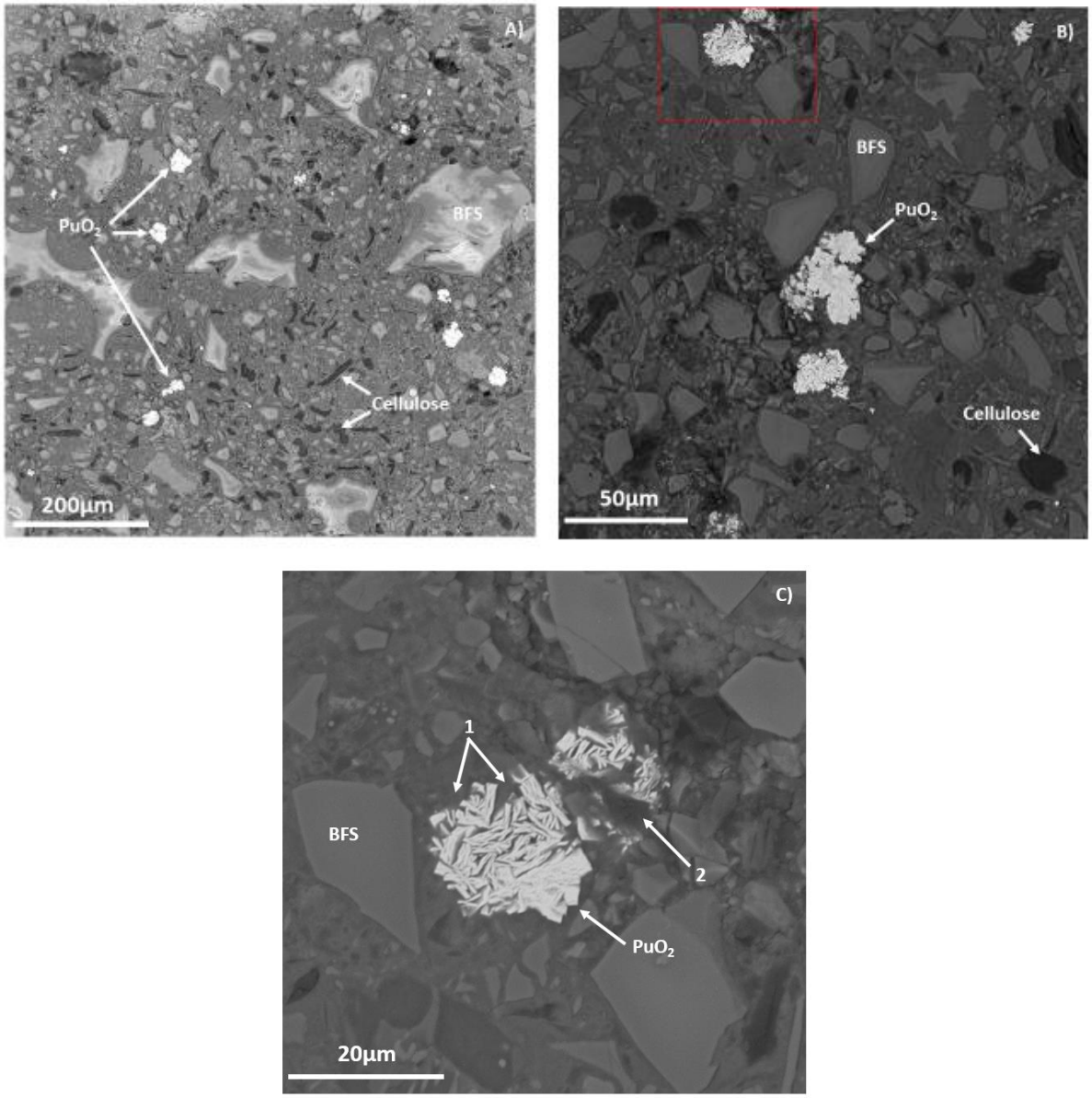

Figure 6.7 BFS:PC + C + Pu at increasing magnification levels in A), B) and C). Red zone in image B) shows PuO_2 particle shown in image C). Labels 1, 2, in image C) are expanded on in text.

6.3.1.2 Phase assemblage

The phase assemblage identified is typical of BFS:PC blended systems. XRD results display reflections attributed to ettringite (PDF# 41-1451), monosulfoaluminate (PDF# 83-1289), hemicarboaluminate (PDF# 014-0221), hydrotalcite (PDF# 14-0191), monocarboaluminate (PDF# 36-0377), portlandite (PDF# 04-0733), C-A-S-H, and calcite (PDF# 01-0837) together with unreacted belite (PDF# 29-0369) and BFS (attributed to the diffuse scatter at 25°<2θ<35°) are indicated in Figure 6.8. The peaks from the PuO_2 are shown by the light grey dashed lines.

Due to the background stripping analysis, the peak intensities and peak widths cannot be used to quantitatively evaluate radiation-induced variations in crystal structure. Qualitative evaluation of phase assemblage was completed by assessing the peak positions and intensity. Variation in the diffraction patterns was observed at low angles, where the peak associated with the (100) ettringite reflection had higher intensity in the BFS:PC + Pu sample. A slight shift in peak position was noted, however this is thought to be a product of the original peak offset having less impact at low angles rather than substitution either of Fe for Al in the ettringite [66], or of a shift in the end member proportions of the AFm phases [69].

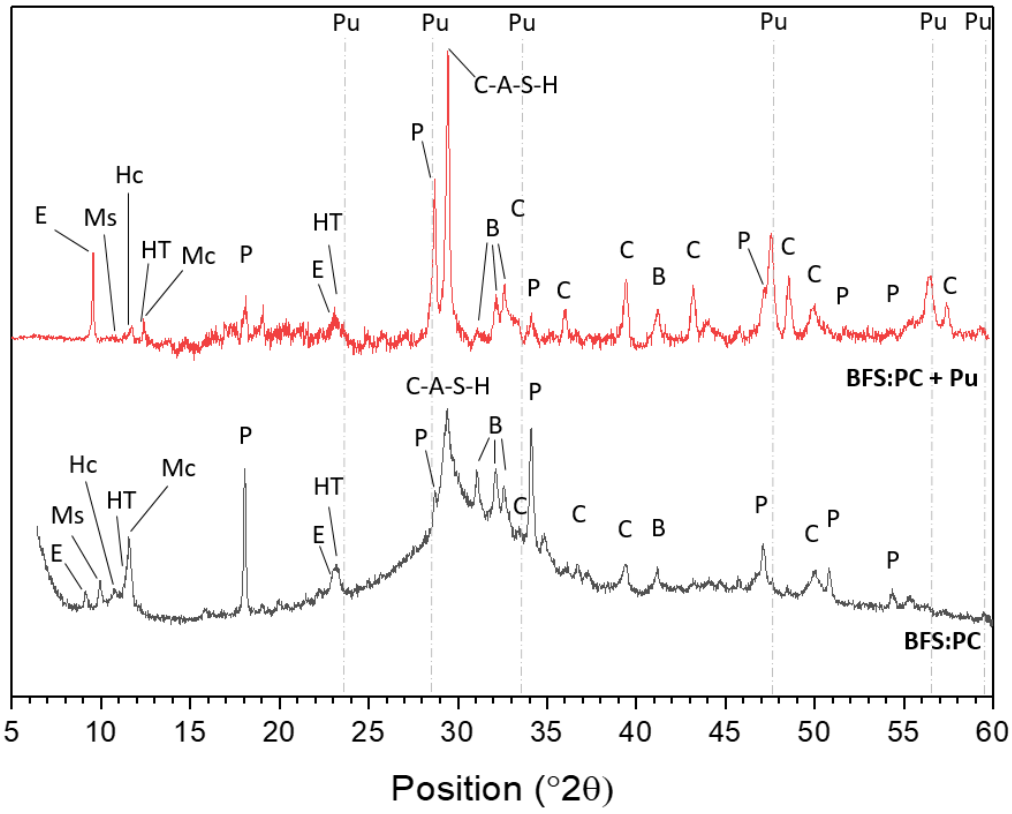

Figure 6.8 X-ray diffractograms of BFS:PC and BFS:PC + Pu grouts. E: ettringite, Ms: monosulfoaluminate, Hc: hemicarboaluminate, HT: hydrotalcite, Mc: monocarboaluminate, P: portlandite, C-A-S-H: aluminium substituted calcium silicate hydrate, B: belite (C_2S), C: calcite, Pu: PuO_2.

The increase in peak intensity for ettringite compared to the peaks for monosulfoaluminate (not present), monocarboaluminate, hydrotalcite, and hemicarboaluminate indicates an increase in the proportion of ettringite present in the BFS:PC + Pu sample. This increase may be the result of radiolytic induced oxidation of sulfide released from the BFS, as observed by Richardson et al. [124] in gamma irradiation studies. The presence of ettringite was not observed at the expense of monosulfoaluminate in that study, unlike the results shown here. The reduction in the peak intensities for the AFm phases (monosulfoaluminate, monocarboaluminate, hemicarboaluminate) in the diffraction patterns may indicate that the increase in sulfate content was sufficient to allow later age conversion back to ettringite. However, as AFm phases are partially XRD amorphous, comparison of peak intensities may be misleading and overlapping dehydration temperatures for these phases in TGA offers no further clarification [161], [162].

The sulfate content of the BFS:PC systems will only increase if both the degree of hydration (DoH) of BFS increases and there is a sufficiently oxidising environment to convert the released sulfide to sulfate. Prentice et al. [82] found the DoH in Sellafield Ltd specification 3:1 BFS:PC system to be between 50-55% for BFS after one year, with alite and belite hydration at 85% and 53% respectively. There was no intermixing of Calumite with the GGBS fraction in the Prentice study, and the larger particle size of the Calumite component will reduce the degree of reaction in the current study; Sanderson et al. found the behaviour of Calumite to be similar to an inert filler [181]. For the 30 wt.% Calumite replacement in the current study, it is estimated that the DoH is reduced by approximately 10 % [176] relative to Prentice et al. This is broadly supported by the findings of DoH testing using EDTA solution on 'Control' samples of 3.44:1 BFS:PC in Chapter 5 (Sections 5.2.1.4, 5.3.1.4 and 5.4.1.4), despite the difference in age of the samples.

The DoH of the slag has been estimated to be between 40 – 50 % given the level of Calumite replacement. The clinker hydration has been modelled using the Parrott and Killoh [241] method, after Lothenbach [242]; the degree of hydration of each clinker phase is shown in Table 6.3.

Table 6.3 Clinker phases present in anhydrous PC calculated (Taylor-Bogue method [243] *using data from Table 3.1, and estimated DoH*

Clinker phases	% present in anhydrous PC	% hydrated	Overall DoH
Alite	63.4	81.2	72.3
Belite	16.0	39.7	
Aluminate	7.4	61.2	
Ferrite	7.9	77.9	

The XRF analysis of the anhydrous materials (Chapter 3, Table 3.1) allows the sulfate content of the 3.44:1 BFS:PC system assuming complete oxidation of sulfide to be estimated given different DoH values for the BFS and PC. Given the estimated range of DoH, the concentrations are not anticipated to vary significantly without oxidation of the sulfide (Table 6.4).

Table 6.4 Sulfate content of 3.44:1 BFS:PC at varying DoH, with and without the contribution of oxidised sulfide from BFS.

		% DoH PC			% DoH PC	
		70	75		70	75
		sulfate (g / 100g solid)	sulfate (g / 100g solid)	+ Sulfide oxidation	sulfate (g / 100g solid)	sulfate (g / 100g solid)
% DoH BFS	40	0.061	0.064		0.233	0.236
	45	0.063	0.066		0.256	0.260
	50	0.065	0.068		0.280	0.283

Thermodynamic modelling of similar systems (unirradiated) [82] predicts ettringite to be replaced by monosulfoaluminate in the phase assemblage by 28 days; monosulfoaluminate and hemicarboaluminate were predicted to be the major AFm components. The persistence of ettringite together with AFm phases can be seen in the XRD data for the BFS:PC control samples (Figure 6.8), indicating the sulfate had not decreased as predicted. The replacement of ettringite requires a reduction in the SO_3/Al_2O_3 ratio of the system, which occurs as depletion of gypsum and hydration of BFS progresses [69], [82], [125]. The stability of the AFm phases that are formed upon replacement of the ettringite is also dependent upon the bulk CO_2 content of the system, as the stability of monosulfoaluminate decreases significantly with increasing carbonate contents; the phase assemblage identified by XRD indicates molar bulk ratios of CO_2/Al_2O_3 and SO_3/Al_2O_3 of below 0.5 and between 1 – 3 respectively [69]. Given the increased carbonation observed in the XRD and TGA results for the PuO_2 samples (Figure 6.8, Figure 6.9), the variations in monosulfoaluminate and ettringite may be in part a product of the destabilisation of monosulfoaluminate due to CO_2 increases rather than dramatic sulfate increase.

As can be seen from the above, later age conversion of the AFm phases to ettringite is not only dependent on an increase in sulfate. As the hydrating BFS is assumed to react congruently, the released sulfide is accompanied by Al_2O_3. In terms of oxidation of sulfide, it is considered that this would likely take place as it is released, as radical formation is continuous, rather than remaining as

sulfide indefinitely until some mass oxidation event allows conversion to sulfate. Given this, for the complete removal of monosulfoaluminate the Al_2O_3 released would have to be bound into a separate hydrate phase; Taylor et al. summarise several factors that can impact on the Al_2O_3 availability, including the MgO, and CO_2 contents allowing formation of hydrotalcite and carboaluminate phases respectively [125].

It seems unlikely that there would be sufficient sulfate together with the necessary reduction in Al_2O_3 and $CaCO_3$ to allow full conversion of all the monosulfoaluminate to ettringite, however further investigation is required, as this represents a complex set of interactions within a simplified system; the interaction of the waste components in final waste packages is not included here.

TGA results also show variations between the PuO_2 containing and control samples (Figure 6.9). The initial weight loss between 30 – 300 °C is the result of the loss of free water, C-A-S-H, ettringite, and AFm phases (likely monocarboaluminate (140 – 180 °C) and monosulfoaluminate (180 – 210 °C)). The initial peak at 100 °C is typical of cements containing ettringite, and slight broadening of this peak in the PuO_2 containing sample may be due to loss of free water or slight variations in experimental setup [161]. Weight losses at 350 – 400 °C and 400 – 480 °C correspond to the dehydroxylation of hydrotalcite and portlandite respectively, and losses > 500 °C are attributed to carbonate decomposition [194].

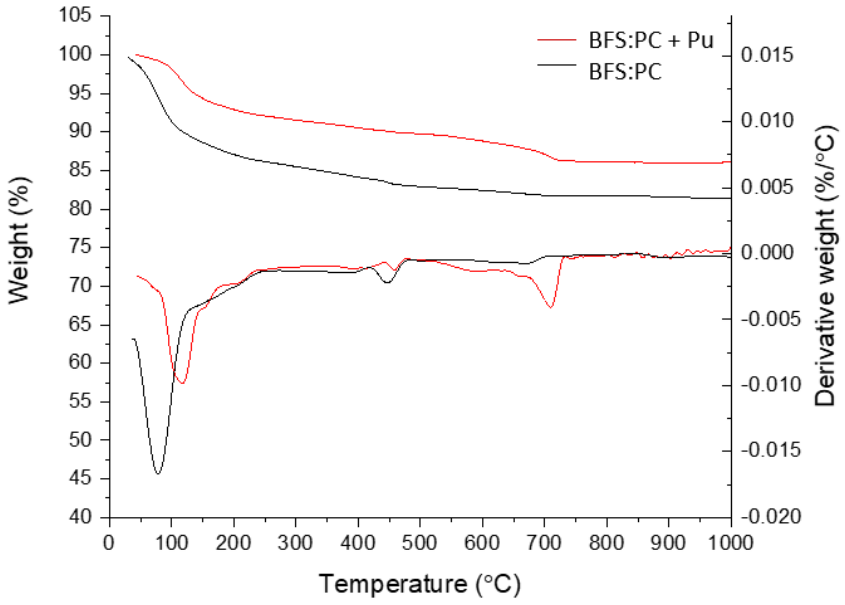

Figure 6.9 Thermogravimetric analysis of BFS:PC and BFS:PC + Pu.

Estimations of free water loss were calculated together with the relative proportions of $Ca(OH)_2$ and $CaCO_3$ for each sample, and the results for all samples are shown in Table 6.5.

Table 6.5 Amount of free water loss, $Ca(OH)_2$ and $CaCO_3$ detected by thermogravimetry. Results should be treated tentatively and considered semi-quantitative.

Cement formulation	Free water loss (mass ratio)	$Ca(OH)_2$ (mass ratio)	$CaCO_3$ (mass ratio)
	PuO_2:Control	PuO_2:Control	PuO_2:Control
BFS:PC	0.3 : 1	0.4 : 1	2.4 : 1
PFA:PC	0.3 : 1	-	1.6 : 1
BFS:PC + C	0.5 : 1	0.6 : 1	0.7 : 1
PFA:PC + C	0.3 : 1	-	1.1* : 1

*Data acquisition for this sample is suspected to contain errors at temperatures > 750 °C

Greater free water loss was seen in the BFS:PC sample, and more $Ca(OH)_2$ remained. Increased weight loss between 500 – 700 °C in the BFS:PC + Pu sample suggests decomposition of mono- and hemi-carbonate species, and may indicate that vaterite / aragonite polymorphs of $CaCO_3$ are present [115], [194], [195]. Given the variations in storage conditions between the radioactive and non-radioactive samples in the period between preparation and analysis, atmospheric carbonation effects cannot be fully evaluated and as such the contribution of radiolytic effects, if any, cannot be ascertained. Maruyama et al. [122] found that an increase in bending strength occurred in gamma-irradiated PC samples, which they attributed to increased deposition of aragonite and vaterite. They considered the carbonation products formed maintained the interlayer space within C-S-H due to the "higher pore filling efficiency" of vaterite counteracting defects in the pore structure around C–S–H. This indicates that the types of carbonate products formed, and their location within the phase assemblage, have implications for strength development. As such, further work is required to assess how potential strengthening competes with damage caused through alpha interactions.

6.3.1.3 Effects of cellulose addition

Cellulose addition caused alteration of the proportions of hydrates but no overall changes to the phase assemblage were observed (Figure 6.10). Peak intensities for ettringite, hydrotalcite and monocarboaluminate increase with cellulose addition, whereas a reduction in the peak intensity for monosulfoaluminate was observed.

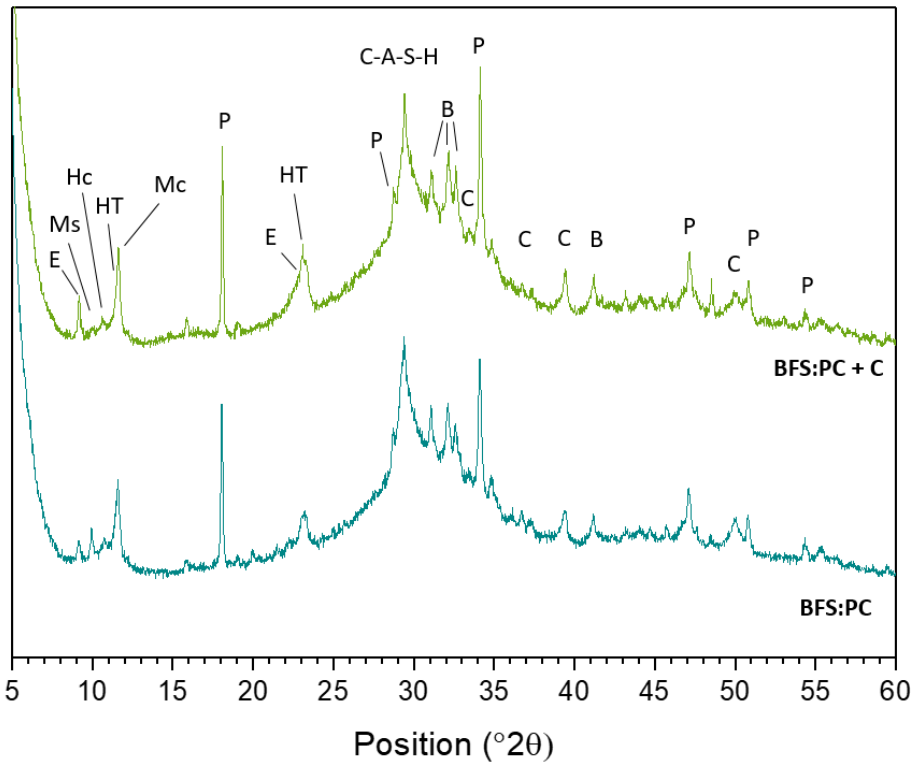

Figure 6.10 X-ray diffractograms of BFS:PC and BFS:PC + C grouts. E: ettringite, Ms: monosulfoaluminate, Hc: hemicarboaluminate, HT: hydrotalcite, Mc: monocarboaluminate, P: portlandite, C-A-S-H: aluminium substituted calcium silicate hydrate, B: belite (C_2S), C: calcite

These variations indicate carbonate rich cellulose degradation products influence the phase assemblage, particularly carbonate rich AFm-type phases. The increase in ettringite may be a product of this, as the Al_2O_3 binding to AFm phases will keep the SO_3/Al_2O_3 ratio high [125]. Cellulose degradation does not appear to influence the calcite content, as reflections are similar in both diffractograms. The effects of atmospheric carbonation are considered negligible in all control samples due to the same curing and preparation conditions.

Addition of PuO_2 causes shifts in the proportions of phases present (Figure 6.11). The loss of free water and $Ca(OH)_2$ are lower in the BFS:PC + C + Pu sample, as seen in the non-cellulose samples (Table 6.5). The split peak at 100 °C in the PuO_2 containing grout may be a due to loss of free water prior to ettringite dehydration, or a result of the sample size and differences in equipment setup [161]. The weight loss between 300 – 400 °C is indicative of cellulose decomposition [244]. The weight loss observed in the BFS:PC + C + Pu sample at temperatures > 550 °C is lower than the control sample, indicating less carbonate products are present. This trend is not observed in any other PuO_2 containing samples, and is surprising as cellulose degradation can lead to increased carbon dioxide formation [236].

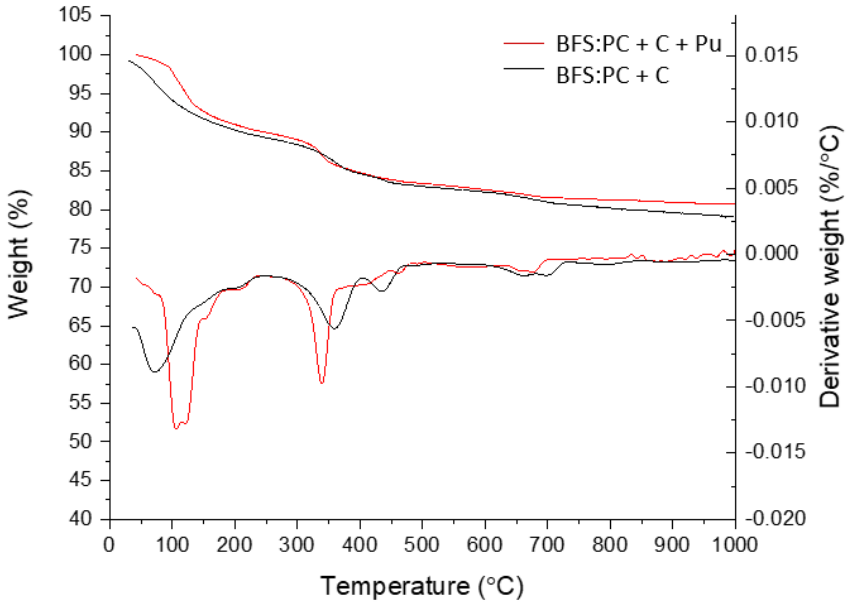

Figure 6.11. Thermogravimetric analysis of BFS:PC +C and BFS:PC + C + Pu

6.3.2 Influence of PuO_2 on PFA:PC

6.3.2.1 Microstructural development

Characteristic microstructures were observed for PFA:PC grouts with textural differences in the matrix indicative of inner and outer product formation during hydration, similar to the results outlined at younger ages in Chapter 4. Unreacted precursor material was identified and no pervasive cracking was observed (Figure 6.12).

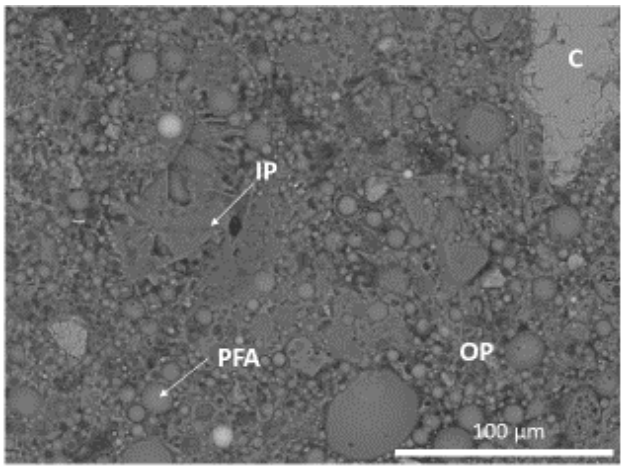

Figure 6.12 BSE micrographs pf PFA:PC sample. Unhydrated cement clinker: C, unreacted PFA: PFA, matrix inner product: IP, matrix outer product: OP

EDX analysis indicates a hydrated phase assemblage containing C-S-H incorporating Al [71], [77] and sulfur containing AFm/AFt phases. Unburnt carbon particles from the PFA were observed as darker zones in the matrix (Figure 6.13). Minor alteration was observed on surface of some PFA particles; aluminium enrichment and dendritic features were identified. These dendritic features may represent mullite crystals that are exposed as the hydration of the glass phase of the PFA consumes the particle [245], [246]. The matrix texture appears slightly less dense than in the BFS:PC samples, which could be the result of the slower rate of reaction of PFA in PC blends [71].

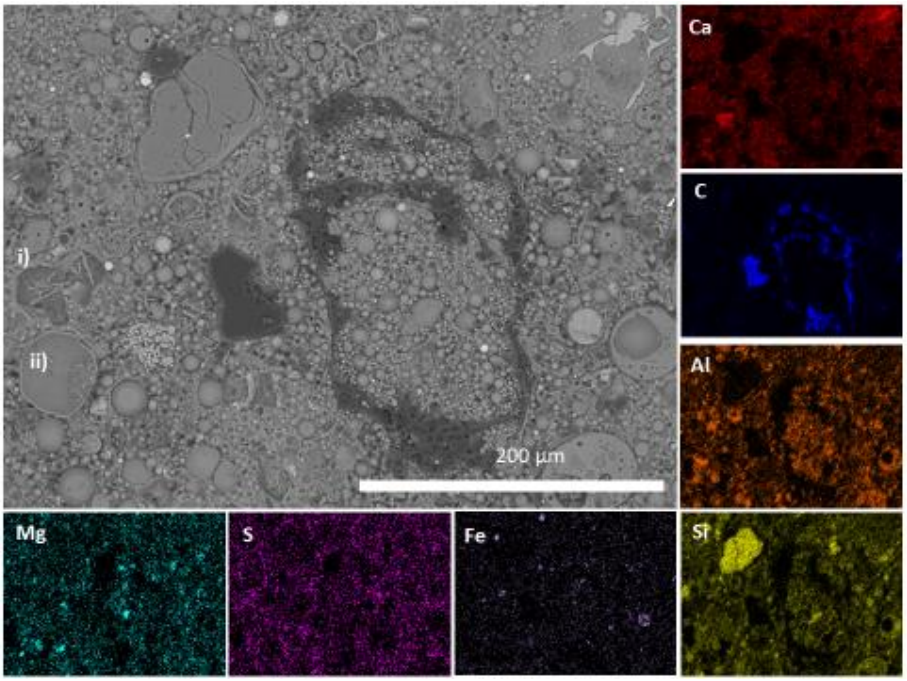

Figure 6.13 BSE micrograph and EDX analysis of PFA:PC showing unburnt carbon particle. Label i) shows ettringite needle formation, and ii) Al enriched PFA rim.

The PFA:PC + Pu samples displayed similar textures, and the PuO_2 does not appear to have significantly impacted the matrix. Optical investigation indicated no pervasive deformation of the bulk, with no large cracks identified (Figure 6.14).

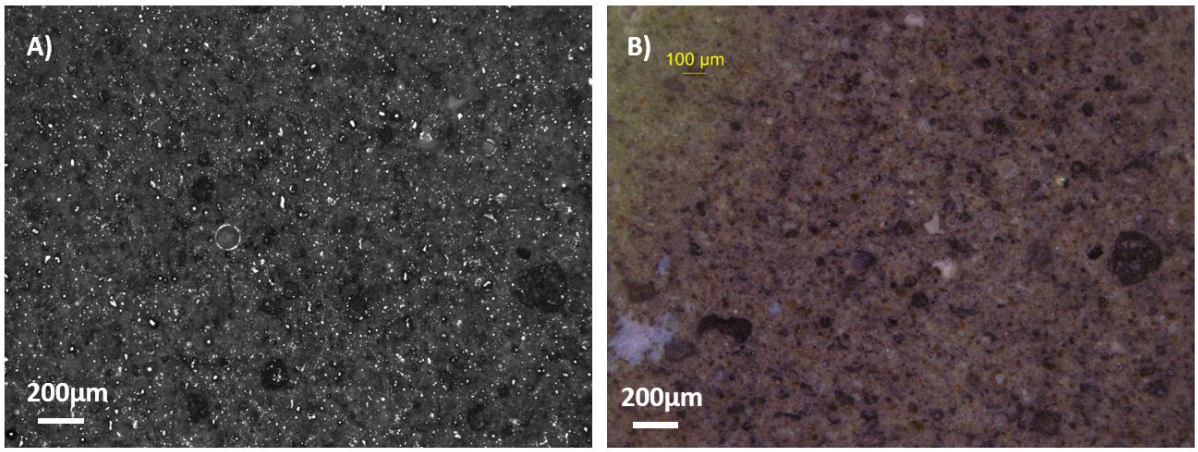

Figure 6.14 Optical images of PFA:PC + Pu. A) Dark field image, B) Bright field image

SEM analysis of PFA:PC + Pu (Figure 6.15) also indicates there is smaller scale cracking, and the PuO_2 particles are well encapsulated albeit with less intimate contact to the grout than seen in the BFS samples (Figure 6.7, Section 6.3.1.1.1). This effect is exaggerated in Figure 6.15 B) due to the high contrast PuO_2 particle; the dark areas adjacent to the particle are likely low contrast hydrate products.

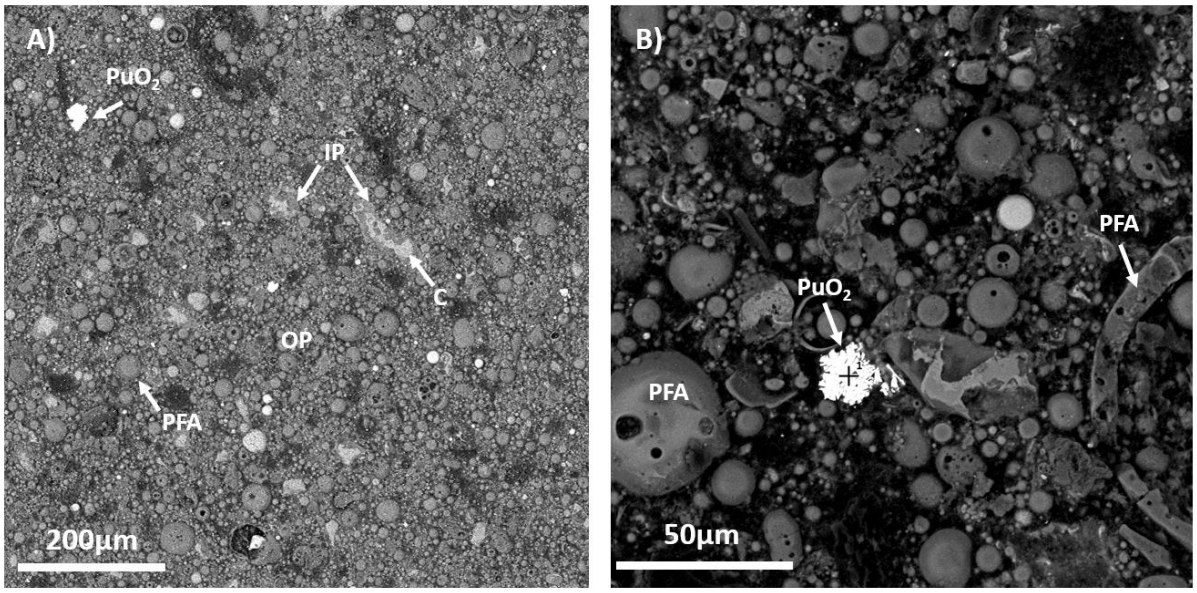

Figure 6.15 BSE images of PFA:PC + Pu at increasing magnification. Unhydrated cement clinker: C, unreacted PFA: PFA, matrix inner product: IP, matrix outer product: OP

6.3.2.1.1 Effects of cellulose addition

The cellulose powder appears well encapsulated in the PFA:PC + C samples with limited impact on the microstructural development. The phase assemblage is as identified in the PFA:PC grout, with similar textural development observed. Some dehydration of the cellulose is apparent, with cracking and shrinkage away from the grout encapsulant (Figure 6.16).

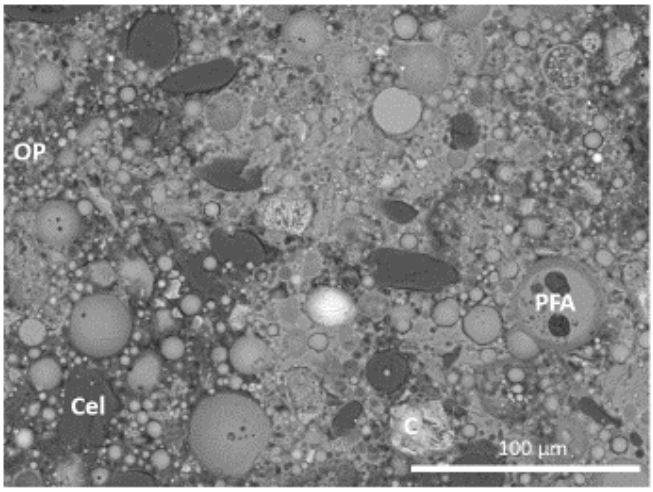

Figure 6.16 BSE micrograph of PFA:PC + C grouts showing encapsulation of cellulose powder in the matrix. Cel: cellulose powder, PFA: unreacted PFA, OP: matrix outer product.

PuO_2 addition does not appear to significantly affect the microstructure, with no pervasive cracking noted in PFA:PC + C + Pu samples (Figure 6.17). Optical images show a dense microstructure, with identifiable unburnt carbon particles and PFA in the hydrate matrix. Porosity was estimated at 2.9% using thresholding of the greyscale histogram. Zones of red brown colouration similar to those identified in the BFS:PC blends are present, together with highly reflective white regions (as seen in Figure 6.14 B and Figure 6.17 B); these may represent zones of unhydrated PC or PFA agglomerations within the matrix.

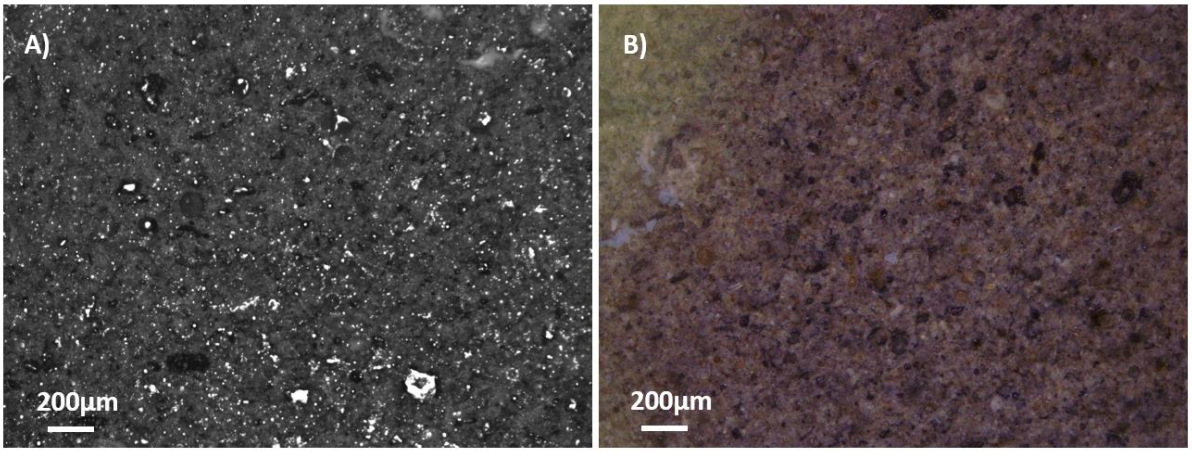

Figure 6.17 Optical images of PFA:PC + C + Pu cements. A) Dark field image, B) Bright field image.

6.3.2.2 Phase assemblage

The PFA:PC materials contained strätlingite (PDF#-29-0285), mullite (PDF#-79-1453), and quartz (PDF#-85-0335) in addition to several phases identified in the BFS containing blend (Figure 6.18).

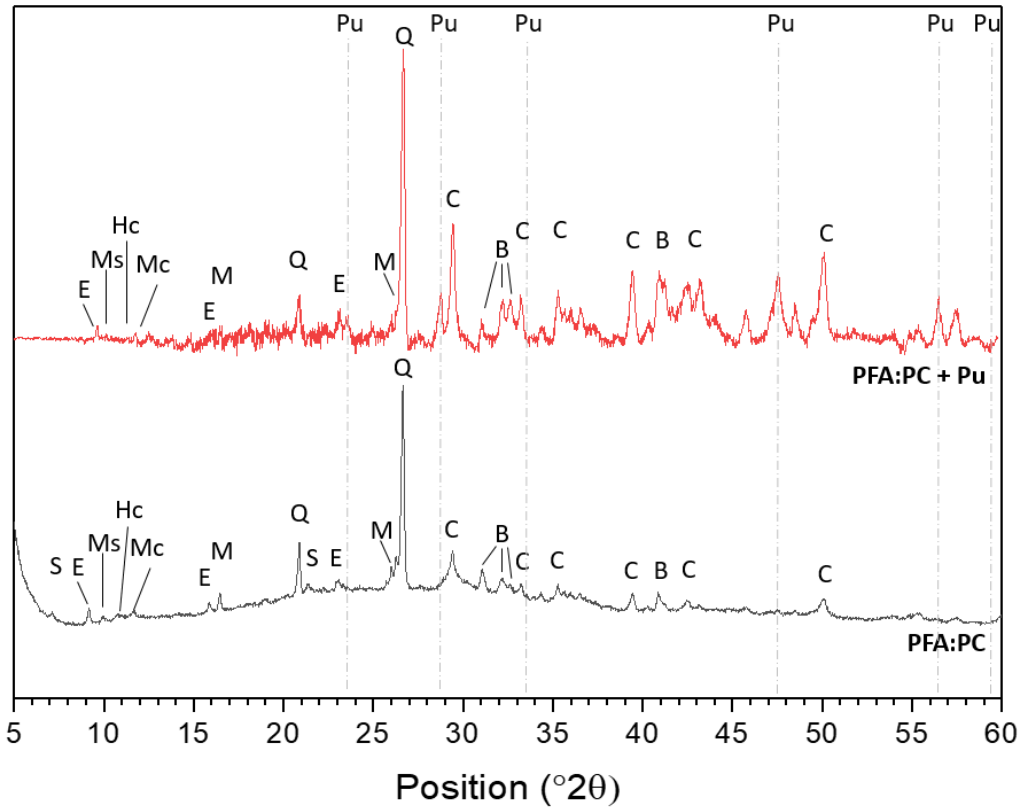

Figure 6.18 X-ray diffractograms of PFA:PC and PFA:PC + Pu grouts. S: strätlingite, E: ettringite, Ms: monosulfoaluminate, Hc: hemicarboaluminate, Mc: monocarboaluminate, M: mullite, Q: quartz, B: belite (C_2S), C: calcite, Pu: PuO_2.

The shift in peak position for the [100] ettringite reflection was observed in the PFA:PC + Pu sample (discussed in section 6.3.1.2), however no significant alteration in the peak intensity was noted. The monosulfoaluminate reflection is not present in the PFA:PC + Pu diffractogram, indicating potential destabilisation of monosulfoaluminate. However, no formation of other sulfate containing phases is noted, and so it is considered a result of the background stripping applied to the data. Strong reflections for calcite are observed in the PFA:PC + Pu sample, and TGA results (Figure 6.19) also show a higher proportion of carbonates (Table 6.5, Section 6.3.1.2). Increased weight loss between 500 – 700 °C was noted with a smaller peak centred at 730 °C, indicating a range of carbonate species were present as discussed in Section 6.3.1.2. Weight losses indicative of ettringite and AFm are also observed. The weight loss < 100 °C is reduced in the PFA control blends compared to the BFS controls, likely a result of fewer AFm phases undergoing dehydration in this formulation together with a smaller weight loss contribution from free water.

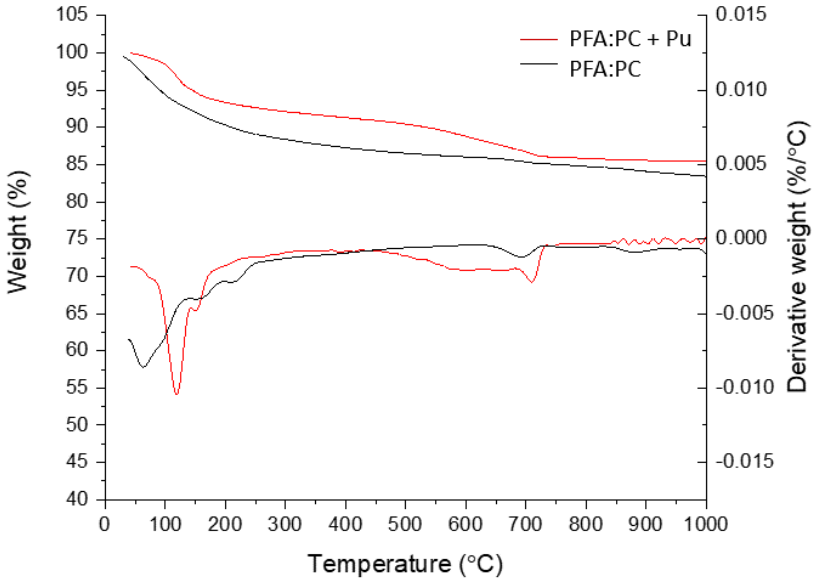

Figure 6.19. Thermogravimetric analysis of PFA:PC and PFA:PC + Pu.

6.3.2.2.1 Effects of cellulose addition

Cellulose addition caused similar variation to those seen in the BFS systems. Peak intensities for ettringite, hemicarbonate and monocarboaluminate increased in the cellulose containing sample (Figure 6.20), whilst the reflection for monosulfoaluminate at 9.9°2θ reduced.

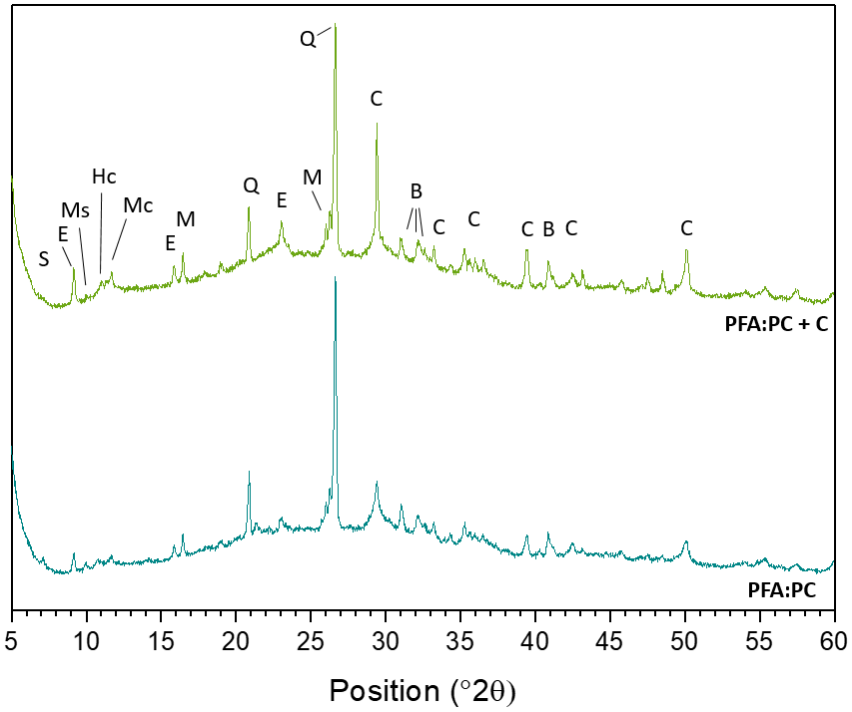

Figure 6.20. X-ray diffractograms of PFA:PC and PFA:PC + C grouts. S: strätlingite, E: ettringite, Ms: monosulfoaluminate, Hc: hemicarboaluminate, Mc: monocarboaluminate, M: mullite, Q: quartz, B: belite (C_2S), C: calcite.

The increase in hemi- and monocarboaluminate indicates higher carbonate contents in the PFA:PC + C sample; this is likely due to the degradation of cellulose, as atmospheric carbonation effects are expected to be limited (see section 6.3.1.3). However, the peak intensities for calcite appear increased in the PFA:PC + C diffraction pattern suggesting the cellulose degradation products could not be accommodated through formation of additional AFm type phases. TGA results support the increase in AFm-type phases (Figure 6.21). Weight loss between 300 – 400 °C indicates decomposition of cellulose, which was greater in the PFA sample than observed in Section 6.3.1.3.

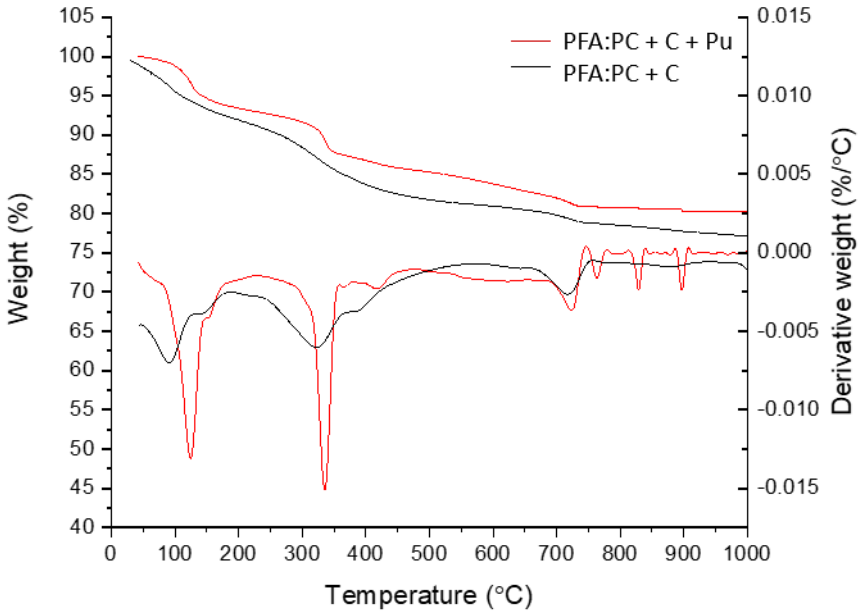

Figure 6.21 Thermogravimetric analysis of PFA:PC + C and PFA:PC + C + Pu. Data acquisition of PFA:PC + C + Pu is considered suspect at T > 750 °C.

The PFA:PC + C + Pu sample shows increased weight loss at temperatures > 500 °C, suggesting increased carbonation in the PFA system which may be linked to an increase in cellulose degradation products; however, the data becomes unreliable at temperatures > 750 °C and so further investigation is required.

6.4 Conclusions

This study provides novel investigation of how PuO_2 encapsulation affects the physico-chemical development of Portland cement blended grouts typically used for waste management in the UK. Many waste streams include alpha emitting species, which will result in extremely localised radiation fields in regions immediately surrounding the alpha source – a situation that cannot be simulated by external gamma radiation. PuO_2 is a particularly intense alpha emitter, and since no UK waste stream currently incorporates particulate PuO_2 at the levels used here, the experiments represent a worst case as regards alpha radiolysis effects on immobilised UK ILW.

Microscopic analysis indicates there is good physical contact between cement hydrates and PuO_2 particle agglomerates, with evidence of some infilling between particles. No microstructural damage to the cement hydrates was observed, even in the regions closest to the PuO_2 particle agglomerates. The mineralogy and morphology of the PuO_2 appears unchanged by contact with cementitious grouts, however limited EDX of the active samples was completed so no information is available on Pu mobility or whether it has been incorporated in hydrate phases. Further characterisation is recommended, particularly focussing on the interface between the PuO_2 particle agglomerates and the encapsulant grouts. The evidence available from this study indicates that Portland cement blends are suitable encapsulating matrices for wastes containing PuO_2 (whether in this physical form or as a component of other waste streams arising from spent fuel reprocessing).

XRD and TGA results indicate phase assemblages characteristic of the blended cements investigated; no significant crystal reflections for new hydrate phases in XRD were observed, and no additional weight loss was seen at temperature ranges inconsistent with these blends. Incorporation of cellulose caused variation in the proportion of phases present, likely due to cellulose degradation, but no microstructural differences were observed.

Comparison of the PuO_2 samples with the controls suggests quantitative differences in the phase assemblage. The ratio of sulfate phases in the BFS blends appear to have altered in the presence of PuO_2, with an increase in ettringite observed. This change may be driven by a combination of factors, including an increase in the CO_2/Al_2O_3 ratio. Despite conversion of monosulfoaluminate to ettringite being linked with structural damage in sulfate attacked concretes, no evidence of structural damage was apparent in these small scale samples. The potential radiolytic oxidation of sulfide released through hydration of BFS increasing the sulfate content is considered insufficient to cause significant structural issues, as the bulk SO_3/Al_2O_3 ratio will be buffered by the alumina also released from the BFS. Further work is needed to assess the extent of chemical variations in the area surrounding the

PuO_2 agglomerate particles with regard to the sulfate phase ratio, and how the carbonate content affects the AFm phase balance in these areas.

Differences in amount of carbonates present were observed, however due to the different storage and handling of the radioactive samples and controls this cannot be attributed to radiation effects. Although the results indicate that radiolytic carbonation may have occurred, no systematic trends were observed for the different samples analysed.

The impact of α-radiation appears to cause more variation to the phase assemblage than observed from gamma exposure (Chapter 5). Moving forward, the following chapters will investigate whether the presence of non-radioactive surrogates for PuO_2 impacts the gamma attenuation and resulting radiation response (Chapter 7), and further probe the impact of α-particles on the interface between encapsulant grouts and α-emitting waste species (Chapter 8).

7 Gamma stability and leaching characteristics of CeO_2 doped cementitious grouts

This chapter aims to link findings on the gamma stability and alpha stability of BFS:PC systems from Chapters 5 and 6. Thus far, the wasteform systems explored have been simplified compared to real ILW systems and so the impact of waste species on the irradiation response of these materials was of interest. Specifically, it was questioned whether the presence of simulant waste species in the grout would impact the gamma response: would the gamma radiation attenuate differently and, if so, would this lead to differences in the microstructure that might affect the leaching characteristics?

As the impact of PuO_2 on the cement system was previously assessed, this seemed a pertinent waste species to investigate further. The characterisation completed on the PuO_2 containing systems in Chapter 6 indicated that little impact to the microstructure had occurred. However, these wastes would be subject to gamma radiation from within the wasteform, or might be located near other gamma emitting packages [8]. The impact of this external radiation interacting with the surrogate was of interest, as it was hypothesised it might lead to an increase in cracking localised to the waste species which could create preferential pathways for radionuclide mobility, reducing the wasteforms effectiveness as discussed in Chapter 2, Sections 2.1 and 2.3.

Due to the problems around acquiring and practicalities of working with actinide species, a non-radioactive analogue for PuO_2 was required for this work. Cerium is commonly used as an analogue for actinides including plutonium and uranium as it has similar ionic radius, oxidation state, hydrolysis and redox behaviour and its oxide takes the fluorite crystal structure similar to PuO_2 and UO_2 ($Fm\bar{3}m$ space group) [247]. Given this, it is commonly used as a structural surrogate in wasteform ceramics and dissolution studies [248]–[250], as well as cement studies for radioactive waste disposal [247], [251]. Cerium dioxide was chosen as it was considered that it would provide a suitable analogue for PuO_2 in this instance and was anticipated that it would behave with the encapsulant grout in the same manner as observed in Chapter 6. Whilst the redox range of cerium is limited compared to actinides (occurring only as Ce (III) and (IV)) this means it is an appropriate choice for use as a PuO_2 surrogate in the current study [250], [252]. As reaction of the CeO_2 powder is anticipated to be low (from the results observed for PuO_2 in Chapter 6) and encapsulation of the powder is required, no redox changes as a result of reaction are anticipated.

As outlined in Chapter 2, the interaction mode of gamma radiation with materials is dependent on the gamma incident energy and the mass of the material with which it is interacting. Given that the decay energies associated with ^{60}Co gamma emissions are 1.173 and 1.333 MeV [93], the dominant

interaction mechanism in cements would be Compton scattering [97], [214]. Incorporation of waste species commonly found in Magnox and PCM waste streams (such as plutonium, uranium or their decay products) or surrogates for these, increases the atomic number of the cement material affecting the interaction and attenuation of the gamma radiation. Although the dominant interaction mechanism would still be Compton scattering, the increased mass will affect the attenuation, which may impact the microstructure of the surrounding grout differently. Despite the atomic number of cerium being lower than plutonium (58 vs 94 respectively), it is considered that the increased molar mass of CeO_2 within the cement matrix will provide an approximation of the potential change in irradiation response without the inherent restrictions and practicalities of working with radionuclides [97].

The degree of interaction of PuO_2 with the encapsulating cement hydrate phases was observed in Chapter 6 to be limited. However, studies investigating the uptake of actinides / actinide analogues including plutonium, uranium and cerium in cement hydrate phases using aqueous radionuclides have shown incorporation into specific U/Ce-bearing mineral phases [247], [253]. Given that encapsulation of the materials is required, and not incorporation into hydrate phases, assessment of how the material is located in the cement microstructure is required before leaching is completed. Sorption of radionuclides to existing hydrate phases – especially C-S-H – has been well documented, with ageing of the cement hydrates having little impact on retention [254]–[258]. Post closure of the GDF, the wasteforms will encounter groundwater and become saturated over time, enabling radionuclides to mobilise and leach from the materials. It is important to assess if contact with groundwater will alter the state of the radionuclides or how they interact with the cement grout, together with assessing if removal from the wasteform occurs.

Although the leaching behaviour of cementitious materials has been widely investigated [26], [259]–[263], the impact of radiation exposure on the leaching characteristics of UK nuclear sector encapsulant grouts requires further analysis. Currently, UK regulatory requirements to retain radionuclides within the engineered barrier system post disposal do not state the retention values required by the wasteform itself [27], [264]. This is, in part, due to the many environmental factors (depth of the GDF, temperature, local geology, groundwater composition and flow) that will influence it, which are inherently dependent on siting of the GDF. This study aims to provide information to assist the development of the safety case as, from previous work in this study and existing literature, the radiation resistance and retention potential of these materials may contribute significantly to the overall multi-barrier concept.

7.1 Experimental setup

The samples were synthesised and cured using the method outlined in Section 3.2 for small volumes of materials. The CeO_2 was added after the grout was mixed and stirred through the grout by hand. The grouts were cured in sealed 15 mL centrifuge tubes for 4 days, after which the samples were demoulded and wrapped in aluminium foil to minimise moisture loss and atmospheric carbonation. Samples were irradiated 4 days after mixing and irradiations were completed over 3 days. Half of the samples produced were sent to the University of Manchester DCF for testing using the facilities outlined in Section 3.3.13, and the remaining samples were retained as controls. The control samples were placed in a 50 °C oven for a time period corresponding to the duration of the irradiation, to minimise differences in sample behaviour due to heating effects. The total dose achieved for these samples was much lower than the samples in Chapter 5. This was due both to access to the ^{60}Co irradiator and the time available within the project to complete analysis. Also, as the samples were irradiated at a younger age than in Chapter 5, the impact of radiolytic dehydration may be increased as more free water would be present. Although the total dose is much lower than seen in Chapter 5, it still represents a significant dose for cemented wasteforms considering the estimated total lifetime dose of 10 MGy [36]. Given this, the overall lower dose is considered appropriate to assess the impact of the dopant on the radiation response. Details of the samples and the irradiation conditions are summarised in Table 7.1.

Table 7.1 Summary of cement composition and irradiation conditions.

BFS:PC	w/cm	CeO_2 (wt.%)	Average gamma dose (kGy/hr)	Total dose (MGy)	Irradiation temperature (°C)
3.44:1	0.35	0.5	23.0 (± 0.2)	1.2 (± 0.01)	50 °C

Characterisation of the irradiated and control samples was completed at 28 days of curing, 21 days after irradiation exposure was completed. Leaching of samples was initiated when the cements were 14 weeks old, which was 13 weeks after radiation exposure had ceased. During the intervening period, the samples remained in the foil wrappings and were stored in sealed bags at 20 °C and 90 % relative humidity. In order to evaluate the leaching characteristics of the cements with and without irradiation exposure, sample monoliths measuring 15 mm x 15 mm were cut for leaching tests and the ends of the cylinders were sealed with epoxy resin to allow only radial diffusion of the solution. The monoliths were placed in contact with 50 mL of simulant granitic groundwater in 60 mL Teflon vessels, providing a cement sample to solution (solid/liquid) ratio of 1:1. Testing was completed in duplicate for

monoliths and 'blanks' (groundwater without cement monoliths) at 50°C in a controlled nitrogen environment to represent the post closure conditions within a GDF [18]. Granitic groundwater was chosen as representative of a geological environment currently considered for the siting of a GDF [18]. The composition is representative of Allard water (characteristic of granitic terrains) and was taken from Gascoyne [265] (Table 7.2), which was used to develop the Onkalo GDF in Finland and has been used for several long term studies into groundwater interactions with cementitious materials as part of the HORIZON 2020 CEBAMA programme [255], [261], [266]. The leaching methodology used was adapted from ASTM C1308-08 [267] with reference to the long term leaching methodology devised by Vasconcelos [268] with UoS, RWM and the CEBAMA programme.

Table 7.2 Synthetic granitic groundwater composition used in leaching tests, after [265].

	Na	K	Ca	Mg	Cl	HCO_3	SO_4	SiO_2	pH
Quantity (mg/L)	65	3.9	18	4.3	70	123	9.6	12	8.2

Two experimental setups were created to compare the effects of aggressive, accelerated testing methods with slower processes more representative of natural processes. Dynamic testing of the samples involved sampling and total replacement of the groundwater at 1, 3, 7, 14, 21, 28 and 35 days in a controlled oxygen and nitrogen environment to exclude CO_2, whilst static testing did not involve replacement of groundwater and involved sampling only at 35 days. The purpose of this testing was to see if a less aggressive testing environment caused significantly different results, or just caused a different scale of change. The dynamic testing was devised as an aggressive accelerated test to accentuate the alteration of the cement in order to provide a worst case scenario of leaching characteristics from these samples, but is not considered representative of potential in-situ conditions. Immediately after sampling, the pH of the solutions was taken. Analysis of the sampled leachate was performed using a Thermofisher Scientific iCAP Duo6300 Inductively Coupled Plasma-Optical Emission Spectrometer, operated using a gold internal standard and ceramic torch. Samples were filtered (0.22 µm), diluted and acidified with 20 µL of concentrated HNO_3 (99.999% purity) prior to analysis. Post leach testing, at 19 weeks of curing, the cement monoliths were placed in acetone to arrest hydration before characterisation using TGA-MS, XRD and SEM-EDX according to the procedures outlined in Chapter 3, Sections 3.3.7, 3.3.8, and 3.3.11.

7.2 Gamma irradiation resistance

7.2.1 Phase assemblage and microstructure

7.2.1.1 XRD

Prior to analysing the impact of irradiation on the CeO_2 doped system, assessment of whether the inclusion of CeO_2 had affected hydration and development of the phase assemblage or microstructure was required. The diffractograms shown in Figure 7.1 A confirm the presence of CeO_2 in the grout but, apart from limited variations in the peak intensities for hydrate phases (potentially a product of preferred orientation), no changes in the phase assemblage were identified. This indicates the CeO_2 is not reacting with the grout but is encapsulated by it, as anticipated. This behaviour is consistent with that of PuO_2 in the findings outlined in Chapter 6. There is overlap in the reflections for the [111] CeO_2 peak and the [010] [100] portlandite peak at 28.6 °2θ; however, this is only a minor reflection for portlandite, which is still clearly identifiable from main reflections for the [001] and [011] planes. Overall, the phase assemblage is as identified for this blended cement in the previous chapters.

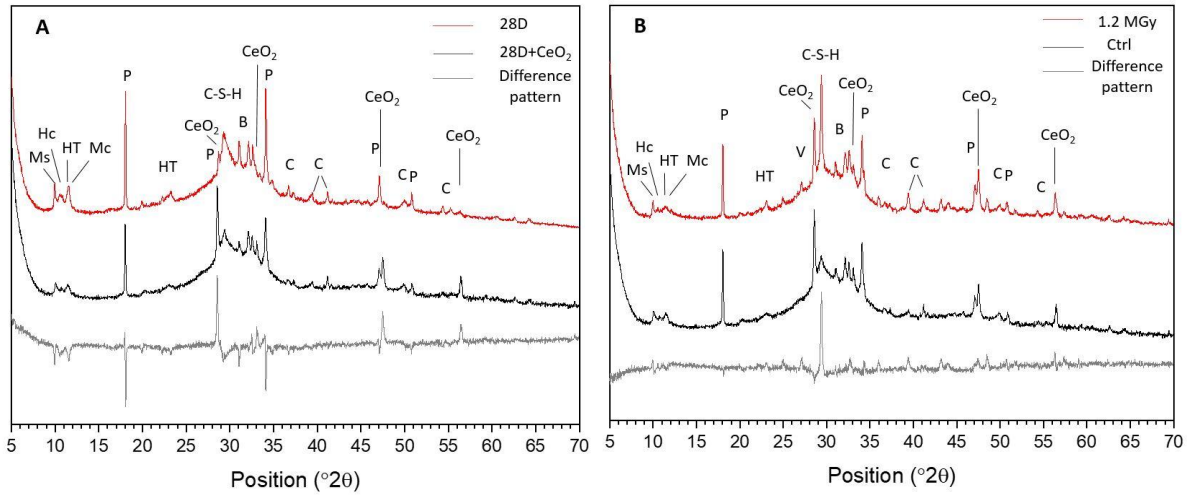

Figure 7.1 X-ray diffractograms of 3.44:1 BFS:PC A: Sample at 28 days age (28D) compared to CeO_2 doped (28D+CeO_2) sample. B: 1.2 MGy irradiated CeO_2 doped sample and CeO_2 doped control (Ctrl). E: Ettringite, Ms: monosulfoaluminate, HC: hemicarboaluminate, HT: hydrotalcite, Mc: monocarboaluminate, P: portlandite, V: vaterite, B: belite (C_2S), C: calcite.

Post irradiation, the difference pattern shown in Figure 7.1 B suggests a marked increase in crystallinity and intensity of the peak located at 29.4 °2θ. The diffuse scattering in this region is typically attributed to C-S-H; however, the [104] reflection for calcite is also centred at 29.4 °2θ and so this sharpening, together with the increased peak intensities for calcite observed at higher angles, indicates an increase in carbonation of the irradiated cement. Reflections from vaterite were also observed in the irradiated sample, which were not present in the control. Reduced peak intensity for monocarboaluminate/ hydrotalcite was observed at 11.5 °2θ in the 1.2 MGy sample, which may be linked to reduced free

water due to radiolytic dehydration limiting BFS hydration although preferred orientation of these phases cannot be ruled out. No cerium containing hydrate phases were observed.

7.2.1.2 TGA

TGA results in Figure 7.2 A showed minor variations between the CeO_2 doped and non-doped sample. These were considered to be a product of the heat exposure the CeO_2 containing samples were subjected to (for irradiated control purposes) rather than as a consequence of CeO_2 reaction. Although the extent of reaction of CeO_2 from these data cannot be fully determined, TGA and XRD results indicate it is most probably behaving as an inert filler in the cement without reacting extensively.

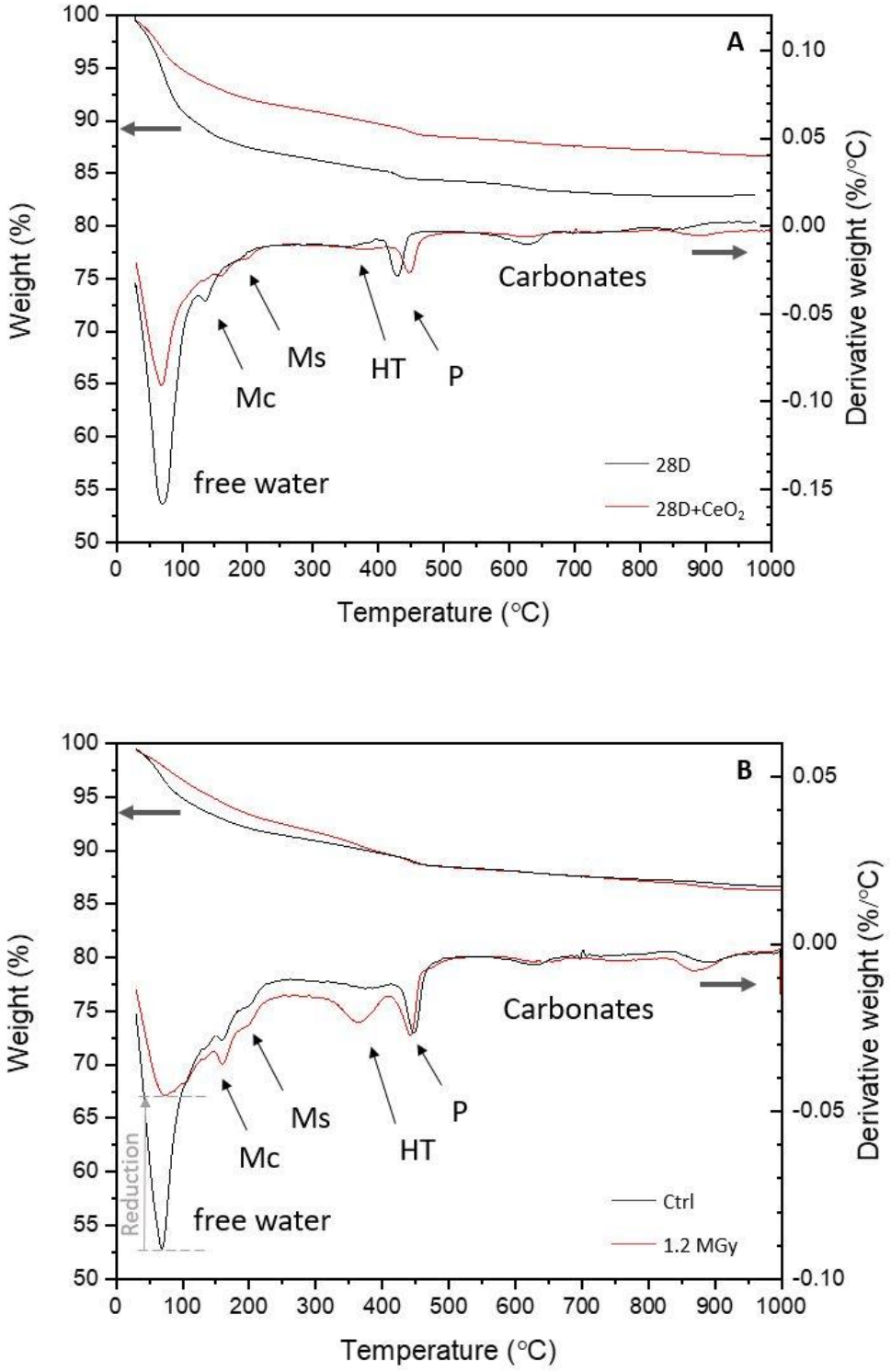

Figure 7.2 TGA of 3.44:1 BFS:PC A: Sample at 28 days age (28D) compared to CeO_2 doped (28D+CeO_2 - also referred to as Ctrl) sample. B: 1.2 MGy irradiated CeO_2 doped sample and CeO_2 doped control (Ctrl). Mc: monocarboaluminate, Ms: monosulfoaluminate, HT: hydrotalcite, P: portlandite. The shift in portlandite decomposition peak in A is due to replacement of equipment requiring recalibration between testing.

Differences between the 1.2 MGy irradiated and control (Figure 7.2 B) are similar to the trends identified in Chapter 5, with a reduction in free water and increased weight loss between 200 – 400 °C and at > 700 °C. The irradiated sample showed increased weight loss from hydrate decomposition between 100 – 450°C, with a significant peak at 370 °C tentatively assigned to a hydrotalcite-like phase. This desorption temperature is slightly lower than anticipated for hydrotalcite and may indicate the formation of an intermediate quintinite-like material, as seen by Parker et al. [86], which has an increased proportion of $Al(OH)_3$ sheets interstratified with the magnesium-aluminium layers as described by Taylor et al. [88], [188]. This would require increased DoH of the BFS fraction to elevate the magnesium and aluminium concentrations in the pore fluid to allow formation. Interlayer charge balancing species would predominantly be CO_3^{2-} , as radiolytic decomposition of free water within the cement would reduce the amount of OH^- available for charge balancing and might increase the carbonate content of the system via calcium peroxide octahydrate formation [96], [101], [122].

Given these factors, attributing the weight loss at 370 °C to a quintinite-like phase is difficult to do with confidence. It is considered plausible that the weight loss at 370 °C could be due to the formation of an amorphous metastable carbonate phase [269] due to the radiolytic impacts outlined above. Although limited reaction of the CeO_2 was observed, it is speculated the particles may provide a reaction site for formation of this amorphous metastable carbonate and that localised increased carbonation at CeO_2 interfaces may have occurred.

The weight loss between 100 – 300 °C was increased by 1% in the 1.2 MGy sample, indicating an increase in AFm hydrate phases. The variations observed from XRD (Figure 7.1 B) show increased peak intensities for monosulfoaluminate in the 1.2 MGy sample, but lower intensities for hemicarboaluminate and the overlapping hydrotalcite / monocarboaluminate reflection. The increased monosulfoaluminate may account for this variation however, the discrepancy between results may be a product of preferred orientation. The overall weight loss in the 1.2 MGy sample was 0.5 wt.% greater than the control, indicating a potential increase in the proportion of hydrates present, which may be due to increased reaction driven by radiolytically formed radicals [115].

Quantification of the TGA data shows a progressive reduction in free water content with heating, which is exacerbated by irradiation, consistent with the findings of Chapter 5. The reduction due to radiation exposure is greater than seen for similar systems previously but this is likely due to the young age at which these samples were irradiated. However, Mobasher et al. [110] found limited difference in the free water content between early age irradiated and heated control samples of 4.7 MGy irradiated 9:1 BFS:PC. The samples in the Mobasher study had undergone hydration stoppage, using acetone to remove free water from the system (unlike the current study) and so this is considered to

be responsible for the differences observed. Nevertheless, there were similarities in the findings; increased weight loss in the irradiated sample compared to the controls in the Mobasher study was linked with an increase in hydration of the BFS or PC components.

Table 7.3 Quantification of free water, portlandite and carbonate contents of BFS:PC (28D), and BFS:PC + CeO_2 doped samples exposed to 1.2 MGy and the corresponding control.

Sample	Free water (%)	$Ca(OH)_2$ (%)	$CaCO_3$ (%)
28D	9.3	3.5	2.3
28D-CeO_2 / Ctrl	5.1	3.2	3.6
1.2 MGy	3.4	3.8	4.3

Minor variations in portlandite quantities were observed between the samples and a slight increase in carbonate content was identified in the CeO_2-doped samples. The increased carbonate content is greater in the irradiated sample and does not relate to a reduced portlandite content. This supports the findings from Chapter 5, where carbonation was proceeding without significant portlandite decomposition, via the decalcification of C-A-S-H.

7.2.1.3 SEM-EDX

Point analysis for the 28D and CeO_2-doped samples (Figure 7.3) shows little variation in the bulk chemistry of the system. The results support the findings of the XRD and TGA results (Figure 7.1 A, Figure 7.2 A), indicating the phase assemblage comprises C-S-H, portlandite, hydrotalcite-like phase, and AFm phases (likely monosulfoaluminate, hemicarboaluminate and monocarboaluminate given XRD results). The incorporation of CeO_2 did not affect the hydration or phase assemblage of the BFS:PC systems, as this phase appeared to remain inert, encapsulated in the cementitious matrix.

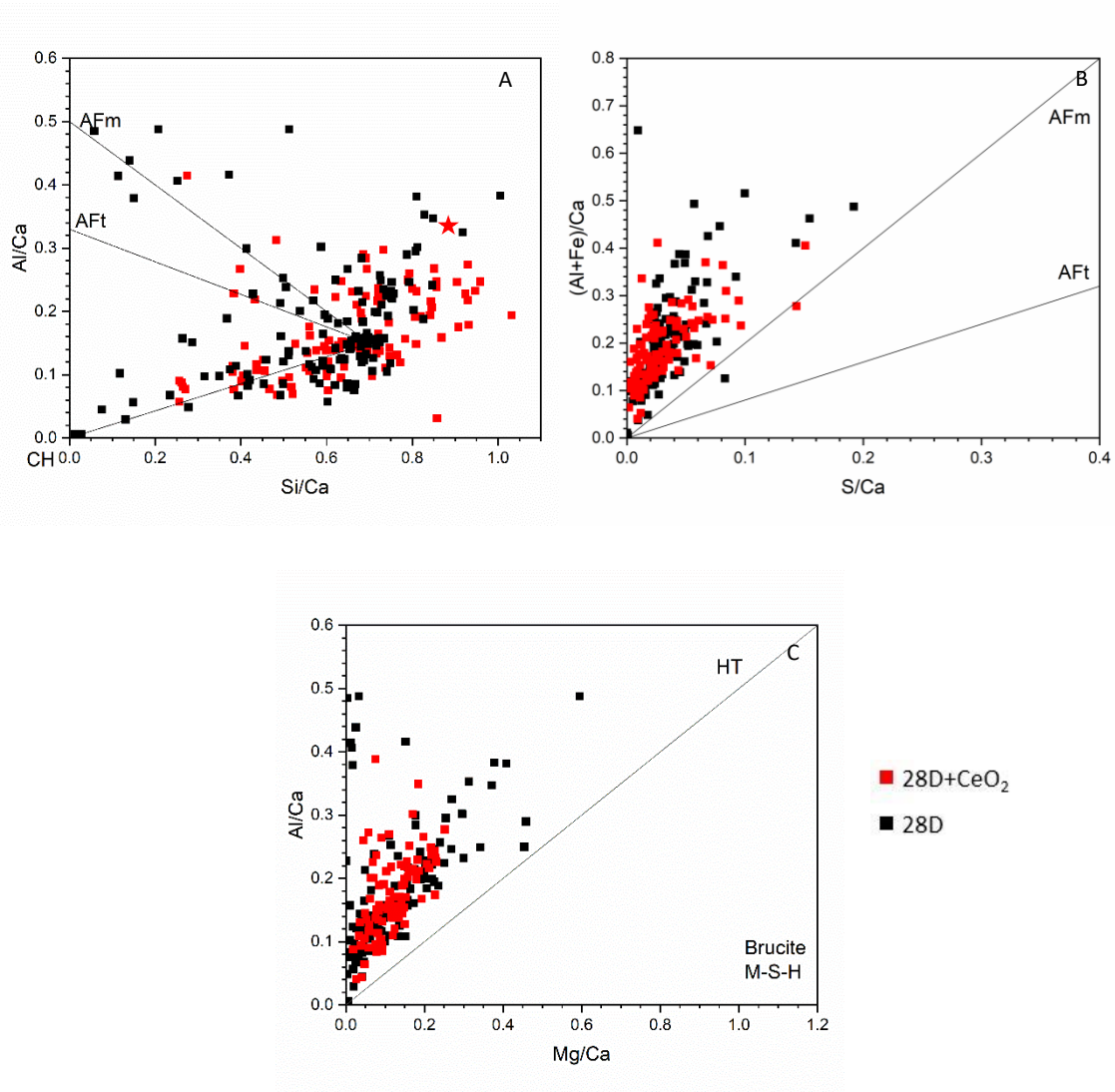

Figure 7.3 EDX point analysis for 28 days aged sample (28D) compared to CeO_2 doped (28D+CeO_2) sample. Each point sample was taken from a region that visually appeared to be binder rather than residual anhydrous phases. Tie lines link to the other prominent hydrate phases; CH: portlandite; AFm: monosulfoaluminate; AFt: ettringite; and HT: hydrotalcite. Composition of anhydrous BFS shown in A by ★ symbol.

SEM-EDX analysis of the CeO_2 doped system after irradiation is shown, compared to the control sample, in Figure 7.4. The BSE images and EDX mapping confirm that the CeO_2 does not react to any noticeable extent in the cement matrix. The development of a typical BFS:PC system was observed, as described in previous chapters.

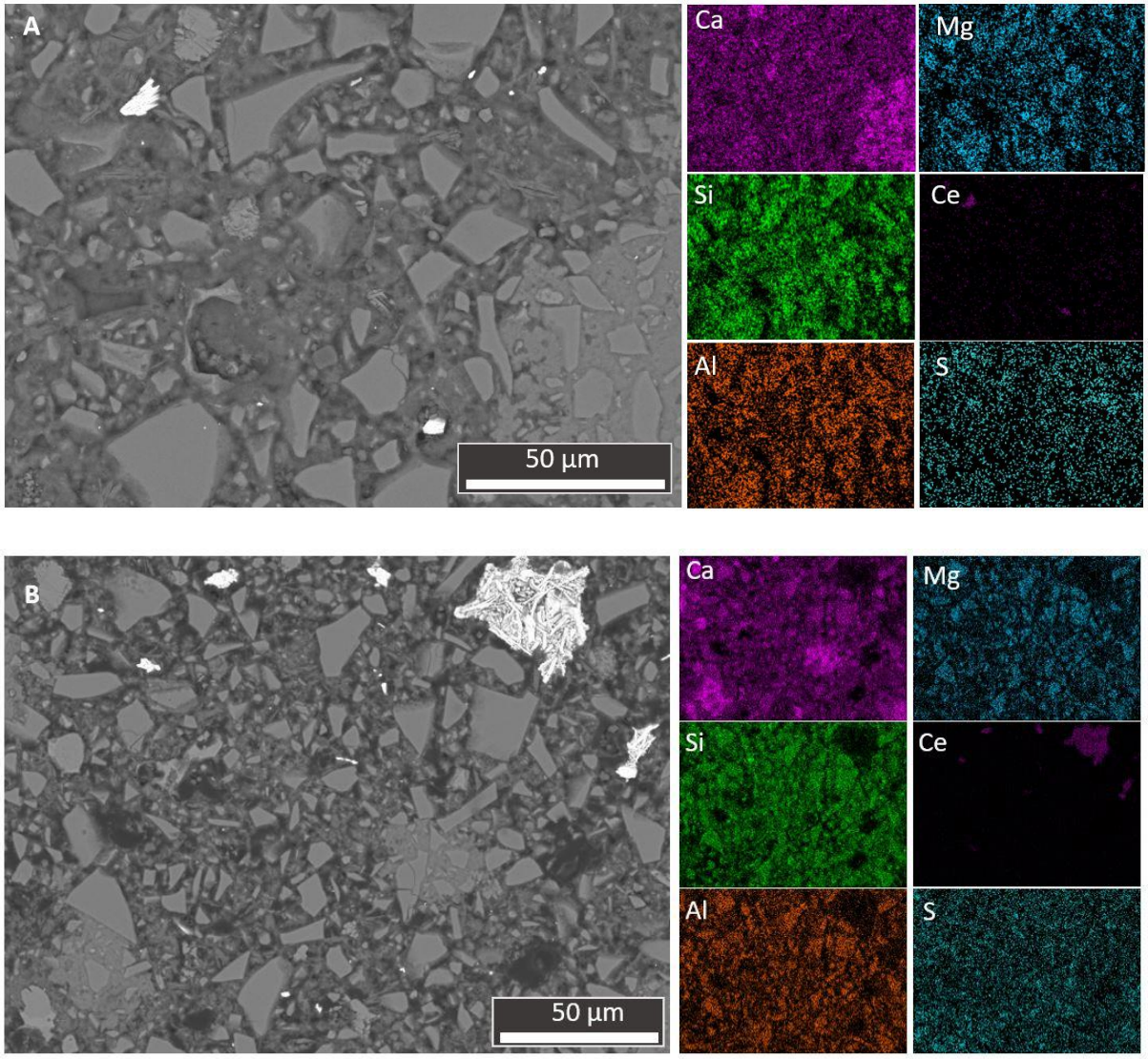

Figure 7.4 SEM EDX of BFS:PC + CeO_2 at 28 days. A: CeO_2 doped control (Ctrl) and B: 1.2 MGy irradiated CeO_2 doped sample.

Post irradiation, no significant alteration in the distribution of phases in the microstructure appears to have occurred. Similarly, the CeO_2 does not appear to have been influenced by the exposure.

Point analysis of the systems indicates a higher Ca/Si ratio in the 1.2 MGy irradiated sample; a mean value of 2.0 was observed for the 1.2 MGy sample, whereas Ca/Si ratio of 1.5 was observed in the control. This supports the increased weight loss observed in the TGA (Section 7.2.1.2) for the irradiated sample, which was attributed to a potential increase in the hydration of BFS and / or PC components. No shift in the magnesium, aluminium or sulfur balance was observed post irradiation. This casts doubt on the potential increase of hydrotalcite observed in the TGA results, instead favouring the formation of a metastable carbonate phase.

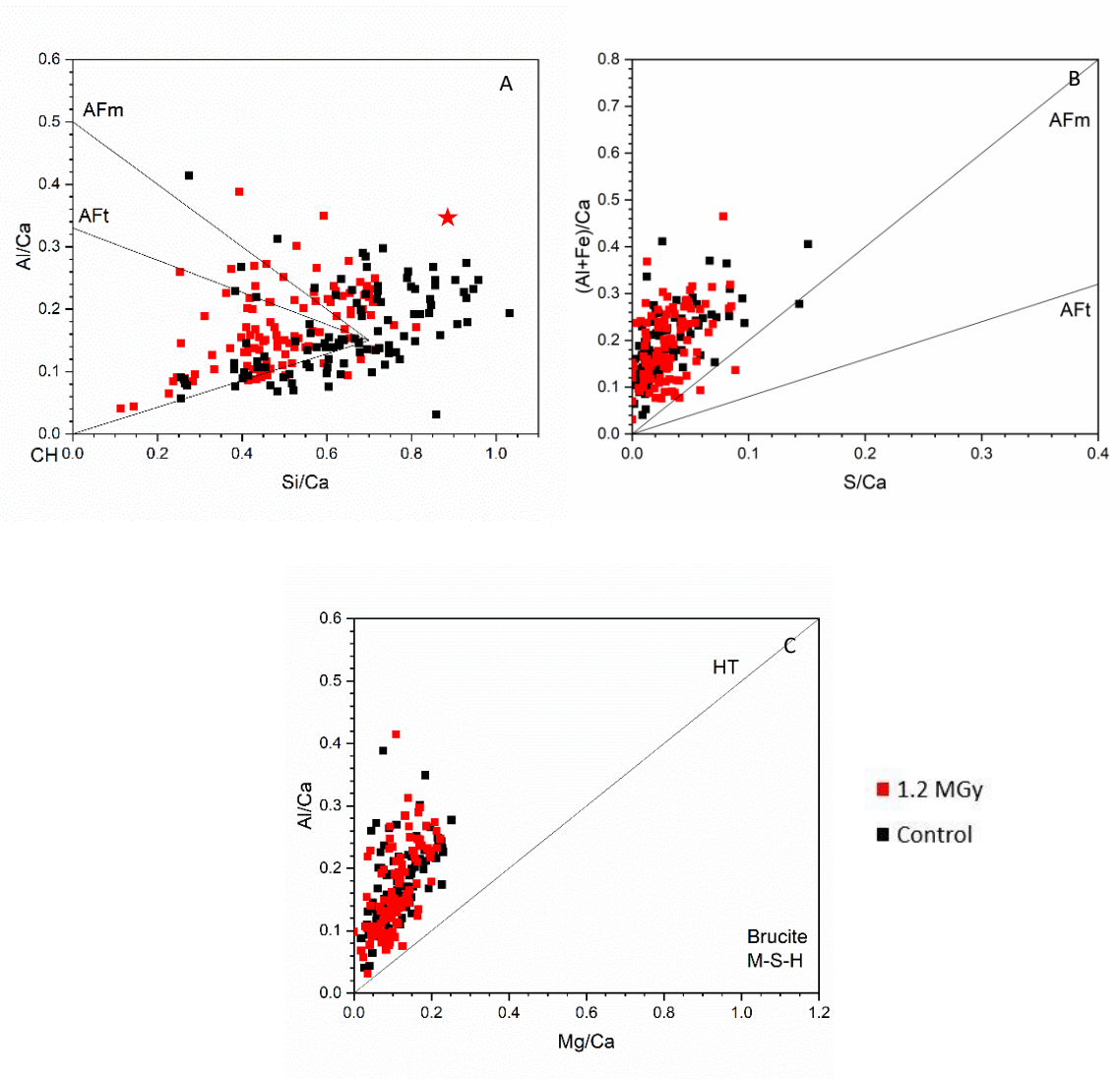

Figure 7.5 EDX point analysis for 1.2 MGy irradiated CeO_2 doped sample and CeO_2 doped control. Each point sample was taken from a region that visually appeared to be binder rather than residual anhydrous phases. Tie lines link to the other prominent hydrate phases; CH: portlandite, AFm: monosulfoaluminate; AFt: ettringite; and HT: hydrotalcite. Composition of anhydrous BFS shown in A by ★ symbol.

The BSE images in Figure 7.6 show that the microstructural development has not been significantly affected by irradiation. The overall appearance is similar to that of the PuO_2 containing grouts seen in Chapter 6, with the CeO_2 well encapsulated in both systems. No large defects were observable at the interface between the particles and the grout and the surrounding matrix appears sound with no large scale cracks evident.

There is an increased frequency of dark areas in the matrix of the 1.2 MGy irradiated sample. These represent areas of very high carbon content, not increased porosity, which may represent the increased carbonate content observed in the TGA. However, given the distribution and frequency

within the matrix it is considered that these are more likely to be the product of clumping of the carbon from coating of the samples prior to SEM analysis.

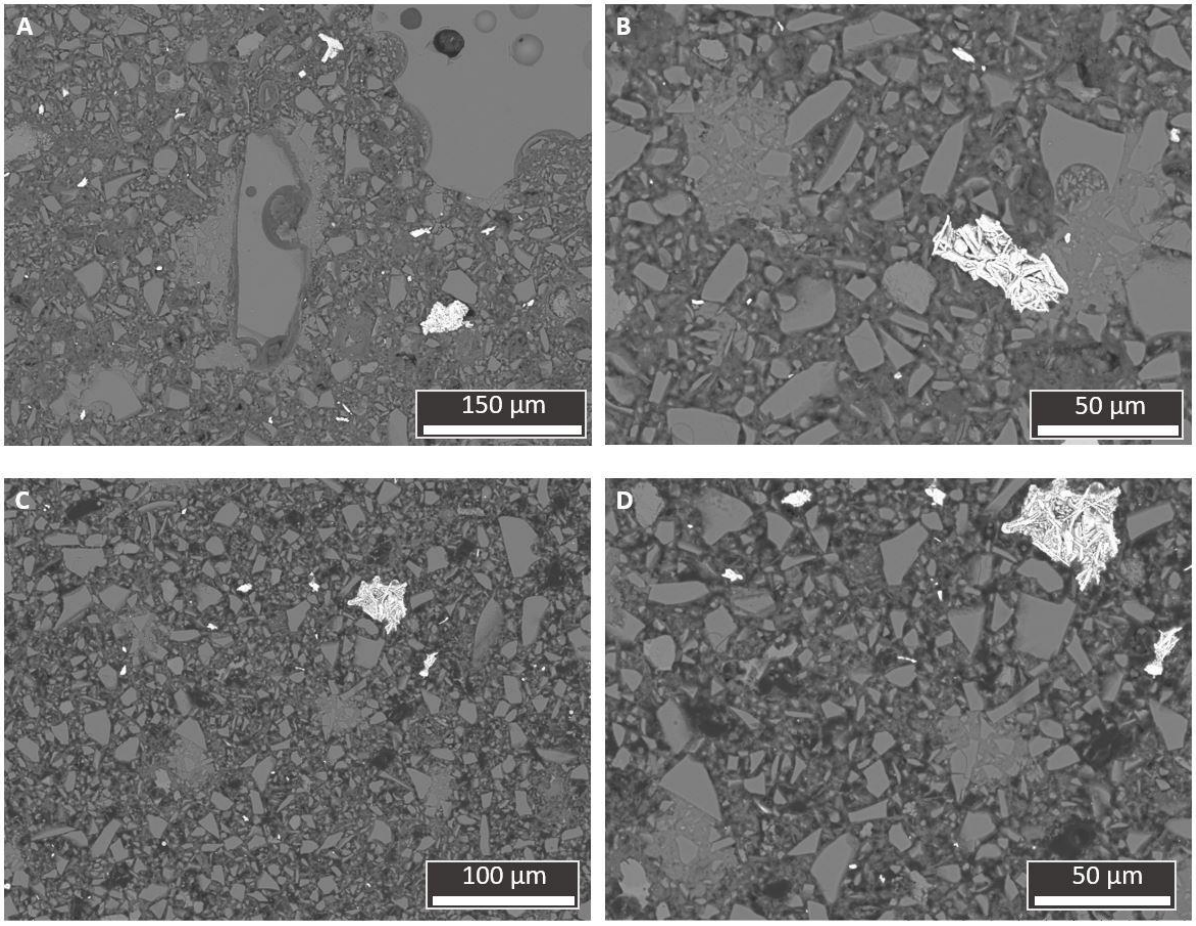

Figure 7.6 SEM images of BFS:PC + CeO_2. A, B: CeO_2 doped control, C, D: CeO_2 doped 1.2 MGy irradiated

To summarise, addition of CeO_2 did not affect the hydration of the BFS:PC systems. The same phase assemblage and microstructure developed with and without doping and the CeO_2 appeared to remain inert, encapsulated in the matrix. Irradiation of the CeO_2 containing system did not result in any major alteration to the phase assemblage identified through XRD or microstructural evolution from SEM. Free water loss as a result of irradiation was noted. There was significant increase in weight loss between 100 – 400 °C observed in the TGA results but, currently, it is unclear what caused this; SEM-EDX did not show an increase in magnesium or aluminium content, which would be expected if increased hydrotalcite formation had occurred, and the possibility of a metastable carbonate phase cannot be ruled out. Although 100 - 120 EDX point analyses were taken for each sample, which has been shown to be sufficient for estimation of the atomic compositions in hydrated cements [210], it is important to note that the results are not quantitative. Given this, there may be variation in the magnesium or aluminium content which are not detected from this analysis due to the techniques

sensitivity and quantitative analysis using electron microprobe analysis or similar would be beneficial to investigate this further. Increased levels of carbonate were observed and the greater weight loss may be linked to carbonate containing phases; however, it does not correspond with any of the carbonate species identified in XRD. The possibility cannot be ruled out that this was caused by contamination from the breakdown of something else that was present in the irradiator during exposure, although it is considered unlikely as the samples were wrapped in aluminium foil which should have prevented interference.

The CeO_2 did not appear to have instigated any defects at the interface with the cementitious grout after irradiation. No macroscopic cracking was present, indicating that attenuation by the dopant does not significantly affect the microstructure.

7.3 Leaching characteristics of CeO_2 doped BFS:PC

7.3.1 Dynamic testing

7.3.1.1 Phase assemblage and microstructure

7.3.1.1.1 XRD

Diffraction patterns of the samples pre and post leaching are shown in Figure 7.7. Prominent reflections for CeO_2 are present, showing the cerium is still present post leaching. Increased peak intensities for the majority of hydrate phases were observed, indicating increased hydration of the remaining anhydrous components upon contact with the groundwater. The disappearance of the metastable vaterite polymorph of $CaCO_3$ was observed in the samples after leaching; however, no increase in calcite peak reflections was noted. The increased peak intensity for hydrotalcite/ monocarboaluminate may account for the redistributed CO_3^{2-} ions.

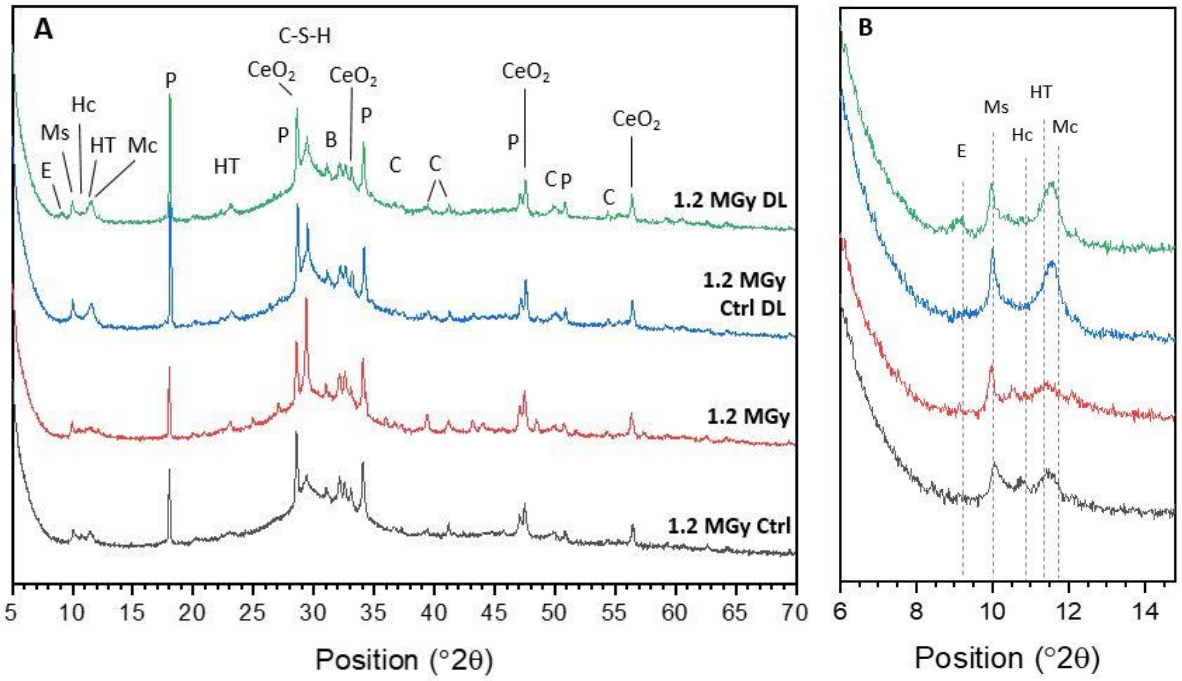

Figure 7.7 X-ray diffractograms of A: 1.2 MGy irradiated and control 3.44:1 BFS:PC+ CeO_2 pre and post dynamic leaching (DL) in simulated granitic groundwater and B: Enlarged view of 6-15 °2θ showing the development of ettringite. E: Ettringite, Ms: monosulfoaluminate, HC: hemicarboaluminate, HT: hydrotalcite, Mc: monocarboaluminate, P: portlandite, B: belite (C_2S), C: calcite.

Figure 7.7 B shows the major reflections associated with key aluminate phases in closer detail. A small reflection associated with ettringite can be seen in the 1.2 MGy irradiated sample after contact with groundwater. This is not observed in the control; however, a greater peak intensity for monosulfoaluminate is observed. Given that the sulfate content of the synthetic groundwater was fairly low (Table 7.2), the presence of ettringite is not considered to be solely due to an increased sulfate level from contact with the groundwater. However, it is clear that the SO_3/Al_2O_3 ratio and the CO_2/Al_2O_3 ratio in the irradiated system have been altered compared to the control, with an increase in either or both of these values favouring ettringite formation [69]. A similar increase in ettringite was also observed in the systems containing PuO_2 (Chapter 6) where the samples were cured in saturated $Ca(OH)_2$ solution, whilst no alteration was seen with progressive irradiation of samples in Chapter 5, which were not cured in water/saturated conditions. Given this, it is considered that the alterations to the AFm/AFt proportions are likely a product of the mobility of the sulfate and/or carbonate ions in a saturated environment.

7.3.1.1.2 TGA

The TGA results from the samples post leaching are shown in Figure 7.8 A and, whilst minor differences between the control and 1.2 MGy sample were observed, overall, the leaching response resulted in a similar material. However, when compared to the pre leached materials in Figure 7.8 B, it is clear that the response to groundwater contact is much more pronounced in the 1.2 MGy system. The weight loss tentatively assigned to a hydrotalcite/quintinite-like phase in Section 7.2.1.2 (Figure 7.2 B) is significantly reduced after contact with groundwater. This could be explained by ion substitution of the interlayer species, where an initial mix of OH^- and CO_3^{2-} changed to OH^- only species, creating an OH-quintinite-like phase ($[Mg_4Al_2(OH_{13})]\cdot 4H_2O$) with a lower associated decomposition weight [86], [270]. Although the positively charged metal oxide sheets have a high affinity for divalent charge balancing ions (i.e. CO_3^{2-}) [84], [271], thermodynamic modelling has shown that the hydroxide form is stable, especially where high pH conditions prevail [272]. However, as SEM-EDX point analysis casts doubt on this phase being hydrotalcite previously (Section 7.2.1.3), the possibility of a metastable carbonate phase re-precipitating in a more stable form upon contact with groundwater is considered more probable [119]; an increased carbonate content is observed at > 600 °C. This may be representative of an amorphous calcium carbonate presence [273]. Amorphous calcium carbonate has been observed to be stabilised by magnesium in alkali activated BFS cements [274], albeit in accelerated carbonation experiments. Although this cannot be confirmed from the current data, it does support the increased carbonate content observed from TGA that is not seen in the XRD results.

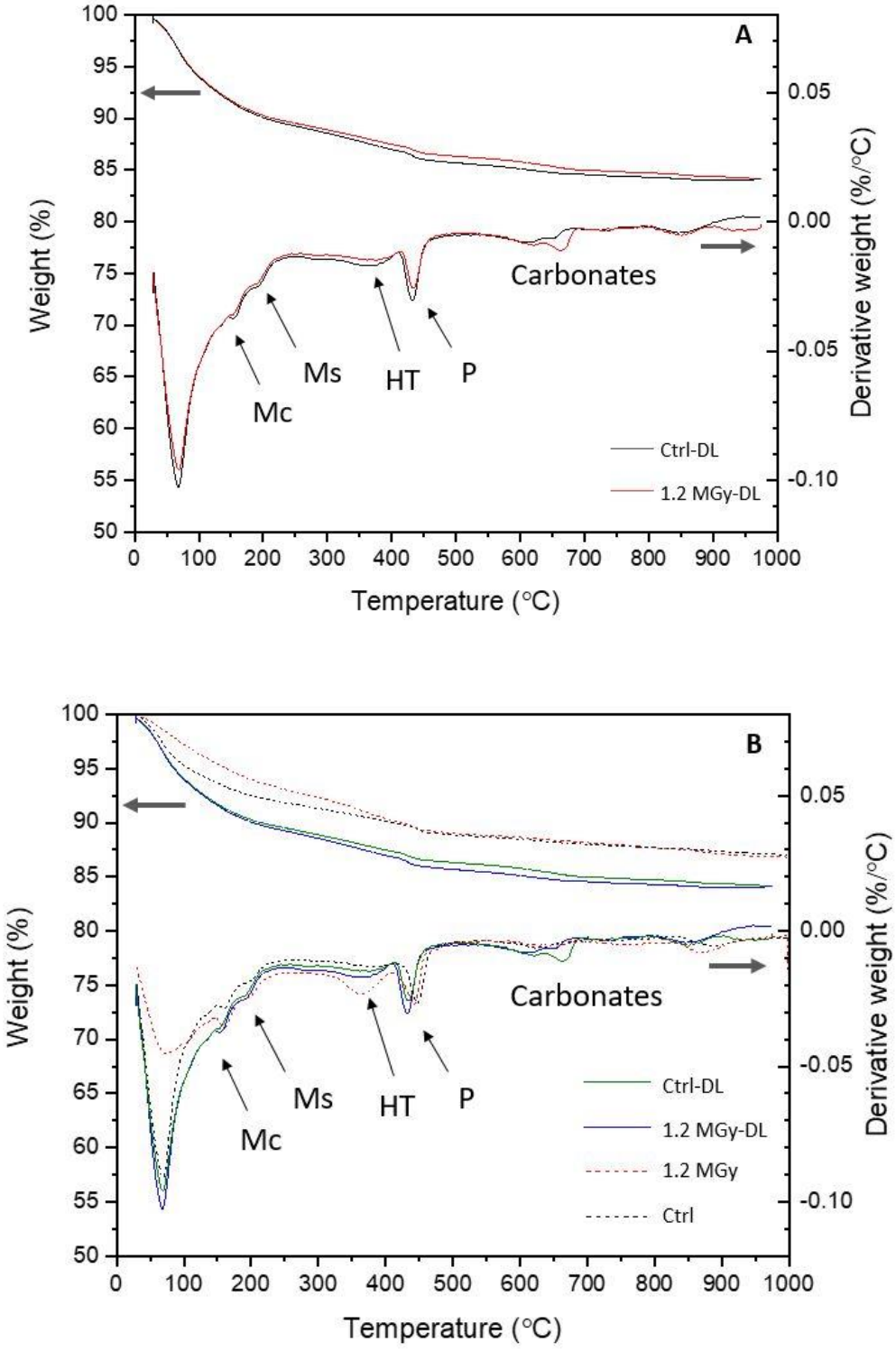

Figure 7.8 TGA of A: 1.2 MGy and control samples post dynamic leaching (DL) and B: 1.2 MGy irradiated and control 3.44:1 BFS:PC+ CeO_2 pre and post dynamic leaching in simulated granitic groundwater. Mc: monocarboaluminate, Ms: monosulfoaluminate, HT: hydrotalcite, P: portlandite.

Given that the samples were solvent exchanged when leach testing was completed, the increase in weight loss observed in both leached samples at < 100 °C is attributed to an increase in C-A-S-H and the removal of loosely bound water from this phase. Quantification of the portlandite and carbonate contents are shown in Table 7.4. A slight increase in carbonate content was noted as a result of groundwater exposure, and the temperature range over which decarbonation occurred became much smaller. In pre leaching samples, progressive weight loss between 550-950 °C was observed, whereas post leaching, a more consolidated weight loss between 600-700 °C was observed. The slight increase in carbonates is attributed to the HCO_3^- content of the synthetic groundwater (Table 7.1). The redistribution of the weight loss associated with carbonate phases shows that the carbonate polymorphs in the system alter as a result of groundwater interaction [163], [194], [275], further supporting that vaterite becomes unstable with water contact and re-precipitation of a more stable carbonate phase occurs.

Table 7.4 Quantification of portlandite and carbonate contents of 1.2 MGy BFS:PC + CeO_2 sample and control post dynamic leaching in simulated granitic groundwater.

Sample	$Ca(OH)_2$ (%)	$CaCO_3$ (%)
Ctrl-DL	3.6	3.7
1.2 MGy-DL	3.3	4.4

7.3.1.1.3 SEM-EDX

Slices through the leached monoliths were taken for SEM analysis and the results for the control sample can be seen in Figure 7.10. From the BSE image, the clear development of a texturally distinct leached zone is evident, extending approximately 100 µm from the surface of the sample towards the centre. The area is defined by the increased porosity that is apparent when compared to the centre of the sample. At the outer surface, a rim had formed where the sample had been in contact with the groundwater. From the elemental mapping, it is evident that the rim is calcium rich and, given that the synthetic groundwater contained a high proportion of HCO_3^-, it is assumed to contain $CaCO_3$; this carbonation reaction will occur as shown in equations 7.1, 7.2 and cause a lowering of the pH of the cement in the leached zone [276].

$$HCO_3^- \rightarrow H^+ + CO_3^{2-} \quad (7.1)$$

$$Ca_{(aq)}^{2+} + CO_3^{2-} \rightarrow CaCO_3 \quad (7.2)$$

This rim is considered to have formed via deposition, with the degraded front of the cement paste located in the leached area adjacent to it.

The formation of the leached zone and the rim feature are consistent with the findings from other leach testing completed on cement systems. Schwotzer et al. [260] also found carbonate-rich rims developed in cement systems in contact with carbonate containing solutions. They also postulated that dense carbonate rims provided a protective barrier as they restricted transport processes across the interface. However, it was noted that the rim properties were linked to the boundary conditions during formation and so reactive transport cannot be assumed to be affected by rim formation. The development of calcium-rich rims, together with calcium depleted zones, in long duration leaching experiments of low pH cements (containing BFS and silica fume) and short term investigation of the interface between these cements and clay backfill materials (bentonite) with synthetic granitic groundwater was also observed by CEBAMA project collaborators [277].

Coarsening of the pore structure in the leached zones of the samples was observed as an increasingly open matrix texture. This has been observed in several other studies after groundwater interaction [259], [278]–[280], and Dauzères et al. [26] noted that the development of this 'macroporosity' provided both the calcium (from decomposition of phases) and space for ettringite formation where requisite sulfate levels were reached. However, such an effect was not noted in these samples, likely due to the lower sulfate content of the groundwater and limited duration of the test.

Chemical mapping shows that the leached zone is depleted in calcium and sulfur; however, cerium is still present in the sample, even in the rim of the sample. The red dashed line denotes the line scan through the sample, which shows the calcium enriched rim, the variable concentrations in the leached zone and more stable levels in the centre of the sample. Slight magnesium enrichment behind the rim was noted, attributed to an increase in BFS hydration and the change in pH at the boundary (the higher pH of the cement causing precipitation of magnesium in a hydrotalcite-like phase) [239].

Faucon et al. [278] also observed the development of a "degraded zone" in BFS:PC systems leached in demineralized water, noting dissolution of portlandite and AFm-phases and precipitation of hydrotalcite towards the sample surface. This was attributed to the formation of a concentration gradient between the leached surface and core which led to diffusion of magnesium to the surface. The leached zone thickness in Figure 7.9 and Figure 7.10 is similar to that seen by Faucon et al. [278] in leaching of BFS:PC pastes.

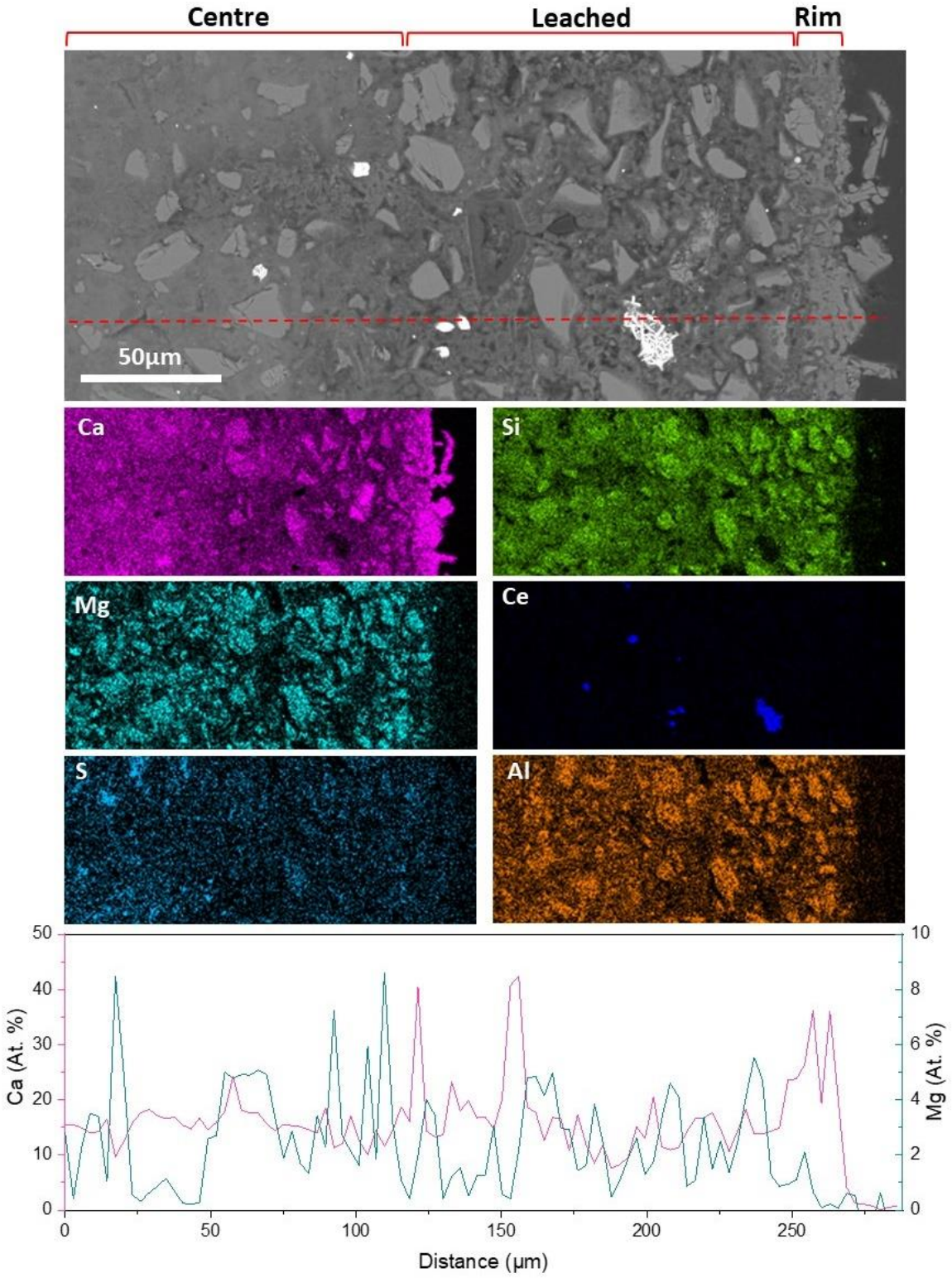

Figure 7.9 SEM-EDX analysis of control sample post dynamic leaching. The red dashed line in the BSE image denotes the line scan transect.

The results for the 1.2 MGy sample can be seen in Figure 7.10. The sample displays formation of the same texturally and chemically distinct zones in response to leaching. A calcium rich rim was noted,

with a leached zone extending approximately 100 µm from the surface towards the unaffected centre. The irradiation exposure does not appear to have altered the permeability of the system compared to the control or the microstructural response to groundwater contact.

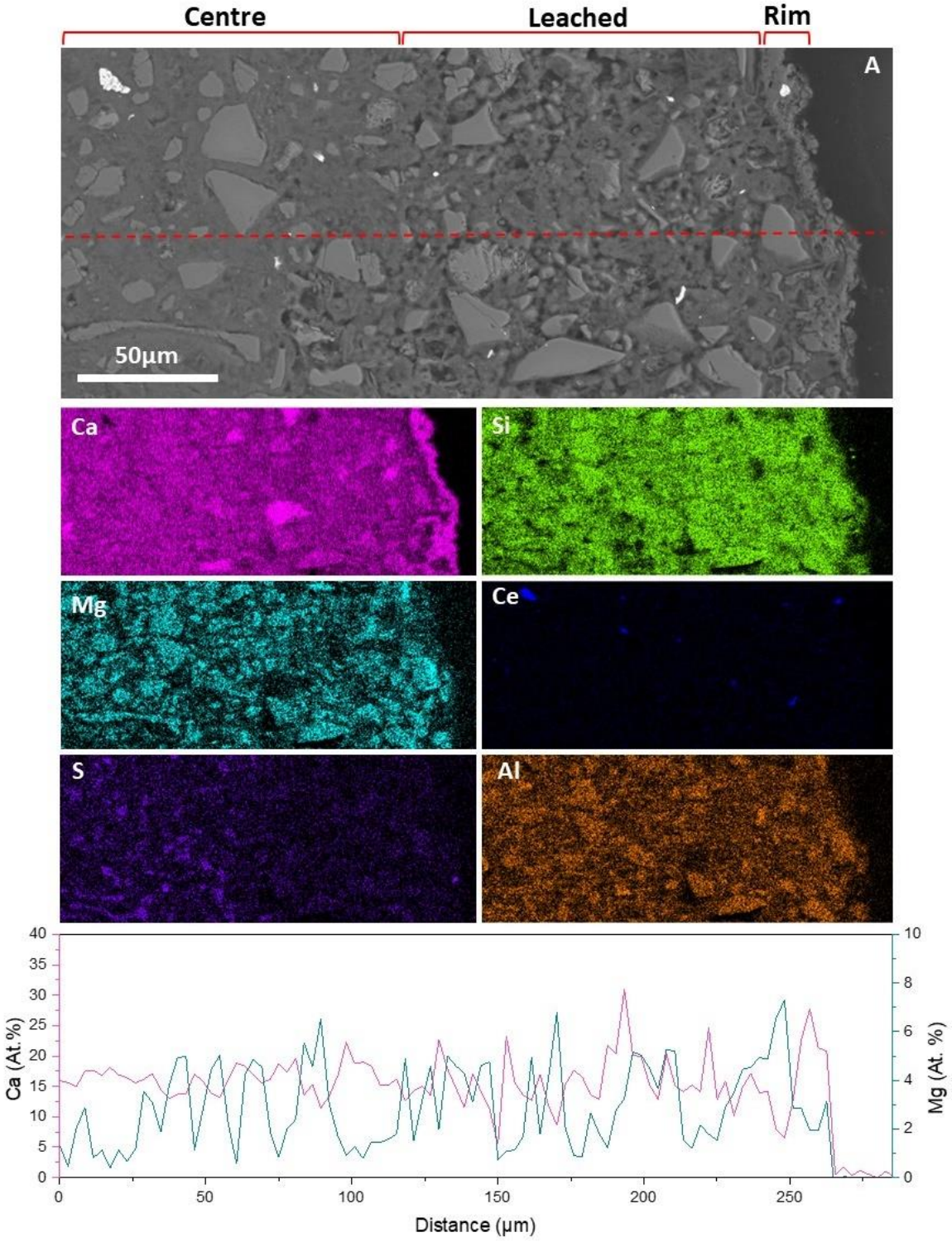

Figure 7.10 SEM-EDX analysis of 1.2 MGy sample post dynamic leaching. The red dashed line in the BSE image denotes the line scan transect.

To assess the variations in the bulk chemistry of the systems across the texturally distinct zones, EDX point analysis was completed in the rim, leached and centre of the sample. The results shown in Figure 7.11 A, B demonstrate that progressive decalcification of the system occurred in the leached zone, with high calcium contents in the rim. Average Ca/Si ratios of 1.3 ± 0.1 were observed for the central region in the 1.2 MGy control samples, which dropped to values closer to 1.0 in the leached zone. Similar values were observed in the irradiated sample; however, less distinct zonation was observed between the different regions. The rim and leached zone point distributions indicate intermixing with other phases on a length scale too small to be observed in the control. The Al/Ca ratio also increased in the leached zone of the samples, further demonstrating that possible decalcification of the C-A-S-H had occurred.

Increased magnesium and aluminium contents consistent with hydrotalcite-like phase formation were observed in the samples (Figure 7.11 C, D). The control sample had higher magnesium content in the leached zone, whereas the 1.2 MGy sample appeared to have increased quantities of Mg in the rim.

There was a slight increase in the number of points containing Mg/Ca > 0.4 noted in the rim and leached zones, which may be due to the uptake of magnesium from the leachant. There was no marked increase in the range of Mg/Ca observed in the leached zone compared to values obtained in the centre of the samples i.e. Mg/Ca values of 0.9 – 1.0 were observed from points designated as being in rim, leached and centre zones. This indicates that the increase in pH in the pore solution of the cement present had a limited effect on the solubility and diffusion of magnesium within the cement and that the changes in proportions of hydrotalcite-like phases may be due to increased hydration of the BFS together with decreased calcium (as leaching progresses) leading to increased aluminium and magnesium levels. No formation of brucite or M-S-H was observed here, although the formation of intermixed M-S-H and C-S-H has been observed where magnesium enrichment and lower pH conditions are encountered [281]. This may be a product of the limited testing period undertaken here.

The results shown in Figure 7.11 E, F clearly demonstrate the removal of sulfur from the degraded leached zone in each sample, as observed in the element mapping. However, the sulfate balance in the 1.2 MGy irradiated sample is altered compared to the control; despite the sulfur removal, formation of ettringite in the rim of the samples is indicated. This supports the findings from XRD, where a small reflection for ettringite was identified. Although identified through ratio plots, no zones of acicular needles were observed in the rim, indicating that ettringite in this region was present in small amounts and intermixed with the other phases. Given that ettringite formation was noted in the rim, which had elevated carbonate concentrations from both groundwater contact and $CaCO_3$

precipitation, it is considered that its formation is due to CO_2 variations rather than increased SO_3. This is related to the stability of monosulfoaluminate and ettringite, which are dependent on the CO_2/Al_2O_3 and SO_3/Al_2O_3 content of the system. Increased carbonate contents can lead to the destabilisation of monosulfoaluminate and result in changes in the monosulfoaluminate/ettringite balance; detailed discussion on this is outlined in Chapter 6, Section 6.3.1.2. The use of high volumes of BFS in sulfate resistant cements [43] supports this hypothesis, as do the findings of Whittaker et al. [192], who found the sulfate resistance of BFS-containing grouts to be good, with small amounts of ettringite formed due to the limiting effect of alumina from increased hydration of BFS. The progressive exposure of samples to sulfate solutions by Whittaker et al. [192] caused portlandite dissolution and decalcification of C-A-S-H, with cracking / physical damage attributed to calcium removal and not ettringite formation.

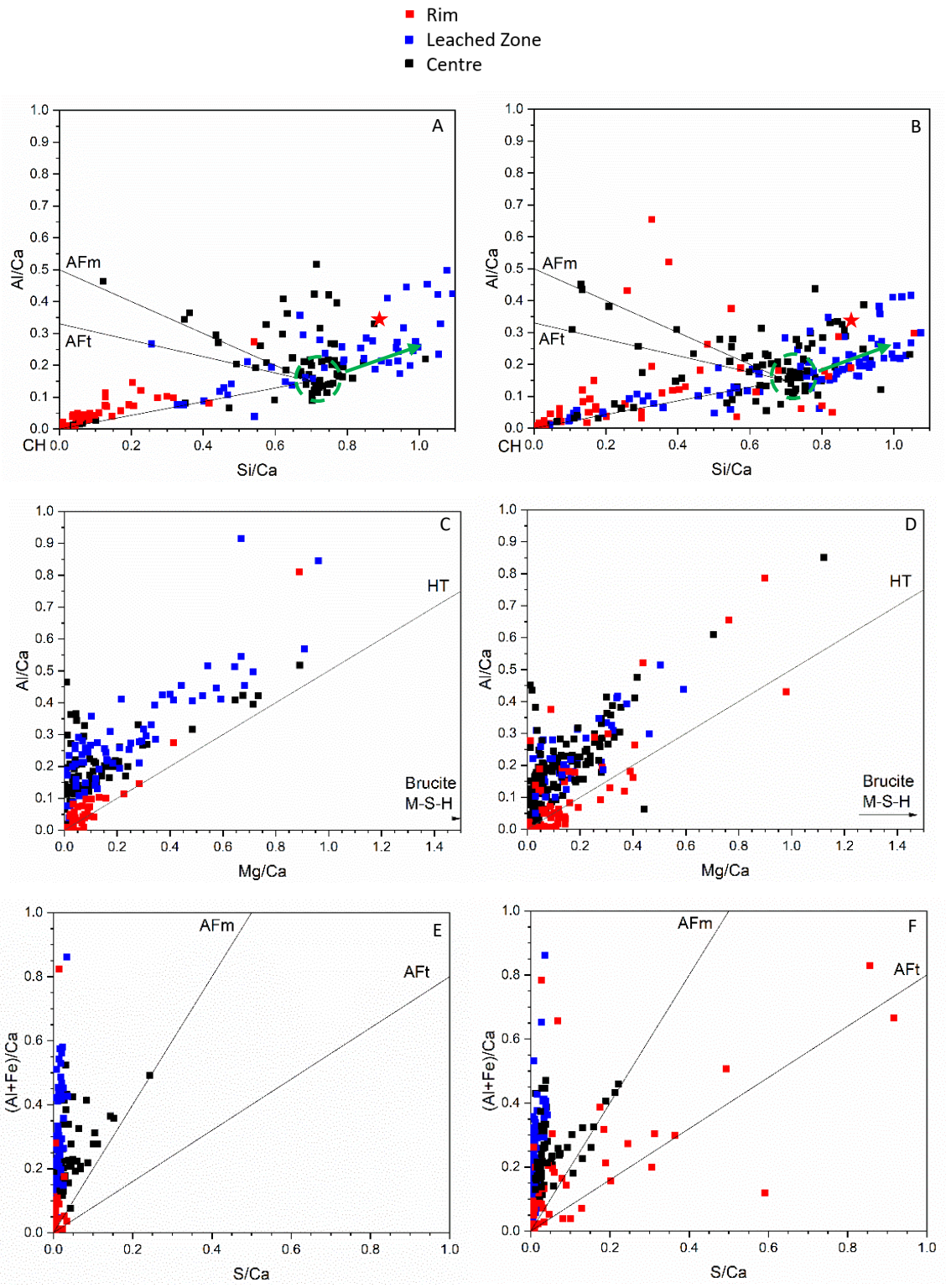

Figure 7.11 EDX point analysis data of 1.2 MGy irradiated and control samples post dynamic leaching. A, C, E: control; B, D, F: 1.2 MGy. Each point sample was taken from a region that visually appeared to be binder rather than residual anhydrous phases. The green dashed circle in A, B denotes the approximate C-A-S-H composition, and the arrow indicates the decalcification of this phase due to groundwater contact. Tie lines link to the other prominent hydrate phases; CH: portlandite; AFm: monosulfoaluminate; AFt, ettringite; and HT: hydrotalcite. Composition of anhydrous BFS shown in A, B by ★ symbol.

7.3.1.2 Solution chemistry

After sampling, pH readings were taken immediately at room temperature in the anaerobic chamber (Figure 7.12 E). For the ICP-OES data, all results are shown as 'difference from blank' to remove the contributions of the synthetic groundwater and better demonstrate the movement of species from/into the sample. This also allows for accountability of the small discrepancies in the composition of the groundwater added at each sampling point; to provide the total volume used, several batches of synthetic groundwater were made, and each solution was not identical due to minor errors in weighing of the chemicals. The dotted lines at 0 on the y axis represent the elemental concentration in the synthetic groundwater (Figure 7.12 A – D).

The pH in all the cells containing samples was increased to higher values than observed in the blanks (11.6 – 9.0 compared to ~8.5 respectively); however, it is noteworthy that the gamma irradiated samples displayed lower mean pH values than the controls at all sampling points (ranges of 11.4 – 9.0 and 11.6 – 9.4 respectively). The pH is initially buffered by leaching of alkali hydroxides and dissolution of $Ca(OH)_2$ [27]. Despite the overall drop in the pH of the leachate over time, $Ca(OH)_2$ was observed to persist in all the systems (see Figure 7.7) which is to be expected given that leaching was limited to the outer zone of the samples. The drop in pH is more pronounced than in leaching experiments on 9:1 BFS:PC using the same synthetic groundwater performed by Rastrick et al. [277], however no replacement of groundwater was completed in that study. The large drop seen in Figure 7.12 E is a product of the more aggressive nature of testing completed.

The lower observed pH in the irradiated samples may be due to several factors, such as the initial quantity of $Ca(OH)_2$ decomposition being lower due to an increase in surface carbonation or reduced alkali concentration in the pore solution [27]. Increased MCL and $Q^3(1Al)$ sites were identified in irradiated samples via ^{29}Si MAS NMR in Chapter 5, which may provide a mechanism for the increased sorption of alkali elements compared to the controls [282]. As the difference in pH remains fairly stable throughout the testing, the variation may be a residual effect from initial decalcification.

Calcium was initially leached from the sample to the solution; however, by day 3, uptake of calcium from the solution had occurred and continued throughout testing (Figure 7.12 A). This fits well with the development of the $CaCO_3$ rim observed from SEM (Figure 7.9, Figure 7.10) and indicates the rim was formed with calcium from the cement and the solution. The formation of this layer may have limited further leaching of the cement, by reducing the available surface area and limiting mass transport [260]; this supports the slower rate at which the pH of the leachate decreased.

An initial rapid uptake of magnesium from the groundwater was observed (Figure 7.12 C), which supports the previously outlined hypothesis of the initial high pH of the system causing precipitation

of Mg-rich phases at the interface (Figure 7.9, Figure 7.10, Figure 7.11 C, D). However, after 7 days the levels returned to those of the blanks, indicating that the formation of the rim limited further contact with the groundwater.

Sulfur concentrations initially increased in the solution as leaching from the cement occurred, as observed by Rastrick et al. for 9:1 BFS:PC cement in the same synthetic groundwater [277], but by day 3 this had reversed and uptake by the cement had occurred (Figure 7.12 D). The formation of the $CaCO_3$ rim may have influenced the leaching of the sulfur by limited groundwater exposure, and this indicates the rim formation is rapid after the initial contact of the cement with the simulant groundwater. The concentration of sulfur taken up from the solution is small, supporting the identification of ettringite formation in the 1.2 MGy sample being primarily caused by CO_3 variations. However, the heterogeneous formation of ettringite due to localised elevated sulfate concentrations in the rim cannot be disregarded. This also supports the findings from SEM EDX and the impact of both factors should be acknowledged.

Where cerium was above the limit of detection for the instrument, concentrations in the leachate were very low, confirming limited removal of cerium from the matrix by leaching (Figure 7.12 B).

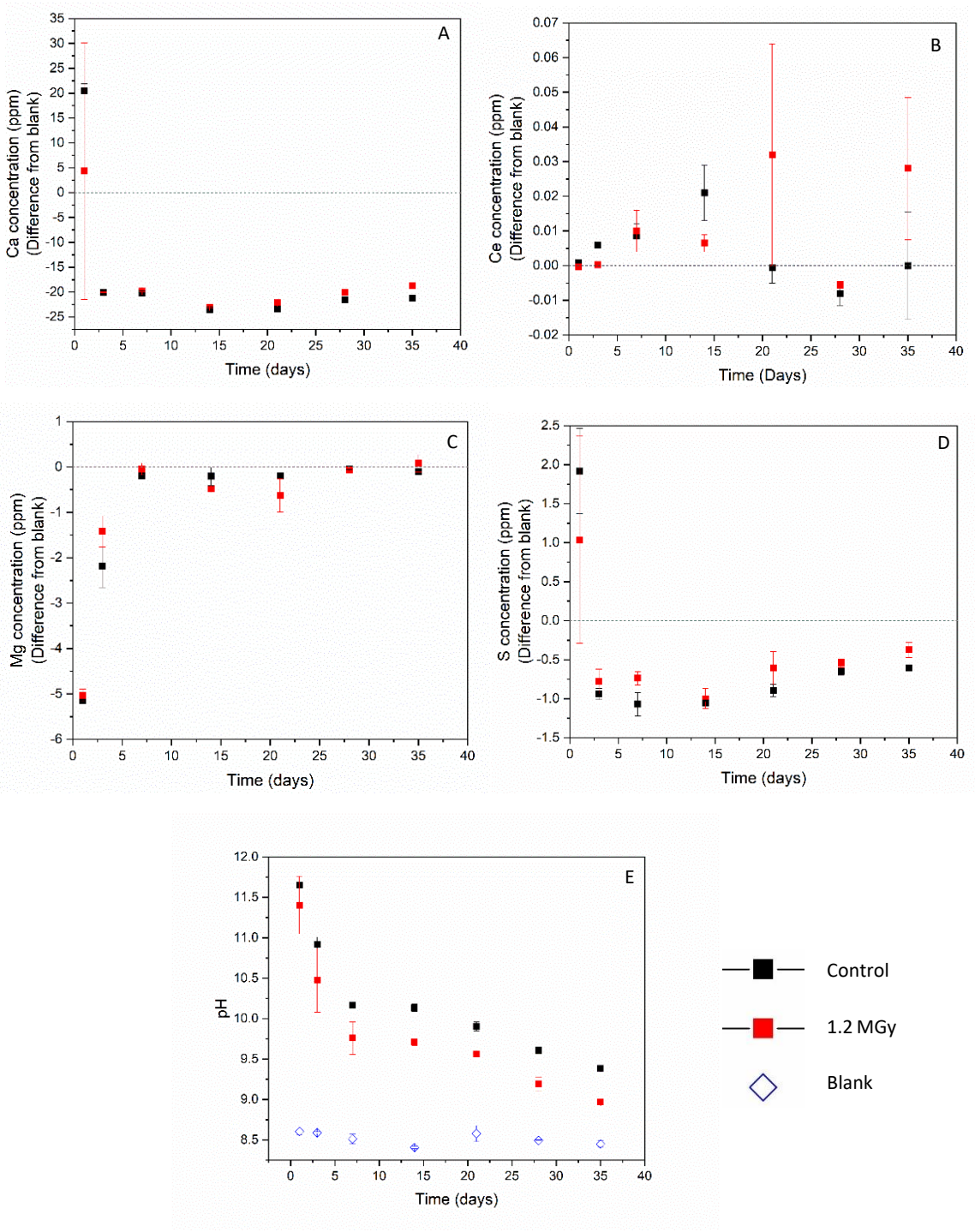

Figure 7.12 ICP-OES analysis of elements in leachate solution for 1.2 MGy and control samples after each replacement in dynamic leaching experiments, showing elemental concentration difference from the blanks of A: calcium, B: cerium, C: magnesium, D: sulfur, and E: the average pH of 2 duplicate samples at each testing point.

The overall response of the samples did not significantly alter as a result of irradiation exposure, with the exception of the lower pH readings from the irradiated samples. This suggests a reduction in the buffering capacity of $Ca(OH)_2$ or soluble alkalis, which may be due to leaching being limited to a surface zone but further investigation is required to establish the cause of this variation.

7.3.2 Static testing

7.3.2.1 Phase assemblage and microstructure

7.3.2.1.1 XRD

The phase assemblage identified through XRD is as observed for the systems pre leaching (Figure 7.13). As seen for the dynamically leached samples, limited variations in the phase assemblage were induced from groundwater contact and prominent peaks for CeO_2 show the dopant is still present post leaching. Increased peak intensities for all hydrate phases suggest increased hydration occurred as a result of groundwater contact. Unlike the dynamically leached samples, the 1.2 MGy static leached sample still displayed reflections for vaterite. Increased proportions of hemicarboaluminate and decreased monosulfoaluminate were observed for the control sample post leaching, with a similar intensity reflection observed for hydrotalcite-like / monocarboaluminate. This might be the result of increased hydration and higher HCO_3^- concentrations (from the simulant groundwater Table 7.2) together with lower SO_3 concentrations inhibiting monosulfoaluminate formation [69], [216], although the cause for this variation from the irradiated sample is not known. The sulfate may be adsorbed to increased proportions of C-S-H formed through increased hydration, although this cannot be ascertained from these data.

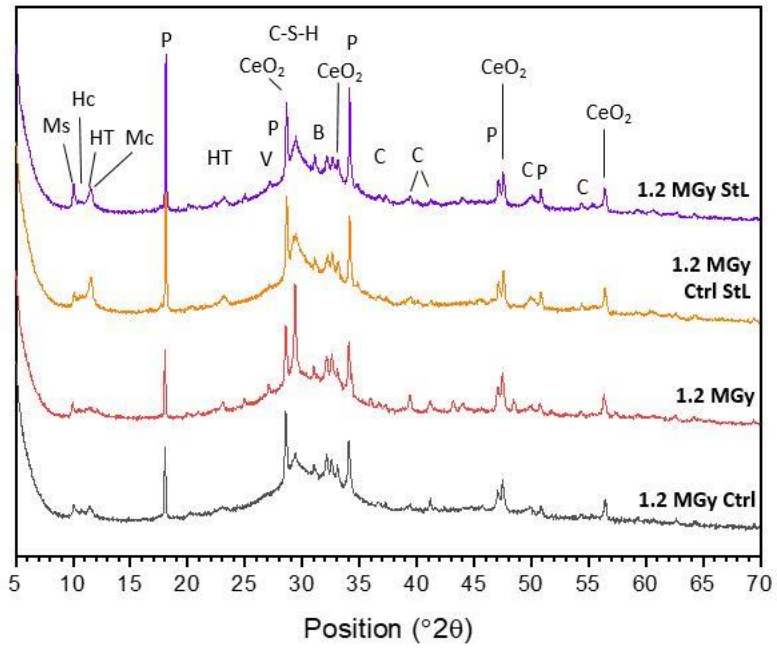

Figure 7.13 X-ray diffractograms of 1.2 MGy irradiated and control 3.44:1 BFS:PC+ CeO_2 pre and post static leaching (StL) in simulated granitic groundwater. Ms: monosulfoaluminate, HC: hemicarboaluminate, HT: hydrotalcite, Mc: monocarboaluminate, P: portlandite, V: vaterite, B: belite (C_2S), C: calcite.

No ettringite formation was noted in any of the samples post leaching, which is to be expected given the limited exchange of groundwater which supplied additional SO_4^{2-} and HCO_3^- in the dynamic testing. The replacement led to alteration in SO_3/Al_2O_3 ratio and the CO_2/Al_2O_3 ratios, which was considered to alter the AFm/AFt proportions due to the mobility of the sulfate and/or carbonate ions in a saturated environment.

7.3.2.1.2 TGA

The TGA results also show minor variations in the phase assemblage as a result of static leaching. The irradiated sample has lower weight loss at temperatures < 100 °C, indicating that less C-S-H had formed and so lower amounts of loosely bound water were removed during heating. Increased weight loss between 600 – 700 °C in the irradiated sample indicates an increase in carbonates present [194].

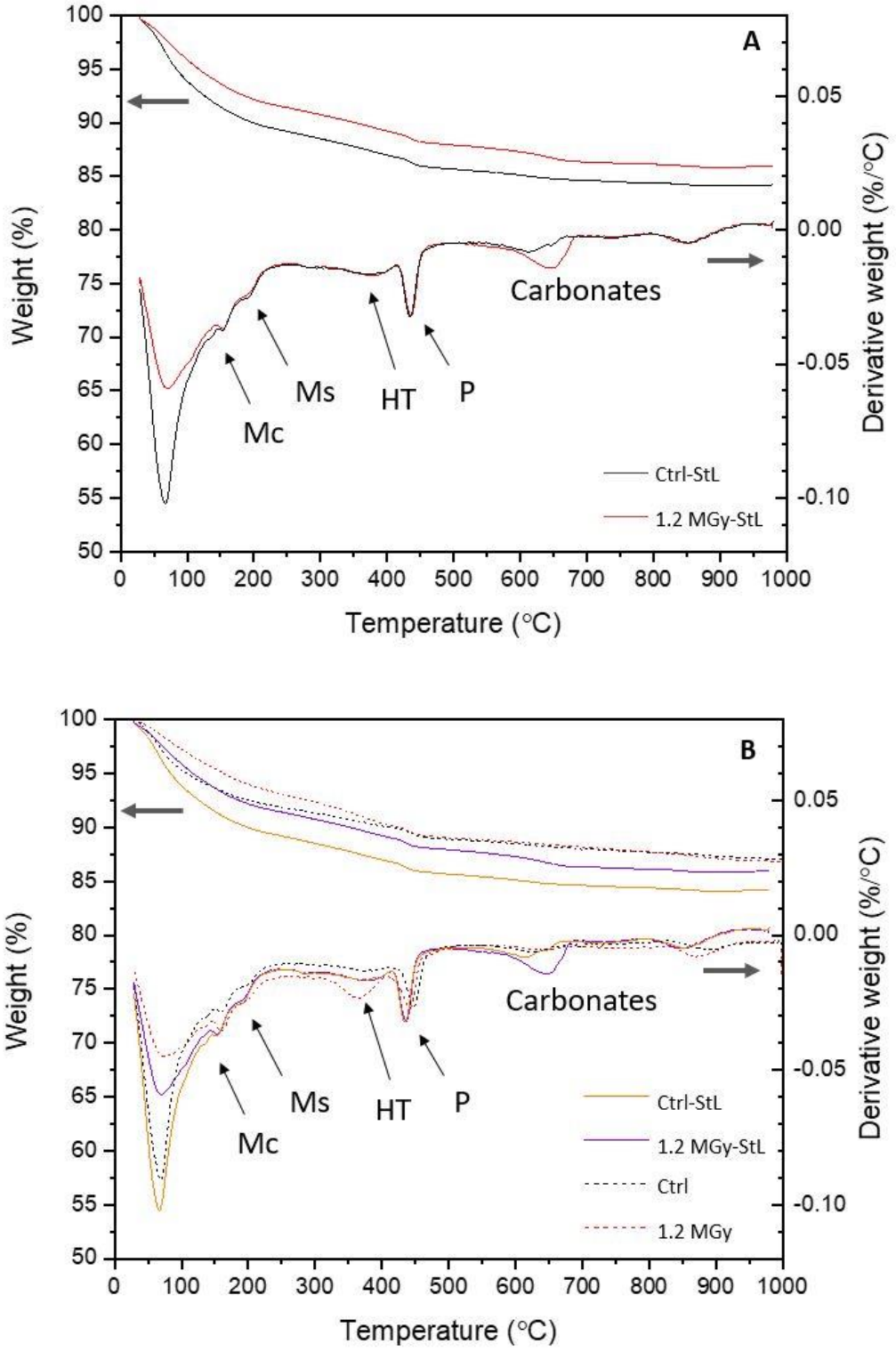

Figure 7.14 TGA of A: 1.2 MGy and control samples post static leaching (StL), B: 1.2 MGy irradiated and control 3.44:1 BFS:PC+ CeO_2 pre and post static leaching in simulated granitic groundwater.

Quantification of the portlandite and carbonate contents was completed, and the results are shown in Table 7.5. Slightly higher portlandite contents in the static leached samples are likely to be the

product of increased hydration, primarily of the BFS but also of PC. Although a high DoH for the clinker components is anticipated (from results in Chapter 5 and previous literature studies [82]), the impact of early age drying in these samples (from heating in the irradiator / oven), together with increased water available for hydration from the leachant, means an increase in PC hydration is anticipated. Elevated carbonate contents, together with the portlandite increase, appear contradictory, and may indicate that potential decalcification of the C-A-S-H and $Ca(OH)_2$ formation had occurred simultaneously to allow $CaCO_3$ formation. This may be a product of the heterogeneity of the leached zone, where localised depletion of $Ca(OH)_2$ allowed the decalcification of C-S-H in some areas, and hydration of PC allowed localised increases in $Ca(OH)_2$ in other areas.

Table 7.5 Quantification of portlandite and carbonate contents of 1.2 MGy BFS:PC + CeO2 sample and control post static leaching in simulated granitic groundwater.

Sample	$Ca(OH)_2$ (%)	$CaCO_3$ (%)
Ctrl-StL	4.3	3.6
1.2 MGy-StL	4.0	4.8

The quantities of carbonates for the control are similar to those observed after dynamic leaching (Table 7.4), whilst they are slightly increased in the irradiated sample despite the limited replenishment of the carbonate rich groundwater. The increased carbonation might be a product of a less distinct rim formed on the surface of the sample, allowing greater dispersion of carbonate-rich pore fluids in the cement.

7.3.2.1.3 SEM-EDX

SEM analysis of the samples showed the development of texturally distinct zones, as seen in the dynamic samples (Figure 7.9, Figure 7.10). However, the rim was not as thick or continuous along the sample edge. The leached zone in the control sample (Figure 7.15) was smaller than observed for the dynamic tests and was not as texturally open. The elemental mapping indicates removal of calcium and sulfur from the cement, as observed in the dynamic testing, and cerium retention in the samples despite the leaching of cement matrix constituents. The leached zone appeared to extend further into the centre of the sample in the 1.2 MGy sample (Figure 7.16), potentially due to breaks in the rim or the presence of cracks allowing ingress of groundwater.

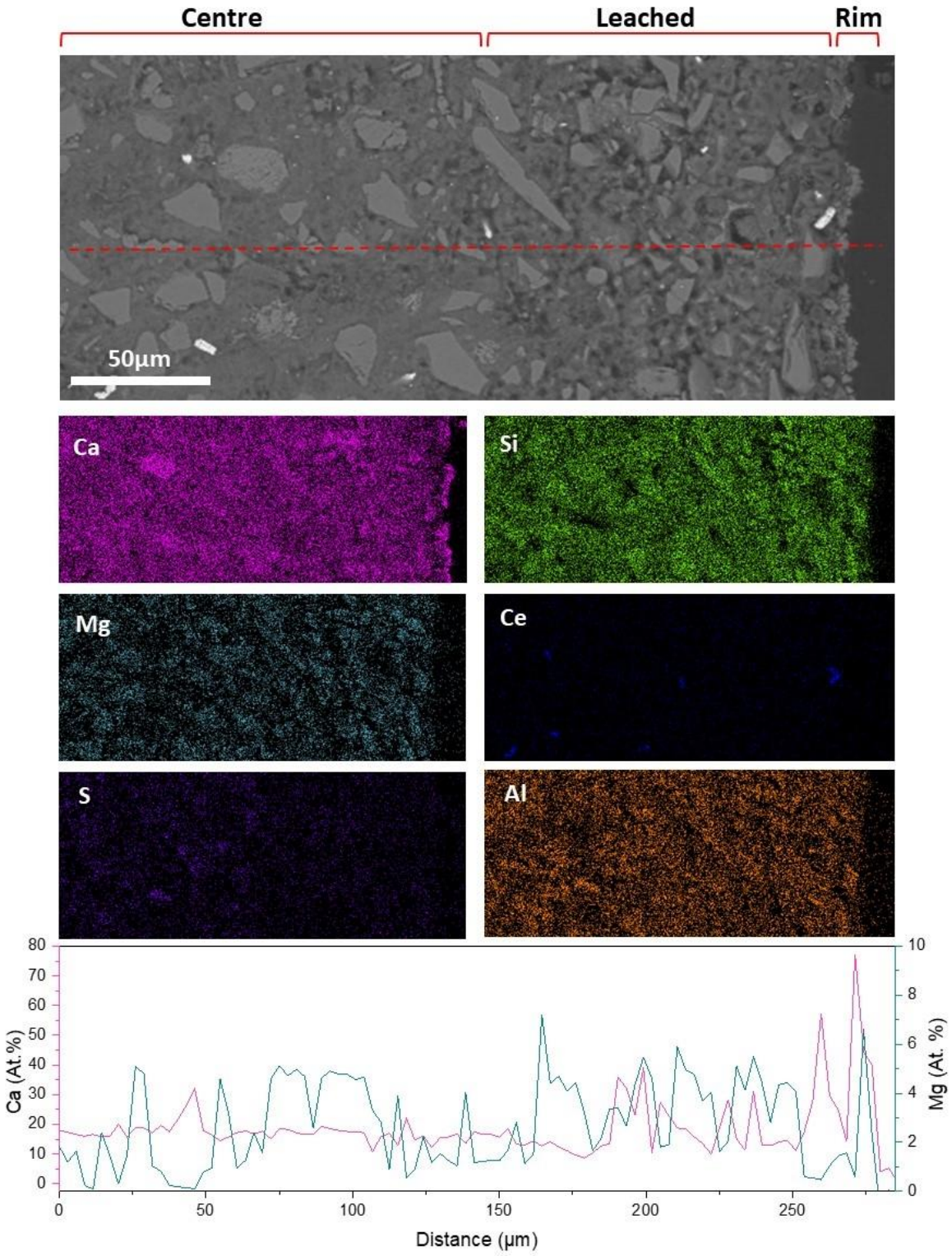

Figure 7.15 SEM EDX of 1.2 MGy control sample post static leaching. The red dashed line in the BSE image denotes the line scan transect

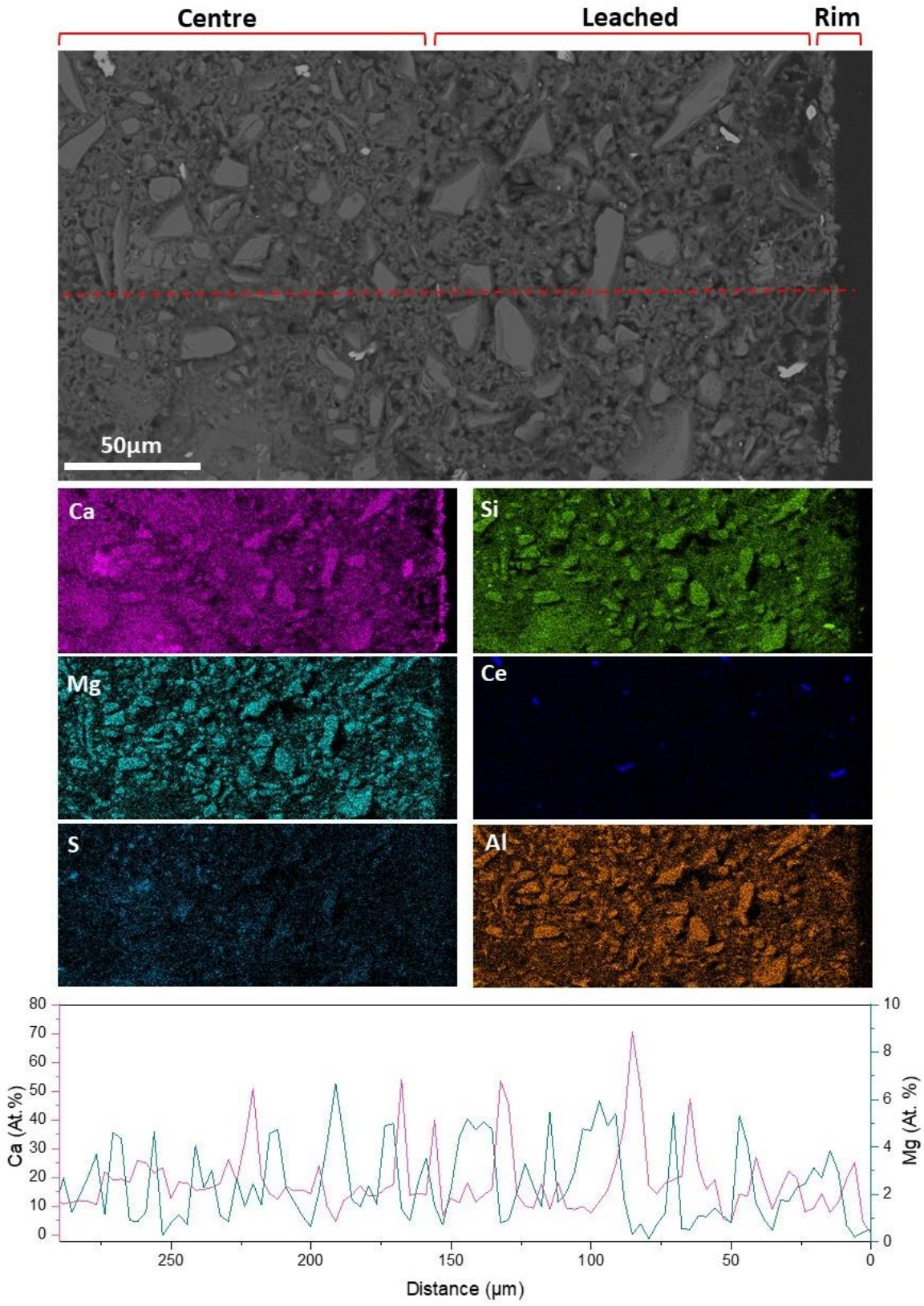

Figure 7.16 SEM EDX of 1.2 MGy sample post static leaching. The red dashed line in the BSE image denotes the line scan transect.

The line scan through the sample shows that the rim thickness is depleted in the static testing and that the precipitation of magnesium at the interface is not as prevalent. This is most likely a product of reduced hydration (discussed below) of the BFS fraction together with the less aggressive pH changes due to no exchange of groundwater taking place during the static test.

Variations in the bulk chemistry of the systems were assessed using EDX point analysis. The overall trends were as observed post dynamic leaching, with a shift to lower Ca/Si ratio values due to the decalcification of phases in the leached zone (Figure 7.17 A, B). However, the reductions in Ca/Si values was not as severe as seen in Section 7.3.1.1.

Whilst an increase in magnesium and aluminium was observed, this was much more pronounced in the 1.2 MGy sample (Figure 7.17 C, D), as the control sample showed very limited increase in any of the texturally distinct zones. This may be a product of the limited extent of the leached zone in this sample leading to less increase in hydration of the BFS fraction. Compared to the dynamic testing results (Section 7.3.1.1.3), Al/Ca ratios were lower, especially in the static control sample, indicating less hydration of the BFS had occurred. The results from the irradiated sample are very similar to those obtained after dynamic leaching, which given the larger leached zone identified, supports the BFS hydration hypothesis.

The sulfate balance of the systems does not appear to have been influenced extensively by groundwater contact, supporting the findings from XRD and SEM analysis (Figure 7.13, Figure 7.15, Figure 7.16). The loss of sulfate from the leached zone is apparent, although evidence of AFm phases in the leached region of the control sample indicate the removal was not as severe as seen for the dynamic testing. No ettringite formation was observed, even in the rim of the samples; given that the sulfate and carbonate levels were not replenished in this test, this is to be expected.

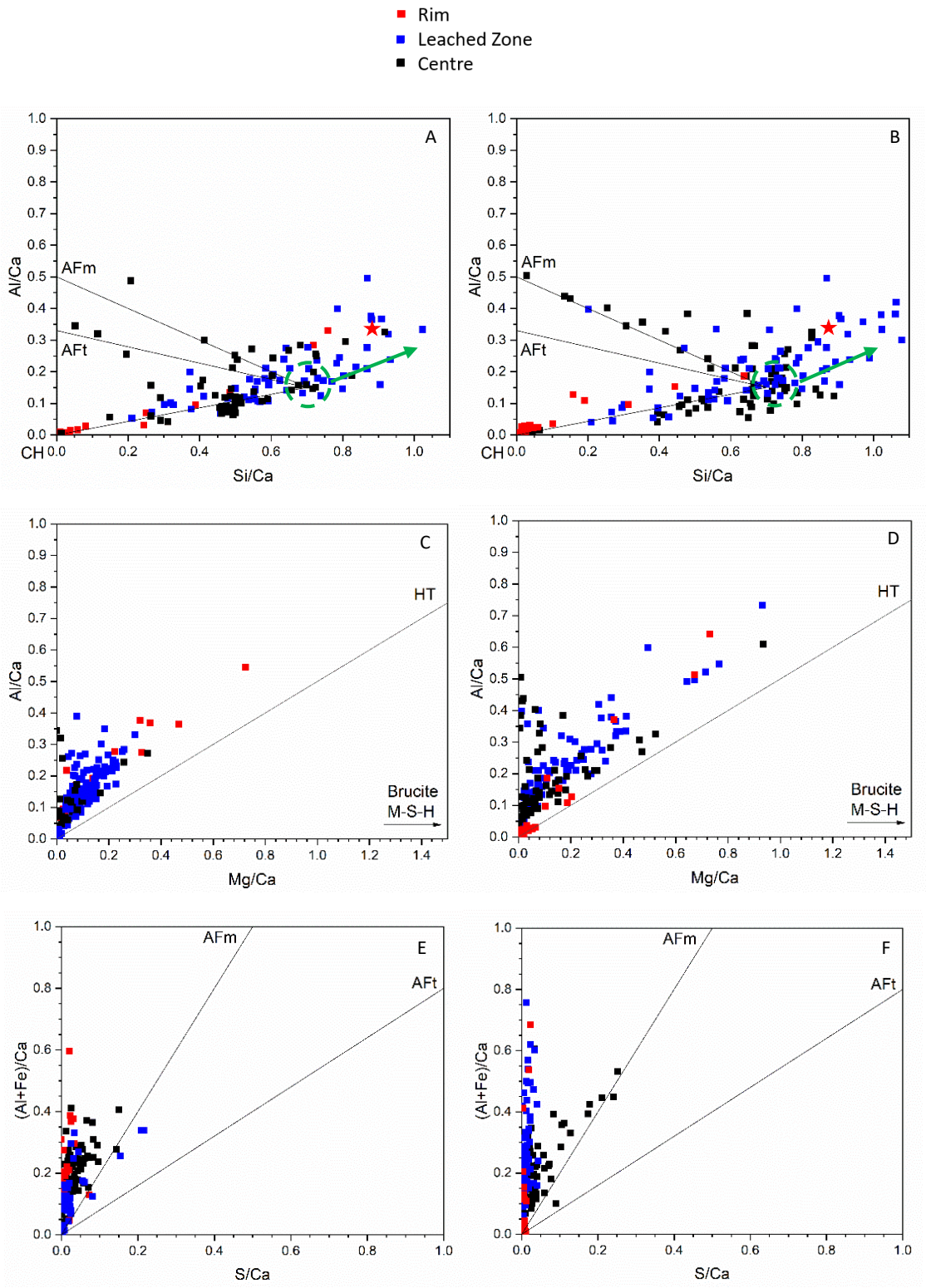

Figure 7.17 EDX point analysis data of 1.2 MGy irradiated and control samples post static leaching. A, C, E: control; B, D, F: 1.2 MGy. Each point sample was taken from a region that visually appeared to be binder rather than residual anhydrous phases. The green dashed circle in A, B denotes the approximate C-A-S-H composition, and the arrow indicates the decalcification of this phase due to groundwater contact. Tie lines link to the other prominent hydrate phases; CH: portlandite; AFm: monosulfoaluminate; AFt, ettringite; and HT: hydrotalcite. Composition of anhydrous BFS shown in A, B by ★symbol.

7.3.2.2 Solution chemistry

The results from ICP-OES analysis are shown in Figure 7.18, where they are compared to the results obtained from the dynamic leaching (transparent points) for reference.

The pH results show the leachate was, to a small degree, buffered to higher values than observed in the dynamic leaching with values of 11.9 in the static test compared to 11.6 in the dynamic testing (Figure 7.18 E). This difference is considered to be due to increased proportions of alkali elements leaching from the cement into the leachate, together with a smaller proportion of $CaCO_3$ forming resulting in a more limited rim feature. No significant difference was observed between the irradiated and control sample pH value.

In terms of calcium content within the leachate, the liquid samples showed much higher concentrations than observed in the dynamic testing indicating progressive leaching of calcium from the cement into groundwater (Figure 7.18 A). The overall concentration was 4-5 times higher than observed for the dynamic testing. This is considered to be a product of the progressive leaching of $Ca(OH)_2$ and possible decalcification of C-S-H (shown in Figure 7.17 A, B) which, without the replenishment of simulant groundwater, is not provided with HCO_3^- to allow formation of a $CaCO_3$ rim on the same scale as seen in Section 7.3.1.1.3. It was noted in Table 7.5 that quantified $Ca(OH)_2$ increased post leaching, which seems counterintuitive to the results here. As discussed in Section 7.3.2.1.2 it is important to consider the heterogeneity of the leached zone, and also to note TGA is representative of the bulk sample whereas analysis of the leachate displays only what is occurring in the leached zone. Further analysis to quantify the changes in leached and un-leached zones using electron microprobe analysis would allow greater understanding of the changes resulting from leaching.

The calcium concentrations were lower in the 1.2 MGy irradiated sample, although the large error associated with the control may be the cause of this difference. The rim formed in the irradiated sample is more consistent across the surface (as in it is more continuous, with fewer gaps present, see Figure 7.16) than in the control sample (Figure 7.15), supporting this theory.

Magnesium concentration data shows initially rapid uptake by the cement (seen at the first sampling points in dynamic testing) that does not reverse over the testing period (Figure 7.18 C). As precipitation is due to the pH difference (magnesium solubility is very low at high pH [239]), it may be inferred that, after the initial pH increase, the value remained static at the interface. This can be attributed to the formation of the outer carbonate rim.

Sulfate was leached from the cement upon contact with the groundwater as anticipated from the SEM elemental mapping (Figure 7.18 D). Overall, the results are similar to those for calcium; greater overall concentrations are measured here than were observed for the dynamic testing, with lower concentrations observed in the irradiated sample leachate. The reduced amount of leached sulfur supports the XRD results for these samples, as higher monosulfoaluminate contents were identified in the irradiated sample. Therefore, removal of sulfate from the control sample may have been due to pore water replacement, or sulfate adsorbed to the C-S-H might have been released as decalcification of this phase progressed.

Cerium concentrations were almost at the limit of detection and within 0.02 ppm of the measured concentration of the blank solution, indicating that no release from the monoliths had occurred during the test period (Figure 7.18 B).

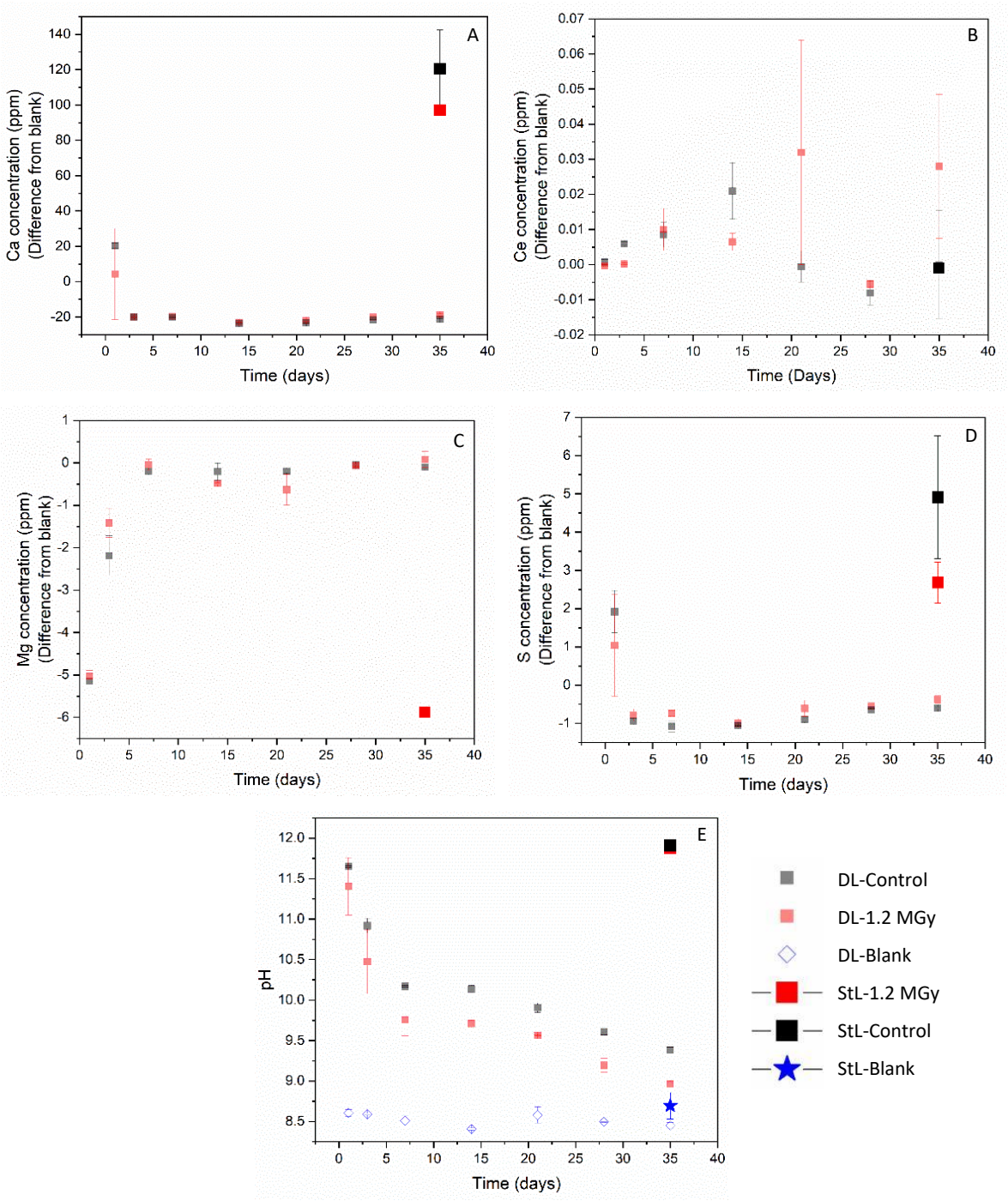

Figure 7.18 ICP-OES analysis for 1.2 MGy and control samples after static leaching showing elemental concentration difference to the blanks of A: calcium, B: cerium, C: magnesium, D: sulfur, and E: the average pH of samples at each testing point. Results are compared to those from dynamic leaching (transparent symbols above)

7.4 Conclusions

Characterisation of the CeO_2 doped BFS:PC identified the development of the same phase assemblage and microstructure as undoped systems. The dopant appeared to remain inert and was well encapsulated in the matrix. The microstructural and textural development was considered to be

similar to that observed in Chapter 6, and the behaviour of the CeO_2 with the cement was considered representative of PuO_2 in this instance.

Irradiation of the CeO_2-containing system produced a similar response in the cement to that seen in Chapter 5. No major alteration to the phase assemblage was identified through XRD or SEM. TGA results showed a loss of free water as a result of irradiation exposure and an overall increased weight loss that suggests increased hydration of the anhydrous precursors. There was a notable increase in weight loss between 300 – 400 °C which was tentatively assigned to hydrotalcite decomposition; however, it is considered more likely that the weight loss represents a metastable carbonate form but, from the current analysis, no firm conclusion can be reached. Post leaching, this distinct weight loss was significantly reduced, indicating that it was not stable upon contact with groundwater. Further work is required to ascertain the cause of this specific weight loss increase.

There was no observable increase in large scale defects within the matrix as a result of irradiation. The CeO_2 did not appear to act as a nucleus for defects, with no cracking observed at the CeO_2-cement grout interface after irradiation. No macroscopic cracking was present, indicating that attenuation of gamma radiation by the dopant does not significantly affect the microstructure.

Exposure to synthetic granitic groundwater appears to have allowed increased hydration of the anhydrous precursors, producing a greater amount of hydrate products in leached samples. The dynamic leaching method caused minor alterations to the phase assemblage, notably to the AFm/AFt balance, carbonate polymorphs and quantities. The development of texturally distinct zones (rim, leached and central zones) of approximately similar thickness was noted in the samples from dynamic and static leach testing. The rim was characterised by high calcium content and is considered to be formed of $CaCO_3$ due to the levels of HCO_3^- present in the groundwater, and this in part may be acting as a protective layer preventing further leaching. The leached zone was calcium-depleted and had increased porosity and open texture, whereas the central zone was unaffected by the leaching exposure. Magnesium uptake from the granitic solution was noted at sampling points < 5 days after which this ceased, potentially due to rim formation limiting groundwater interaction. The relatively high pH of the cement pore solution limited movement of the magnesium throughout the cement. Ettringite formation was noted in the rim of the 1.2 MGy irradiated sample, considered to be a result of the increased carbonate content and minor increases in sulfate from the groundwater. Cerium was retained in the cement after leaching, even in the leached zone, and ICP-OES results indicated no release of cerium into the groundwater.

The irradiated samples did not buffer the pH of the leachate to values as high as the control, which is attributed to a reduction in the buffering capacity of $Ca(OH)_2$ or soluble alkalis. Further investigation

of this is required to understand the mechanism responsible for this difference. Notwithstanding the small variation in pH and formation of ettringite in the irradiated sample, the overall response to groundwater contact was similar in both samples, indicating that irradiation exposure does not cause large scale variations.

The leaching methodologies are considered to provide a worst case scenario of the response of these cements to groundwater ingress. The development of similar textural domains, albeit on different scales, from both the dynamic and static testing indicates the same processes are occurring in both. It should be noted that neither method provides conditions representative of a GDF, where slow replenishment of the groundwater would occur.

8 Simulation of radiation damage via alpha decay in BFS:PC grouts using $^{4}He^{2+}$ ion acceleration

This chapter aims to further probe the interface between alpha emitting species and cements used for waste encapsulation. Due to equipment issues, limited microscopic investigation was completed on the PuO_2 doped samples characterised in Chapter 6. The region directly adjacent to the alpha emitting particle was of considerable interest, so attempts to recreate this zone through non-radioactive experiments were pursued. This type of experimental technique has not previously been applied to encapsulation grouts composed of BFS:PC and, as such, this work provides a novel and important scoping trial to assess the suitability of this testing methodology for cementitious materials.

8.1 Introduction

As outlined in Chapter 2 Section 2.1, ILW materials can contain radionuclides that emit radiation at levels >4 GBq / t alpha and >12 GBq / t beta/gamma, meaning the encapsulating grouts are exposed to high levels of ionising radiation throughout their service life. Current UK guidelines require maintenance of the wasteform properties for 150 years post manufacture, and the package forms a component of the multi-barrier system employed by the geological disposal concept that aims to isolate waste for over 100,000 years [19]. It is imperative that we understand how radiation affects these materials so a robust safety case for waste disposal can be created.

The effects of alpha radiation on cementitious grouts are not well understood. The majority of irradiation studies focus on the potential for degradation of mechanical properties for structural concrete in reactor environments and for biological shielding, where neutron and gamma irradiation are the most pertinent. Studies tend to focus on Portland cement, a component of structural concrete, whereas the grouts used for encapsulation are commonly blends of Portland cement and supplementary cementitious materials (SCMs), such as blast furnace slag (BFS), which have a distinct chemistry and microstructure. These changes are likely to result in a different response to radiation compared with the more Ca-rich binders based on plain PC.

As outlined in Chapter 2, Section 2.5, the impact of alpha radiation on cements will manifest via two processes: radiolysis and atomic displacements [36]. Radiolytic decomposition of pore fluid will result in the generation of gaseous products, reactive species and overpressure which could cause crack development. Due to the short path length of alpha particles within cements, these radiolysis reactions will occur in an extremely small volume surrounding each radiation source. This may create more molecular products, increasing gas production, and thus generate distinct chemical variations in the zone of influence of the radicals. These variations together with ballistic impacts from the alpha

recoil and emitted particles (potentially causing amorphisation) may produce damage zones similar to radiohaloes observed in natural inclusions [136] (Figure 8.1). The majority of alpha studies are linked to gas evolution, and data on microstructural impact are limited, but observations of the bulk have indicated that alpha encapsulation may be more likely to cause chipping/spallation and reduction in strength than similar doses of gamma irradiation [130]. The impacts of these effects on the cement microstructure and any resulting changes in the physico-chemical properties are currently unknown. More information is required on the potential mechanisms responsible.

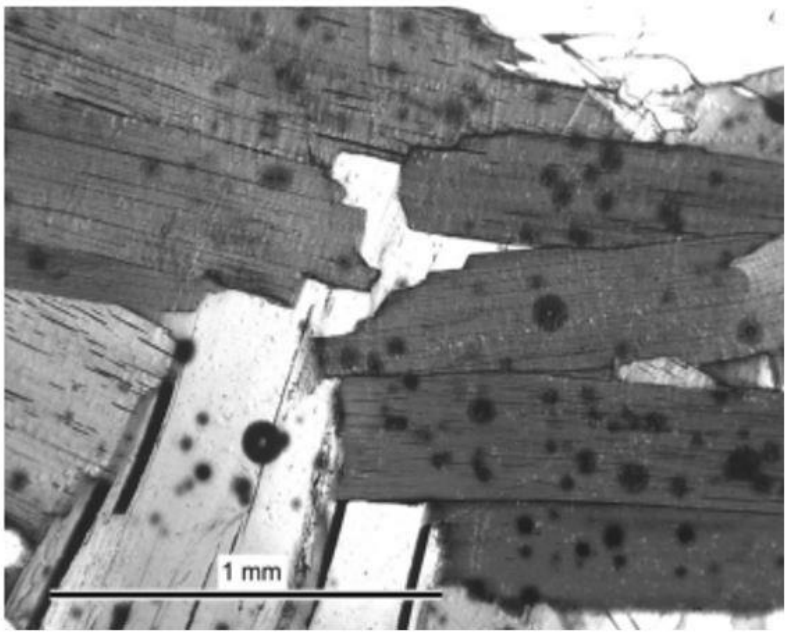

Figure 8.1 Optical micrograph of radiohaloes observed in biotite with thorium rich inclusions, from [135].

Previous work completed in collaboration with the UK National Nuclear Laboratory (Chapter 6) investigated the bulk effects of encapsulation of alpha emitting radionuclides on the characteristics of PC-blended cements. The results of XRD analysis in that chapter indicated potential changes to the phase assemblage in BFS containing grouts as a result of chemically induced variations leading to potentially expansive sulfate containing phase formation. However, limited microstructural investigation of these samples was completed.

The aim of the current chapter is therefore to determine the impact of alpha decay on the microstructure of cementitious grouts used for encapsulation of nuclear waste. Establishing whether ion acceleration provides an appropriate technique for simulating this in cementitious materials was a key objective, as due to the hydrated nature of the phase assemblage, care must be taken to ensure the experiment setup does not produce excessive sample heating. The influence of radiolytic decomposition of pore fluid causing distinct zones of chemical variations was also of interest, as

electronic stopping effects have the potential to cause significant chemical changes in the wasteform binder chemistry.

8.2 Experimental methods

8.2.1 Sample synthesis

Samples were synthesised and cured using the method outlined in Section 3.2 for small volumes of materials. Grouts were cured in sealed 50 mL centrifuge tubes for 3.3 years, and were removed approximately 10 days prior to ion irradiation to undergo sample preparation. Thin slices were taken from the monolith using a slow saw and wafering blade. These were further thinned using SiC grit papers, after which the sample surface was polished using progressively finer cashmere cloths coated with diamond suspensions (6 µm decreasing to 0.25 µm). As hydration was not halted for these samples, no isopropanol was used during the preparation. After polishing, the dimensions of the cement samples were < 15mm diameter and < 1 mm thick. The density of the samples was obtained using an Archimedes balance, with an average of 2.03 ± 0.01 g cm^{-3} observed over three samples.

8.2.2 Ion irradiations

Irradiations were completed at the Helmholtz Zentrum Dresden Rossendorf (HZDR) Ion Beam Center (IBC), using 5 MeV He^{2+} ions to simulate alpha particle energies replicating those of plutonium and uranium decay products [92], [283]. Sample and irradiation conditions are outlined in Table 8.1.

Table 8.1 Details of samples and irradiation parameters

Sample	Material	Age (Yrs)	Ion type and Energy	Current	Fluence (cm^{-2})	Flux
CEM3Y	3.44:1 BFS:PC	3.3	5 MeV He^{2+}	5 nA/cm^2	1 x 10^{15}	1.56 x 10^{10} He^{2+} ions/s/cm^2

Irradiations were completed at room temperature in air and samples were mounted on a water cooled stage using carbon adhesive tape to reduce sample heating during exposure. The current density and flux were also kept low (Table 8.1) to minimise heating effects. Trials of the experimental setup using thermal-sensitive tapes together with consideration of the thermal conductivity of the samples (2.05 W/mK) indicated that approximate temperature variations of less than 1°C would be achieved across the sample using this configuration. The ion beam angle of incidence was kept perpendicular to the sample surface throughout irradiation, with a scanning ion beam (spot size 5 mm) moving in X and Y directions with a frequency of 1 kHz.

Estimation of damage induced in the sample via electronic and nuclear stopping was calculated with SRIM [127] using the 'Detailed Calculation with Full Damage Cascades' option (SRIM 2013) operated with 99,999 ions. Given the variable composition of the material and the unknown proportion of elements/phases within the specific sample, displacement energies were set to 50 eV for all elements to allow an estimation of damage [284]. The damage-depth profile calculated from SRIM for the sample is shown in Figure 8.2, and shows that these irradiation conditions are predicted to create a damage region extending from the surface to approximately 5 µm with peak damage of 4 x 10^{-3} displacements per atom (dpa) at 4.5 µm depth. Electronic stopping (Se) was observed to dominate energy loss, with maximum nuclear to electronic stopping (Sn/Se) values of 9.5 x 10^{-4} observed.

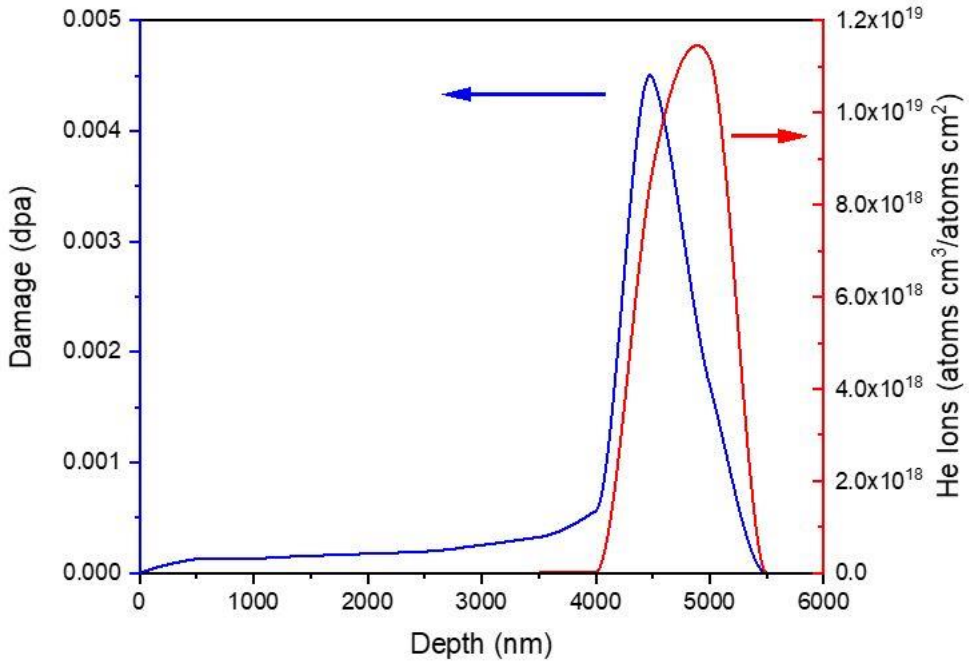

Figure 8.2 Estimated displacement-damage depth and ion density profiles for 3.44:1 BFS:PC cements irradiated with 5 MeV He^{2+} to a fluence of 1 x 10^{15} ions cm^{-2} calculated using SRIM [127].

The fluence of 1 x 10^{15} ions/cm^2 was chosen as representative of ion irradiation studies on other wasteform materials such as ceramics, glass, and minerals [285], [286] and so it seemed appropriate to trial this experimental technique using comparable testing parameters. Ion accelerator testing has been completed on clay minerals that will form either backfill materials or the near-field geological environment in GDFs and the fluence chosen here was also based on those experimental methods [224], [287].

Estimation of the total absorbed alpha dose indicates this fluence will provide a significantly higher dose than observed for the samples in Chapter 6 where, at the age of characterization, the total

absorbed dose was ~ 1 MGy. The estimated dose from the experimental setup outlined above is approximately 300 MGy, using the relationship defined in equation 8.1 [224]:

$$D = \phi \cdot S \cdot m^{-1} \cdot 1.6 \times 10^{-19} \int_0^y \frac{dE}{dy} \cdot dx \quad (8.1)$$

where D is the dose expressed in grays, ϕ is the fluence (ions/cm^2), S is the irradiated surface area (cm^2), *dE*/*dy* is the deposited energy (eV) per micron of range, x is the range (µm), and *m* is the mass (kg). Although this dose is far in excess of that which was experienced by the PuO_2-containing samples in Chapter 6, it was considered to give the best test of experimental robustness and a conservative approximation of alpha irradiation tolerance.

8.2.3 Post irradiation characterisation

Characterisation was completed at the UoS MIDAS facility using optical microscopy, SEM-EDX, XRD and FTIR as outlined in Chapter 3. Additional analysis was completed in conjunction with Oak Ridge National Laboratory, availing of their experience preparing and analysing TEM of cementitious materials.

TEM allows investigation of hydrate morphology and chemical composition in the scale of hundreds of nanometers, reducing the problems of intermixing that are associated with SEM. As the interaction volume is greatly reduced in TEM, characterisation of finely intermixed hydrate phases can be completed [168], [288]. Bright field images were obtained via collection of the transmitted electron beam on the image plane of the objective lens; this was magnified and projected to the CCD camera to allow viewing. Diffraction patterns of the samples were obtained by changing the focal point from the image plane to the back focal point [288]. The basis of EDX analysis in the TEM is as outlined for SEM-EDX (Chapter 3); however, in order to prevent shadowing effects during analysis in the TEM, the stage was tilted to 20°. This also maximised X-ray collection and minimised spurious readings from thicker areas of the sample [168].

Although becoming an increasingly common characterisation technique for cementitious materials, the preparation of TEM samples and their observation without causing undue damage is challenging [168]. In order to minimise differences between the samples in this comparative study, the same preparation methods were used to attempt to ensure that artefacts would not be mistaken for He^{2+} effects. Although investigation of radiation damage using high resolution TEM (HRTEM) is commonly used on mineral and ceramic specimens to assess if changes to the crystal lattice have occurred [137], [289], [290], attempts to do this on cement samples have often led to decomposition of the hydrate phases [288]. HRTEM removes the aperture which blocks the diffracted beam during bright field TEM, allowing the image to be formed from both the transmitted and diffracted beams. This can potentially

produce images with atomic resolution, enabling very detailed crystallographic studies [137]. However, thermal and irradiation damage from the beam cause rapid damage to the delicate crystalline phases in cement before data can be collected and instances where data has been published claiming success, have been contested in the literature [288].

SEM-FIB was conducted on a FEI Quanta 3D 200i Dual Beam instrument, which was used to produce lift out specimens of the irradiated sample for TEM analysis. Upon locating a suitable area of cement matrix, the stage was tilted to 52° and a platinum strip deposited to protect the surface. Trenches were cut adjacent to this using a gallium beam with a current of 5-7 nA and energy of 30 kV, after which the stage was tilted to 7° and the lamella undercut using a reduced beam current of 3 nA. The liftout needle was platinum welded to the lamella; the remaining final cut was made to free the lamella and to allow lift out, and the sample was then mounted on a copper TEM grid. Thinning of the samples was completed using progressively lower beam currents (1, 0.5. 0.3 and 0.15 nA), with final cleaning completed using beam energies and currents of 5, 2 kV and 48, 43 pA respectively.

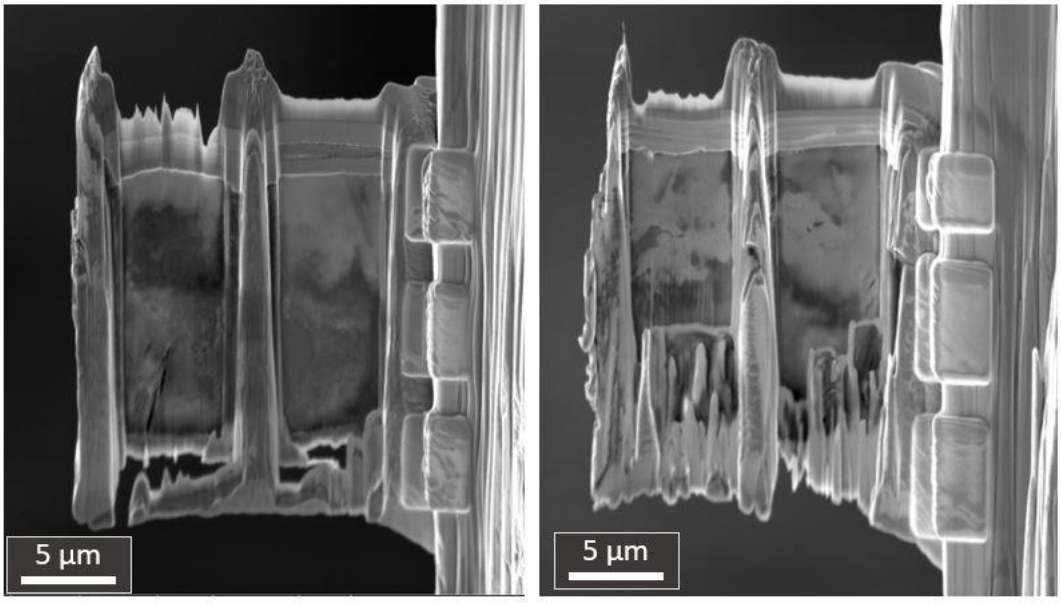

Figure 8.3 FIB samples of CEM3Y after cutting, thinning and polishing completed. Variations in finish are due to the multiphase nature of the material; hard unreacted BFS particles adjacent to softer hydrates complicate preparation of a uniformly thick sample.

TEM was completed using a JEOL JEM-2100F TEM/STEM 200keV field-emission system with Oxford X-Max 80 mm^2 SDD-EDS. Bright field images were collected at a magnification of 20 kx using spot size 1. For each sample, between 30–50 EDX points were taken at 15 kx magnification using spot size 1, and a beam diameter of 200 nm. Selected area diffraction patterns were collected from areas containing crystal clusters to ascertain the phase and from regions of C-S-H to attempt to limit intermixing during

chemical analysis. Indexing of crystalline phases was completed by measuring the distance from the central point to pairs of reflections in the diffraction pattern and calculating the d-spacing using the camera length used to capture the image. The values were compared with standard crystallographic patterns to identify phases.

8.3 Results and discussion

8.3.1 Optical microscopy

Visual inspection of the samples post irradiation indicated a colour variation had been caused by He^{2+} exposure. The matrix appeared lighter, with a yellow sheen observed. Sections taken perpendicular to the irradiated face showed the discolouration to be a surface effect.

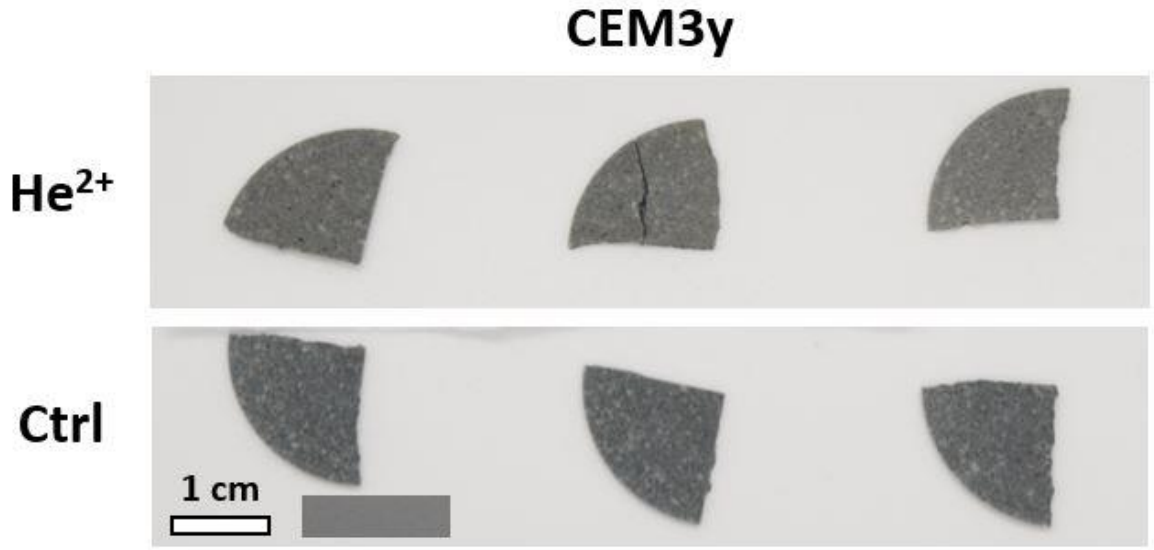

Figure 8.4 Photograph of CEM3Y post He^{2+} irradiation compared to control samples showing colour variation. Reference grey card shown at base of figure.

In order to quantify the difference between the samples, photographs were taken using a grey card of known RGB value and an in-house methodology of colour measurement [291] was used to extract RGB values, allowing indexing of the mean values (Table 8.2).

Table 8.2 Indexed RGB values for irradiated and control CEM3Y samples.

Sample	CEM3YA	CEM3YA Ctrl	CEM3YB	CEM3YB Ctrl	CEM3YC	CEM3YC Ctrl
RGB	106/105/102	97/99/99	115/114/110	97/100/100	118/117/113	99/101/101

The variation in colour is similar to the discolouration effect observed in radiohaloes. Although these typically tend to be darkened rims adjacent to the alpha emitter, lighter yellow occurrences have been observed in cordierite ($Mg_2Al_4Si_5O_{18}$) [136], [138]. The mechanism of the discolouration is not well defined. Whilst point defects have been outlined as a potential cause of radiohaloes in biotite [134], there is debate regarding the impact of ionisation effects on their formation and the increased prevalence of these features within hydrated phases [135]–[138]. In hydrous materials such as biotite, the radiolysis of OH^- groups has been linked to reduction of Fe^{3+} from the metal rich octahedral sheets. The relocation of interlayer charge balancing species together with increased electron density has been attributed as a potential cause for twisting or buckling of sheets leading to structural collapse [135], [137].

Investigation of the characteristic blue-green colour of BFS:PC cement by Chaouche [292]et al. [292] found it was associated with the presence of a trisulfur radical ion which is a blue chromophore. This might indicate that the colour change observed here is related to sulfur redox changes, although typically a decrease in this species leads to bleaching (to white) rather than the yellowing observed in the samples in this investigation. It should be noted that the disulfur radical anion is a yellow chromophore [293], however the presence of this species was not detected by Chaouche et al. [292]. It was also noted that the involvement of transition metals in the colouration of the cement was not considered as part of this study and they may significantly contribute to colour together with the sulfur chromophores.

Colour response in materials due to irradiation exposure is a well-documented phenomenon and is commonly used industrially to produce gemstones [294], [295]. Alteration to $[AlO_4]^0$ colour centres is responsible for the formation of 'smoky' quartz, creating the characteristic darkening upon irradiation [296]. Lima and Lameiras [295] found that upon irradiation of quartz, the intensity of colour change was linked to the movement of charge balancing Li^+ away from $[AlO_4]^0$ centres; this corresponds well with the loss of interlayer K^+ from He^{2+} irradiated biotite [287].

It is noteworthy that the same colour variation was not observed after gamma exposure of these materials (Chapters 5, 7). However, due to the time taken to complete the gamma testing and the

contribution of atmospheric carbonation over the testing period which leads to bleaching of the blue colour, these effects may have been obscured.

Analysis of the redox states of S and Fe is considered valuable further work for these samples, as assessment of changes in oxidation states will help inform regarding the mechanism of colour change. Unfortunately, this was not able to be completed within the scope of this thesis.

8.3.2 XRD

XRD was completed on the polished surfaces of the ion irradiated and control samples to allow comparison post irradiation. Grazing incidence XRD (GIXRD) is commonly used to investigate ion irradiated samples to assess changes in the surface "damaged layer" of the material, however, attempts to obtain GIXRD data on the samples were unsuccessful; no meaningful data were observed as the signal to noise ratio could not be effectively minimised. Given this, the results shown in this section are from reflection-mode XRD. Although stronger preferred orientation effects are likely to be present in the results here compared to powdered samples presented in previous chapters, the phase assemblage was as observed for this cement in previous chapters. There was a higher proportion of hydrotalcite noted, which is to be expected in samples of this advanced age due to increased BFS hydration [82], [188].

The difference pattern in Figure 8.5 shows that the diffraction patterns from both samples were very similar. No shift in peak position or width was observed, indicating that ballistic damage to the crystalline phases was limited, as anticipated from SRIM modelling. Although a weak reflection associated with vaterite was observed in the He^{2+} irradiated sample at 27.1 °2θ, no significant increase in carbonate products was observed. The consistency in the phase assemblage indicates that ionisation effects from electronic stopping of the He^{2+} ions have not caused bulk changes to the crystalline components of the cement.

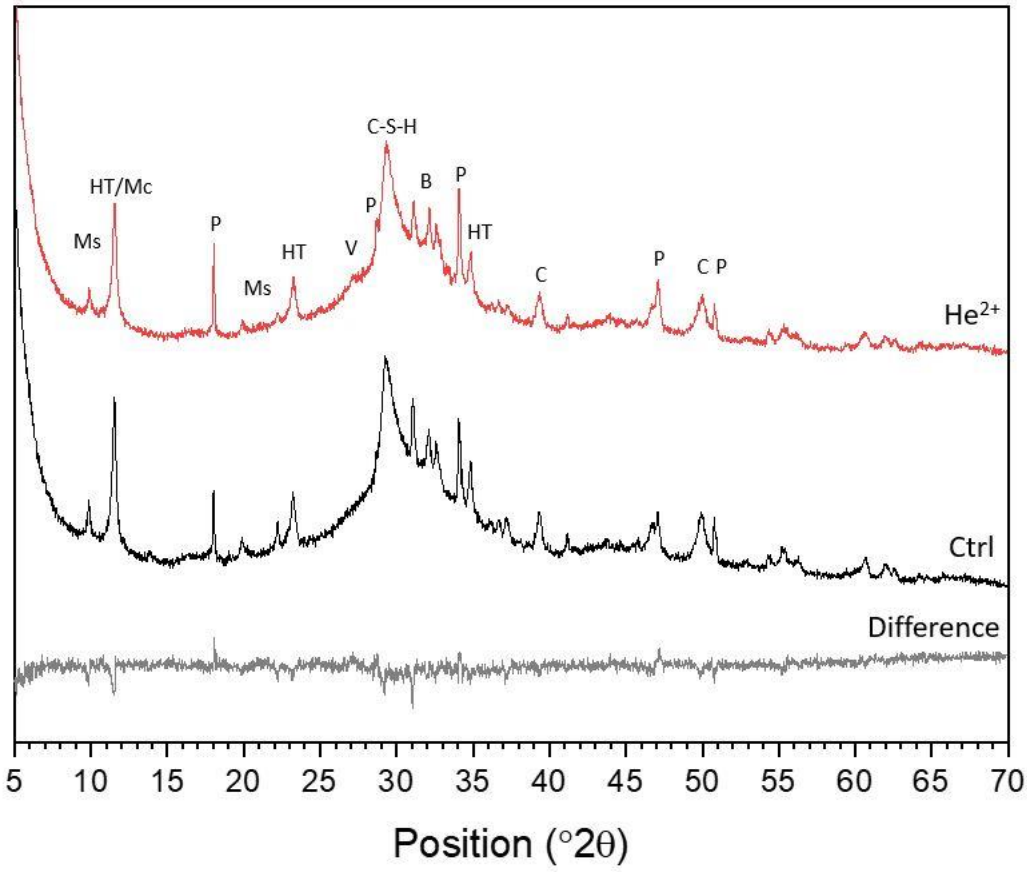

Figure 8.5 X-ray diffractograms of He^{2+} irradiated (He^{2+}) and control (Ctrl) CEM3Y samples. Difference pattern shows He^{2+}-Ctrl. Ms: monosulfoaluminate, HT: hydrotalcite, Mc: monocarboaluminate, V: vaterite, P: portlandite, B: belite (C_2S), C: calcite.

8.3.3 FTIR

FTIR spectra of control and He^{2+} irradiated samples are shown in Figure 8.6. Overall, these data support the XRD findings; similar phase assemblages are identified in both samples. However, the FTIR response from the He^{2+} irradiated sample shows lower resonances between 900 – 1100 cm^{-1} indicating a decrease in the asymmetric stretching vibration in Si-O-Si, which here can be associated with Q^2 species in the C-S-H chains [297]. Increased resonances at 875 cm^{-1} and 1300 – 1600 cm^{-1} in the He^{2+} irradiated sample are associated with out of plane deformation mode vibration and asymmetric stretching of CO_3^{2-} respectively, therefore indicating increased carbonate content [297]. The peak symmetry observed at 1300 – 1600 cm^{-1} shifts in the irradiated sample indicating a difference in the polymorphs of $CaCO_3$ present; vaterite and aragonite peaks at 1485 cm^{-1} dominate over amorphous carbonates at 1425 cm^{-1} [298]. The reduction in response associated with Q^2 species and the increased carbonate content suggest that increased carbonation is proceeding at the expense of C-S-H, which is undergoing decalcification and becoming less polymerised. However, there is no peak shift observed, which would be anticipated if the Ca/Si ratio had decreased significantly [297]. This minor variation

cannot be responsible for the difference in the XRD results, which showed a small reflection associated with vaterite in the He^{2+} irradiated sample. The formation of vaterite must also be due to the carbonation of other phases too. In terms of the mechanism of the increased carbonation, atmospheric effects cannot be discounted. However, the irradiated samples was stored under vacuum (during testing) when the control samples were not, which should minimise potential atmospheric effects. Given this, the potential for radiolytically generated formation of metastable calcium peroxide octahydrate facilitating carbonate production [100], [109], [115] (discussed in Section 2.5.1) cannot be dismissed.

The peak located at 1640 cm^{-1} and the broad resonance centred at 3450 cm^{-1} are due to H-O-H bending vibrations in molecular H_2O and stretching vibrations of O-H groups in H_2O or hydroxyls respectively [297]. The slight peak reduction in the irradiated sample at 1640 cm^{-1} is indicative of water loss through drying of the samples and the reduced resonance at 3450 cm^{-1} shows a reduction in interlayer water molecules. This drying is likely a product of the vacuum exposure as heating effects were minimised during testing; however, the difference in FTIR response is fairly small and so the water loss is considered minimal.

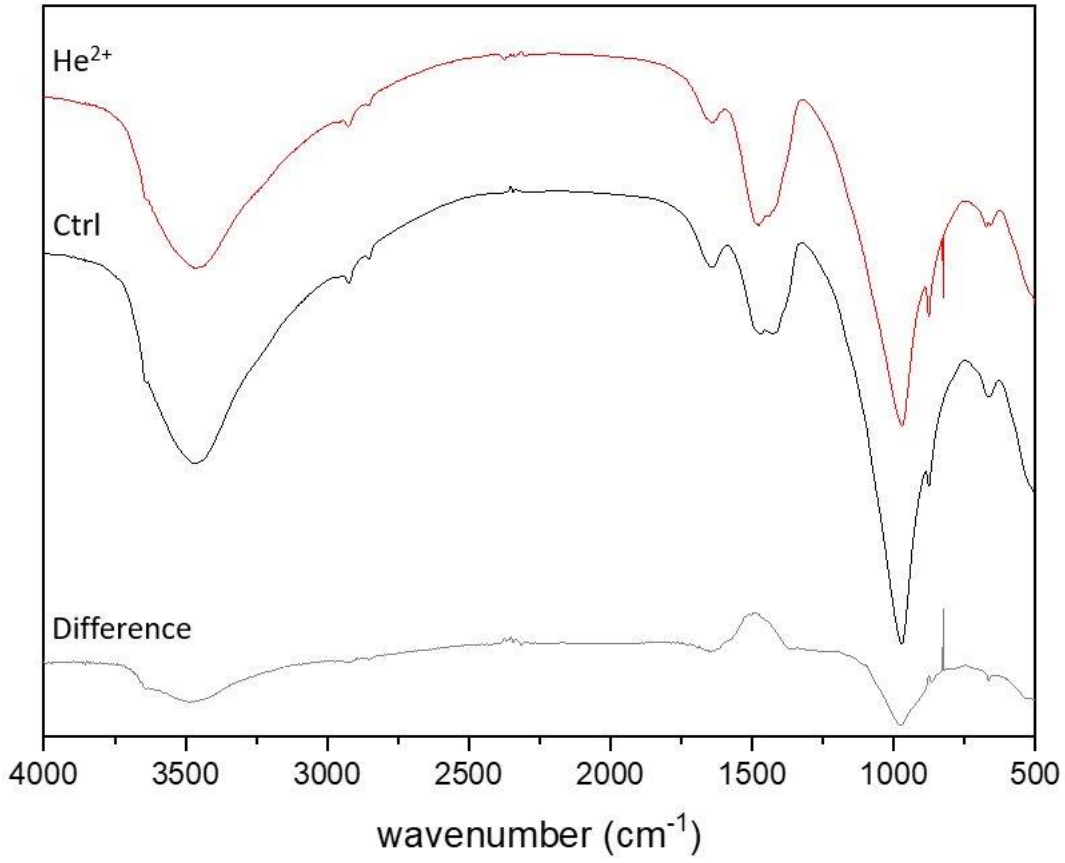

Figure 8.6 FTIR spectra of CEM3Y He^{2+} irradiated (He^{2+}) and control (Ctrl) samples. Difference pattern shows Ctrl - He^{2+}. Spike at 800 cm^{-1} in He^{2+} results considered to be due to equipment error.

8.3.4 SEM-EDX

SEM was completed on the surface of, and on the cross section through, the samples. BSE micrographs of the control sample are shown in Figure 8.7, and the characteristic microstructure described in previous chapters was observed. Minor cracking was noted on the surface of the sample (Figure 8.7 A, B) and some pull out of grains had occurred during sample preparation (black regions). The development of a dense matrix surrounding unreacted BFS and clinker grains was noted both on the surface and in the cross sections. Small, dark, angular features in the matrix represent fully hydrated BFS particles; larger grains developed dark reaction rims as hydration of the grains progressed.

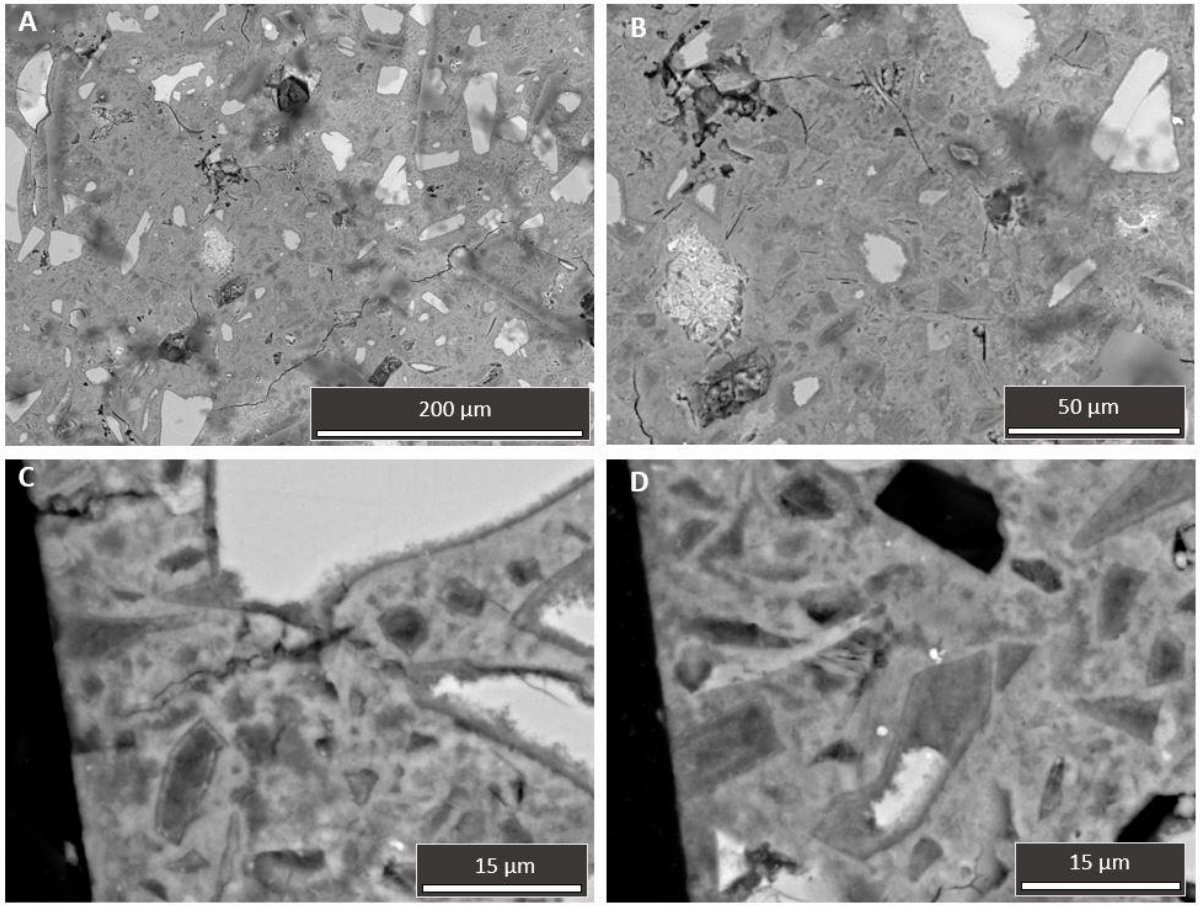

Figure 8.7 SEM micrographs of CEM3Y control. A, B: Surface of sample; C, D: Cross section through sample (surface on left hand side of image). Slight smudging of surface in A, B due to inconsistent carbon coating.

The irradiated samples have a greater proportion of cracking on the sample surface (Figure 8.8 A, B), which are considered to be a product of the prolonged period they were kept under vacuum during the irradiation or be a product of transport of these samples. Despite the increased cracking, the microstructure is as seen in the control samples.

Cross sections through the samples show that the irradiated surface has maintained good microstructural integrity, although a slight increase in surface roughness was noted (Figure 8.8 C, D). Minor cracks were observed but the surface cracking does not seem to have penetrated to significant depths. No distinct textural features were noted in the anticipated damage zone (denoted by the dashed red lines in Figure 8.8C, D); the matrix appeared the same as for the undamaged bulk at increased depth and in the control sample.

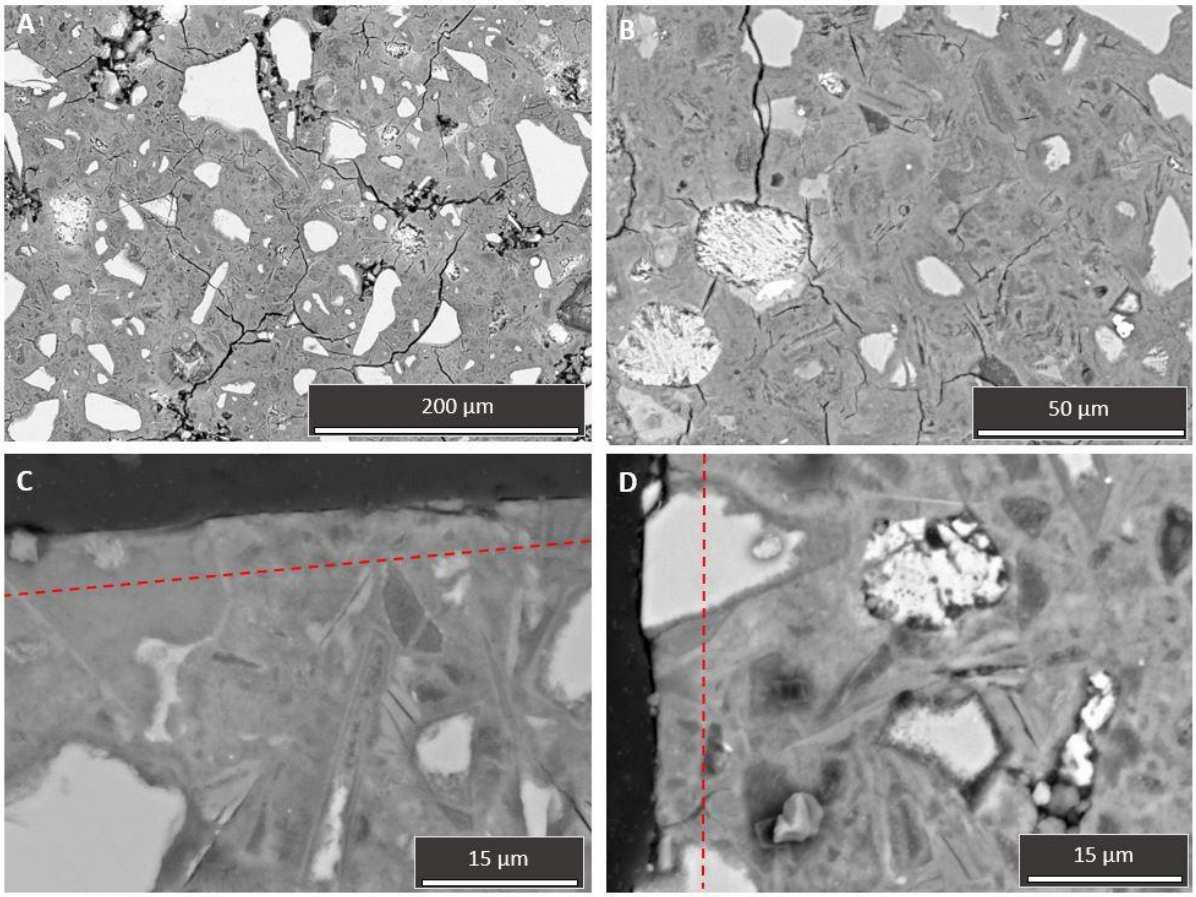

Figure 8.8 SEM micrographs of CEM3Y He^{2+} irradiated. A, B: Surface of sample; C, D: Cross section through sample (surface on top and left hand side of image respectively). Dashed red line shows estimated damage zone from SRIM calculations.

Chemical mapping of the samples was completed to assess changes to the bulk chemistry. The EDX mapping for the control sample is shown in Figure 8.9 A, where evident regions of portlandite, magnesium rich hydrated BFS grains, and dense C-A-S-H were visible. The sample surface was predominantly flat and no stark chemical segregation was observed.

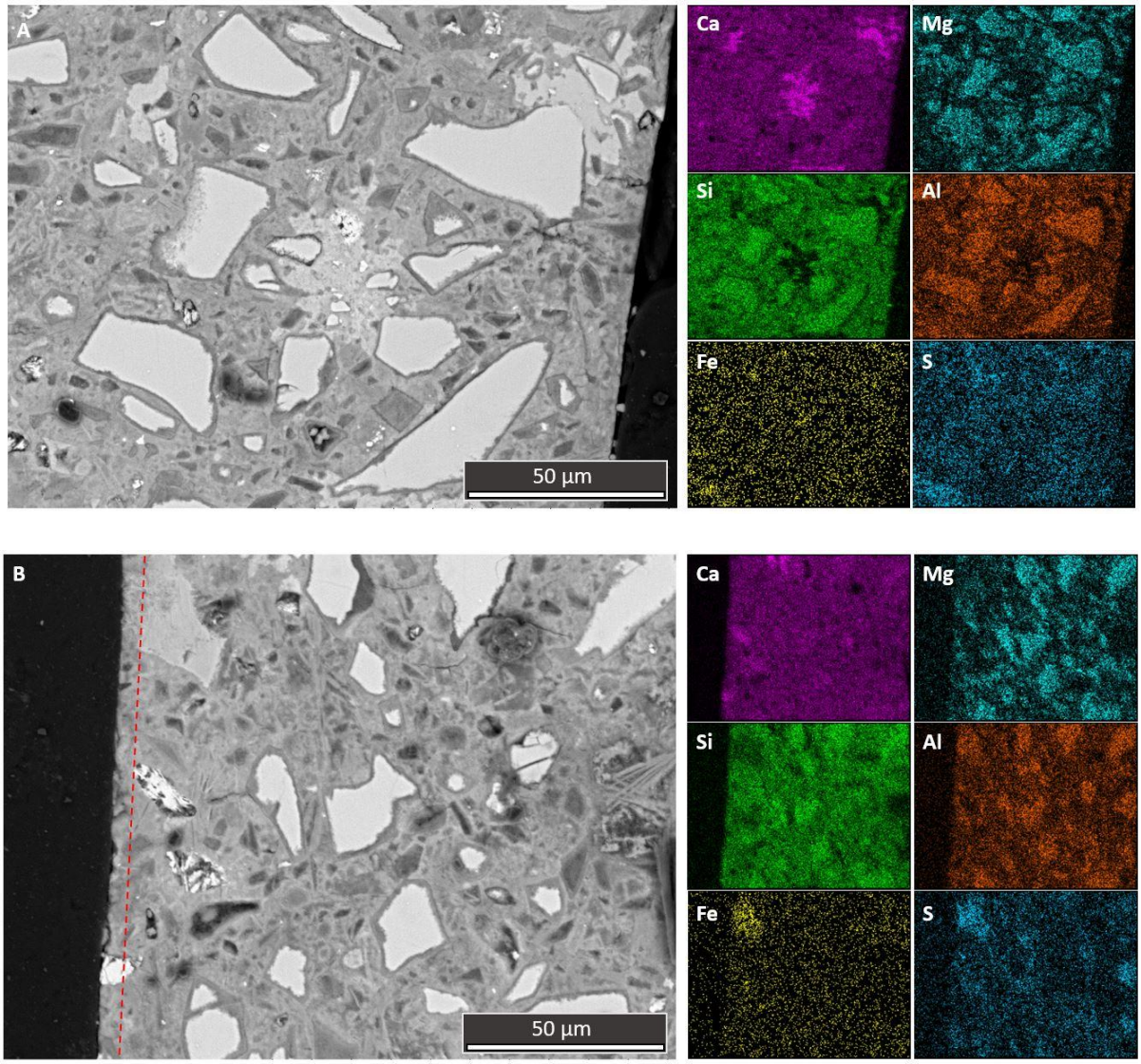

Figure 8.9 SEM-EDX of cross sections through CEM3Y. A: control, sample surface on right hand side; B: He^{2+} irradiated, sample surface on left hand side. Red Dashed line shows estimated damage zone from SRIM calculations.

The irradiated surface of the sample appears rougher than the control; however, this does not appear to correlate to any broad chemical changes in the damage zone. No chemical or textural zoning was observed in the samples as a result of He^{2+} irradiation.

8.3.5 TEM EDX

TEM micrographs were collected for the He^{2+} irradiated and control samples, allowing investigation of the C-S-H morphology and closer investigation of potential chemical changes from irradiation. Currently, no chemical mapping of the sections has been completed due to equipment issues; however, EDX point analysis data were collected. Overviews of the FIB samples are shown in Figure 8.10. Due to the multiphase nature of the sample, preparation of a uniformly thick sample was not possible. Harder phases (such as unreacted BFS) could not be thinned to the same extent as the

hydrate matrix, and so in the micrographs thicker regions appear darker and holes in the delicate C-S-H matrix developed in some regions.

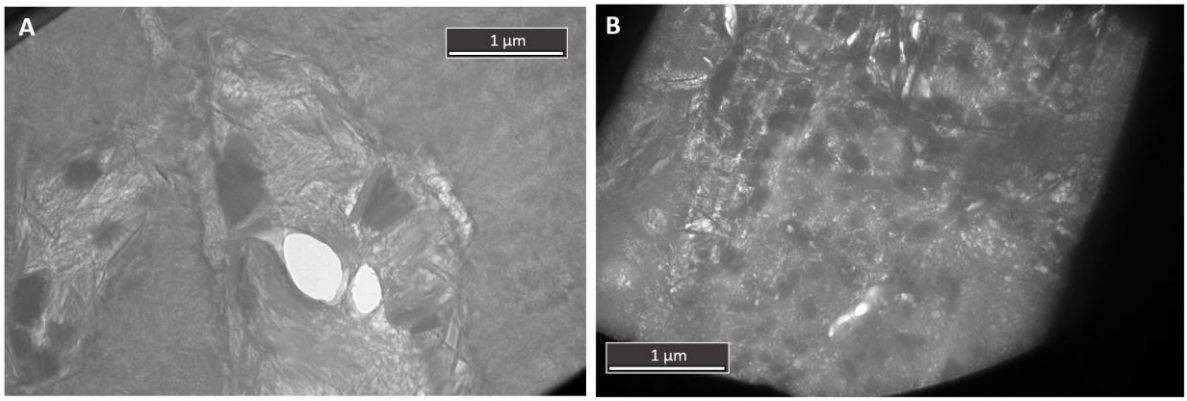

Figure 8.10 Overview of CEM3Y He^{2+} irradiated TEM samples. Irradiated surface on bottom left of image.

Clear textural regions of morphologically distinct C-S-H product were visible in Figure 8.10 A; fine, dense regions were interspersed with more open textured zones that appeared to have more porosity. This open texture is considered to represent areas of inner product; mature pastes have been observed to contain fully hydrated alite or BFS grains, which display a coarse texture [60]. The boundary of these regions was often marked by the presence of lath shaped crystals, likely hydrotalcite, which is associated with the boundary between areas of inner and outer product [60].

Foil-like and fibrillar morphologies of C-S-H were observed in the matrix of the control sample. Fibrillar textures were identifiable by the strong linear directionality (Figure 8.11 D), which is not seen in the more crumpled foil-like morphologies. The overall matrix texture was dense and the C-S-H was predominantly foil-like although different coarseness of foils was observed, for example, tight, dense foils seen in the centre and top of Figure 8.11 B compared with more open coarse textures seen intermixing with lath-shaped crystals in Figure 8.11 A. Space constraints during formation are likely responsible for these differences [44], [88]. Clear distinction between zones of inner and outer product was not as defined as in Figure 8.10; however, Figure 8.11 B shows the shift from outer product in the top half of the image to areas more representative of inner product in the bottom right and left corners. Given the age of the sample, the differences between inner and outer product would be expected to decrease; as such, it is not surprising that a clear distinction cannot be made throughout the sample or that different stages of microstructural development are present within the heterogeneous bulk [88].

Zones of microcrystalline calcite were observed within the C-S-H matrix (Figure 8.11 B, 1), which were identified via SAED. However, attempts to collect diffraction data from the hydrotalcite laths was not

successful; the patterns were not strong enough for identification. The SAED pattern of C-S-H free from other hydrate products is shown in Figure 8.11D, 2.

High proportions of hydrotalcite laths were observed; however, as noted previously, the distribution of this phase was predominantly in areas of inner product and adjacent to boundaries between inner / outer product. Given that examination of similar cement formulations at 20 years of age showed distribution of hydrotalcite in areas thought tentatively to be representative of outer product in terms of texture [188], it can be assumed that significant microstructural refinement will occur as time and hydration progress. This is important, as the impact of radiation on the system may alter depending on the microstructure, and this could affect the performance of the material differently i.e. in terms of creep behaviour [299].

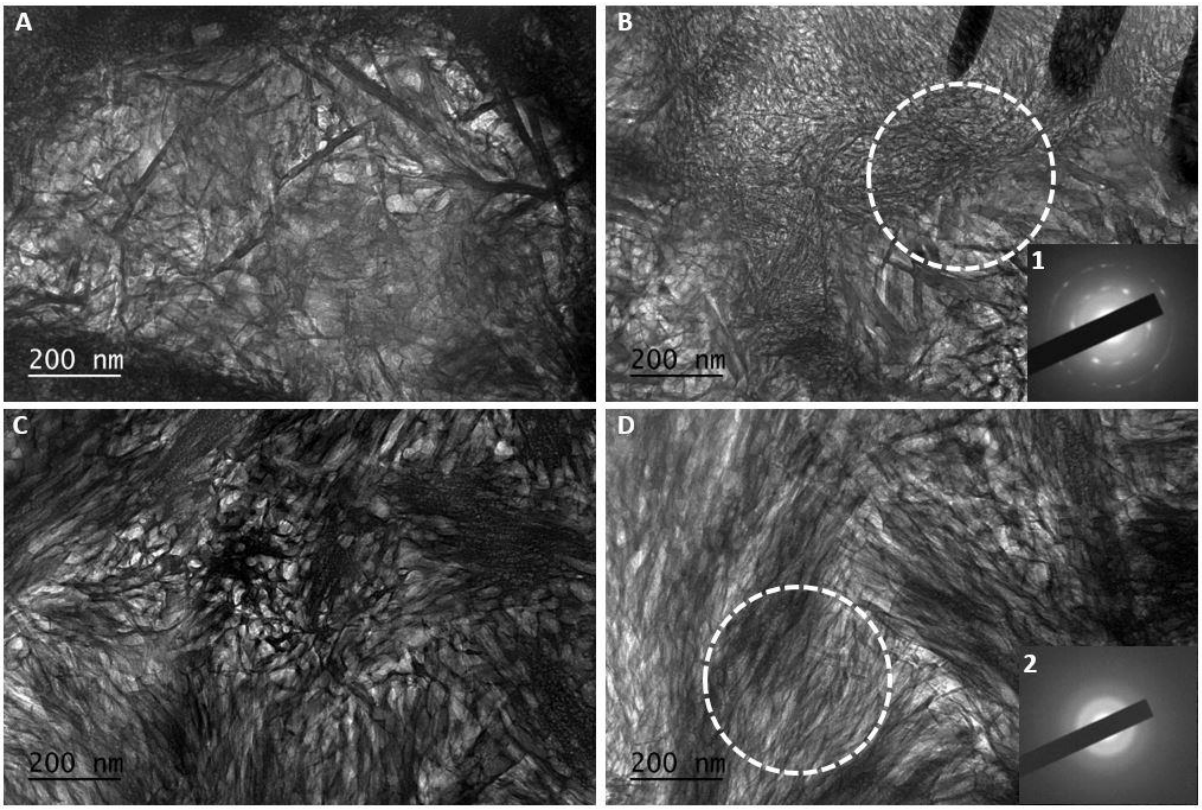

Figure 8.11 TEM micrographs of CEM3Y control. A: Hydrotalcite laths observed; B: dense C-S-H foils with microcrystals / laths, dashed circle represents area of SAED pattern 1: calcite; C,D: Dense fibrillar C-S-H with zones of foil-like C-S-H, dashed circle represents area of SAED pattern 2: C-S-H

Analysis of the He^{2+} irradiated sample showed the same microstructural development as observed for the control sample: a dense C-S-H matrix of predominantly foil-like morphology with some fibrillar regions noted, zones of microcrystals within the matrix, and lath-like hydrotalcite found at textural

boundaries. The coarseness of the C-S-H foils was also variable, again considered to be representative of inner and outer product regions due to space constraints during formation.

The images shown in Figure 8.12 show regions of the sample at increasing depth (from A – D respectively) from the irradiated surface. Although the sample is heterogeneous throughout, there were no identifiable systematic changes to the C-S-H morphologies as a function of depth that could be attributed to electronic stopping of the He^{2+} ions. The micrographs shown in Figure 8.12 A and D represent material from within 1 µm and > 4 µm of the irradiated surface. Estimations of damage depth from SRIM (Figure 8.2) indicate that peak damage should occur at approximately 4.5 µm; however, the previously mentioned images show no differences in terms of overall microstructure or more specifically C-S-H morphology. Dense foil-like C-S-H with minor microcrystals predominates throughout. The presence of calcite microcrystals in the sample at greater depth was not distinctive, as regions were also observed closer to the surface. The irradiation response of foil-like morphologies with varying coarseness was not observed to change as a result of He^{2+} exposure; no difference was observed.

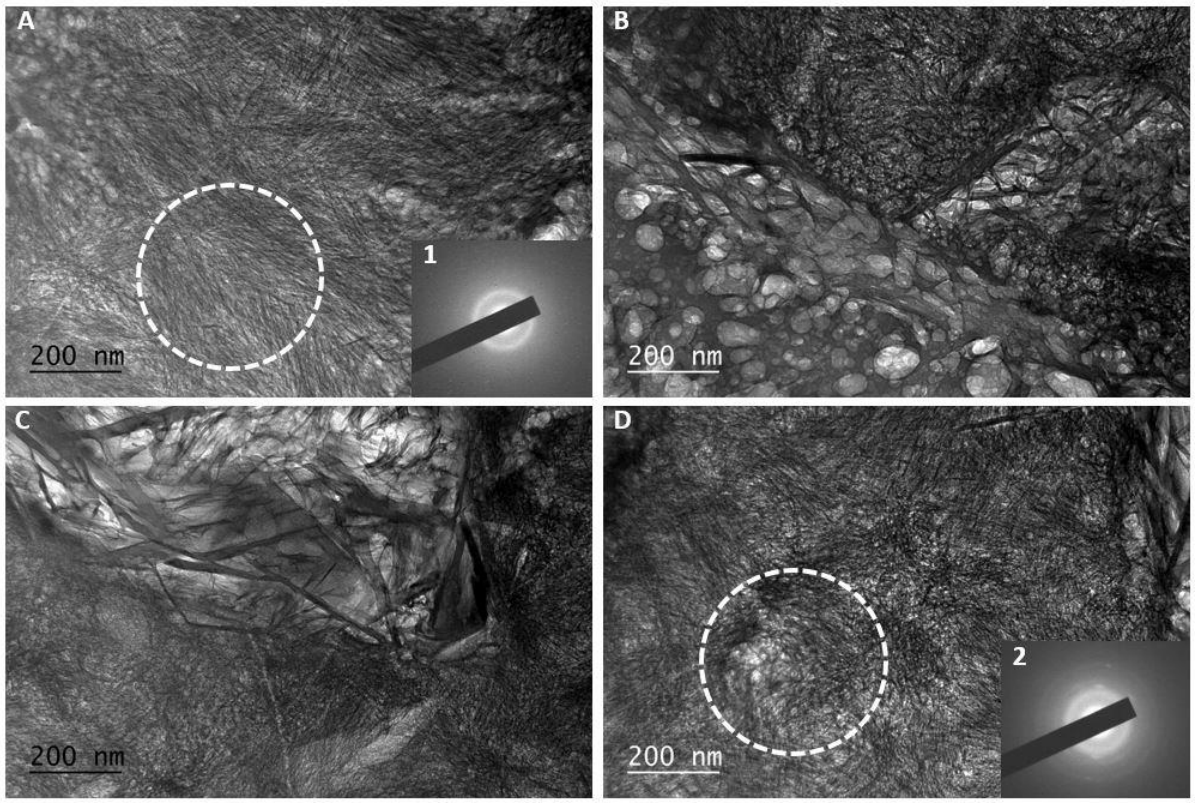

Figure 8.12 TEM micrographs of CEM3Y He^{2+} irradiated. A: < 1 µm from irradiated surface: dashed circle represents area of SAED pattern 1: C-S-H; B: Approximately 2.8 µm from irradiated surface, interface between dense C-S-H foils and more open foils, with many crystal laths; C: 4 µm from irradiated surface, interface of open foil like C-S-H and dense foils; D: >4 µm from irradiated surface, dense fibrillar and foil like C-S-H with zones of microcrystals, dashed circle represents area of SAED pattern 2: calcite.

Despite the overall similarities between the control and irradiated sample, there were regions in the He^{2+} irradiated sample where the microstructure appeared to have lost its characteristic morphology; an example of this can be seen in the bottom left corner of Figure 8.12 B. The globular appearance of the matrix in this region may be the product of variable sample thickness combined with cross sectioning through crumpled C-S-H foils [188], or may be the product of beam damage from either the SEM-FIB preparation or TEM examination. However, areas of beam damage were observed in both the control and irradiated samples that were considered more characteristic of FIB and TEM than the above features. FIB damage is generally linear due to beam direction and so tends to present as channels called 'curtaining' where in some cases gallium becomes embedded at the base [300], [301] and burning from TEM exposure leaves a circular rim denoting the beam circumference within which the damage occurs [168].

Where areas of similar featureless/globular microstructure were seen in the control sample it was pervasive across large areas, with a gradual reintroduction of distinct morphologies unlike the sharp distinction seen here. Given the current analysis and the complex nature of the hydrate morphologies, it is difficult to say with certainty what caused these features. The possibility that He^{2+} irradiation contributed either fully or in part to the formation of these zones must likewise be considered. There are similarities between the features seen here and with helium bubble formation observed in glass that has been implanted with He^{2+} ions [302]. In order to better clarify the contributions of the He^{2+} irradiation impact, in situ irradiation with concurrent TEM observation would be required to allow differentiation of preparation artefacts from the ion implantation effects.

EDX analysis was completed throughout the irradiated and control samples. The CEM3Y control FIB sample contained a smaller area of electron transparency than the He^{2+} sample, purely due to unreacted BFS content that was not visible when sample area selection was completed. Also, when the stage was tilted to allow EDX analysis, some of the sample was obscured, further reducing the available area for analysis. This resulted in fewer points being analysed for the control sample. Typically, when analysing Ca/Si ratios from hardened cement paste using TEM-EDX, SAED patterns are taken to ensure there is limited intermixing from other phases. This was not completed for all sites in the current work, as it was considered that the presence of intermixed phases within the C-S-H might be a result of the He^{2+} irradiation.

The overall Ca/Si ratio for both samples appears similar (Figure 8.13), with average Ca/Si ratios of 1.21 ± 0.05 and 1.13 ± 0.07 for the irradiated and control sample were obtained, indicating that there was limited bulk chemical response to irradiation. However, this applies to averages across the samples which are inherently problematic, as large variation in local composition are known to occur

[60]; nevertheless, for assessment of bulk properties these figures are relevant and are similar to values previously stated in the literature for BFS:PC cements [60], [188]. Analysis of cements with the same composition at 80 weeks of curing in Chapter 5 produced Ca/Si values of 1.4 ± 0.5 using SEM-EDX, whereas ^{29}Si MAS NMR deconvolutions estimated Ca/Si values ~1.1 These values were considered likely to over- and under-estimate the Ca/Si ratio respectively, which appears to be true given the results here, but overall there is consensus in the similarity of values obtained for irradiated and control samples.

In order to assess whether the He^{2+} affected the different C-S-H morphologies differently, assessment of areas identified as inner and outer product was undertaken. Differentiation of these areas was done via textural identification and through assessment of Mg/Si ratios; hydrotalcite is the only Mg containing phase identified and, as discussed earlier, laths were identified within inner product zones or on textural boundaries, and so this was considered a suitable proxy [42], [60]. This segregation is shown in Figure 8.13, where the points considered to be inner product show a much higher Al/Ca ratio, which is to be expected given the criteria used for identification, as hydrotalcite is also rich in Al. The overall range of Ca/Si values was the same for both inner and outer product regions, as expected from previous work on these cements [60], [188], although a minor increase in the average value for outer product was observed. This shift is a product of the level of intermixing from hydrotalcite, which likely masks any other changes in Ca/Si ratio that may have occurred. Despite the increased resolution provided by TEM analysis, the hydrotalcite laths are too small and pervasively intermixed with the C-S-H matrix in inner product to allow separate analysis.

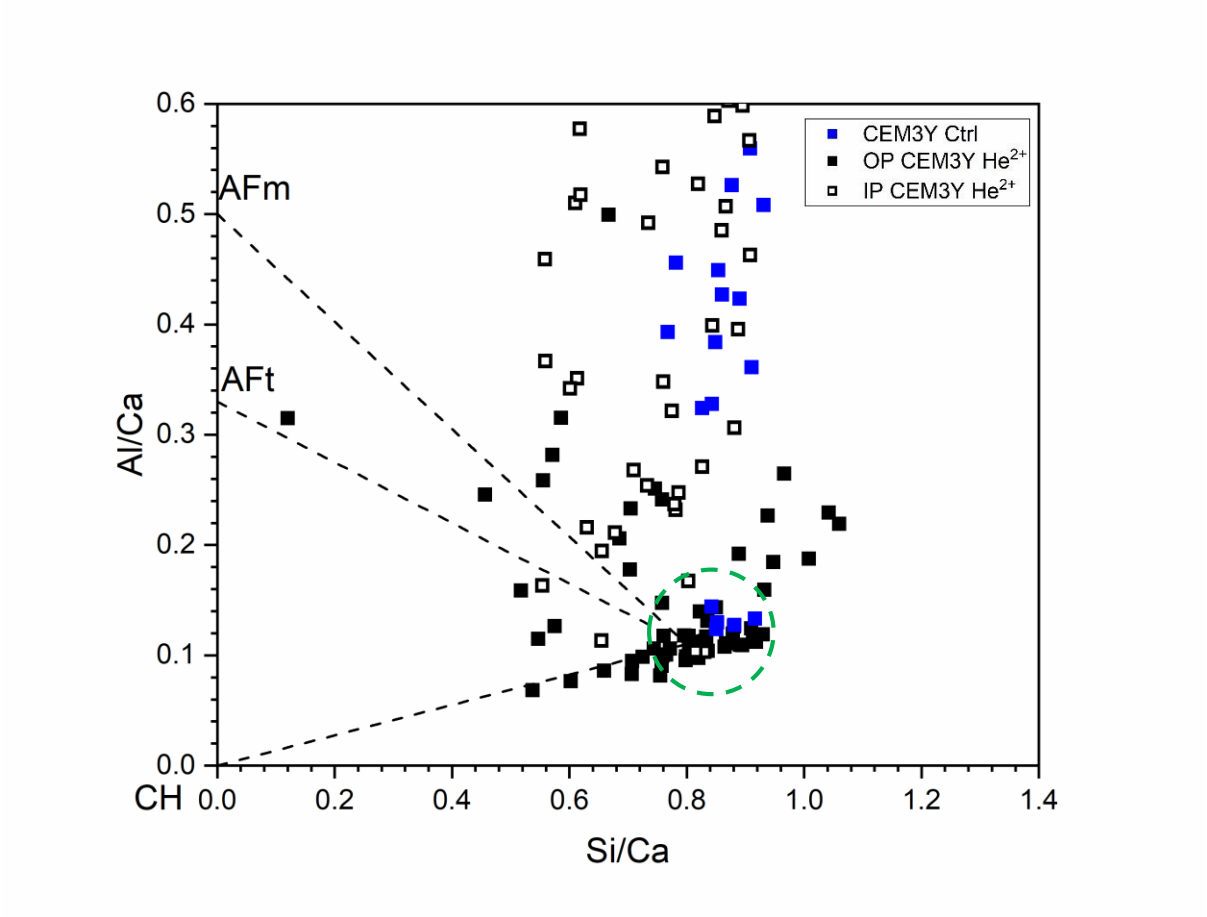

Figure 8.13 EDX point analysis of He^{2+} irradiated and control samples. The green dashed circle denotes the approximate C-A-S-H composition. Tie lines link to the other prominent hydrate phases; CH: portlandite, AFm: monosulfoaluminate, AFt: ettringite.

The relationship between Mg/Si and Al/Si is shown in Figure 8.14. There is clear confirmation of a Mg-rich hydrotalcite-like phase present within both the irradiated and control samples, which supports the XRD findings. The data correlates broadly with the tie line to quintinite-like composition ($Mg_4Al_2(OH)_{12}CO_3{\cdot}4H_2O$) containing an Mg/Al ratio of 2, although it tracks slightly below this value indicating estimated true values of 1.8-1.9, which are comparable to values previously determined in similar formulations [188]. These values are lower than the minimum value required for hydrotalcite-type phase formation, which has been attributed to interstratification of $Al(OH)_3$ layers within the phase [88], [303].

Comparison between regions of inner and outer product indicates that some outer product zones also contain the magnesium-rich hydrotalcite-like phase. The slightly higher Al content within the inner product is due to the initial differences in local chemistry rather than irradiation exposure [60]. The assessment here indicates that exposure to He^{2+} irradiation does not cause significant variation in the

Mg/Al ratio, although further analysis of the control sample would be required to have complete confidence in this statement.

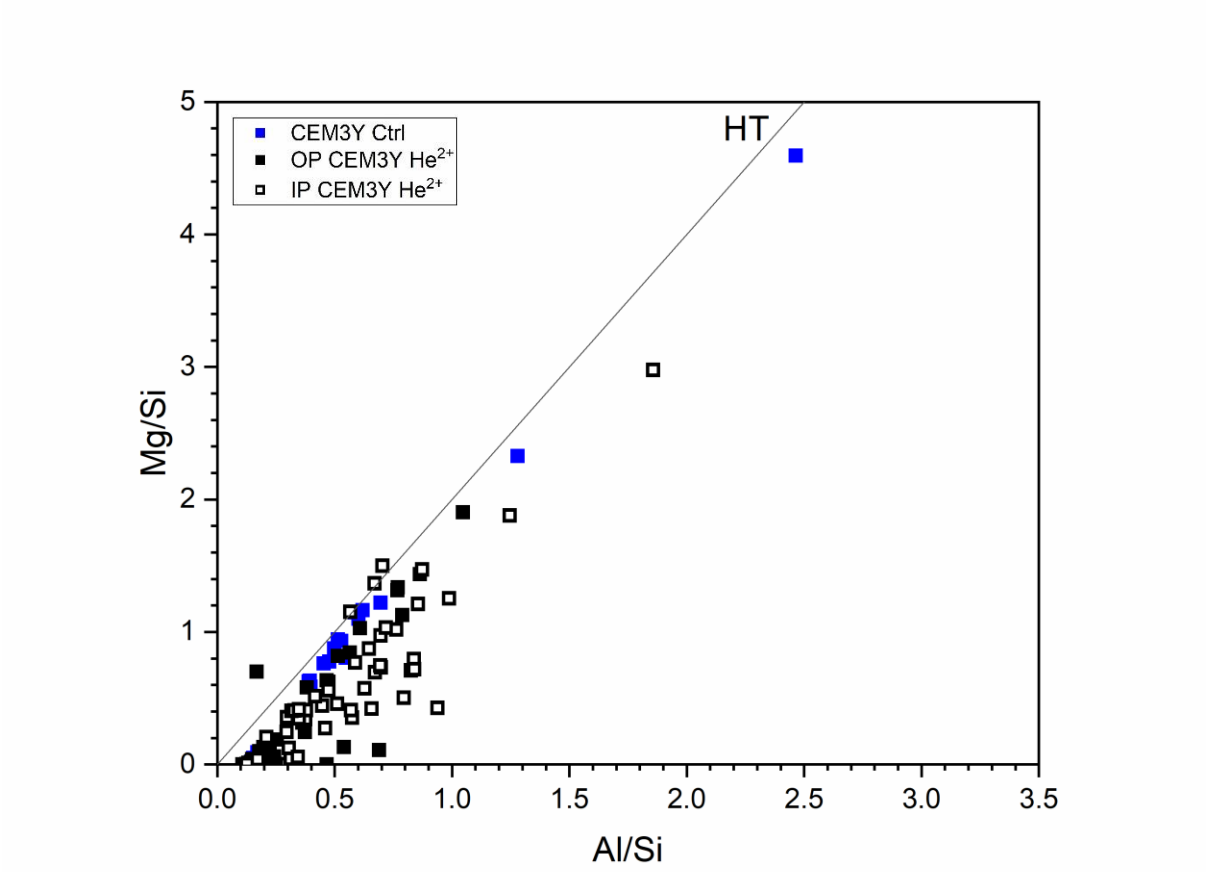

Figure 8.14 Mg/Si and Al/Si atomic plots from EDX point analysis of He^{2+} irradiated and control samples. Tie line links to idealised hydrotalcite-like composition with Mg/Al = 2.

Although monosulfoaluminate was identified from the XRD results, no evidence for this phase was observed within the microstructure of the sample. Assessment of the EDX data showed very low S/Ca ratios were present within the control sample (S/Ca <0.02), with slightly increased mean values in the irradiated sample (S/Ca <0.06) but no significant sulfur concentrations were observed. This indicates that there was not a large amount of intermixed monosulfoaluminate within the C-S-H that underwent analysis. Given the large amount of inner product associated with BFS identified in these samples, it is not overly surprising that such low S/Ca ratios were observed. Nevertheless, it does appear that He^{2+} exposure has not caused redox changes in the sulfide species from the BFS, that have previously been postulated to cause later age ettringite formation [124].

8.4 Conclusions

The experimental setup outlined here provides proof of concept for ion accelerator use to simulate alpha particle damage in cementitious materials. Heating of the sample was successfully minimised; although minor cracking was observed on the surface of the He^{2+} sample, it is considered this may have been a product of the vacuum rather than heating effects. Preservation of the phase assemblage appeared successful when compared to the control sample. This is valuable for future experimental work investigating the long term aging of cement materials used for wasteform purposes, and in construction of long term disposal facilities for radioactive waste.

He^{2+} irradiation induced a colour change in the cement sample surface, similar to the discolouration observed in radiohaloes. The cause of this is currently unknown, although as no evidence of ballistic damage was observed from analysis of XRD, investigation of alterations to oxidation states may provide the necessary information to clarify the mechanism responsible for the colour change.

Minor increased carbonation was observed through XRD and FTIR, potentially supporting the radiolytic production of calcium peroxide octahydrate due to He^{2+} exposure. However, this minor increase was not observed from microscopic investigation and no increased microcrystalline zonation was seen from SAED data collected in the damaged region.

SEM and TEM-EDX investigation showed no textural or chemical distinctions between the estimated damage zone and pristine bulk / control sample. The surface of the irradiated sample appeared slightly rougher than the control; this may be a product of water loss due to irradiation, which was shown in the FTIR results. Despite the overall similarities between the control and irradiated sample, some regions of damaged microstructure were observed in the He^{2+} irradiated sample. The cause of these features cannot be assigned with certainty, as although beam damage from SEM-FIB or TEM may be responsible, they may represent He^{2+} damage. To effectively resolve this, in situ irradiation with concurrent TEM observation would be required to allow differentiation of preparation artefacts from the ion implantation effects.

The minor variations observed from this study pose interesting avenues for future investigations, although the impact of these differences on the ability of the cement to perform as a wasteform material is considered limited.

9 Conclusions and further work

9.1 Conclusions

The aim of this thesis was to elucidate the effects of radiation on the cement systems currently used for immobilisation of ILW in the UK. The influence of alpha and gamma radiation on the microstructural and chemical behaviour of cementitious wasteforms was explored, with specific focus on the impact of radiolytic processes at high total absorbed dose. The influence of radiation exposure on the capacity of cements to chemically condition radionuclides was also investigated.

Baseline characterisation of cements using Sellafield Ltd specification powders showed that changes to the phase assemblage and microstructural development of the hydrated materials were mainly in line with literature studies of cements with similar levels of SCM replacement in the grout. Analysis of the Ca/Si ratios of the 28 day cured blended cements with the same level, but different types, of SCM replacement showed that early age hydration products are primarily PC related, indicating that radiation studies of pure PC in the literature may still provide relevant information for young blended cements. The development of UPV – compressive strength correlation curves for four BFS:PC blended cements was completed, and these were used for semi-quantitative data on how radiation impacts compressive strength, considered appropriate to assess trends in mechanical properties after radiation exposure.

Gamma irradiation was observed to cause progressive radiolytic dehydration in BFS:PC samples; this was linearly associated with total dose in higher replacement BFS samples but variable at lower replacement levels. Minor variations to the phase assemblage were noted after irradiation, and these were attributed to increased carbonation. The precise mechanism by which this occurred was not directly identified, but it was speculated that the formation of calcium peroxide octahydrate due to peroxide generation during radiolytic decomposition might be responsible. Increased carbonation was accompanied by a shift in carbonate polymorphs, with increased vaterite present after irradiation. Samples with lower BFS replacement levels showed reduction of portlandite content as carbonation progressed, whereas in higher replacement samples carbonation of C-A-S-H and AFm rather than portlandite occurred, causing a shift in the pore size distribution due to a reduced proportion of small pores. Analysis of ^{29}Si and ^{27}Al MAS NMR data was consistent with the identification of irradiation-induced carbonation, with changes to C-A-S-H structural characteristics (increased MCL) and the reduction of TAH resonances associated with vaterite formation observed, which were more pronounced with higher BFS content. Irradiation was also observed to increase the resonances associated with aluminium inclusion in C-A-S-H and in AFm/hydrotalcite phases, indicating an increase

in hydration; however, DoH testing produced mixed results. Minor variations to the microstructure were observed in the irradiated samples, with a shift in the pore size distribution indicating that nano- or micro-cracking had occurred. UPV measurements indicated trends of reduced compressive strength and increased potential deformation with irradiation.

Encapsulation of PuO_2 in cementitious grouts assessed the effect of an intense alpha emitter on the physico-chemical properties of cements. Good encapsulation of the PuO_2 was observed, with no microstructural damage observed in the cement after 1 year of curing. The mineralogy and morphology of the PuO_2 appeared unchanged by contact with cementitious grouts from the completed analysis; however, further assessment is required to ascertain the extent of reaction and incorporation in hydrate phases. Quantitative differences in the phase assemblage were observed in PuO_2 containing samples, particularly in the BFS blended cements. The ratio of sulfate phases altered in the presence of PuO_2, with an increase in ettringite observed. This is considered to be due to a combination of factors including an increase in the CO_2/Al_2O_3 ratio, although full assessment of carbonation differences was not possible due to differences in storage conditions in this experiment. The presence of cellulose was seen to impact the proportion of phases present in the hydrate assemblage, but no microstructural differences were observed.

The introduction of CeO_2 as a non-radioactive waste simulant did not appear to significantly impact the microstructural development of gamma irradiated grouts, indicating that attenuation of gamma radiation by the dopant did not significantly affect the microstructure. Similar minor alterations to the phase assemblage were observed as identified in previous gamma testing, considered likely to be a product of increased carbonation. The potential presence of larger amounts of amorphous $CaCO_3$ was identified from a weight loss between 300 – 400 °C in the TGA results, which disappeared after contact with synthetic groundwater during leaching, potentially being redistributed and contributing to higher calcite contents.

Leaching of gamma irradiated and control samples in synthetic granitic groundwater resulted in the development of texturally distinct zones (rim, leached and central zones) of approximately the same thickness independent of radiation exposure. Increased hydration of unreacted anhydrous precursor was observed after contact with the groundwater, and local variation to the phase assemblage was also noted in terms of the AFm/AFt balance and carbonate quantities. The rim was considered to be composed of $CaCO_3$ that formed due to the levels of HCO_3^- present in the groundwater, which is supported by the increased thickness of this feature in the dynamic testing (where regular sampling and replacement of the groundwater was completed) compared to the static testing. The leached zone was calcium-depleted and had increased porosity and open texture, with the leaching of $Ca(OH)_2$

and potential decalcification of C-A-S-H causing release of bound alkalis possibly responsible for the observed pH increase in the leachate. Irradiated samples did not buffer the pH to values as high as the control and further investigation is required to understand the mechanism responsible for this difference. Cerium was retained in the cement after leaching, with ICP-OES results indicating no release into the groundwater. Notwithstanding the minor variations to phase assemblage and pH difference, the leaching response was similar in irradiated and control samples. The development of similar textural domains, albeit on different scales, from both the dynamic and static testing indicates the same processes were occurring in both testing setups.

Proof of concept for ion accelerator use to simulate alpha particle damage in cementitious materials was achieved using the specific experimental setup outlined in Chapter 8. Heating of the sample was successfully minimised. Although minor cracking was observed on the surface of the He^{2+} irradiated sample, this may have been a product of the vacuum rather than heating effects. Preservation of the phase assemblage appeared successful when compared to the control sample. He^{2+} irradiation induced a colour change in the cement sample surface, similar to the discolouration observed in radiohaloes: however, the cause for this is currently unknown. Minor increased carbonation of the bulk was observed through XRD and FTIR. Although SEM and TEM-EDX investigation showed no distinct textural or chemical distinctions between the estimated damage zone and pristine bulk / control sample, some regions of damaged microstructure were observed in the He^{2+} irradiated sample. The cause of these features cannot be assigned with certainty from the current data. The minor variations observed from this study pose interesting avenues for future investigations, although the impact of these differences on the cements ability to perform as wasteform materials is considered limited.

The findings of this thesis have added to the knowledge of radiation effects in blended cements used for nuclear waste storage and disposal. The results indicate that high doses of radiation which exceed current estimates for “lifetime” doses for ILW packages cause minor differences to the phase assemblage and microstructure. Whilst these changes are of interest and require further investigation, they are not considered to represent specific limitations in terms of these cements performance in radiation environments at the current stage of investigation.

9.2 Further work

Additional work is required to improve the mechanistic understanding of radiation effects in cementitious materials. Also, given the time scales for, which these materials are required to function, no laboratory based experiments will be able to realistically replicate the whole life cycle. As such, thermodynamic and reaction kinetic modelling of the cements will be required, and to allow that, high

quality input data on the mechanisms responsible for radiation induced variations is needed. Specifically, this could include:

- Control of atmospheric carbonation during gamma/alpha irradiation to ascertain mechanisms by which radiation induced carbonation occurs; if this changes with increasing levels of SCM replacement, and whether this changes as a function of dose rate.
- Alternative investigation (i.e. XRD with subsequent Rietveld refinement and PONKCS analysis, high resolution SEM and image analysis) of DoH of PC and SCM in irradiated and control samples to assess whether radiation drives the hydration of anhydrous precursors.
- Multiple quantum magic angle spinning (MQMAS) NMR of irradiated BFS:PC samples to allow deconvolution of the ^{27}Al MAS NMR spectra which would provide better clarity on which sites are occupied by aluminium and the apparent increased aluminium levels observed within the irradiated samples.
- Investigation of the extent of reaction of alpha emitting waste species (such as PuO_2) and potential incorporation in hydrate phases.
- Assessment of the extent of chemical variations in the area surrounding the PuO_2 agglomerate particles with regard to the sulfate phase ratio and how the carbonate content affects the AFm phase balance in these areas.
- Investigation of the mechanisms responsible for the difference in pH buffering capacity of irradiated cements.
- Targeted quantitative analysis of mineralogy (i.e. using electron microprobe analysis) within texturally distinct zones that result from leaching of irradiated cement to compliment bulk analysis completed.
- Long term leaching of irradiated cement samples using conditions representative of a GDF, allowing evaluation of the extent of decalcification of hydrate phases and what impact this would have on radionuclide retention.
- Establishing the cause of colour change observed in He^{2+} irradiated cements; analysis of oxidation states of transition metals would be an appropriate starting point for this.
- In situ ion irradiation with concurrent TEM observation to allow full certainty of damage to microstructure caused from ion implantation effects.

10 Appendix

10.1 Dose rate variations from ^{60}Co irradiations completed in Chapter 5

In order to achieve total gamma doses exceeding the lifetime anticipated dose for an ILW package, testing using the ^{60}Co irradiator was ongoing for approximately 342 days. Over this time period, the dose rate from the ^{60}Co decreased and so the dose rate experienced by the samples also decreased. Also, movement of the samples within the irradiator was required to enable samples to reach the targeted dose in the time frame required. This means placement was not consistent for each dose (i.e. the 9:1 and 5.67:1 samples did not have the same position for the full duration of the 20 MGy irradiations), as shown in Figure 10.1. Given this, as outlined in Chapter 5, the effect of dose rate cannot be evaluated from the current data.

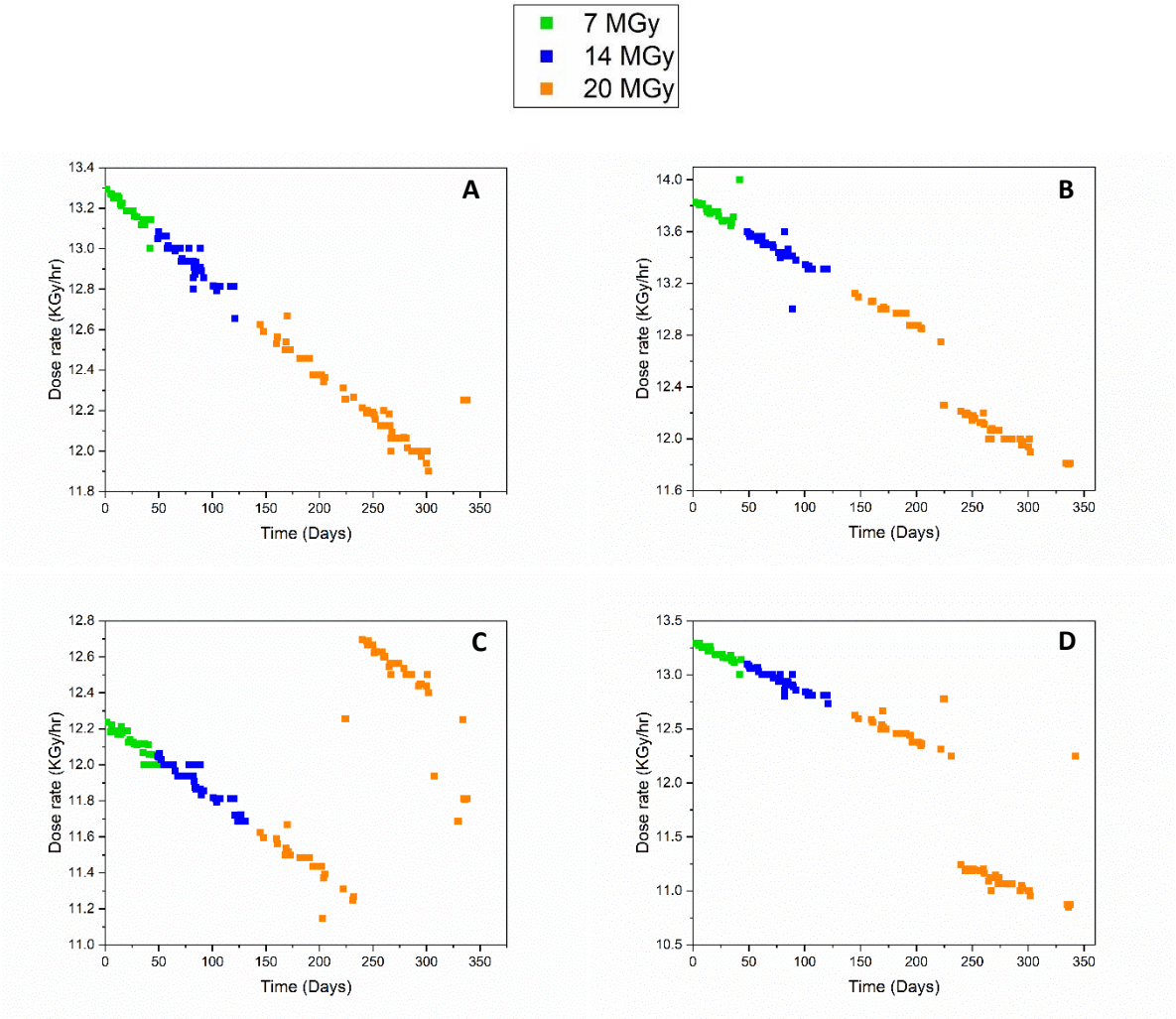

Figure 10.1 Variation in dose rate for each sample over time taken to complete irradiations. A: 3:1 BFS:PC, B: 3.44:1, C: 5.67:1, D:5.67:1

10.2 TGA-MS data for 3.44:1 and 9:1 BFS:PC with increasing total absorbed dose

Mass spectrometry data was taken for the majority of samples where TGA was conducted, however periods of equipment failure and unreliability of results due to detector issues resulted in some unreliable data. As such, these data were not included in all thesis chapters as they were not available for all samples. However, for Chapter 5 the results from 3.44:1 BFS:PC and 9:1 BFS:PC samples were predominantly reliable (with the exception of H_2O response from 3.44:1 7 MGy) and are shown in Figure 10.2 A and B respectively. These are intended to provide an overview of the MS response with increasing total absorbed dose and how this alters as a function of BFS content.

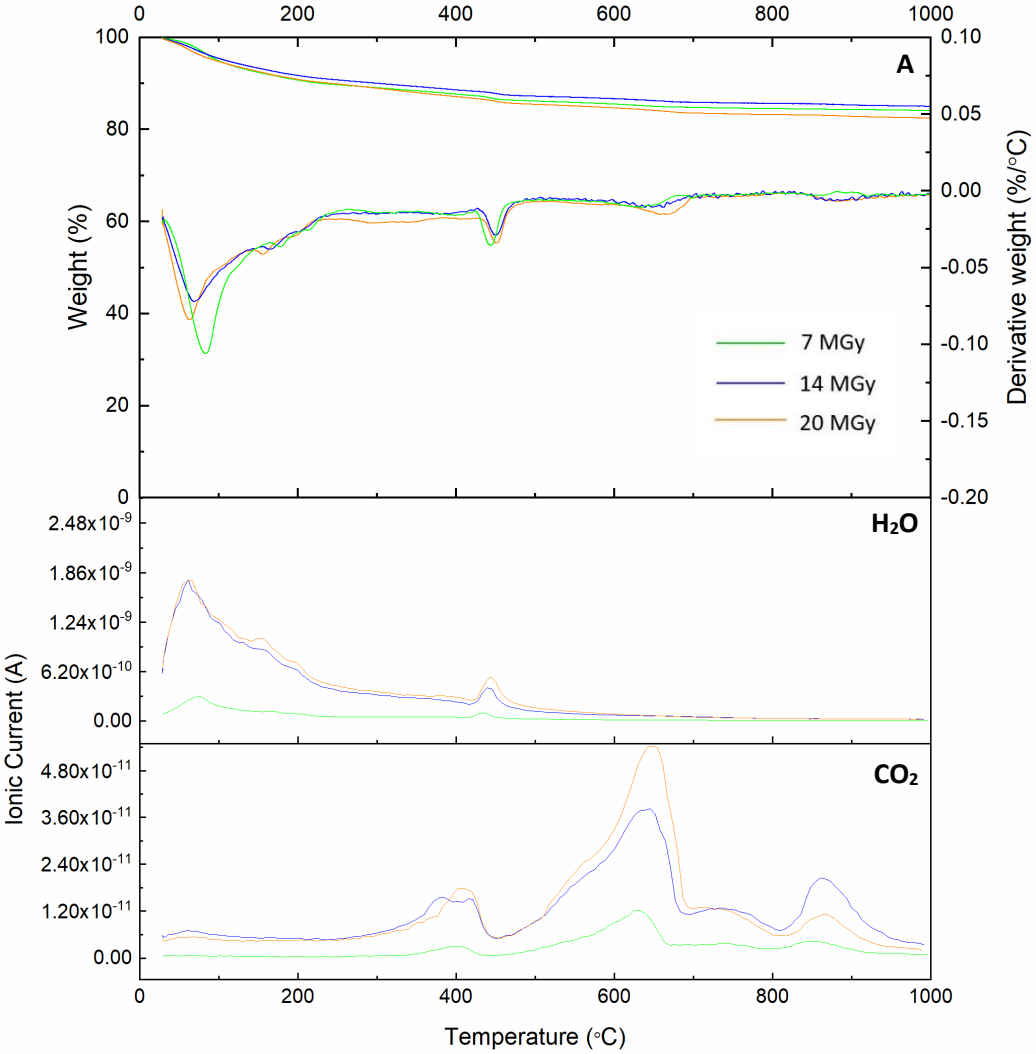

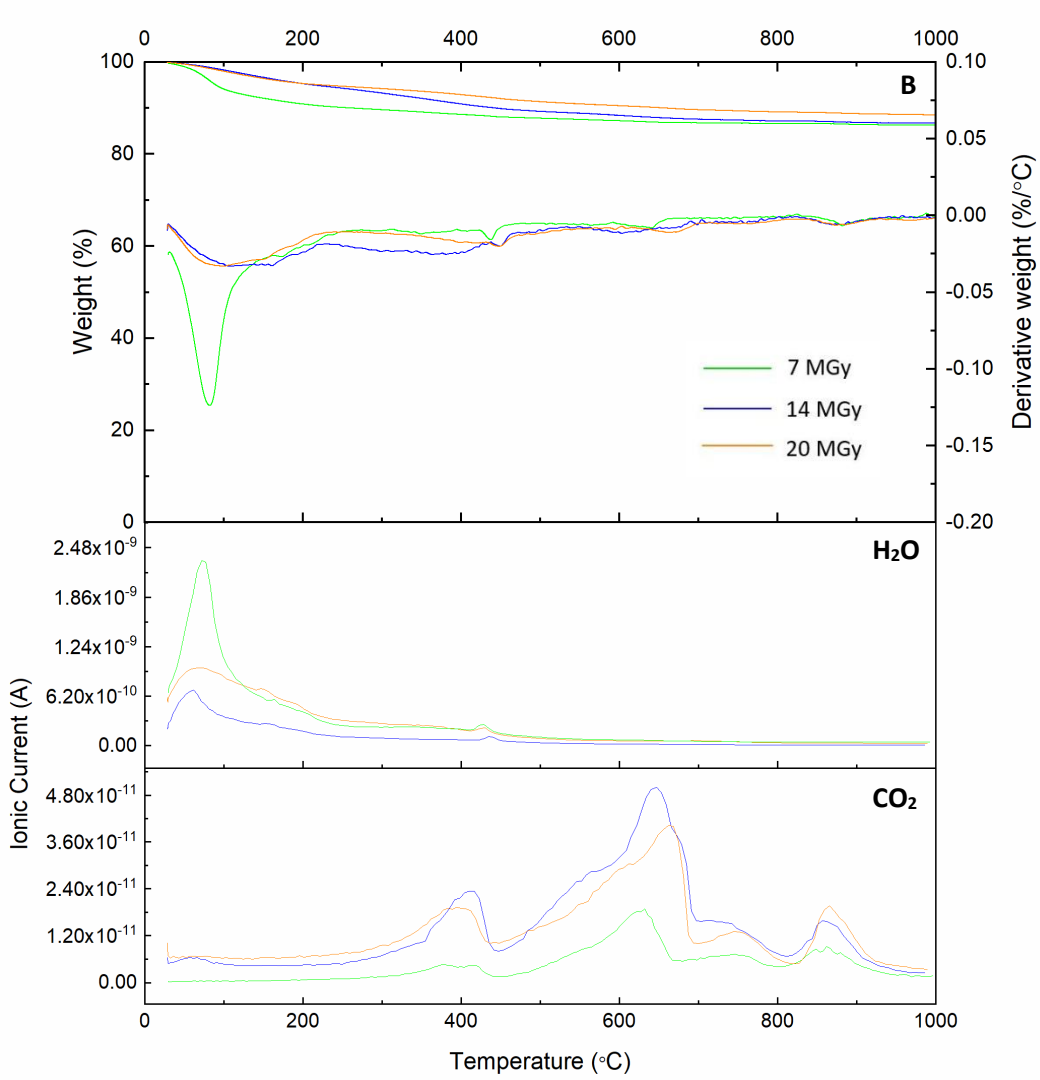

Figure 10.2 TGA-MS from BFS:PC blends exposed to increasing total gamma dose, A: 3.44:1, B: 9:1. MS results for 3.44:1 7 MGy suspected to be erroneous, particularly for H_2O.

The CO_2 response for both blends show a clear response centred at 400 °C which increases with total absorbed dose (although not linearly). This is associated with a mass loss that centres between 300 - 400 °C and is considered to be the product of a hydrotalcite-like phase decomposing [194] (likely a quintinite type member of the hydrotalcite group, $(Mg_4Al_2(OH)_{12}CO_3{\cdot}4H_2O)$).

References

[1] Nuclear Decommissioning Authority, “Radioactive wastes in the UK: UK radioactive waste inventory report,” NDA, 2017.

[2] Radioactive Waste Management, “Geological disposal Guidence on the production of encapsulated wasteforms,” NDA Report number WPS/502/01, RWM-NDA, Didcot, UK, 2015.

[3] Radioactive Waste Management, "Geological disposal, RWM HAW innovation and delivery: A review of cement powders security of supply, specifications and disposability issues", NDA Report number NDA/RWM/144, RWM-NDA, Didcot, UK, 2016.

[4] Department of Energy and Climate Change, “History of nuclear generation development timeline,” 2010. [Online]. *Available: https://www.gov.uk/government/publications/nuclear-energy-milestones-and-goals-for-new-nuclear* [Accessed 06/04/17].

[5] Department of Energy and Climate Change, “Table of past and present UK nuclear reactors,” 2010. [Online]. Available: https://www.gov.uk/government/publications/nuclear-energy-milestones-and-goals-for-new-nuclear [Accessed 06/04/17].

[6] J. Cronin and N. Collier, “Corrosion and expansion of grouted Magnox,” *Mineral. Mag.*, vol. 76, no. 8, pp. 2901–2909, 2012.

[7] G. R. Choppin, J.-O. Liljenzin, and J. Rydberg, “Appendix A – Solvent extraction separations,” in *Radiochemistry and Nuclear Chemistry*, Third Edition, Oxford, UK, Butterworth-Heinemann, 2002, pp. 674–682.

[8] Nuclear Decommissioning Authority, “Radioactive wastes in the UK: UK radioactive waste inventory report,” NDA, 2017.

[9] G. A. Fairhall and J. D. Palmer, “The encapsulation of Magnox swarf in cement in the United Kingdom,” *Cem. Concr. Res.*, vol. 22, no. 2–3, pp. 293–298, 1992.

[10] D. Bodansky, *Nuclear Energy: Principles, Practices, and Prospects*, Second Edition, New York, Springer-Verlag, 2004.

[11] M. Grimston, W. J. Nuttall, and G. Vaughan, “The siting of UK nuclear reactors.,” *J. Radiol. Prot.*, vol. 34, no. 2, pp. R1–R24, 2014.

[12] Nuclear Decommissioning Authority, “Radioactive wastes in the UK: A summary of the 2016 inventory,” NDA,Didcot, UK, 2016.

[13] M. I. Ojovan and W. E. Lee, “Chapter 1. Introduction to Immobilisation,” in *An Introduction to Nuclear Waste Immobilisation*, Oxford, UK, Elsevier, 2005, pp. 1–8.

[14] I. W. Donald, B. L. Metcalfe, and R. N. Taylor, “Review: The immobilization of high level radioactive wastes using ceramics and glasses,” *J. Mater. Sci.*, vol. 32, pp. 5851–5887, 1997.

[15] M. J. Angus, I. H. Godfrey, M. Hayes, and S. Foster, “Managing change in the supply of cement powders for radioactive waste encapsulation – twenty years of operational experience,” *Waste Management 2010 Conference Proceedings*, Phoenix, Arizona, 2010.

[16] M. Atkins and F. P. Glasser, “Application of portland cement-based materials to radioactive waste immobilization,” *Waste Manag.*, vol. 12, no. 2–3, pp. 105–131, 1992.

[17] F. Glasser, “Application of inorganic cements to the conditioning and immobilisation of radioactive wastes,” in *Handbook of Advanced Radioactive Waste Conditioning Technologies*,

Woodhead Publishing Limited, Cambridge, UK, 2011, pp. 67–135.

[18] Radioactive Waste Management, “Geological disposal: waste package evolution status report,” NDA Report number: DSSC/451/01, RWM-NDA, Didcot, UK, 2016.

[19] Radioactive Waste Management, “Geological disposal: guidance on the production of encapsulated wasteforms,” NDA Report number: WPS/502/01, RWM-NDA, Didcot, UK, 2015.

[20] Committee on Radioactive Waste Management, “Managing our radioactive waste safely, CoRWM’s recommendations to Government.,” CoRWM Doc 700, 2006.

[21] Committee on Radioactive Waste Management, “Committee on radioactive waste management ninth annual report 2012-2013,” CoRWM doc. 3107, 2013.

[22] Radioactive Waste Management, “Making sense of geological disposal,” RWM-NDA, Didcot, UK, 2017.

[23] Department for Business, Energy and Industrial Strategy, “Implementing geological disposal – working with implementing geological disposal – working with communities,” BEIS, London, UK, 2018.

[24] OECD Nuclear Energy Agency's Radioactive Waste Management Committee, “Moving forward with geological disposal of radioactive waste: a collective statement,” NEA Report number: 6433, Paris, France, 2008.

[25] Nuclear Decommissioning Authority, “Geological disposal: an introduction to the generic disposal system safety case,” NDA, Didcot, UK, 2010.

[26] A. Dauzeres, P. Le Bescop, P. Sardini, and C. Cau Dit Coumes, “Physico-chemical investigation of clayey/cement-based materials interaction in the context of geological waste disposal: Experimental approach and results,” *Cem. Concr. Res.*, vol. 40, no. 8, pp. 1327–1340, 2010.

[27] Nuclear Decommissioning Authority, "Geological disposal: near-field evolution status report," Report number: NDA/RWMD/033, NDA, Didcot, UK, 2010.

[28] R. G. W. Vasconcelos, N. Beaudoin, A. Hamilton, N. C. Hyatt, J. L. Provis, and C. L. Corkhill, “Characterisation of a high pH cement backfill for the geological disposal of nuclear waste: The Nirex Reference Vault Backfill,” *Appl. Geochem.*, vol. 89, pp. 180–189, 2018.

[29] Department for Energy & Climate Change, “Implementing geological disposal: a framework for the long-term management of higher activity radioactive waste,” Report number: URN 14D/235, DECC, London, UK, 2014.

[30] G. A. Fairhall and F. J. Welch, “Joint BNFL / DOE intermediate level waste programme. Product evaluation task force: phase three report for magnox swarf summary,” British Nuclear Fuels and Department of Energy, Report number: PETF(85)P32, Harwell, Oxfordshire, UK, 1986.

[31] A. Francis, “Joint BNFL / DOE intermediate level waste programme. Product evaluation task force: phase two report for magnox swarf summary,” British Nuclear Fuels and Department of Energy, Report number: PETF(84)P70, Harwell, Oxfordshire, UK, 1986.

[32] S. Curwen and F. Ridley, “Joint BNFL/DOE intermediate level waste research programme,” British Nuclear Fuels and Department of Energy, Report number: PETF(89)P40, Harwell, Oxfordshire, UK, 1989.

[33] J. H. Sharp, J. Hill, N. B. Milestone, and E. W. Miller, “Cementitious systems for encapsulation of intermediate level waste,” *Proceedings of the 9th International Conference on Environmental Remediation and Radioactive Waste Management*, Paper No. ICEM03-4554, Oxford, UK, 2003.

[34] P. C. Hewlett and M. Liska, *Lea's Chemistry of Cement and Concrete*. Fifth Edition. Oxford, UK, Butterworth-Heinemann, 2019.

[35] M. I. Ojovan and W. E. Lee, "Chapter 15: Immobilisation of Radioactive Waste in Cement," in *An Introduction to Nuclear Waste Immobilisation*, Oxford, UK, Elsevier, 2005, pp. 205–232.

[36] Nuclear Decommissioning Authority, "Waste package specification and guidance documentation, WPS/800: wasteform specification for 500 litre drum waste package: explanatory material and design guidelines," NDA Report number: 9699292, NDA, Didcot, UK, 2008.

[37] Nuclear Decommissioning Authority, "Waste package specification for 500 litre drum waste packages," NDA Report number: WPS/361/01, NDA, Didcot, UK, 2014.

[38] Nuclear Decommissioning Authority, "Geological disposal: guidance on the application of the waste package specifications for unshielded waste packages," NDA report number: w*ps/701/01*, NDA, Didcot, UK, 2014.

[39] Nuclear Decommissioning Authority, "Waste package specification and guidance documentation, WPS/906: guidance on the packaging of closed sources," NDA Report number: 10157950, NDA, Didcot, UK, 2009.

[40] Nuclear Decommissioning Authority, "Geological disposal: generic specification for waste packages containing high heat generating waste", NDA Report number: NDA/RWMD/068, NDA, Didcot, UK, 2016.

[41] J. Newman and B. S. Choo, *Advanced Concrete Technology: Constituent Materials*, vol. 2. Oxford, UK, Elsevier Butterworth-Heinemann, 2003.

[42] H. F. W. Taylor, *Cement Chemistry*, 2nd Edition, London, UK, Thomas Telford Publishing, 1997.

[43] British Standards Institute, Cement Part 1: Composition, Specifications and Conformity Criteria for Common Cements," BS EN197-1:2011, 2011.

[44] K. L. Scrivener and A. Nonat, "Hydration of cementitious materials, present and future," *Cem. Concr. Res.*, vol. 41, no. 7, pp. 651–665, 2011.

[45] J. W. Bullard, H. M. Jennings, R. A. Livingston, A. Nonat, G. W. Scherer, J. S. Schweitzer, K. L. Scrivener, J. J. Thomas, "Mechanisms of cement hydration," *Cem. Concr. Res.*, vol. 41, no. 12, pp. 1208–1223, 2011.

[46] I. G. Richardson, "The calcium silicate hydrates," *Cem. Concr. Res.*, vol. 38, no. 2, pp. 137–158, 2008.

[47] A. Nonat, "The structure and stoichiometry of C-S-H," *Cem. Concr. Res.*, vol. 34, no. 9, pp. 1521–1528, 2004.

[48] B. Lothenbach and A. Nonat, "Calcium silicate hydrates: Solid and liquid phase composition," *Cem. Concr. Res.*, vol. 78, pp. 57–70, 2015.

[49] I. G. Richardson, "Model structures for C-(A)-S-H(I)," *Acta Crystallogr. Sect. B Struct. Sci. Cryst. Eng. Mater.*, vol. 70, no. 6, pp. 903–923, 2014.

[50] S. Grangeon, F. Claret, C. Roosz, T. Sato, S. Gaboreau, and Y. Linard, "Structure of nanocrystalline calcium silicate hydrates: Insights from X-ray diffraction, synchrotron X-ray absorption and nuclear magnetic resonance," *J. Appl. Crystallogr.*, vol. 49, pp. 771–783, 2016.

[51] S. A. Bernal, R. San Nicolas, R. J. Myers, R. Mejía de Gutiérrez, F. Puertas, J. S. J. van Deventer,

J. L. Provis, “MgO content of slag controls phase evolution and structural changes induced by accelerated carbonation in alkali-activated binders,” *Cem. Concr. Res.*, vol. 57, pp. 33–43, 2014.

[52] S.-Y. Hong and F. P. Glasser, “Alkali binding in cement pastes,” *Cem. Concr. Res.*, vol. 29, no. 12, pp. 1893–1903, 1999.

[53] B. Walkley and J. L. Provis, “Solid-state nuclear magnetic resonance spectroscopy of cements,” *Mater. Today Adv.*, vol. 1, p. 100007, 2019.

[54] T. F. Sevelsted and J. Skibsted, “Carbonation of C-S-H and C-A-S-H samples studied by ^{13}C, ^{27}Al and ^{29}Si MAS NMR spectroscopy,” *Cem. Concr. Res.*, vol. 71, pp. 56–65, 2015.

[55] G. W. Groves, A. Brough, I. G. Richardson, and C. M. Dobson, “Progressive Changes in the Structure of Hardened C_3S Cement Pastes due to Carbonation,” *J. Am. Ceram. Soc.*, vol. 74, no. 11, pp. 2891–2896, 1991.

[56] E. L’Hôpital, B. Lothenbach, G. Le Saout, D. Kulik, and K. Scrivener, “Incorporation of aluminium in calcium-silicate-hydrates,” *Cem. Concr. Res.*, vol. 75, pp. 91–103, 2015.

[57] R. J. Myers, S. A. Bernal, R. San Nicolas, and J. L. Provis, “Generalized structural description of calcium-sodium aluminosilicate hydrate gels: The cross-linked substituted tobermorite model,” *Langmuir*, vol. 29, no. 17, pp. 5294–5306, 2013.

[58] K. L. Scrivener, “Backscattered electron imaging of cementitious microstructures: Understanding and quantification,” *Cem. Concr. Compos.*, vol. 26, no. 8, pp. 935–945, 2004.

[59] I. G. Richardson, “Nature of the hydration products in hardened cement pastes,” *Cem. Concr. Compos.*, vol. 22, no. 2, pp. 97–113, 2000.

[60] I. G. Richardson and G. W. Groves, “Microstructure and microanalysis of hardened cement pastes involving ground granulated blast-furnace slag,” *J. Mater. Sci.*, vol. 27, no. 22, pp. 6204–6212, 1992.

[61] H. J. H. Brouwers, “The work of Powers and Brownyard revisited: Part 1,” *Cem. Concr. Res.*, vol. 34, no. 9, pp. 1697–1716, 2004.

[62] P. D. Tennis and H. M. Jennings, “A model for two types of calcium silicate hydrate in the microstructure of Portland cement pastes,” *Cem. Concr. Res.*, vol. 30, pp. 855–863, 2000.

[63] G. Constantinides and F. J. Ulm, “The nanogranular nature of C-S-H,” *J. Mech. Phys. Solids*, vol. 55, no. 1, pp. 64–90, 2007.

[64] Radioactive Waste Management, “Geological disposal: behaviour of radionuclides and non-radiological species in the groundwater status report,” NDA Report number: DSSC/456/01, 2016.

[65] M. L. D. Gougar, B. E. Scheetz, and D. M. Roy, “Ettringite and C-S-H portland cement phases for waste ion immobilization: A review,” *Waste Manag.*, vol. 16, no. 4, pp. 295–303, 1996.

[66] G. Möschner, B. Lothenbach, F. Winnefeld, A. Ulrich, R. Figi, and R. Kretzschmar, “Solid solution between Al-ettringite and Fe-ettringite ($Ca_6[Al_{1-x}Fe_x(OH)_6]2(SO_4)_3\cdot 26H_2O$),” *Cem. Concr. Res.*, vol. 39, no. 6, pp. 482–489, 2009.

[67] G. Möschner, B. Lothenbach, J. Rose, A. Ulrich, R. Figi, and R. Kretzschmar, “Solubility of Fe-ettringite ($Ca_6[Fe(OH)_6]_2(SO_4)_3\cdot 26H_2O$),” *Geochim. Cosmochim. Acta*, vol. 72, no. 1, pp. 1–18, 2008.

[68] L. G. Baquerizo, T. Matschei, K. L. Scrivener, M. Saeidpour, and L. Wadsö, “Hydration states of

AFm cement phases," *Cem. Concr. Res.*, vol. 73, pp. 143–157, 2015.

[69] T. Matschei, B. Lothenbach, and F. P. Glasser, "The AFm phase in Portland cement," *Cem. Concr. Res.*, vol. 37, no. 2, pp. 118–130, 2007.

[70] B. Z. Dilnesa, E. Wieland, B. Lothenbach, R. Dähn, and K. L. Scrivener, "Fe-containing phases in hydrated cements," *Cem. Concr. Res.*, vol. 58, pp. 45–55, 2014.

[71] B. Lothenbach, K. Scrivener, and R. D. Hooton, "Supplementary cementitious materials," *Cem. Concr. Res.*, vol. 41, no. 12, pp. 1244–1256, 2011.

[72] S. A. Bernal, M. C. G. Juenger, X. Ke, W. Matthes, B. Lothenbach, N. De Belie, J. L. Provis, "Characterization of supplementary cementitious materials by thermal analysis," *Mater. Struct.*, vol. 50, no. 26, pp. 1–13, 2017.

[73] D. G. Mantel, "Investigation into the hydraulic activity of five granulated blast furnace slags with eight different Portland cements," *ACI Mater. J.*, no. 91, pp. 471–477, 1994.

[74] ASTM International, "Standard Specification for Coal Fly Ash and Raw or Calcined Natural Pozzolan for Use," ASTM C618 - 19, 2019.

[75] British Standards Institute, "Fly ash for concrete Part 1 : Definition, specifications and conformity criteria," BS EN 450-1:2012, 2012.

[76] K. De Weerdt, M. Ben Haha, G. Le Saout, K. O. Kjellsen, H. Justnes, and B. Lothenbach, "Hydration mechanisms of ternary Portland cements containing limestone powder and fly ash," *Cem. Concr. Res.*, vol. 41, no. 3, pp. 279–291, 2011.

[77] F. Deschner, F. Winnefeld, B. Lothenbach, S. Seufert, P. Schwesig, S. Dittrich, F. Goetz-Neunhoeffer, J. Neubauer, "Hydration of Portland cement with high replacement by siliceous fly ash," *Cem. Concr. Res.*, vol. 42, no. 10, pp. 1389–1400, 2012.

[78] P. Faucon, A. Delagrave, J. C. Petit, C. Richet, J. M. Marchand, and H. Zanni, "Aluminum incorporation in calcium silicate hydrates (C-S-H) depending on their Ca/Si ratio," *J. Phys. Chem. B*, vol. 103, no. 37, pp. 7796–7802, 1999.

[79] G. K. Sun, J. F. Young, and R. J. Kirkpatrick, "The role of Al in C-S-H: NMR, XRD, and compositional results for precipitated samples," *Cem. Concr. Res.*, vol. 36, no. 1, pp. 18–29, 2006.

[80] M. D. Andersen, H. J. Jakobsen, and J. Skibsted, "A new aluminium-hydrate species in hydrated Portland cements characterized by ^{27}Al and ^{29}Si MAS NMR spectroscopy," *Cem. Concr. Res.*, vol. 36, no. 1, pp. 3–17, 2006.

[81] J. Skibsted and M. D. Andersen, "The effect of alkali ions on the incorporation of aluminum in the calcium silicate hydrate (C-S-H) phase resulting from portland cement hydration studied by ^{29}Si MAS NMR," *J. Am. Ceram. Soc.*, vol. 96, no. 2, pp. 651–656, 2013.

[82] D. P. Prentice, S. A. Bernal, M. Bankhead, M. Hayes, and J. L. Provis, "Phase evolution of slag-rich cementitious grouts for immobilisation of nuclear wastes: an experimental and modelling approach," *Adv. Cem. Res.*, vol. 30, no. 8, pp. 345-360, 2018.

[83] M. Ben Haha, B. Lothenbach, G. Le Saout, and F. Winnefeld, "Influence of slag chemistry on the hydration of alkali-activated blast-furnace slag - Part II: Effect of Al_2O_3," *Cem. Concr. Res.*, vol. 42, no. 1, pp. 74–83, 2012.

[84] X. Ke, S. A. Bernal, and J. L. Provis, "Uptake of chloride and carbonate by Mg-Al and Ca-Al layered double hydroxides in simulated pore solutions of alkali-activated slag cement," *Cem.*

Concr. Res., vol. 100, no. October 2016, pp. 1–13, 2017.

[85] C. Altenhein-Haese, H. Bischoff, L. Fu, J. Mao, and G. Marx, “Adsorption of actinides on cement compounds,” *J. Alloys Compd.*, vol. 213–214, no. C, pp. 554–556, 1994.

[86] L. M. Parker, N. B. Milestone, and R. H. Newman, “The Use of Hydrotalcite as an Anion Absorbent,” *Ind. Eng. Chem. Res.*, vol. 34, no. 4, pp. 1196–1202, 1995.

[87] Radioactive Waste Management, "Geological disposal steps, Carbon-14 Project Phase 2: Overview Report ", NDA report number: NDA/RWM/137, 2016.

[88] R. Taylor, I. G. Richardson, and R. M. D. Brydson, “Nature of C–S–H in 20 year old neat ordinary Portland cement and 10% Portland cement–90% ground granulated blast furnace slag pastes,” *Adv. Appl. Ceram.*, vol. 106, no. 6, pp. 294–301, 2007.

[89] A. V. Girão, I. G. Richardson, R. Taylor, and R. M. D. Brydson, “Composition, morphology and nanostructure of C–S–H in 70% white Portland cement–30% fly ash blends hydrated at 55°C.,” *Cem. Concr. Res.*, vol. 40, no. 9, pp. 1350–1359, 2010.

[90] Nuclear Decommissioning Authority, “Waste Stream 2D24: Magnox Cladding and Miscellaneous Solid Waste,” 2013.

[91] Nuclear Decommissioning Authority (NDA), “Waste Stream 2D03 Plutonium Contaminated Material; Drums,” 2016.

[92] G. R. Choppin, J.-O. Liljenzin, and J. Rydberg, “Chapter 4 – Unstable Nuclei and Radioactive Decay,” in *Radiochemistry and Nuclear Chemistry*, Third Edition, Oxford, UK, Elsevier Butterworth Heinemann, 2002, pp. 58–93.

[93] M. Kelly and M. Thorne, "Radionuclides handbook", The Environment Agency, R&D Technical Report P3-101/SP1b, Almondesbury, Bristol, UK, 2003.

[94] K. G. Field, I. Remec, and Y. Le Pape, “Radiation effects in concrete for nuclear power plants - Part I: Quantification of radiation exposure and radiation effects,” *Nucl. Eng. Des.*, vol. 282, pp. 126–143, 2015.

[95] Y. Le Pape, K. G. Field, and I. Remec, “Radiation effects in concrete for nuclear power plants, Part II: Perspective from micromechanical modeling,” *Nucl. Eng. Des.*, vol. 282, pp. 144–157, 2015.

[96] I. Maruyama, “Aging management of concrete structures in nuclear power plants,” *J. Adv. Concr. Technol.*, vol. 14, p. 368, 2016.

[97] G. R. Choppin, J.-O. Liljenzin, and J. Rydberg, “Chapter 6 – Absorption of Nuclear Radiation,” in *Radiochemistry and Nuclear Chemistry*, Third Edition, Oxford, UK, Elsevier Butterworth Heinemann, 2002, pp. 123–165.

[98] I. Maruyama, O. Kontani, A. Ishizawa, M. Takizawa, and O. Sato, “Development of system for evaluating concrete strength deterioration due to radiation and resultant heat,” *Proceedings of 3rd International Conference on NPP Life Management for Long Term Operations*, IAEA-CN-194-096, Salt Lake City, 2012.

[99] J. Spinks and R. Woods, *An Introduction to Radiation Chemistry*, 2nd edition. New York, Wiley, 1976.

[100] P. Bouniol and A. Aspart, “Disappearance of oxygen in concrete under irradiation: the role of peroxides in radiolysis,” *Cem. Concr. Res.*, vol. 28, no. 11, pp. 1669–1681, 1998.

[101] P. Bouniol and E. Bjergbakke, “A comprehensive model to describe radiolytic processes in cement medium,” *J. Nucl. Mater.*, vol. 372, pp. 1–15, 2008.

[102] P. Bouniol, “The influence of iron on water radiolysis in cement-based materials,” *J. Nucl. Mater.*, vol. 403, no. 1–3, pp. 167–183, 2010.

[103] G. R. Choppin, J.-O. Liljenzin, and J. Rydberg, “Chapter 7 – Radiation Effects on Matter,” in *Radiochemistry and Nuclear Chemistry*, Third Edition, Oxford, UK, Elsevier Butterworth Heinemann, 2002, pp. 166–191.

[104] N. E. Bibler and M. L. Hyder, “Radiolytic Gas Production From Concrete Containing Savannah River Plant Waste,” 1978.

[105] K. Crapse, C. A. Langton, J. M. Duffey, L. N. Oji, and C. L. Crawford, “Updated G-values and radiolysis data for hydrated waste forms containing alpha oxide,” in *41st Actinides Separation Conference, Argonne, Illinois*, 2017.

[106] F. Vodák, K. Trtík, V. Sopko, O. Kapičková, and P. Demo, “Effect of γ-irradiation on strength of concrete for nuclear-safety structures,” *Cem. Concr. Res.*, vol. 35, no. 7, pp. 1447–1451, 2005.

[107] A. Łowińska-Kluge and P. Piszora, “Effect of gamma irradiation on cement composites observed with XRD and SEM methods in the range of radiation dose 0-1409 MGy,” *Acta Phys. Pol. A*, vol. 114, no. 2, pp. 399–411, 2008.

[108] G. Bar-Nes, A. Katz, Y. Peled, and Y. Zeiri, “The combined effect of radiation and carbonation on the immobilization of Sr and Cs ions in cementitious pastes,” *Mater. Struct.*, vol. 41, no. 9, pp. 1563–1570, 2008.

[109] F. Vodák, V. Vydra, K. Trtík, and O. Kapičková, “Effect of gamma irradiation on properties of hardened cement paste,” *Mater. Struct.*, vol. 44, no. 1, pp. 101–107, 2010.

[110] N. Mobasher, S. A. Bernal, H. Kinoshita, C. A. Sharrad, and J. L. Provis, “Gamma irradiation resistance of an early age slag-blended cement matrix for nuclear waste encapsulation,” *J. Mater. Res.*, vol. 30, no. 9, pp. 1563–1571, 2015.

[111] O. Kontani, S. Sawada, I. Maruyama, M. Takizawa, and O. Sato, “Evaluation of irradiation effects on concrete structure - background and preparation of neutron irradiation test.,” *Proceedings of the ASME 2013 Power Conference*, Boston, Massachusetts, USA, 2013.

[112] P. Soo and L. Milian, “The effect of gamma radiation on the strength of Portland cement mortars,” *J. Mater. Sci. Lett.*, vol. 20, pp. 1345–1348, 2001.

[113] T. Ichikawa and H. Koizumi, “Possibility of Radiation-Induced Degradation of Concrete by Alkali-Silica Reaction of Aggregates,” *J. Nucl. Sci. Technol.*, vol. 39, no. 8, pp. 880–884, 2002.

[114] M. Robira, B. Hilloulin, A. Loukili, G. Potin, X. Bourbon, and A. Abdelouas, “Multi-scale investigation of the effect of γ irradiations on the mechanical properties of cementitious materials,” *Constr. Build. Mater.*, vol. 186, pp. 484–494, 2018.

[115] I. Maruyama, S. Ishikawa, J. Yasukouchi, S. Sawada, R. Kurihara, M. Takizawa, O. Kontani, “Impact of gamma-ray irradiation on hardened white Portland cement pastes exposed to atmosphere,” *Cem. Concr. Res.*, vol. 108, no. April, pp. 59–71, 2018.

[116] L. Black, C. Breen, J. Yarwood, K. Garbev, P. Stemmermann, and B. Gasharova, “Structural features of C-S-H(I) and its carbonation in air-A Raman spectroscopic study. Part II: Carbonated phases,” *J. Am. Ceram. Soc.*, vol. 90, no. 3, pp. 908–917, 2007.

[117] E. T. Stepkowska, “Calcite, vaterite and aragonite forming on cement hydration from liquid and

gaseous phase," *J. Therm. Anal. Calorim.*, vol. 73, pp. 247–269, 2003.

[118] A. Morandeau, M. Thiéry, and P. Dangla, "Investigation of the carbonation mechanism of CH and C-S-H in terms of kinetics, microstructure changes and moisture properties," *Cem. Concr. Res.*, vol. 56, pp. 153–170, 2014.

[119] T. Ogino, T. Suzuki, and K. Sawada, "The formation and transformation mechanism of calcium carbonate in water," *Geochim. Cosmochim. Acta*, vol. 51, no. 10, pp. 2757–2767, 1987.

[120] D. C. McDowall, "The effect of gamma irradiation on the creep properties of concrete," Commission of the European Communities, Brussels, Belgium, Report number: EUR--4751, 1972.

[121] B. Hilloulin, M. Robira, and A. Loukili, "Coupling statistical indentation and microscopy to evaluate micromechanical properties of materials: Application to viscoelastic behavior of irradiated mortars," *Cem. Concr. Compos.*, vol. 94, no. February, pp. 153–165, 2018.

[122] I. Maruyama O. Kontani, M. Takizawa, S. Sawada, S. Ishikawa, J. Yasukouchi, O. Sato, J. Etoh, T. Igari, "Development of soundness assessment procedure for concrete members affected by neutron and gamma-ray irradiation," *J. Adv. Concr. Technol.*, vol. 15, no. 9, pp. 440–523, 2017.

[123] P. Bouniol, W. Guillot, V. Dauvois, W. Dridi, and S. Le Caër, "Original behavior of pore water radiolysis in cement-based materials containing sulfide: Coupling between experiments and simulations," *Radiat. Phys. Chem.*, vol. 150, no. March, pp. 172–181, 2018.

[124] I. G. Richardson, G. W. Groves, and C. R. Wilding, "Effect of gamma radiation on the microstructure and microchemistry of GGBFS/OPC cement blends," *MRS Symp. Proc.*, vol. 176, pp. 31–37, 1990.

[125] H. F. W. Taylor, C. Famy, and K. L. Scrivener, "Delayed ettringite formation," *Cem. Concr. Res.*, vol. 31, no. 5, pp. 683–693, 2001.

[126] R. C. Ewing, W. J. Weber, and F. W. Clinard, "Radiation effects in nuclear waste forms for high-level radioactive waste," *Prog. Nucl. Energy*, vol. 29, no. 2, pp. 63–127, 1995.

[127] J. F. Ziegler, M. D. Ziegler, and J. P. Biersack, "SRIM - The stopping and range of ions in matter (2010)," *Nucl. Instruments Methods Phys. Res. Sect. B Beam Interact. with Mater. Atoms*, vol. 268, no. 11–12, pp. 1818–1823, 2010.

[128] Nuclear Decommissioning Authority, "Waste Stream 2D22: Magnox Cladding and Miscellaneous Solid Waste," 2013.

[129] Nuclear Decommissioning Authority, "Waste Stream 2N01 Plutonium Contaminated Material; Drummed (Legacy Drums)," 2013.

[130] S. Curwen and M. J. Angus, "Review of hydraulic cements for plutonium encapsulation," Nexia solutions Report number: (07) 8903, Risley, UK, 2007.

[131] W. A. Deer, R. A. Howie, and J. Zussman, *An Introduction to the Rock-Forming Minerals*. 3rd edition, London, UK, The Mineralogical Society of Great Britain and Ireland, 2013.

[132] R. V. Gentry, "Fossil alpha-recoil analysis of certain variant radioactive halos," *Science*, vol. 160, no. 3833, pp. 1228–1230, 1968.

[133] R. V. Gentry, "Giant radioactive halos: Indicators of unknown radioactivity?," *Science*, vol. 169, no. 3946, pp. 670–673, 1970.

[134] L. Nasdala, M. Wenzel, M. Andrut, R. Wirth, and P. Blaum, "The nature of radiohaloes in biotite:

Experimental studies and modeling," *Am. Mineral.*, vol. 86, no. 4, pp. 498–512, 2001.

[135] R. A. D. Pattrick, J. M. Charnock, T. Geraki, J. F. W. Mosselmans, C. I. Pearce, S. Pimblott, G. T. R. Droop, "Alpha particle damage in biotite characterized by microfocus X-ray diffraction and FeK-edge X-ray absorption spectroscopy," *Mineral. Mag.*, vol. 77, no. 6, pp. 2867–2882, 2013.

[136] W. R. Bower, C. I. Pearce, G. T. R. Droop, J. F. W. Mosselmans, K. Geraki, and R. A. D. Pattrick, " Radiation damage from long-term alpha particle bombardment of silicates – a microfocus XRD and Fe K -edge XANES study ," *Mineral. Mag.*, vol. 79, no. 6, pp. 1455–1466, 2015.

[137] W. R. Bower, R. A. D. Pattrick, C. I. Pearce, G. T. R. Droop, and S. J. Haigh, "Radiation damage haloes in biotite investigated using high-resolution transmission electron microscopy," *Am. Mineral.*, vol. 101, no. 1, pp. 105–110, 2016.

[138] L. Nasdala, M. Wildner, R. Wirth, N. Groschopf, D. C. Pal, and A. Möller, "Alpha particle haloes in chlorite and cordierite," *Mineral. Petrol.*, vol. 86, no. 1–2, pp. 1–27, 2006.

[139] R. A. Sanderson, "Optimising blends of blast furnace slag for the immobilisation of nuclear waste," Eng.D. thesis, Dept. of Materials Science and Engineering, University of Sheffield, Sheffield, UK, 2019.

[140] British Standards Institute, "Methods of testing cement. Determination of fineness," BS EN 196-6:2018, London, UK, 2018.

[141] J. Zhang and G. W. Scherer, "Comparison of methods for arresting hydration of cement," *Cem. Concr. Res.*, vol. 41, no. 10, pp. 1024–1036, 2011.

[142] F. Winnefeld, A. Schöler, and B. Lothenbach, "Sample Preparation," in *A Practical Guide to Microstructural Analysis of Cementitious Materials*, K. Scrivener, R. Snellings, B. Lothenbach, New York, USA, CRC Press, Taylor and Francis Group, 2015, pp. 1–35.

[143] E. C. Arvaniti, M. C. G. Juenger, S. A. Bernal, J. Duchesne, L. Courard, S. Leroy, J. L. Provis, A. Klemm, N. De Belie, "Determination of particle size, surface area, and shape of supplementary cementitious materials by different techniques," *Mater. Struct.*, vol. 48, no. 11, pp. 3687–3701, 2015.

[144] L. Wadsö, F. Winnefeld, K. Riding, and P. Sandberg, "Calorimetry," in *A Practical Guide to Microstructural Analysis of Cementitious Materials*, K. Scrivener, R. Snellings, B. Lothenbach, New York, USA, CRC Press, Taylor and Francis Group, 2015, pp. 37–74.

[145] J. S. Lumley, R. S. Gollop, G. K. Moir, and H. F. W. Taylor, "Degrees of reaction of the slag in some blends with Portland cements," *Cem. Concr. Res.*, vol. 26, no. 1, pp. 139–151, 1996.

[146] K. Luke and F. P. Glasser, "Selective dissolution of hydrated blast furnace slag cements," *Cem. Concr. Res.*, vol. 17, no. 2, pp. 273–282, 1987.

[147] V. Kocaba, E. Gallucci, and K. L. Scrivener, "Methods for determination of degree of reaction of slag in blended cement pastes," *Cem. Concr. Res.*, vol. 42, no. 3, pp. 511–525, 2012.

[148] V. Kocaba, "Development and evaluation of methods to follow microstructural development of cementitious systems including slags," Ph.D. thesis, Faculty of Science, Department of Materials Science and Engineering, École Polytechnique Fédérale de Lausanne, Lausanne, 2009.

[149] P. T. Durdziński M. Ben Haha, S. A. Bernal, N. De Belie, E. Gruyaert, B. Lothenbach, E. Menéndez Méndez, J. L. Provis, A. Schöler, C. Stabler, Z. Tan, Y. Villagrán Zaccardi, A. Vollproacht, F. Winnefeld, M. Zając, K. Scrivener, "Outcomes of the RILEM round robin on degree of reaction of slag and fly ash in blended cements," *Mater. Struct.*, vol. 50, #135, 2017.

[150] H. M. Dyson, I. G. Richardson, and A. R. Brough, “A combined 29Si MAS NMR and selective dissolution technique for the quantitative evaluation of hydrated blast furnace slag cement blends,” *J. Am. Ceram. Soc.*, vol. 90, no. 2, pp. 598–602, 2007.

[151] ASTM International, “Standard test method for compressive strength of hydraulic cement mortars (using 2-in. or [50-mm] cube specimens),” ASTM C 109/C 109M-20a, West Conshohocken, PA, 2020.

[152] K. Tharmaratnam and B. S. Tan, “Attenuation of ultrasonic pulse in cement mortar,” *Cem. Concr. Res.*, vol. 20, no. 3, pp. 335–345, 1990.

[153] ASTM International, “Standard test method for pulse velocity through concrete,” C567-16, West Conshohocken, PA, 2016.

[154] J. H. Bungey and S. G. Millard, *Testing of concrete in structures*, Third Edition. Glasgow, Scotland, UK, Blackie Academic & Professional, 1996.

[155] American Concrete Institute Committee 228, “In-place methods to estimate concrete strength peported,” *ACI Comm. Reports*, Report no. 228.1R-03, p. 41, 2003.

[156] Proceq, “Operating instructions Pundit Lab / Pundit Lab + Ultrasonic Instrument,” Schwerzenbach, Switzerland, 2014.

[157] E. Berodier and K. Scrivener, “Evolution of pore structure in blended systems,” *Cem. Concr. Res.*, vol. 73, pp. 25–35, 2015.

[158] E. Berodier, J. Bizzozero, and A. C. A. Muller, “Mercury Intrusion Porosimetry,” in *A Practical Guide to Microstructural Analysis of Cementitious Materials*, K. Scrivener, R. Snellings, B. Lothenbach, New York, USA, CRC Press, Taylor and Francis Group, 2015, pp. 419–444.

[159] J. P. Gorce and N. B. Milestone, “Probing the microstructure and water phases in composite cement blends,” *Cem. Concr. Res.*, vol. 37, no. 3, pp. 310–318, 2007.

[160] H. Ma, “Mercury intrusion porosimetry in concrete technology: Tips in measurement, pore structure parameter acquisition and application,” *J. Porous Mater.*, vol. 21, no. 2, pp. 207–215, 2014.

[161] K. Scrivener, R. Snellings, and B. Lothenbach, *A Practical Guide to Microstructural Analysis of Cementitious Materials*, New York, USA, CRC Press, Taylor and Francis Group, 2016.

[162] V. Ramachandran, R. M. Paroli, J. J. Beaudoin, and A. H. Delgado, *Handbook of Thermal Analysis of Construction Materials*, First Edition. Norwich, NY, USA, William Andrew, 2002.

[163] B. Lothenbach, P. Durdziński, and K. De Weerdt, “Thermogravimetric Analysis,” in *A Practical Guide to Microstructural Analysis of Cementitious Materials*, K. Scrivener, R. Snellings, B. Lothenbach, New York, USA, CRC Press, Taylor and Francis Group, 2016, pp. 177–212.

[164] R. Guinebretière, *X-ray Diffraction by Polycrystalline Materials*. London, UK, ISTE, 2007.

[165] R. Snellings, “X-ray powder diffraction applied to cement,” in *A Practical Guide to Microstructural Analysis of Cementitious Materials*, K. Scrivener, R. Snellings, B. Lothenbach, New York, USA, CRC Press, Taylor and Francis Group, 2016, pp. 107–176.

[166] R. Snellings, A. Salze, and K. L. Scrivener, “Use of X-ray diffraction to quantify amorphous supplementary cementitious materials in anhydrous and hydrated blended cements,” *Cem. Concr. Res.*, vol. 64, pp. 89–98, 2014.

[167] B. C. Smith, *Fundamentals of Fourier Transform Infrared Spectroscopy*, Second Edition. Florida,

USA, CRC Press, 2011.

[168] K. Scrivener, A. Bazzoni, B. Mota, and J. E. Rossen, “Electron Microscopy,” in *A Practical Guide to Microstructural Analysis of Cementitious Materials*, K. Scrivener, R. Snellings, B. Lothenbach, New York, USA, CRC Press, Taylor and Francis Group, 2015, pp. 351–417.

[169] J. Skibsted, “High-resolution solid-state nuclear magnetic resonance spectroscopy of portland cement-based systems,” in *A Practical Guide to Microstructural Analysis of Cementitious Materials*, K. Scrivener, R. Snellings, B. Lothenbach, New York, USA, CRC Press, Taylor and Francis Group, 2016, pp. 213–286.

[170] Bruker, “TopSpin 4.0.6.” 2018.

[171] S. L. Poulsen, V. Kocaba, G. Le Saoût, H. J. Jakobsen, K. L. Scrivener, and J. Skibsted, “Improved quantification of alite and belite in anhydrous Portland cements by ^{29}Si MAS NMR: Effects of paramagnetic ions,” *Solid State Nucl. Magn. Reson.*, vol. 36, no. 1, pp. 32–44, 2009.

[172] M. D. Andersen, H. J. Jakobsen, and J. Skibsted, “Incorporation of aluminum in the calcium silicate hydrate (C-S-H) of hydrated Portland cements: A high-field ^{27}Al and ^{29}Si MAS NMR investigation,” *Inorg. Chem.*, vol. 42, no. 7, pp. 2280–2287, 2003.

[173] L. Leay, W. Bower, G. Horne, P. Wady, A. Baidak, M. Pottinger, M. Nancekievill, A. D. Smith, S. Watson, P. R. Green, B. Lennox, J. A. LaVerne, S. M. Pimblott, “Development of irradiation capabilities to address the challenges of the nuclear industry,” *Nucl. Instruments Methods Phys. Res. B*, vol. 343, pp. 62–69, 2015.

[174] C. A. Utton, M. Hayes, J. Hill, N. B. Milestone, and J. H. Sharp, “Effect of temperatures up to 90°C on the early hydration of Portland-blastfurnace slag cements,” *J. Am. Ceram. Soc.*, vol. 91, no. 3, pp. 948–954, 2008.

[175] J. I. Escalante-Garcia and J. H. Sharp, “The chemical composition and microstructure of hydration products in blended cements,” *Cem. Concr. Compos.*, vol. 26, no. 8, pp. 967–976, 2004.

[176] R. A. Sanderson, G. M. Cann, and J. L. Provis, “Comparison of calorimetric methods for the assessment of slag cement hydration,” *Adv. Appl. Ceram.*, vol. 116, no. 4, pp. 186–192, 2017.

[177] K. Scrivener, A. Ouzia, P. Juilland, and A. Kunhi Mohamed, “Advances in understanding cement hydration mechanisms,” *Cem. Concr. Res.*, vol. 124, no. August, p. 105823, 2019.

[178] British Standards Institute, “Cement composition, specifications and conformity criteria for very low heat special cements.,” BS EN 14216:2015, London, UK, 2015.

[179] D. Jansen, F. Goetz-Neunhoeffer, B. Lothenbach, and J. Neubauer, “The early hydration of Ordinary Portland Cement (OPC): An approach comparing measured heat flow with calculated heat flow from QXRD,” *Cem. Concr. Res.*, vol. 42, no. 1, pp. 134–138, 2012.

[180] B. Klemczak and M. Batog, “Heat of hydration of low-clinker cements,” *J. Therm. Anal. Calorim.*, vol. 123, no. 2, pp. 1351–1360, 2016.

[181] R. A. Sanderson, J. L. Provis, and G. M. Cann, “The effect of blast-furnace slag particle size on the hydration of slag – Portland cement grouts at elevated temperatures,” *Adv. Cem. Res.*, vol. 30, no. 8, pp. 337–344, 2018.

[182] W. A. Gutteridge and J. A. Dalziel, “Filler cement: The effect of the secondary component on the hydration of Portland cement: Part 1: A Fine Non-hydraulic Filler,” *Cem. Concr. Res.*, vol. 20, pp. 778–782, 1990.

[183] W. A. Gutteridge and J. A. Dalziel, “Filler cement: The effect of the secondary component on the hydration of Portland cement: Part 2: Fine hydraulic binders,” *Cem. Concr. Res.*, vol. 20, pp. 853–861, 1990.

[184] E.M.J. Berodier, “Impact of the Supplementary Cementitious Materials on the kinetics and microstructural development of cement hydration,” École Polytechnique Fédérale de Lausanne, 2015.

[185] T. Oey, A. Kumar, J. W. Bullard, N. Neithalath, and G. Sant, “The filler effect: The influence of filler content and surface area on cementitious reaction rates,” *J. Am. Ceram. Soc.*, vol. 96, no. 6, pp. 1978–1990, 2013.

[186] E. Berodier and K. Scrivener, “Understanding the filler effect on the nucleation and growth of C-S-H,” *J. Am. Ceram. Soc.*, vol. 97, no. 12, pp. 3764–3773, 2014.

[187] X. Wu, D. M. Roy, and C. A. Langton, “Early stage hydration of slag-cement,” *Cem. Concr. Res.*, vol. 13, no. 2, pp. 277–286, 1983.

[188] R. Taylor, I. G. Richardson, and R. M. D. Brydson, “Composition and microstructure of 20-year-old ordinary Portland cement-ground granulated blast-furnace slag blends containing 0 to 100% slag,” *Cem. Concr. Res.*, vol. 40, no. 7, pp. 971–983, 2010.

[189] A. Schöler, B. Lothenbach, F. Winnefeld, and M. Zajac, “Hydration of quaternary Portland cement blends containing blast-furnace slag, siliceous fly ash and limestone powder,” *Cem. Concr. Compos.*, vol. 55, pp. 374–382, 2015.

[190] X. Ke, S. A. Bernal, and J. L. Provis, “Controlling the reaction kinetics of sodium carbonate-activated slag cements using calcined layered double hydroxides,” *Cem. Concr. Res.*, vol. 81, pp. 24–37, 2016.

[191] S. J. Mills, A. G. Christy, J.-M. R. Génin, T. Kameda, and F. Colombo, “Nomenclature of the hydrotalcite supergroup: natural layered double hydroxides,” *Mineral. Mag.*, vol. 76, no. 5, pp. 1289–1336, 2012.

[192] M. Whittaker, M. Zajac, M. Ben Haha, and L. Black, “The impact of alumina availability on sulfate resistance of slag composite cements,” *Constr. Build. Mater.*, vol. 119, pp. 356–369, 2016.

[193] B. Lothenbach *et al.*, “Cemdata18: A chemical thermodynamic database for hydrated Portland cements and alkali-activated materials.,” *Cem. Concr. Res.*, vol. 115, no. October 2017, pp. 472–506, 2019.

[194] N. C. Collier, “Transition and Decomposition Temperatures of Cement Phases - a Collection of Thermal Analysis Data,” *Ceram. - Silikaty*, vol. 60, no. 4, pp. 1–10, 2016.

[195] B. Wu and G. Ye, “Development of porosity of cement paste blended with supplementary cementitious materials after carbonation,” *Constr. Build. Mater.*, vol. 145, pp. 52–61, 2017.

[196] M. Whittaker, M. Zajac, M. Ben Haha, F. Bullerjahn, and L. Black, “The role of the alumina content of slag, plus the presence of additional sulfate on the hydration and microstructure of Portland cement-slag blends,” *Cem. Concr. Res.*, vol. 66, pp. 91–101, 2014.

[197] J. A. Herterich, “Microstructure and phase assemblage of low-clinker cements during early stages of carbonation,” Ph.D. thesis, School of Civil Engineering, University of Leeds, Leeds, UK, 2017.

[198] J. I. Escalante, L. Y. Gómez, K. K. Johal, G. Mendoza, H. Mancha, and J. Méndez, “Reactivity of blast-furnace slag in Portland cement blends hydrated under different conditions,” *Cem. Concr.*

Res., vol. 31, no. 10, pp. 1403–1409, 2001.

[199] J. . Escalante-García and J. . Sharp, "The microstructure and mechanical properties of blended cements hydrated at various temperatures," *Cem. Concr. Res.*, vol. 31, no. 5, pp. 695–702, 2001.

[200] British Standards Institute, "Testing concrete — Part 4 : Determination of ultrasonic pulse velocity," BS EN 12504-4:2004, London, UK, 2004.

[201] J. Mandel, "Fitting straight lines when both variables are subject to error," *J. Qual. Technol.*, vol. 16, no. 1, pp. 1–14, 1984.

[202] R. Demirboğa, I. Türkmen, and M. B. Karakoç, "Relationship between ultrasonic velocity and compressive strength for high-volume mineral-admixtured concrete," *Cem. Concr. Res.*, vol. 34, no. 12, pp. 2329–2336, 2004.

[203] R. Gül, R. Demirboğa, and T. Güvercin, "Compressive strength and ultrasound pulse velocity of mineral admixtured mortars," *Indian J. Eng. Mater. Sci.*, vol. 13, no. 1, pp. 18–24, 2006.

[204] S. A. Omer, R. Demirboga, and W. H. Khushefati, "Relationship between compressive strength and UPV of GGBFS based geopolymer mortars exposed to elevated temperatures," *Constr. Build. Mater.*, vol. 94, pp. 189–195, 2015.

[205] C. Yang and R. Gupta, "Prediction of the Compressive Strength from Resonant Frequency for Low-Calcium Fly Ash – Based Geopolymer Concrete," *J. Mater. Civ. Eng.*, vol. 30, no. 4, pp. 1–6, 2018.

[206] I. G. Richardson, A. V. Girão, R. Taylor, and S. Jia, "Hydration of water- and alkali-activated white Portland cement pastes and blends with low-calcium pulverized fuel ash," *Cem. Concr. Res.*, vol. 83, pp. 1–18, 2016.

[207] S. Dittrich, J. Neubauer, and F. Goetz-Neunhoeffer, "The influence of fly ash on the hydration of OPC within the first 44 h - A quantitative in situ XRD and heat flow calorimetry study," *Cem. Concr. Res.*, vol. 56, pp. 129–138, 2014.

[208] P. T. Durdziński, C. F. Dunant, M. Ben Haha, and K. L. Scrivener, "A new quantification method based on SEM-EDS to assess fly ash composition and study the reaction of its individual components in hydrating cement paste," *Cem. Concr. Res.*, vol. 73, pp. 111–122, 2015.

[209] K. L. Aughenbaugh, P. Stutzman, and M. C. G. Juenger, "Identifying glass compositions in fly ash," *Front. Mater.*, vol. 3, no. January, 2016.

[210] J. E. Rossen and K. L. Scrivener, "Optimization of SEM-EDS to determine the C–A–S–H composition in matured cement paste samples," *Mater. Charact.*, vol. 123, pp. 294–306, 2017.

[211] P. T. Durdziński, M. Ben Haha, M. Zajac, and K. L. Scrivener, "Phase assemblage of composite cements," *Cem. Concr. Res.*, vol. 99, no. September 2016, pp. 172–182, 2017.

[212] L. C. Lange, C. D. Hills, and A. B. Poole, "Effect of carbonation on properties of blended and non-blended cement solidified waste forms," *J. Hazard. Mater.*, vol. 52, no. 2–3, pp. 193–212, 1997.

[213] W. Ashraf, "Carbonation of cement-based materials: Challenges and opportunities," *Constr. Build. Mater.*, vol. 120, pp. 558–570, 2016.

[214] O. Kontani, S. Sawada, I. Maruyama, M. Takizawa, and O. Sato, "Evaluation of irradiation effects on concrete structure - gamma-ray irradiation tests on cement paste," *Proceedings of the ASME 2013 Power Conference*, Boston, Massachusetts, USA, 2013.

[215] P. Feng, C. Miao, and J. W. Bullard, “Factors Influencing the Stability of AFm and AFt in the Ca - Al - S - O - H System at 25 ° C,” *J. Am. Ceram. Soc.*, vol. 99, no. 3, pp. 1031–1041, 2016.

[216] D. Damidot, S. Stronach, A. Kindness, M. Atkins, and F. P. Glasser, “Thermodynamic investigation of the $CaOAl_2O_3CaCO_3H_2O$ closed system at 25°C and the influence of Na2O,” *Cem. Concr. Res.*, vol. 24, no. 3, pp. 563–572, 1994.

[217] A. Vollpracht, B. Lothenbach, R. Snellings, and J. Haufe, “The pore solution of blended cements: a review,” *Mater. Struct. Constr.*, vol. 49, no. 8, pp. 3341–3367, 2016.

[218] D. P. Prentice, B. Walkley, S. A. Bernal, M. Bankhead, M. Hayes, and J. L. Provis, “Thermodynamic modelling of BFS-PC cements under temperature conditions relevant to the geological disposal of nuclear wastes,” *Cem. Concr. Res.*, vol. 119, no. January, pp. 21–35, 2018.

[219] S. A. Bernal, J. L. Provis, B. Walkley, R. San Nicolas, J. D. Gehman, D. G. Brice, A. R. Kilcullen, P. Duxson, J. S. J. van Devener “Gel nanostructure in alkali-activated binders based on slag and fly ash, and effects of accelerated carbonation,” *Cem. Concr. Res.*, vol. 53, pp. 127–144, 2013.

[220] K. L. Scrivener, B. Lothenbach, N. De Belie, E. Gruyaert, J. Skibsted, R. Snellings, A. Vollpracht, “TC 238-SCM: hydration and microstructure of concrete with SCMs: State of the art on methods to determine degree of reaction of SCMs,” *Mater. Struct. Constr.*, vol. 48, no. 4, pp. 835–862, 2015.

[221] R. J. Myers, S. A. Bernal, J. D. Gehman, J. S. J. Van Deventer, and J. L. Provis, “The role of al in cross-linking of alkali-Activated slag cements,” *J. Am. Ceram. Soc.*, vol. 98, no. 3, pp. 996–1004, 2015.

[222] B. Walkley, X. Ke, O. H. Hussein, S. A. Bernal, and J. L. Provis, “Incorporation of strontium and calcium in geopolymer gels,” *J. Hazard. Mater.*, vol. 382, no. August 2019, p. 121015, 2020.

[223] B. Walkley, S. J. Page, G. J. Rees, J. L. Provis, and J. V. Hanna, “Nanostructure of CaO-(Na_2O)-Al_2O_3-SiO_2-H_2O gels revealed by multinuclear solid-state magic angle spinning and multiple quantum magic angle spinning nuclear magnetic resonance spectroscopy,” *J. Phys. Chem. C*, vol. 124, pp. 1681–1694, 2020.

[224] T. Allard, J. P. Muller, J. C. Dran, and M. T. Ménager, “Radiation-induced paramagnetic defects in natural kaolinites: Alpha dosimetry with ion beam irradiation,” *Phys. Chem. Miner.*, vol. 21, no. 1, pp. 85–96, 1994.

[225] A. Nilsen and P.-C. Aitcin, “Static Modulus of Elasticity of High-Strength Concrete from Pulse Velocity Tests,” *Cem. Concr. Aggregates*, vol. 14, no. 1, p. 64, 1992.

[226] B. Kolani, L. Buffo-Lacarrière, A. Sellier, G. Escadeillas, L. Boutillon, and L. Linger, “Hydration of slag-blended cements,” *Cem. Concr. Compos.*, vol. 34, no. 9, pp. 1009–1018, 2012.

[227] J. Hill and J. H. Sharp, “The mineralogy and microstructure of three composite cements with high replacement levels,” *Cem. Concr. Compos.*, vol. 24, no. 2, pp. 191–199, 2002.

[228] B. Šavija and M. Luković, “Carbonation of cement paste: Understanding, challenges, and opportunities,” *Constr. Build. Mater.*, vol. 117, pp. 285–301, 2016.

[229] J. Skibsted, H. J. Jakobsen, and C. Hall, “Quantification of calcium silicate phases in Portland cements by ^{29}Si MAS NMR spectroscopy,” *J. Chem. Soc. Faraday Trans.*, vol. 91, no. 24, pp. 4423–4430, 1995.

[230] M. Auroy *et al.*, “Comparison between natural and accelerated carbonation (3% CO2): Impact on mineralogy, microstructure, water retention and cracking,” *Cem. Concr. Res.*, vol. 109, no. February, pp. 64–80, 2018.

[231] S. A. Kearney, B. McLuckie, K. Webb, R. Orr, I. A. Vatter, A. S. Yorkshire, C. L. Corkhill, M. Hayes, M. J. Angus, J. L. Provis "Effects of plutonium dioxide encapsulation on the physico-chemical development of Portland cement blended grouts," *J. Nucl. Mater.*, vol. 530, #151960, 2020.

[232] Radioactive Waste Management, "Packaging of plutonium contaminated material at the waste treatment complex (extension to final stage and periodic review) summary of assessment report," NDA, 2008.

[233] F. P. Glasser, "Cements in radioactive waste disposal," *International Atomic Energy Agency, IAEA-TECDOC-CD--1701*, IAEA, Vienna, 2013.

[234] H. Christensen and E. Bjergbakke, "Radiolysis of concrete," Swedish Nuclear Fuel Supply: SKBF KBS Technical Report 84-02, 1984.

[235] T. M. Rosseel, I. Maruyama, Y. Le Pape, O. Kontani, A. B. Giorla, I. Remec, J. J. Wall, M. Sitcar, C. Andrade, M. Ordonez, "Review of the current state of knowledge on the effects of radiation on concrete," *J. Adv. Concr. Technol.*, vol. 14, no. 7, pp. 368–383, 2016.

[236] P. N. Humphreys, A. Laws, and J. Dawson, "A review of cellulose degradation and the fate of degradation products under repository conditions," SERCO report to RWM-NDA ref: WT 15 05 15, Harwell, Oxfordshire, UK, 2010.

[237] I. Pavasars, J. Hagberg, H. Borén, and B. Allard, "Alkaline degradation of cellulose: mechanisms and kinetics," *J. Polym. Environ.*, vol. 11, no. 2, pp. 39–47, 2003.

[238] A. S. Lubansky, Y. L. Yeow, Y. K. Leong, S. R. Wickramasinghe, and B. Han, "A general method of computing the derivative of experimental data," *AIChE J.*, vol. 52, no. 1, pp. 323–332, 2006.

[239] R. Snellings, T. Paulhiac, and K. Scrivener, "The effect of Mg on slag reactivity in blended cements," *Waste and Biomass Valorization*, vol. 5, no. 3, pp. 369–383, 2014.

[240] S. A. Bernal, V. Rose, and J. L. Provis, "The fate of iron in blast furnace slag particles during alkali-activation," *Mater. Chem. Phys.*, vol. 146, no. 1–2, pp. 1–5, Jul. 2014.

[241] L. J. Parrot and D. C. Killoh, "Prediction of cement hydration," *Proc. Br. Ceram. Soc.*, 1984.

[242] B. Lothenbach, T. Matschei, G. Möschner, and F. P. Glasser, "Thermodynamic modelling of the effect of temperature on the hydration and porosity of Portland cement," *Cem. Concr. Res.*, vol. 38, no. 1, pp. 1–18, 2008.

[243] H. F. W. Taylor, "Modification of the Bogue calculation," *Adv. Cem. Res.*, vol. 2, no. 6, pp. 73–77, 1989.

[244] H. Yang, R. Yan, H. Chen, D. H. Lee, and C. Zheng, "Characteristics of hemicellulose, cellulose and lignin pyrolysis," *Fuel*, vol. 86, no. 12–13, pp. 1781–1788, 2007.

[245] R. R. Lloyd, J. L. Provis, and J. S. J. Van Deventer, "Microscopy and microanalysis of inorganic polymer cements. 1: Remnant fly ash particles," *J. Mater. Sci.*, vol. 44, no. 2, pp. 608–619, 2009.

[246] P. T. Durdziński, "Hydration of multi-component cements containing cement clinker , slag , calcareous fly ash and limestone," Ph.D. thesis, Faculty of Science, Department of Materials Science and Engineering, École Polytechnique Fédérale de Lausanne, Lausanne, 2016.

[247] C. L. Dickson and F. P. Glasser, "Cerium(III, IV) in cement. Implications for actinide (III, IV) immobilization," *Cem. Concr. Res.*, vol. 30, no. 10, pp. 1619–1623, 2000.

[248] C. L. Corkhill D. J. Bailey, F. Y. Tocino, M. C. Stennett, J. A. Miller, J. L. Provis, K. P. Travis, N. C. Hyatt, "Role of Microstructure and Surface Defects on the Dissolution Kinetics of CeO_2, a UO_2

Fuel Analogue," *ACS Appl. Mater. Interfaces*, vol. 8, no. 16, pp. 10562–10571, 2016.

[249] M. C. Stennett, C. L. Corkhill, L. A. Marshall, and N. C. Hyatt, "Preparation, characterisation and dissolution of a CeO_2 analogue for UO_2 nuclear fuel," *J. Nucl. Mater.*, vol. 432, no. 1–3, pp. 182–188, 2013.

[250] X. Beaudoux, M. Virot, T. Chave, G. Leturcq, G. Jouan, L. venault, P. Moisy, S. I. Nikitenko, "Ultrasound-assisted reductive dissolution of CeO_2 and PuO_2 in the presence of Ti particles," *Dalt. Trans.*, vol. 45, no. 21, pp. 8802–8815, 2016.

[251] R. Motny and S. Phongikaroon, "Compositional analysis of cerium in rapid setting cement as an immobilization agent for nuclear waste," *Trans. Am. Nucl. Soc.*, vol. 117, pp. 285–287, 2017.

[252] G. R. Choppin, J.-O. Liljenzin, and J. Rydberg, *Radiochemistry and Nuclear Chemistry*, Third Edition, Oxford, UK, Butterworth-Heinemann, 2002.

[253] A. S. Yorkshire, J. L. Provis, M. C. Stennett, D. J. Bailey, B. Walkley, S. van Meurs, S. Parry, L. Martel, O. Walters, N. C. Hyatt, C. L. Corkhill, "Understanding cement- [U , Pu , Tc] mineral systems for radioactive waste management," *Proceedings of Cement-based materials for Nuclear Wastes (NUWCEM) 2018,* Avignon, France*,* 2018.

[254] G. M. N. Baston, M. M. Cowper, and T. A. Marshall, "Sorption properties of aged cements," *Mineral. Mag.*, vol. 76, no. 8, pp. 3411–3423, 2012.

[255] E. Wieland and L. R. Van Loon, "Cementitious near-field sorption data base for performance assessment of an ILW repository in opalinus clay," *Nuclear Energy and Safety Research Department Laboratory for Waste Management, PSI technical report No. 03-06,* Paul Scherrer Institut, Villigen, Switzerland, 2003.

[256] M. Felipe-Sotelo, J. Hinchliff, N. Evans, P. Warwick, and D. Read, "Sorption of radionuclides to a cementitious backfill material under near-field conditions," *Mineral. Mag.*, vol. 76, no. 8, pp. 3401–3410, 2012.

[257] J. Tits, A. Laube, E. Wieland, and X. Gaona, "Influence of the redox state on the neptunium sorption under alkaline conditions: Batch sorption studies on titanium dioxide and calcium silicate hydrates," *Radiochim. Acta*, vol. 102, no. 5, pp. 385–400, 2014.

[258] X. Gaona, R. Dähn, J. Tits, A. C. Scheinost, and E. Wieland, "Uptake of Np(IV) by C-S-H phases and cement paste: An EXAFS study," *Environ. Sci. Technol.*, vol. 45, no. 20, pp. 8765–8771, 2011.

[259] S. Berger, G. Aouad, C. Cau Dit Coumes, P. Le Bescop, and D. Damidot, "Leaching of calcium sulfoaluminate cement pastes by water at regulated pH and temperature: Experimental investigation and modeling," *Cem. Concr. Res.*, vol. 53, pp. 211–220, 2013.

[260] M. Schwotzer, K. Konno, J. Kaltenbach, and A. Gerdes, "The rim zone of cement-based materials – Barrier or fast lane for chemical degradation?," *Cem. Concr. Compos.*, vol. 74, pp. 236–243, 2016.

[261] R. G. W. Vasconcelos, N. C. Hyatt, J. L. Provis, and C. L. Corkhill, "Long-duration leaching experiments using high-pH cement," *Proceedings of Cement-based Materials for Nuclear Wastes (NUWCEM) 2018,* Avignon, France, 2018.

[262] J. L. García Calvo, M. C. Alonso, A. Hidalgo, L. Fernández Luco, and V. Flor-Laguna, "Development of low-pH cementitious materials based on CAC for HLW repositories: Long-

term hydration and resistance against groundwater aggression," *Cem. Concr. Res.*, vol. 51, pp. 67–77, 2013.

[263] S. Jia, "Micro / nano-structural evolution in blended cement paste due to progressive deionised water leaching," Ph.D. thesis, School of Engineering, University of Leeds, Leeds, UK, 2014.

[264] Nuclear Decomissioning Authority, "Geological Disposal: Radionuclide behaviour status report" Report number NDA/RWMD/034, 2010.

[265] M. Gascoyne, *Influence of grout and cement on groundwater composition*, POSIVA working report 2002–07, Helsinki, Finland, 2002.

[266] M. Altmaier, V. Montoya, L. Duro, and A. Valls, P*roceedings of the second workshop of the Horizon 2020 CEBAMA project*, *Espoo, Finland.* KIT Scientific Publishing, Karlsruhe, Germany, 2019.

[267] ASTM International, "Standard test method for accelerated leach test for diffusive releases from solidified waste and a computer program to model diffusive, fractional leaching from cylindrical waste," ASTM C1308 – 08(2017), 2017.

[268] R. G. W. Vasconcelos, "The influence of groundwater on the mineralogy of cement for nuclear waste disposal," Ph.D. thesis, Department of Materials Science and Engineering, Faculty of Engineering, University of Sheffield, Sheffield, UK, 2019.

[269] R. Narayanan and R. M. Laine, "Synthesis of soluble aluminium carboxylates directly from aluminium hydroxide," *J. Mater. Chem.*, vol. 10, no. 9, pp. 2097–2104, 2000.

[270] S. Koritnig and P. Süsse, "Meixnerit, $Mg_6Al_2(OH)_{18}{\cdot}4H_2O$, ein neues Magnesium-Aluminium-Hydroxid-Mineral," *TMPM Tschermaks Mineral. und Petrogr. Mitteilungen*, vol. 22, no. 1, pp. 79–87, 1975.

[271] S. Miyata, "Anion-exchange properties of hydrotalcite-like compounds.," *Clays Clay Miner.*, vol. 31, no. 4, pp. 305–311, 1983.

[272] R. J. Myers, B. Lothenbach, S. A. Bernal, and J. L. Provis, "Thermodynamic modelling of alkali-activated slag cements," *Appl. Geochemistry*, vol. 61, pp. 233–247, 2015.

[273] E. T. Stepkowska, J. M. Blanes, F. Franco, C. Real, and J. L. Pérez-Rodríguez, "Phase transformation on heating of an aged cement paste," *Thermochim. Acta*, vol. 420, no. 1-2, pp. 79–87, 2004.

[274] A. E. Morandeau and C. E. White, "Role of Magnesium-Stabilized Amorphous Calcium Carbonate in Mitigating the Extent of Carbonation in Alkali-Activated Slag," *Chem. Mater.*, vol. 27, no. 19, pp. 6625–6634, 2015.

[275] P. H. R. Borges, J. O. Costa, N. B. Milestone, C. J. Lynsdale, and R. E. Streatfield, "Carbonation of CH and C-S-H in composite cement pastes containing high amounts of BFS," *Cem. Concr. Res.*, vol. 40, no. 2, pp. 284–292, 2010.

[276] F. P. Glasser, J. Marchand, and E. Samson, "Durability of concrete — Degradation phenomena involving detrimental chemical reactions," *Cem. Concr. Res.*, vol. 38, no. 2, pp. 226–246, 2008.

[277] CEBAMA, *CEBAMA Draft of the 4th and Final Project Workshop Proceedings in Karlsruhe, Germany*, Ref. Ares(2019)5084717-05/08/2019. Amphos 21 and KIT Scientific Publishing, Karlsruhe, Germany, 2019.

[278] P. Faucon, P. Le Bescop, F. Adenot, P. Bonville, J. F. Jacquinot, F. Pinneau, B. Felix, "Leaching of cement: Study of the surface layer," *Cem. Concr. Res.*, vol. 26, no. 11, pp. 1707–1715, 1996.

[279] K. Haga, M. Shibata, M. Hironaga, S. Tanaka, and S. Nagasaki, "Change in pore structure and composition of hardened cement paste during the process of dissolution," *Cem. Concr. Res.*, vol. 35, no. 5, pp. 943–950, 2005.

[280] K. G. Papadokostaki and A. Savidou, "Study of leaching mechanisms of caesium ions incorporated in Ordinary Portland Cement," *J. Hazard. Mater.*, vol. 171, no. 1–3, pp. 1024–1031, 2009.

[281] E. Bernard, A. Dauzères, and B. Lothenbach, "Magnesium and calcium silicate hydrates, Part II: Mg-exchange at the interface 'low-pH' cement and magnesium environment studied in a C-S-H and M-S-H model system," *Appl. Geochem.*, vol. 89, no. July 2017, pp. 210–218, 2018.

[282] S. Y. Hong and F. P. Glasser, "Alkali sorption by C-S-H and C-A-S-H gels: Part II. Role of alumina," *Cem. Concr. Res.*, vol. 32, no. 7, pp. 1101–1111, 2002.

[283] Health Physics Society, "Human health fact sheet, Plutonium," Argonne National Laboratory, Argonne IL, 2001.

[284] R. C. Ewing, W. J. Weber, and J. Lian, "Nuclear waste disposal-pyrochlore ($A_2B_2O_7$): Nuclear waste form for the immobilization of plutonium and 'minor' actinides," *J. Appl. Phys.*, vol. 95, no. 11 I, pp. 5949–5971, 2004.

[285] C. A. Taylor, M. K. Patel, J. A. Aguiar, Y. Zhang, M. L. Crespillo, J. Wen, H. Xue, Y. Wang, W. J. Weber, "Bubble formation and lattice parameter changes resulting from He irradiation of defect-fluorite $Gd_2Zr_2O_7$," *Acta Mater.*, vol. 115, no. 225, pp. 115–122, 2016.

[286] L. Nasdala, D. Grambole, J. Götze, U. Kempe, and T. Váczi, "Helium irradiation study on zircon," *Contrib. to Mineral. Petrol.*, vol. 161, no. 5, pp. 777–789, 2011.

[287] W. R. Bower, C. I. Pearce, A. D. Smith, S. M. Pimblott, J. F. W. Mosselmans, S. J. Haigh, J. P. McKinley, R. A. D. Pattrick, "Radiation damage in biotite mica by accelerated α-particles : A synchrotron microfocus X-ray diffraction and X-ray absorption spectroscopy study," *Am. Mineral.*, vol. 101, pp. 928–942, 2016.

[288] J. Bensted and P. Barnes, *Structure and Performance of Cements*, 2nd Edition, SPON Press, Taylor and Francis Group, London, UK, 2008.

[289] A. M. Seydoux-Guillaume, R. Wirth, L. Nasdala, M. Gottschalk, J. M. Montel, and W. Heinrich, "An XRD, TEM and Raman study of experimentally annealed natural monazite," *Phys. Chem. Miner.*, vol. 29, no. 4, pp. 240–253, 2002.

[290] D. C. Pal and T. Chaudhuri, "Radiation damage-controlled localization of alteration haloes in albite: implications for alteration types and patterns vis-à-vis mineralization and element mobilization," *Mineral. Petrol.*, vol. 110, no. 6, pp. 823–843, 2016.

[291] N. B. A. Thompson, S. E. O'Sullivan, R. J. Howell, D. B. Bailey, M. G. Gilbert, and N. C. Hyatt, "Objective Colour Analysis from Digital Images as a Nuclear Forensic Tool," *submitted to Journal of Nuclear Materials,* 2020.

[292] M. Chaouche, X. X. Gao, M. Cyr, M. Cotte, and L. Frouin, "On the origin of the blue/green color of blast-furnace slag-based materials: Sulfur K-edge XANES investigation," *J. Am. Ceram. Soc.*, vol. 100, no. 4, pp. 1707–1716, 2017.

[293] R. Steudel and T. Chivers, "The role of polysulfide dianions and radical anions in the chemical, physical and biological sciences, including sulfur-based batteries," *Chem. Soc. Rev.*, vol. 48, no.

12, pp. 3279–3319, 2019.

[294] M. Levy and J. H. O. Varley, “Radiation induced colour centres in fused quartz,” *Proc. Phys. Soc. Sect. B*, vol. 68, no. 4, pp. 223–233, 1955.

[295] G. L. C. De Lima and F. S. Lameiras, “Color change of gemstones by exposure to gamma rays,” *International Nuclear Atlantic Conference (INAC) 2015 conference proceedings,* São Paulo, Brazil, 2015.

[296] M. R. Krbetschek, J. Götze, A. Dietrich, and T. Trautmann, “Spectral information from minerals relevant for luminescence dating,” *Radiat. Meas.*, vol. 27, no. 5–6, pp. 695–748, 1997.

[297] P. Yu, R. J. Kirkpatrick, B. Poe, P. F. McMillan, and X. Cong, “Structure of Calcium Silicate Hydrate (C-S-H): Near-, Mid-, and Far-Infrared Spectroscopy,” *J. Am. Ceram. Soc.*, vol. 82, no. 3, pp. 742–748, 1999.

[298] F. A. Andersen and L. Brečević, “Infrared spectra of amorphous and crystalline calcium carbonate,” *Acta Chemica Scandinavica*, vol. 45. pp. 1018–1024, 1991.

[299] E. Tajuelo Rodriguez, W. A. Hunnicutt, P. Mondal, and Y. Le Pape, “Examination of gamma irradiated calcium silicate hydrates. Part I: chemical-structural properties,” *J. Am. Ceram. Soc.*, no. April, pp. 1–11, 2019.

[300] J. D. Arregui-Mena, P. D. Edmondson, A. A. Campbell, and Y. Katoh, “Site specific, high-resolution characterisation of porosity in graphite using FIB-SEM tomography,” *J. Nucl. Mater.*, vol. 511, pp. 164–173, 2018.

[301] S. Kelly, H. El-Sobky, C. Torres-Verdín, and M. T. Balhoff, “Assessing the utility of FIB-SEM images for shale digital rock physics,” *Adv. Water Resour.*, vol. 95, pp. 302–316, 2016.

[302] G. Gutierrez *et al.*, “Helium bubble formation in nuclear glass by in-situ TEM ion implantation,” *J. Nucl. Mater.*, vol. 452, no. 1–3, pp. 565–568, 2014.

[303] G. W. Brindley and S. Kikkawa, “A crystal-chemical study of Mg, Al and Ni, Al hydroxy-perchlorates and hydroxy- carbonates,” *Am. Mineral.*, vol. 64, no. 7–8, pp. 836–843, 1979.